

A PREDICTIVE MODEL FOR MAXIMUM INTERSTORY DRIFT RATIO (MIDR)
AND ITS IMPLEMENTATION IN PROBABILITY-BASED DESIGN AND
PERFORMANCE ASSESSMENT PROCEDURES

A THESIS SUBMITTED TO
THE GRADUATE SCHOOL OF NATURAL AND APPLIED SCIENCES
OF
MIDDLE EAST TECHNICAL UNIVERSITY

BY

TUBA EROĞLU AZAK

IN PARTIAL FULFILLMENT OF THE REQUIREMENTS
FOR
THE DEGREE OF DOCTOR OF PHILOSOPHY
IN
CIVIL ENGINEERING

JULY 2013

Approval of the thesis:

**A PREDICTIVE MODEL FOR MAXIMUM INTERSTORY DRIFT RATIO
(MIDR) AND ITS IMPLEMENTATION IN PROBABILITY-BASED DESIGN AND
PERFORMANCE ASSESSMENT PROCEDURES**

submitted by **TUBA EROĞLU AZAK** in partial fulfillment of the requirements for the degree of **Doctor of Philosophy in Civil Engineering Department, Middle East Technical University** by,

Prof. Dr. Canan Özgen
Dean, Graduate School of **Natural and Applied Sciences**

Prof. Dr. Ahmet Cevdet Yalçiner
Head of Department, **Civil Engineering**

Prof. Dr. Sinan Akkar
Supervisor, **Civil Engineering Dept., METU**

Examining Committee Members:

Prof. Dr. Polat Gülkan
Civil Engineering Dept., Çankaya University

Prof. Dr. Sinan Akkar
Civil Engineering Dept., METU

Prof. Dr. Murat Dicleli
Dept. of Engineering Sciences, METU

Prof. Dr. Haluk Sucuoğlu
Civil Engineering Dept., METU

Prof. Dr. Mehmet Nuray Aydınoglu
Earthquake Engineering Dept. KOERI, Boğaziçi University

Date: 19.07.2013

I hereby declare that all information in this document has been obtained and presented in accordance with academic rules and ethical conduct. I also declare that, as required by these rules and conduct, I have fully cited and referenced all material and results that are not original to this work.

Name, Last Name : Tuba Erođlu Azak

Signature :

ABSTRACT

A PREDICTIVE MODEL FOR MAXIMUM INTERSTORY DRIFT RATIO (MIDR) AND ITS IMPLEMENTATION IN PROBABILITY-BASED DESIGN AND PERFORMANCE ASSESSMENT PROCEDURES

Erođlu Azak, Tuba
Ph.D., Department of Civil Engineering
Supervisor : Prof. Dr. Sinan Akkar

July 2013, 242 pages

Estimating nonlinear deformation demands is important for the implementation of rational seismic design and assessment methodologies to ensure the safe and reliable response of existing and new buildings against seismic action. The nonlinear deformation demand estimations should consider the variability in ground motions as well as the uncertainties involved in structural response. This study presents probability-based seismic design and assessment procedures for code-confirming low- and mid-rise reinforced concrete Turkish buildings. The proposed methodologies account for the regional seismicity, randomness in earthquake ground motions and uncertainty in nonlinear structural response while estimating the maximum interstory drift ratio (MIDR) demands on frame type buildings. The buildings of interest have story numbers ranging between 3 and 9 stories with fundamental periods (T_1) ranging from 0.7s to 1.4s. The proposed methodologies are based on probabilistic seismic demand analysis (PSDA) that uses structure-specific predictive models. Thus, a predictive model on MIDR is also presented within the context of this study. The MIDR predictive model is a function of moment magnitude (M_w), source-to-site distance (Joyner-Boore distance, R_{jb}), site conditions (soft and stiff sites with average shear-wave velocities ranging between 180 m/s and 760 m/s in the upper 30 m of the soil profile) and strength reduction factor (R_y). The proposed probability-based methodologies can be used together with the current force-based design (FBD) and hybrid seismic

performance assessment procedures to improve their efficiency for the expected behavior of structural response under target hazard demands.

Keywords: Probability-based seismic design, probability-based seismic performance assessment, nonlinear structural response, MIDR predictive model, probabilistic seismic demand analysis (PSDA).

ÖZ

MAKSİMUM GÖRELİ KAT ÖTELEMESİ İÇİN TAHMİN DENKLEMİ VE BU DENKLEMİN İHTİMALE DAYALI TASARIM VE PERFORMANS DEĞERLENDİRME YÖNTEMLERİNE UYGULANMASI

Erođlu Azak, Tuba
Doktora, İnşaat Mühendisliđi Bölümü
Tez Yöneticisi : Prof. Dr. Sinan Akkar

Temmuz 2013, 242 sayfa

Lineer olmayan deformasyon istemlerinin ölçülmesi, mevcut ve yeni binaların sismik etkiler altında emniyetli ve güvenilir şekilde davranmalarının sağlanmasına yönelik rasyonel sismik tasarım ve değerlendirme yöntemlerinin uygulanması için önemlidir. Lineer olmayan deformasyon istemlerimin belirlenmesinde yer hareketindeki deđişkenliđin ve yapı davranımındaki belirsizliđin hesaba katılması gerekir. Bu çalışma yönetmelik uyumlu az ve orta katlı betonarme Türk binaları için ihtimale dayalı sismik tasarım ve değerlendirme yöntemleri sunmaktadır. Önerilen yöntemler çerçeve tipi binalarda maksimum görelî kat öteleme isteminin hesaplanmasında bölgesel depremselliđi, deprem yer hareketindeki rassallıđı ve lineer olmayan yapı davranımındaki belirsizliđi hesaba katmaktadır. Temel periyodları 0.7 ve 1.4 saniye arasında, kat sayıları 3 ve 9 arasında deđişen binalar üzerinde çalışılmıştır. Sunulan yöntemler yapıya-özel tahmin denklemi kullanan ihtimale dayalı sismik istem analizine dayanmaktadır. Bu nedenle, bu çalışmanın kapsamı içerisinde maksimum görelî kat öteleme istemi için bir tahmin denklemi de sunulmaktadır. Maksimum görelî kat öteleme istemi için sunulan tahmin denklemi, moment büyüklüğünün (M_w), kaynak-istasyon mesafesinin (Joyner-Boore mesafesi, R_{jb}), zemin koşullarının (zemin profilinin üst 30 m'lik kısmında ortalama kayma-dalgası hızı 180m/s ve 760m/s arasında deđişen yumuşak ve sert zemin tipleri) ve dayanım azaltma katsayısının (R_y) bir fonksiyonudur. Sunulan ihtimale dayalı yöntemler, mevcut kuvvete dayalı tasarım ve hibrid sismik performans belirleme yöntemleri ile birlikte kullanılarak

hedef tehlike istemleri altında beklenen yapısal davranımın belirlenmesindeki verimliliklerinin artırılması için kullanılabilir.

Anahtar kelimeler: İhtimale dayalı sismik tasarım, ihtimale dayalı sismik performans değerlendirme, lineer olmayan yapı davranışı, maksimum göreli kat öteleme istemi için tahmin denklemi, ihtimale dayalı sismik istem analizi.

To my family
and
in memory of my beloved brother Haydar Er...

ACKNOWLEDGMENTS

I would like to express my deepest gratitude to my supervisor Prof. Dr. Sinan Akkar for his guidance, advice, criticism, encouragements and insight throughout the research.

I would also like to thank to Prof. Dr. Polat Gülkan and Prof. Dr. Murat Dicleli for their support and advice during this research.

I owe thanks to Dr. Rui Pinho who provided me the opportunity to work as a researcher at EUCENTRE in Italy during one year. I also want to thank my colleagues Danai Kazantzidou, Romain Sousa, Luis Miguel Sousa and Mohsen Kohrangi for their support and friendship.

I would like to express my sincere thanks to Bekir Özer Ay, Özkan Kale, Abdullah Sandıkkaya, Barış Erdil, Abdullah Dilsiz and Dilek Okuyucu for their friendship, support and motivation.

My dear friend Müge Yavuzer Dündar has always been with me throughout the last ten years of my life. Thank you for your invaluable love and support whenever I need.

Ricardo Nuno Carvalho Monteiro “my dear friend” deserves my sincere thanks. Thank you so much for your friendship. I really miss our “saen-de-gor-day” lunch times.

Sevgi and Güney Özcebe deserve my special thanks for their friendship, support and motivation.

I would like to thank my lovely husband Salim for his confidence in me, for his understanding, support, patience and love.

Finally, I would like to express my deepest appreciation to my parents Müşerref Eroğlu, Ali Rıza Eroğlu, my sisters Ayşe and Aysun, for the support, understanding and motivation that they provided me throughout my life. I would also thank my niece Bilge Begüm “minik kelebeğim”, my nephews Arda Efe and Mehmet Ali for being in my life and making me smile whenever I need.

TABLE OF CONTENTS

ABSTRACT.....	v
ÖZ	vii
ACKNOWLEDGMENTS	x
TABLE OF CONTENTS.....	xi
LIST OF TABLES	xiv
LIST OF FIGURES	xv
LIST OF SYMBOLS	xxii
ABBREVIATIONS	xxiv
CHAPTERS	
1. INTRODUCTION.....	1
1.1 General.....	1
1.2 Brief Review of Probabilistic Seismic Demand Analysis (PSDA).....	4
1.3 Focus of This Study and its Contributions.....	6
1.4 Literature Review	7
1.4.1 Approximate Methods for the Estimation of Lateral Deformation Demands	7
1.4.2 Studies Based on PSDA.....	8
1.5 Organization of the Thesis.....	9
2. A STATISTICAL STUDY ON TURKISH BUILDING STOCK, DESCRIPTION OF FRAME MODELS AND GROUND MOTION DATABASE	13
2.1 General.....	13
2.2 Statistical Study on General Characteristics of Turkish Residential Buildings....	14
2.2.1 Statistics on Story Heights.....	15
2.2.2 Statistics on Plan Dimensions.....	15
2.2.3 Statistics on Number of Continuous Frames	16
2.2.4 Statistics on Span Length.....	18
2.2.5 Statistics on Geometry and Orientation of Columns	18
2.3 Description of Building Models	23
2.4 General Characteristics of the Ground Motion Database Used in this Study	27
3. INTERPRETATIONS AND OBSERVATIONS ON NONLINEAR MDOF RESPONSE	33
3.1 Introduction.....	33
3.2 Critical Remarks on the Determination of Building Response Parameters	34
3.3 Nonlinear Global Demands on Code Confirming MDOF Systems.....	37
3.4 Nonlinear IDR and MIDR Demands on Code Confirming MDOF Systems.....	44

3.4.1	Log-normality of MIDR.....	44
3.4.2	Variation of IDR Profiles in Terms of Magnitude and Distance	48
3.4.3	Dependence of MIDR on Style-of-Faulting.....	56
3.4.4	Dependence of MIDR on Soft and Stiff Site Conditions.....	61
3.4.5	Variation of MIDR with Distance and Magnitude.....	64
3.4.6	Dependence of MIDR on Fundamental Period and Story Number	74
3.4.7	Overall Statistics of MIDR for Magnitude and Distance Influence.....	75
4.	INTERPRETATIONS AND OBSERVATIONS ON NONLINEAR SDOF RESPONSE.....	79
4.1	Introduction.....	79
4.2	Identification of the Most Proper Nonlinear Static Procedure	80
4.2.1	Alternative Nonlinear Static Procedures (NSPs)	80
4.2.2	Conversion of Idealized Pushover Curves to SDOF Format	84
4.2.3	Comparisons of Nonlinear Static Procedures	85
4.3	Observations on R_y : Effects of Various Parameters on R_y	88
4.3.1	Log-normality of R_y	88
4.3.2	Dependence of R_y on Fundamental Period and Story Number.....	91
4.3.3	Relationship between MIDR and R_y	91
4.4	Further Discussions on Strength Reduction Factor.....	95
5.	A PREDICTIVE MODEL FOR ESTIMATING NONLINEAR MIDR DEMANDS ON MOMENT RESISTING FRAME SYSTEMS	99
5.1	Introduction.....	99
5.2	Estimation of MIDR Demands Using Approximate Methods	100
5.2.1	MIDR Predictive Model by Miranda (1999)	101
5.2.2	MIDR Predictive Model by Akkar et al. (2005)	108
5.2.3	MIDR Predictive Model by Medina and Krawinkler (2005).....	111
5.3	A Summary of Important Observations on MIDR from Alternative MIDR Predictive Models	113
5.4	The Predictive Model for MIDR.....	114
5.5	Evaluation of the Predictive Model.....	116
5.6	Limitations and General Features of the Proposed MIDR Model.....	121
6.	USE OF MIDR PREDICTIVE MODEL IN PROBABILITY-BASED DESIGN AND PERFORMANCE ASSESSMENT	123
6.1	Introduction.....	123
6.2	Use of Probabilistic Concepts Together with the MIDR Predictive Model.....	124
6.3	Proposed Probability-based Design and Seismic Performance Assessment Procedures.....	130
6.4	Case studies for the Proposed Seismic Design Procedure	135
6.5	Case Studies for the Proposed Seismic Performance Assessment Procedure.....	143
6.6	Addressing the Uncertainties Inherent in Ground Motions and Structural Response by the Proposed Probability Based Procedure	149

7. SUMMARY AND CONCLUSIONS.....	159
7.1 Summary.....	159
7.2 Conclusions and Contributions.....	162
7.3 Limitations and Future Work.....	163
REFERENCES	165
APPENDICES	
APPENDIX A. GROUND-STORY FLOOR PLANS OF THE 3-D BUILDINGS .	177
APPENDIX B. GEOMETRY AND MEMBER DIMENSIONS OF THE FRAMES	183
APPENDIX C. GROUND-MOTION RECORDS	189
APPENDIX D. A COMPUTER SOFTWARE FOR ESTIMATING PROBABILISTIC MIDR DEMANDS	209
D.1 Introduction.....	209
D.2 General Rules and Assumptions of the Software	210
D.2.1 Linear Fault Source.....	210
D.2.2 Background Source.....	212
D.2.3 Graphical User Interface of the Software	213
APPENDIX E. RELATIONSHIP BETWEEN MIDR AND MRDR.....	217
APPENDIX F. LATERAL STIFFNESS ESTIMATION IN FRAMES AND ITS IMPLEMENTATION TO CONTINUUM MODELS FOR LINEAR AND NONLINEAR STATIC ANALYSIS	219
F.1 General	219
F.2 Introduction	219
F.3 Continuum Model Characteristics	221
F.4 Lateral Stiffness Approximations for MRFs	222
F.5 Proposed Methodology for Describing Lateral Stiffness in Continuum Models	223
F.5.1 Computation of Story-dependent α	223
F.5.2 Calibrating the Differences in the Lateral Loading Patterns of Discrete and Continuum systems	226
F.6 Evaluation of Proposed Methodology	227
F.7 Extension of the Proposed Methodology to Nonlinear Frame Behavior.....	231
F.8 Evaluation of Proposed Method for Nonlinear Frame Behavior.....	235
F.9 Concluding Remarks	240
CURRICULUM VITAE.....	241

LIST OF TABLES

TABLES

Table 2.1 Averages and corresponding standard deviations of building floor dimensions	16
Table 2.2 Average span length statistics of continuous frames in short- and long-direction	18
Table 2.3 Important dynamic features of model frames.....	27
Table 3.1 Number of accelerograms in each magnitude and distance bin	36
Table 3.2 p values calculated from Lilliefors test to verify the normality of logarithmic MIDR for the frame set.....	45
Table 3.3 Results of ANOVA and F-Tests in terms of magnitude sub-bins (grey shaded cells show the results where null-hypothesis, independency of MIDR on T_1 and building height, cannot be rejected).....	75
Table 3.4 Results of ANOVA and F-Tests in terms of distance sub-bins (grey shaded cells show the results where null-hypothesis cannot be rejected)	75
Table 4.1 Properties of idealized pushover curves.....	82
Table 4.2 R_y and Ω values calculated using equivalent SDOF models.....	98
Table 5.1 The list of α , β_1 and β_2 parameters for each model building	103
Table 5.2 Equation constants of the MIDR predictive model	115
Table 6.1 Important dynamic and material properties of the buildings designed in the cities of Ankara and Düzce	140
Table 6.2 Important dynamic and structural parameters of 3-, 5- and 8-story frames ...	146
Table 6.3 Properties of dominating earthquake scenario and corresponding target spectral acceleration	150
Table 6.4 Major seismological properties of the candidate ground-motion set	151
Table 6.5 Final list of accelerograms that are used in nonlinear RHAs	152
Table C.1 Important features of the employed accelerograms.....	190
Table F.1. Important features of model buildings used in the derivation of story-dependent α variation, comparison of their elastic fundamental periods with those estimated from the continuum model.....	224
Table F.2 Calculated α values for the methods other than the one proposed in this study	228

LIST OF FIGURES

FIGURES

Figure 2.1 Distribution of building database in terms of total number of stories	14
Figure 2.2 Mean values and standard deviations of short and long floor plan directions (S refers to short-direction on floor plan; L refers to long-direction on floor plan; Stdev is the standard deviation about the mean of short- or long-direction lengths)	15
Figure 2.3 Mean values and standard deviations of short-to-long directions (S/L ratio) in terms of story number (Stdev refers to standard deviation about mean S/L)	16
Figure 2.4 Percentages of continuous and discontinuous frames in terms of their floor plan directions (The abbreviations “Cont” and “DisC” stand for continuous and discontinuous frames, respectively).....	17
Figure 2.5 Percentages of continuous frames in short- and long-directions	17
Figure 2.6 Distribution of strong directions of columns according to floor plan directions	19
Figure 2.7 Average column width statistics in short direction of the floor plan with respect to story number.....	19
Figure 2.8 Average column width statistics in long direction of the floor plan with respect to story number.....	20
Figure 2.9 Average column depth statistics in short direction of the floor with respect to story number	20
Figure 2.10 Average column depth statistics in long direction of the floor plan with respect to story number.....	21
Figure 2.11 Average column depth-to-width ratio (d_2/d_1) statistics in short direction of the floor plan as a function of story number.....	22
Figure 2.12 Average column depth-to-width ratio (d_2/d_1) statistics in long direction of the floor plan as a function of story number.....	22
Figure 2.13 Mean column area statistics along the total building height.....	23
Figure 2.14 Ground-story floor plan of the 3-story building that is generated and designed using PROBINA Orion Software (Prota, 2008). The design complies with all relevant Turkish codes including Turkish Earthquake Code (TEC, 2007).....	24
Figure 2.15 Stress-strain relationship of Concrete01 (left panel) and EPP (right panel) material objects.....	25
Figure 2.16 3-story model frame and its member dimensions.....	26

Figure 2.17 M_w versus R_{jb} distribution of the selected ground motion database in terms of style-of-faulting (i.e., normal, strike slip and reverse).....	28
Figure 2.18 M_w versus R_{jb} distribution of the selected ground motion database in terms of NEHRP C and D site classes.....	28
Figure 2.19 Design spectrum for $A_0=0.4g$ and Z3 site conditions (TEC07) versus acceleration response spectra of accelerograms in M_w - R_{jb} bins.....	30
Figure 2.20 Design spectrum for $A_0=0.4g$ and Z3 site conditions (TEC07) versus acceleration response spectra of accelerograms in M_w - R_{jb} bins.....	31
Figure 3.1 Comparison of maximum base shear $(V_{base})_{max}$ versus maximum roof displacement demands of 3-story building (3S_MRF) for adjacent magnitude bins	38
Figure 3.2 Comparison of maximum base shear $(V_{base})_{max}$ versus maximum roof displacement demands of 4-story building (4S_MRF) for adjacent magnitude bins	39
Figure 3.3 Comparison of maximum base shear $(V_{base})_{max}$ versus maximum roof displacement demands of 5-story building (5S_MRF) for adjacent magnitude bins	40
Figure 3.4 Comparison of maximum base shear $(V_{base})_{max}$ versus maximum roof displacement demands of 7-story building (7S_MRF) for adjacent magnitude bins	41
Figure 3.5 Comparison of maximum base shear $(V_{base})_{max}$ versus maximum roof displacement demands of 8-story building (8S_MRF) for adjacent magnitude bins	42
Figure 3.6 Comparison of maximum base shear $(V_{base})_{max}$ versus maximum roof displacement demands of 9-story building (9S_MRF) for adjacent magnitude bins	43
Figure 3.7 Log-normal fits on MIDR demands for the frame set and their comparison with the actual distribution of observed MIDR as well as the Kolmogorov-Smirnov goodness-of-fit test at 5% significance	46
Figure 3.8 Normal Q-Q plots for the logarithmic MIDR demands for the entire frame set	47
Figure 3.9 Variation of median IDR profiles along the building height for different magnitude bins	49
Figure 3.10 Variation of median + σ IDR profiles along the building height for different magnitude bins	50
Figure 3.11 Variation of median IDR profiles along the building height for different distance bins	51
Figure 3.12 Variation of median + σ IDR profiles along the building height for different distance bins	52
Figure 3.13 Comparison of MIDR demands between the largest two magnitude bins. The red circles enclosing some of the MIDR values from the $M_w +7$ bin designate the nonlinear RHA results of the 1999 Düzce Earthquake	53

Figure 3.14 (a) Distribution of failed and not-converged records in terms of distance and magnitude (b) outlier MIDR values (scatters to the right of vertical red line) that are disregarded in the statistical analyses	54
Figure 3.15 Influence of SoF on MIDR.....	57
Figure 3.16 Scatter plots of each M_w - R_{jb} bin where ANOVA tests are performed to assess the influence of normal (N) and strike slip (SS) faulting on MIDR demands computed from each model frame	58
Figure 3.17 Scatter plots of each M_w - R_{jb} bin where ANOVA tests are performed to assess the influence of normal (N) and reverse (R) faulting on MIDR demands computed from each model frame	59
Figure 3.18 Scatter plots of each M_w - R_{jb} bin where ANOVA tests are performed to assess the influence of strike-slip (SS) and reverse (R) faulting on MIDR demands computed from each model frame	60
Figure 3.19 Variation of MIDR as functions of (a) distance and (b) magnitude bins for different site classes	62
Figure 3.20 Scatter plots of each M_w - R_{jb} bin where ANOVA tests are performed to assess the influence of NEHRP C and NEHRP D site class on MIDR demands computed from each model frame	63
Figure 3.21 Comparison of MIDR demands on 3-story model for adjacent magnitude bins	65
Figure 3.22 Comparison of MIDR demands on 4-story model for adjacent magnitude bins	65
Figure 3.23 Comparison of MIDR demands on 5-story model for adjacent magnitude bins	66
Figure 3.24 Comparison of MIDR demands on 7-story model for adjacent magnitude bins	66
Figure 3.25 Comparison of MIDR demands on 8-story model for adjacent magnitude bins	67
Figure 3.26 Comparison of MIDR demands on 9-story model for adjacent magnitude bins	67
Figure 3.27 Comparison of MIDR demands on 3-story model for adjacent distance bins	68
Figure 3.28 Comparison of MIDR demands on 4-story model for adjacent distance bins	69
Figure 3.29 Comparison of MIDR demands on 5-story model for adjacent distance bins	70
Figure 3.30 Comparison of MIDR demands on 7-story model for adjacent distance bins	71
Figure 3.31 Comparison of MIDR demands on 8-story model for adjacent distance bins	72
Figure 3.32 Comparison of MIDR demands on 9-story model for adjacent distance bins	73
Figure 3.33 Dependency of MIDR on (a) fundamental period and (b) total height. The solid squares represent the median values of each frame model. The MIDR logarithmic standard deviations (σ) of each model are also given on these plots .	74
Figure 3.34 Variation of median MIDR together with ± 1 standard deviation error bars against distance for different magnitude bins. The solid lines are nonlinear fits to show the overall trend in MIDR variation	77

Figure 3.35 Variation of median MIDR together with ± 1 standard deviation error bars against magnitude for different distance bins. The solid lines are nonlinear fits to show the overall trend in MIDR variation	78
Figure 4.1 Illustrative sketch of idealized PO curves for (a) FEMA-356 (FEMA, 2000), (b) modified FEMA-356, (c) ATC-40 (ATC, 1996) and (d) ASCE/SEI 41-06 (ASCE, 2007).....	81
Figure 4.2 Pushover curves of model buildings together with their idealizations. The base shear values are normalized by the total building weight whereas roof displacement are normalized by building height	83
Figure 4.3 Force-displacement relation of equivalent SDOF models	84
Figure 4.4 Roof displacement ratios calculated from nonlinear RHA of equivalent SDOF and MDOF models of 3-, 4-, 5-, 7-, 8- and 9- story frames. The red solid circles represent the mean value of each group.....	86
Figure 4.5 The cumulative probability densities of C values computed from each idealization method.....	87
Figure 4.6 Kolmogorov-Smirnov goodness-of-fit results for the log-normality assumption of R_y -distribution.....	89
Figure 4.7 Q-Q plots of the logarithms of R_y values for the frame set used in this study	90
Figure 4.8 Dependence of R_y on (a) fundamental period and (b) total building height ...	91
Figure 4.9 Dependence of MIDR on R_y using entire database.....	92
Figure 4.10 Variation of MIDR as a function of R_y for different magnitude bins	93
Figure 4.11 Variation of MIDR as a function of R_y for different distance bins	94
Figure 4.12 Unreduced design spectrum together with the elastic response spectra of the ground-motion dataset.....	96
Figure 4.13 Reduced design spectrum for $R=8$ together with the idealized capacities of the model buildings in ADRS format	96
Figure 4.14 Comparison of elastic demand and general force versus displacement demands of structures.....	97
Figure 5.1 Overall variations of β_3 and β_4	105
Figure 5.2 Error scatters of inelastic MIDR predictions against R_y for the Miranda (1999) procedure.....	106
Figure 5.3 Residual scatters of the MIDR predictions from Miranda (1999) in terms of M_w and R_{jb}	107
Figure 5.4 Variation of γ_3 in terms of ρ together with real estimations for each frame .	109
Figure 5.5 Error scatters of inelastic MIDR predictions according to Akkar et al. (2005) procedure.....	110
Figure 5.6 Residual scatters of the MIDR estimations by Akkar et al. (2005) in terms of M_w (upper panel) and R_{jb} (lower panel).....	111
Figure 5.7 Error scatters of MIDR estimates for Medina and Krawinkler (2005)	112
Figure 5.8 Residual scatters of the MIDR estimations of Medina and Krawinkler (2005) in terms of M_w (upper panel) and R_{jb} (lower panel).....	113

Figure 5.9 Residual plots of the predictive model in terms of (a) M_w and (b) R_{jb} . The overall trends of the residuals are shown with red lines; a 2 nd order fit on the residual scatters.....	117
Figure 5.10 Comparison of predicted and observed MIDR scatters together with difference and error scatter diagrams for strength reduction factor.....	118
Figure 5.11 Variation of median MIDR estimations with R_{jb} for $R_y=1$ (top, left panel), $R_y=2$ (top, right panel), $R_y=3$ (bottom, left panel) and $R_y=4$ (bottom, right panel)	119
Figure 5.12 Variation of median MIDR estimations with M_w for $R_y=1$ (top, left panel), $R_y=2$ (top, right panel), $R_y=3$ (bottom, left panel) and $R_y=4$ (bottom, right panel) ...	120
Figure 5.13 Variation of median and median $\pm \sigma$ MIDR estimations with M_w for $R_y=4$ and NEHRP C site class	121
Figure 6.1 Illustration of $P(\text{MIDR} > x _{M_w, R_{jb}})$ for constant strength reduction factor and known site class. The site class is assumed as homogenous in the location of interest in this illustrative example. (Modified from Baker, 2008)	127
Figure 6.2 Schematic illustration of the proposed probabilistic concept	129
Figure 6.3 Schematic illustration of the proposed seismic design procedure	132
Figure 6.4 Schematic illustration of the proposed seismic performance assessment procedure	134
Figure 6.5 UHS versus TEC07 design spectra for $T_R=475$ years for the Düzce and Ankara case studies	137
Figure 6.6 Typical floor plans and the cross-sectional views of 2D frames that are designed for the Ankara and Düzce case studies. The dashed rectangular boxes show the frames designed for each case.	139
Figure 6.7 Comparisons of idealized PO curves and UHS utilized for design in ADRS format.....	141
Figure 6.8 MIDR curves for the Düzce and Ankara case studies in terms of (a) annual exceedance rate (b) return period	143
Figure 6.9 UHS versus TEC07 design spectra for $T_R=475$ years for Düzce case study	144
Figure 6.10 Comparison of idealized PO curves of (a) 3S_MRF, (b) 5S_MRF, (c) 8S_MRF with UHS and code-based design spectrum for Düzce in ADRS format	145
Figure 6.11 Estimated $\text{MIDR}_{\text{performance}}$ levels for the three frames	147
Figure 6.12 Plastic hinge pattern at the estimated $\text{MIDR}_{\text{performance}}$ for frames 3S_MRF, 5S_MRF and 8S_MRF	148
Figure 6.13 UHS for different return periods for the case studies of Section 6.6.....	150
Figure 6.14 Pseudo acceleration response spectra of scaled accelerograms of 3-story building for CMS computed for different return periods	153
Figure 6.15 Pseudo acceleration response spectra of scaled accelerograms of 5-story building for CMS computed for different return periods	153
Figure 6.16 Pseudo acceleration response spectra of scaled accelerograms of 8-story building for CMS computed for different return periods	154

Figure 6.17 Probabilistic MIDR curves computed for distinct R_y values that correspond to different target hazard levels (or return periods) for 3-story model building. Their comparisons with the corresponding MIDR values of nonlinear RHA that are obtained from the scaled accelerogram of the same target hazard levels. The median MIDR for each scatter group is designated by solid square in these plots	155
Figure 6.18 Probabilistic MIDR curves computed for distinct R_y values that correspond to different target hazard levels (or return periods) for 5-story model building. Their comparisons with the corresponding MIDR values of nonlinear RHA that are obtained from the scaled accelerogram of the same target hazard levels. The median MIDR for each scatter group is designated by solid square in these plots	156
Figure 6.19 Probabilistic MIDR curves computed for distinct R_y values that correspond to different target hazard levels (or return periods) for 8-story model building. Their comparisons with the corresponding MIDR values of nonlinear RHA that are obtained from the scaled accelerogram of the same target hazard levels. The median MIDR for each scatter group is designated by solid square in these plots	156
Figure A.1 Ground-story floor plan of the 4-story building that is generated and designed using PROBİNA Orion Software (Prota, 2008). The design complies with all relevant Turkish codes including Turkish Earthquake Code (TEC, 2007)	178
Figure A.2 Ground-story floor plan of the 5-story building that is generated and designed using PROBİNA Orion Software (Prota, 2008). The design complies with all relevant Turkish codes including Turkish Earthquake Code (TEC, 2007)	179
Figure A.3 Ground-story floor plan of the 7-story building that is generated and designed using PROBİNA Orion Software (Prota, 2008). The design complies with all relevant Turkish codes including Turkish Earthquake Code (TEC, 2007)	180
Figure A.4 Ground-story floor plan of the 8-story building that is generated and designed using PROBİNA Orion Software (Prota, 2008). The design complies with all relevant Turkish codes including Turkish Earthquake Code (TEC, 2007)	181
Figure A.5 Ground-story floor plan of the 9-story building that is generated and designed using PROBİNA Orion Software (Prota, 2008). The design complies with all relevant Turkish codes including Turkish Earthquake Code (TEC, 2007)	182
Figure B.1 4S_MRF model and member dimensions	184
Figure B.2 5S_MRF model and member dimensions	185
Figure B.3 7S_MRF model and member dimensions	186
Figure B.4 8S_MRF model and member dimensions	187
Figure B.5 9S_MRF model and member dimensions	188
Figure D.1 Simple sketch of possible fault ruptures on a single-line fault. On the upper panel, the centers of the fault ruptures are indicated with black dots. On the lower panel, the centers of fault ruptures and the rupture segments are designated with the same color code	211

Figure D.2 Schematic illustration of rupture locations (upper panel) and top-view of the selected rupture surfaces of a representative multi-line fault with a slip rate different than 90^0 (lower panel)	212
Figure D.3 Schematic illustration of background source geometry, sub-division into the smaller areas	213
Figure D.4 GUI of the developed software	214
Figure D.5 View of the analysis window of the software	215
Figure D.6 Sample view of deaggregation analysis window of the program	216
Figure E.1 The relationship between MIDR and MRDR	217
Figure F.1 Heightwise variation of α in (a) 10-story and (b) 15-story frames of building sets 1 to 8	225
Figure F.2 Variation of CF (solid line) computed from fundamental-mode loading patterns of each building set	227
Figure F.3 Error surfaces of roof displacements in percent as a function of story number and ρ for (a) HS73, (b) HI99, (c) Muto and (d) this study under first-mode loading pattern	230
Figure F.4 (a) Exact and approximate elastic lateral displacement profiles of the 15-story frame from Building Set 4, (b) Exact vs. approximate fundamental periods of the entire building models	231
Figure F.5 Failure mechanisms and the conservation of work concept	232
Figure F.6 (a) Representative moment-curvature relations and their idealizations for RC column and beam sections; (b) their implementation to global $M-\phi$ relation of the continuum model	233
Figure F.7 Flowchart that summarizes the entire steps in the proposed procedure	235
Figure F.8 3- and 8-story RC MRFs from Turkish construction practice that are used in the evaluation of continuum model in the nonlinear range. 3-story frame fails under the hybrid mechanism whereas 8-story frame shows a beam-sway failure pattern	236
Figure F.9 Sensitivity analyses on the verification of α behavior along the building height for systems failing under beam-sway mechanism	237
Figure F.10 Comparisons of PO curves and corresponding lateral displacement profiles during the nonlinear static analysis of the sample RC MRFs and the corresponding continuum models. Note that lateral profiles of discrete systems (computed from OpenSees) are given in discrete intervals to compare the genuine and approximate profiles more clearly	238
Figure F.11 Exact vs. approximate $S_{d,ie}$ computed from the idealized PO curves of discrete and continuum models	239

LIST OF SYMBOLS

A_0	: Effective ground acceleration coefficient
a	: A control parameter for the shape of the lateral load (Miranda, 1999)
α	: A parameter defined by Heidebrecht and Stafford Smith (1973) to control shear and flexural deformations in continuum model
α_1	: First mode effective modal mass factor
α_{sig}	: Significance level
b_1 - b_9	: Equation constants of the proposed MIDR predictive model
β	: Parameter of the exponential magnitude distribution
β_1 - β_4	: Parameters of the MIDR predictive model by Miranda (1999)
DR_{ave}	: Average instantaneous drift ratio
d_1	: Column depth
d_2	: Column width
Δ	: Roof displacement
$\Delta_{j,i}$: Lateral displacement at the bottom end of the j^{th} column at the i^{th} story
$\Delta_{j,i+1}$: Lateral displacement at the top end of the j^{th} column at the $(i+1)^{th}$ story
$(\Delta_{roof})_{max}$: Maximum roof displacement demand
Δ_y	: Yield roof displacement
Δ_u	: Ultimate roof displacement
E	: Error
\bar{E}	: Mean error
EI	: Total flexural stiffness
ε	: Number of standard deviations above and below central estimations
ε_{cu}	: Concrete strain at crushing strength
ε_{c0}	: Concrete strain at maximum strength
ε_{sy}	: Steel yield strain
$\phi_{1,r}$: First-mode modal amplitude at the roof
ψ_j	: Mode shape of the continuum model at the height corresponding to the j^{th} floor
GA	: Total shear stiffness
$GSDR_{sh}$: Ground story drift ratio for shear beam
Γ_1	: First-mode modal participation factor
γ_1, γ_2	: Parameters of the MIDR predictive model by Akkar et al. (2005)
γ_3	: The product of the parameters γ_1 and γ_2
H	: Total building height
h	: Column height

K_e	: Effective stiffness
K^*	: Effective stiffness of equivalent SDOF system
M	: Total building mass
M_w	: Moment magnitude
$MIDR_{\text{predicted}}$: Predicted MIDR using approximate methods
$MIDR_{\text{observed}}$: Estimated MIDR using nonlinear RHA
μ_{SDOF}	: Displacement ductility ratio of the equivalent SDOF system
μ_{story}	: Maximum story displacement ductility ratio
n	: Number of columns at each story
v	: IDR reduction factor of Eurocode 8 (CEN, 2004)
R	: Structural behavior factor
R_{jb}	: Joyner and Boore distance (Joyner and Boore, 1981)
R_y	: Strength reduction factor
S_d	: Spectral displacement
$S_{d,e}$: Elastic displacement of equivalent SDOF system
$S_{d,ie}$: Inelastic displacement of equivalent SDOF system
$S_{d,y}$: Yield displacement of equivalent SDOF system
σ	: Standard deviation
σ_c	: Concrete compressive strength
σ_E	: Standard deviation of error
$\sigma_{\log 10(\text{MIDR})}$: Standard deviation term of the proposed MIDR equation
$\sigma_{\log 10(\text{MRDR})}$: Standard deviation term of the proposed MRDR equation
σ_y	: Steel yield strength
σ_1	: Intra-event variability
σ_2	: Inter-event variability
T_{eff}	: Effective period of equivalent SDOF system
T_R	: Return period
T_1	: Fundamental period
$\theta_{s,\text{max}}$: Median maximum interstory drift ratio (Medina and Krawinkler, 2005)
$u(z)$: Lateral deformation profile
V	: Base shear
$(V_{\text{base}})_{\text{max}}$: Maximum base shear
V_E	: Elastic base shear
V_M	: Ultimate base shear
V_S	: Reduced base shear
$V_{s,30}$: Average shear wave velocity of the first 30 m
V_y	: Yield base shear
W_{max}	: The intensity of the distributed load at the roof
ζ	: Damping ratio

ABBREVIATIONS

ADRS	: Acceleration-Displacement Response Spectrum
ANOVA	: Analysis of Variance
AveSL	: Average Span Length
CDF	: Cumulative Distribution Function
CMS	: Conditional Mean Spectrum
Cont	: Continuous
CP	: Collapse Prevention
DisC	: Discontinuous
DR	: Drift Ratio
EDP	: Engineering Demand Parameter
EPP	: Elastic Perfectly Plastic
FBD	: Force Based Design
GMPE	: Ground-Motion Prediction Equation
GSDR	: Ground Story Drift Ratio
GUI	: Graphical User Interface
HS73	: Heidebrecht and Stafford Smith (1973)
I	: Interior
IM	: Intensity Measure
IO	: Immediate Occupancy
IDR	: Interstory Drift Ratio
KS	: Kolmogorov Smirnov
L	: Long direction
LS	: Life Safety
MaxSL	: Maximum Span Length
MinSL	: Minimum Span Length
MDOF	: Multi-Degree-of-Freedom
MIDR	: Maximum Interstory Drift Ratio
MRDR	: Maximum Roof Drift Ratio
MRF	: Moment Resisting Frame
NSP	: Nonlinear Static Procedure
O	: Exterior
PBD	: Performance-Based Design
PBEE	: Performance-Based Earthquake Engineering
PDE	: Partial Differential Equation
PEER	: Pacific Earthquake Engineering Research

PGA	: Peak Ground Acceleration
PGV	: Peak Ground Velocity
PO	: Pushover
PSA	: Pseudo Spectral Acceleration
PSDA	: Probabilistic Seismic Demand Analysis
PSHA	: Probabilistic Seismic Hazard Analysis
Q-Q	: Quantile-Quantile
RC	: Reinforced Concrete
RHA	: Response History Analyses
S	: Short direction
SDOF	: Single-Degree-of-Freedom
SMRF	: Steel Moment Resisting Frame
SoF	: Style-of-Faulting
SSE	: Sum of Squared Errors
Stdev	: Standard deviation
SWF	: Shear Wall Frame
US	: United States
2-D	: 2 Dimensional
3-D	: 3 Dimensional
3S_MRF	: 3 story Moment Resisting Frame
4S_MRF	: 4 story Moment Resisting Frame
5S_MRF	: 5 story Moment Resisting Frame
7S_MRF	: 7 story Moment Resisting Frame
8S_MRF	: 8 story Moment Resisting Frame
9S_MRF	: 9 story Moment Resisting Frame

CHAPTER 1

INTRODUCTION

1.1 General

Turkey, located in a highly seismic region, has experienced many destructive earthquakes in the past. A total number of 82 earthquakes with moment magnitudes $M_w \geq 6$ hit the country in the last century. Eight of these earthquakes resulted in thousands of casualties and collapsed buildings (Erzincan 1939, Tosya 1943, Gerede 1944, Varto 1966, Adapazarı 1967, Erzincan 1992, Kocaeli 1999, Düzce 1999 and Bingöl 2003). Among them, the Erzincan earthquakes, with 53 years of difference, nearly destroyed the city of Erzincan and the city had to be rebuilt twice in the last century. These devastating earthquakes caused high economic losses with a consequence of significant socio-economic impact. For example, the total direct loss of the Kocaeli Earthquake (17 August 1999) is estimated to be U.S. \$6 billion (Sezen et al., 2000). Although the indirect losses caused by the Kocaeli Earthquake cannot be estimated accurately and are wide spread over a very long term, the speculations point figures as much as direct losses (Erdik and Durukal, 2003). Beyond its damaging effects and large numbers of casualties, the Kocaeli Earthquake served as a milestone for questioning the seismic performance and safety of the Turkish building stock against seismic action. The recent Van Earthquake (23 October 2011) with M_w 7.2 and the Van-Edremit Earthquake (M_w 5.9, 9 November 2011) once again called for the importance of proper earthquake resistant design and construction quality that can significantly reduce the socio-economic impacts of moderate to large scale earthquakes in Turkey. To this end, the probability-based design and seismic performance assessment tools introduced in this dissertation are believed to contribute to the ongoing engineering efforts in mitigating the earthquake induced hazard in Turkey.

The current design approach of the Turkish Earthquake Code (TEC, 2007) uses force-based design (FBD) concept. Confined to four seismic zones within the Turkish territory, the design spectrum is defined as a function of seismic zone, site class and building importance factor. The design spectrum is allowed to be reduced by the structural behavior

factor (R) that is defined according to the structure type (e.g., cast in-situ or prefabricated reinforced concrete buildings and steel building) and ductility level (i.e., normal and high ductility levels). The seismic design approach provided by the code aims at achieving a structural performance such that buildings suffer some damage within the limits of predefined damage states rather than responding elastically when subjected to moderate or large size earthquakes. This concept is primarily driven by the economic constraints provided that structures can sustain inelastic deformations by conforming the code-based detailing requirements. The main focus of FBD is the lateral strength capacity although structural and non-structural deformations are checked against some code-driven displacement limits at the end of the design process. If these limits are satisfied, the design process is finalized. Otherwise the design is revised by increasing member sizes to satisfy the code-based drift limits. The design procedure works only in one direction and does not properly verify the final structural performance on the basis of target seismic demands. The code limits overlook the uncertainty associated with the structural response, seismicity level and record-to-record variability. This is particularly true for the imposed maximum interstory drift limit that is defined as 2% regardless of the structural type. Structural designs that differ significantly in terms of structural response or levels of seismic demands are checked against the same drift limit. Consequently, buildings that satisfy this drift limit are assumed to satisfy the expected performance as well.

It should be noted that the story drift control is necessary to warrant the sufficiency of lateral capacity to prevent excessive structural and non-structural damage. Drift demands due to seismic action essentially depend on level of seismicity, record-to-record variability and nonlinear structural response. Controlling the story drifts with a constant drift limit that is described in a deterministic manner will provide a certain level of lateral capacity but would not reveal solid information about the optimum structural behavior against future earthquakes resulting from different seismic activity. In other words, such deterministic drift limits may result in either over safe or unsafe structural performance depending on the level of seismicity at the target hazard level. A rationale seismic design approach must consider the design process as a multi-level problem. It should impose drift limits to ensure the likely building capacity from a probabilistic perspective by considering the level of seismicity, structural response and intricate nature of ground-motion variability.

Similar to other seismic rehabilitation codes (e.g., ASCE/SEI 41-06, 2007; Eurocode 8, 2004), the Turkish Earthquake Code (TEC, 2007) provides several methodologies for seismic performance assessment of existing buildings. These methodologies differ in accuracy as well as complexity due to the underlying assumptions and simplifications inherent in different analysis types (i.e., linear static, nonlinear static and nonlinear dynamic analysis). Although nonlinear response history analysis (RHA) is the most accurate way to predict nonlinear demands of structures compared to the other alternative solutions, it is generally not preferred due to its complex and time consuming nature. On the other hand, nonlinear static procedures (NSPs), or their simplified derivatives, are

widely preferred in most of the recent seismic guidelines (e.g., the above cited documents) due to their conceptual simplicity and practicality in implementation.

Regardless of the methodology applied for assessing the seismic performance of structural systems, their roots originate from deterministic structural analysis. For example, the current NSPs are devised for estimating the median response of structural behavior and do not consider random nature of ground motions. The methods that rely on RHA use acceleration time histories that match a target response spectrum. Depending on the number of accelerograms used in RHA or the record scaling methodology implemented for matching with the target seismic demand, the average or the maximum structural response is used to define the performance of the structure for a predefined target. The exceedance or non-exceedance likelihoods of structural response for the target performance level (or damage limit state) are not considered after RHA (Shome and Cornell, 1999). Moreover, the record scaling methodologies have different aspects while addressing the ground-motion uncertainty (Shome and Cornell, 1999) and should be used carefully depending on the objectives of seismic performance assessment (Jayaram et al., 2011). Nevertheless, the current RHA approach, with the limitations discussed in the above lines, is still appealing with respect to NSPs as the latter methods totally disregard the uncertainties involved between the ground motion and building response (Valley, 2011).

The target seismic performance levels used in current assessment procedures are generally defined by certain drift limits that also have deterministic basis. These drift limits do not properly account for the level of seismicity or aleatory variability inherent in earthquake induced ground motions. For example, in Turkish Earthquake Code (TEC, 2007) the immediate occupancy, life safety and collapse prevention drift limits are defined as 1%, 3% and 4% of maximum interstory drift ratios, respectively. These suggested limits do not carry any indication about their likely variability due to the uncertainties that may arise from different seismic activity, record-to-record variability or interaction between ground motions and structural behavior. Under the light of these discussions robust seismic design and performance assessment procedures that properly combine the uncertainties in ground motions as well as dynamic structural response are still of need for seismic design and rehabilitation guidelines.

The cited limitations of seismic design and performance assessment procedures have motivated many researchers to propose methodologies with different levels of complexity under the framework of performance-based earthquake engineering (PBEE). The main objective of PBEE is to ensure the expected structural behavior by satisfying target performance levels with realistic quantification of seismic demand and structural capacity through the incorporation of randomness in seismic action and uncertainties in structural response. This way, the performance objectives can be estimated in terms of exceedance probabilities of engineering demand parameters (EDPs) that can be further associated with structural capacity, damage and loss functions. This philosophy leads to predictable and quantitatively definable seismic performance for the given level of seismic risk. This way,

structures with the same performance expectations (e.g., life safety) can be designed on the basis of uniform risk. Accordingly, protection and safety of building stocks against seismic action can be ensured in a more reliable manner. One particular outcome of this approach is the risk-targeted design spectrum (Luco et al., 2007) that is currently implemented in ASCE/SEI 7-10 (ASCE, 2010).

The above summarized PBEE philosophy has been the inspiration of this study that aims at estimating the nonlinear structural demands on the basis of a target engineering demand parameter (EDP). The EDP chosen in this study is maximum interstory drift ratio (MIDR) as it correlates well with structural damage and is used extensively in current seismic design and rehabilitation guidelines. The MIDR is estimated in a fully probabilistic manner for a given annual exceedance rate. This approach is initially presented by Bazzurro (1998) under the probabilistic seismic demand analysis (PSDA) concept. The PSDA-based design and performance assessment methods proposed in this study can be considered as auxiliary tools to remedy the missing components of FBD procedures that are implemented extensively in current seismic design codes such as the Turkish Earthquake Code (TEC, 2007). The following sections first describe the rationale and recent developments in PSDA and then introduce the major focus and contributions of this study. The chapter concludes with a literature review on the topics studied by the thesis and the organization of the report.

1.2 Brief Review of Probabilistic Seismic Demand Analysis (PSDA)

PSDA can be carried out by following different approaches (Shome and Cornell, 1999). One of the alternatives is based on Monte Carlo simulations. For a given site, the nonlinear building response is calculated from nonlinear RHA under earthquake induced ground motions that can be produced by the seismic sources in the proximity of the site. Since actual ground motions compiled from strong-motion databases would not be sufficient to fully assess the nonlinear structural response, the Monte Carlo simulations are used to generate synthetic ground motions that can occur on the seismic sources of interest. The exceedance probability of the chosen EDP is then calculated by summing up the contributions from all seismic sources. Although this methodology provides accurate information in terms of nonlinear structural response, it has certain disadvantages. Firstly, thousands of nonlinear RHA need to be carried out for reliable estimations of nonlinear demands (e.g., Collins et al. 1996; Han and Wen 1997; Wen 2001). This computational burden compromises the practical use of this methodology for several engineering applications. The mixed use of synthetic and actual ground motions may also result in several compatibility problems because synthetic ground motions, based on the methodology used in their generation, have limitations (Akkar et al., 2012).

The PSDA methodology by Pacific Earthquake Engineering Research (PEER) Center (Cornell and Krawinkler, 2000) decouples PSDA into probabilistic seismic hazard

assessment (PSHA) and nonlinear RHA components. These modules are studied and executed independently and linked together using a ground-motion intensity measure (IM). This approach directly correlates the chosen EDP with the IM (e.g., pseudo-spectral acceleration, peak ground acceleration or peak ground velocity). Thus, the number of nonlinear RHA required for the calculation of seismic demands is considerably less when compared to the Monte Carlo approach. There are several complexities due to the underlying assumptions of PEER-PSDA model. One of the assumptions in this model is the conditional independence among the analysis stages. The chosen EDP that is the biproduct of nonlinear RHA module is assumed to depend only on the IM of concern and its variation with other ground-motion parameters of seismological importance (e.g., magnitude, source-to-site distance) is overlooked. The independency of the selected EDP from seismological ground-motion parameters is defined as sufficiency condition in PSDA-based procedures (Luco, 2002). This requirement should be verified by certain statistical analysis tools for a reliable PSDA methodology. Thus, many researchers have looked for alternative intensity measures that comply with the sufficiency requirement (Luco, 2002; Luco and Cornell, 2007; Akkar and Özen, 2005; Vamvatsikos and Cornell, 2005; Tothong, 2007, Lin et al., 2011). Luco (2002) also puts forward the efficiency condition on the concerned IM such that an efficient IM should result in small dispersion about median EDP values in order to reduce the number of nonlinear RHA required for relating the chosen EDP with IM. The literature is also abundant in different IM proposals that fulfill the efficiency and sufficiency conditions. However, none of the proposed IMs fully complies with the efficiency and sufficiency conditions required by Luco (2002) as no IM can perfectly correlate with EDPs of common engineering interest (e.g., maximum roof or interstory roof drifts) for the entire spectral period band (Luco and Cornell, 2007). Thus, EDP vs. IM relationships will always be prone to errors due to random nature of ground motions and complex structural behavior. In passing, it should be noted that the representation of hazard curves that are conditioned on the chosen IM may also be exposed to a certain level of error as they are generally expressed by simple mathematical approximations (Aslani and Miranda, 2005; Bradley and Dhakal, 2008; Vamvatsikos, 2012).

The final PSDA approach is based on the estimation of structural demands (EDPs) through predictive models that make use of seismological estimator parameters (Shome and Cornell, 1999). This dissertation further improves the aforementioned PSDA concept by including a structural parameter for increasing the accuracy of EDP estimations. The structure-specific predictive model identifies the uncertainties associated with ground motions (source, path and site effects) and structural response and pools them in a single functional form that is associated with a standard deviation. The standard deviation accounts for these uncertainties over the median estimations of concerned EDP. In a way, the derived predictive model describes the probability distribution of EDP conditioned on the chosen ground-motion and structural parameters. The major advantage of this approach is the direct estimation of EDP from independent structural and seismological variables. In essence, the PSDA approach of this study does not utilize ground-motion IMs (e.g., pseudo

spectral acceleration, pseudo spectral velocity) as intermediate variables between seismic hazard and structural response and it provides a practical methodology by direct estimation of EDPs from seismological and structural parameters. As indicated, the likely uncertainties of these independent estimator parameters as well as their interaction are addressed by the standard deviation of the EDP predictive model. The number of nonlinear RHA of this methodology is less when compared to the Monte Carlo simulations. However, the size of nonlinear RHA is significantly larger than the PEER-PSDA concept as the EDP predictive model tries to establish a solid relationship for accurate estimation of median EDP trends as well as the uncertainty about median EDPs. This PSDA approach is considered for this dissertation after evaluating its advantages and disadvantages with respect to other alternatives that are described in the previous paragraphs.

1.3 Focus of This Study and its Contributions

The main focus of this dissertation is to propose probability-based seismic design and performance assessment methodologies for code-conforming mid- and low-rise reinforced concrete (RC) Turkish frame buildings. The proposed methodologies consider the randomness in earthquake ground motions and uncertainty in nonlinear structural response. They are the products of PSDA approach that aims at expressing the earthquake induced structural displacements in a probabilistic manner. The proposed methodologies can address the limitations of the FBD design methods and hybrid seismic performance assessment procedures that make use of force- and displacement-based concepts within a deterministic framework. Although the proposed methodologies are confined to RC frames and do not consider high-rise buildings, proper adjustments can extend their use for other structural systems (e.g., dual RC buildings with shear walls or steel structures).

While correlating the seismic demands with nonlinear structural response, the proposed methodologies make use of maximum interstory drift ratio (MIDR) as the engineering demand parameter (EDP). The main reason for using MIDR as the decisive EDP relies on its good performance with structural and non-structural damage. Past earthquakes have revealed that the earthquake induced damage is primarily caused by lateral deformations (Miranda, 1999). In this sense, MIDR is a proper EDP for identifying the required lateral deformation capacity. Notwithstanding, the MIDR-based PSDA models can be converted to maximum roof drift ratio (MRDR) through simple modifications as discussed in the dissertation.

In order to achieve the major objective of this study, there is a need for a predictive model for estimating MIDR demands under seismic action. This secondary objective is accomplished by deriving a predictive model for estimating MIDR demands using important seismological and structural estimator parameters. The proposed MIDR predictive model is developed as a function of moment magnitude (M_w), source-to-site distance (Joyner-Boore distance, R_{jb}), site conditions (soft and stiff sites with average

shear-wave velocities ranging between 180 m/s and 760 m/s in the upper 30 m of the soil profile) and strength reduction factor (elastic to yield strength of a single-degree-of-freedom system, R_y). The predictive model produces median (logarithmic mean) MIDR estimations and considers the aleatory variability (record-to-record variability) with a logarithmic standard deviation.

The major contribution of the proposed procedures (besides the MIDR predictive model) is the estimation of annual exceedance rates of MIDR demands at predefined levels. This information can easily be converted to exceedance or non-exceedance probabilities for a certain MIDR value by using Poisson process assumption. Thus, the MIDR exceedance rates as well as the exceedance rates of ground-motion demands can be compared consistently provided that the seismic demands (i.e., spectral ordinates for design or performance verification) follow Poisson process. Essentially, under these practical assumptions, the proposed PSDA-based seismic design and performance assessment procedures can convey reliable lateral capacity information of buildings that is compatible with the seismicity of the region of concern.

1.4 Literature Review

The study areas and major products of this dissertation are mainly related to two particular fields of research that can be classified as “studies concerning the estimation of lateral deformation demands” and “studies based on PSDA.” The subsequent sections present a brief review on some of the prominent studies about these topics.

1.4.1 Approximate Methods for the Estimation of Lateral Deformation Demands

So far, much effort has been devoted on the estimation of lateral deformation demands on buildings. These studies are mainly based on simplified models of actual structural systems. Representative continuum models as a combination of shear and flexural beams are widely used as approximations to real buildings. First attempts to calculate lateral deformations of buildings date back to the first half of the 20th century. Westergaard (1933) used the equivalent undamped shear beam concept for modeling tall buildings under earthquake induced shocks through the implementation of shear waves propagating in the continuum media to estimate lateral deformation demands. Later, the shear beam model has been implemented by many researchers (e.g. Iwan, 1997; Gülkan and Akkar, 2002; Akkar et al., 2005; Chopra and Chintanapakdee, 2001) to approximate the earthquake induced deformation demands (maximum interstory drift ratios, MIDR) on frame systems.

The idea of using equivalent shear beams was extended to the combination of continuous shear and flexural beams by Khan and Sbarounis (1964). Heidebrecht and Stafford Smith (1973) (hereinafter HS73) defined a continuum model for approximating tall shear wall-frame type hybrid structures that is based on the solution of a fourth order partial

differential equation (PDE). Miranda (1999) presented the solution of this PDE under a set of lateral static loading cases to approximate the maximum roof and interstory drift demands on first-mode dominant structures. Later, Heidebrecht and Rutenberg (2000) developed a different version of the HS73 method to draw the upper and lower bounds of interstory drift ratio (IDR) demands on frame systems. Medina and Krawinkler (2005) focused on non-deteriorating regular moment resisting frames subjected to ordinary ground motions. They investigated the dependence of drift demands on different ground motion intensities, fundamental period (T_1) and number of stories. They proposed formulations for average drift ratio in terms of IMs, period and total height. Miranda and Taghavi (2005) used the HS73 model to assess the approximate structural behavior up to 3 modes. As a follow-up study, Miranda and Akkar (2006) expressed MIDR in terms of mode shape, modal participation factor and relative displacement response of a SDOF system. They used the continuum model as an approximation to the general building behavior. They combined the SDOF response with mode shape using the continuum model for the first six modes of vibration.

The above mentioned studies significantly differ from the proposed MIDR predictive model (Chapter 5) in approximating the MIDR values. They make use of spectral ordinates while estimating the MIDR demands on structures whereas the proposed model directly estimates MIDR by considering the important seismological and structural parameters. The record-to-record to variability and uncertainty in structural response is considered by the associated standard deviation. In this sense, it is believed that the proposed MIDR model can meet the current engineering needs in terms of structural design and seismic performance assessment.

1.4.2 Studies Based on PSDA

The first proposal for a structure related parameter in probability-based risk integral is relatively new. Inoue and Cornell (1990) defined a damage index that is the ratio of maximum story drift to story drift capacity and used it together with spectral velocity (IM) to calculate the annual exceedance probability of the damage index. Bazzurro and Cornell (1994) formulized post-elastic damage conditional on magnitude and source-to-site distance within a probabilistic framework. Luco and Cornell (1998) aimed to combine the conventional spectral acceleration hazard curve with the results of nonlinear RHA of steel moment resisting frames (SMRF). They presented a procedure by evaluating the drift demand hazard and the annual probability when the drift exceeds the drift capacity. The relationship between spectral acceleration and drift is established by performing nonlinear RHA of MDOF models under various ground motions of different intensities. Later, Bazzurro (1998) proposed the Probabilistic Seismic Demand Analysis (PSDA) concept. In his study, Bazzurro (1998) presented procedures for the probabilistic estimation of structural displacements. Shome and Cornell (1999) summarized the drawbacks of conventional procedures that are used for estimating seismic demands of MDOF structures. They proposed alternative PSDA methodologies that aim to overcome the shortcomings of conventional nonlinear seismic analysis procedures. Gupta and

Krawinkler (1999) established a relationship between story drifts and spectral acceleration and derived annual exceedance probabilities of story drift demands by using the studies of Cornell (1996) and Luco and Cornell (1998). Krawinkler et al. (2003) established statistically sound mathematical relationships between intensity measures (spectral acceleration) and engineering demand parameters (interstory drift ratio) for regular frames subjected to ordinary ground motions that do not show any pulse-type signal. Krawinkler et al. (2003) used these relationships with hazard curves of pseudo spectral acceleration to define the exceedance probability of chosen EDPs for certain threshold levels. The authors stated that EDPs can be related with reasonable accuracy to an IM such as elastic spectral acceleration. Jalayer (2003) conducted direct probabilistic seismic analysis and proposed an alternative way to link ground motion hazard and structural response. Aslani and Miranda (2005) also conducted probability-based seismic response analysis and considered the uncertainty in structural response together with record-to-record variability. They established a relationship between spectral displacement (IM) and interstory drift ratio (EDP) to derive annual exceedance rates of this structural demand parameter. Baker and Cornell (2005) intended to improve the accuracy of PSDA by searching better IMs. In his work, Baker and Cornell (2005) proposed vector-valued IM concept that combines pseudo-spectral acceleration and epsilon (number of standard deviations above or below the median pseudo-spectral acceleration obtained from a ground-motion prediction equation). In a latter study Luco and Cornell (2007) investigated structure-specific scalar intensity measures to suggest optimum IMs that comply with the efficiency and sufficiency requirements of PSDA. Tothong (2007) implemented PSDA by making use of complex IMs and ground-motion prediction equations by focusing on near-fault effects. Goulet et al. (2007) evaluated the seismic performance of a code-complying building by applying a fully probabilistic approach for the entire performance assessment process starting from seismic hazard analysis and ending with loss estimation. Lin (2008) also worked on improved IMs for PSDA. Similar studies that propose optimum IMs for reliable PSDA outputs are conducted by various researchers as well (e.g., Cordova et al., 2000; Baker and Cornell 2004; Luco et al. 2002; Tothong and Luco, 2007). The major objective of these studies is to provide improvements on PEER-PSDA approach. Recently, risk-targeted design spectrum concept has been introduced by Luco et al. (2007) that further combines the outputs of PSDA with seismic damage and loss within a probabilistic framework. By making use of several fragility curves, Luco et al. (2007) produced risk-targeted design maps for the US territory that is implemented in ASCE/SEI 7-10 (ASCE, 2010).

1.5 Organization of the Thesis

This dissertation is composed of seven chapters. The first chapter discusses the importance of probability-based seismic design and performance assessment procedures within the framework of PSDA that can provide improvements over the currently used code-based FBD and hybrid (combination of force- and displacement-based concepts) seismic performance assessment procedures. The introduction of these concepts is used for

describing the philosophical background of probability-based seismic design and assessment procedures that are proposed in this study. These procedures can serve as auxiliary tools for improving the relevant design and performance assessment provisions of the Turkish Earthquake Code (TEC, 2007) as well as other similar seismic guidelines.

Chapter 2 presents a statistical study on the general characteristics of Turkish RC building stock. This chapter presents 3-D building models that are generated on the basis of this statistical study. The general properties of these buildings as well as assumptions made in their modeling and design are given. Representative 2-D frames are extracted from these buildings that are used in the derivation of MIDR predictive model. This chapter also presents the general features of the ground-motion database that is utilized together with the 2-D frames to develop the aforementioned MIDR model.

Chapter 3 summarizes the nonlinear response history analysis (RHA) results of the 2-D model frames used in this study. The log-normality of MIDR as well as its dependence on important ground-motion characteristics (i.e., magnitude, source-to-site distance, style-of-faulting and site conditions) are investigated. This chapter also presents the statistical results about the dependence of MIDR on fundamental period and total building height that are used in the development of the MIDR predictive equation.

Chapter 4 presents the idealized equivalent SDOF representations of model frames by making use of several NSPs. A detailed analysis is carried out to obtain the most accurate description for the idealization of equivalent SDOF systems among the alternative NSPs. After identifying the optimum NSP, the rest of the chapter discusses the nonlinear RHA results of equivalent SDOF systems to investigate (a) the log-normality of R_y (strength reduction factor), (b) the dependence of R_y on fundamental period and building height, and (c) the relationship between R_y and MIDR. The observations made from these studies are also used in Chapter 5 while developing the MIDR predictive model. The chapter concludes with a limited discussion on the over strength factors that are computed from the 2-D model buildings used in this study.

Chapter 5 presents the performance of three approximate MIDR methods that use spectral information to estimate MIDR demands on frame type buildings. The common approach used by these methods (i.e., utilization of spectral ordinates for estimating MIDR demands) is similar to the current code applications. The performance of these methods are assessed through simple statistical measures and discussions about their performance on estimating MIDR emphasize the conceptual difference in the proposed MIDR predictive model of this dissertation. The final part of this chapter is devoted to the introduction of proposed MIDR model and its major features in terms of seismological and structural parameters.

Chapter 6 presents the PSDA-based seismic design and performance assessment procedures together with their underlying theory. These methods make use of the MIDR predictive model described in Chapter 5. Several case studies are discussed throughout this

chapter to describe the implementation of these methodologies as auxiliary tools for the current force-based design and hybrid seismic performance assessment procedures. The chapter ends with an additional set of case studies that investigates the limitations of the proposed methods in terms of modeling uncertainty.

Chapter 7 gives a general summary of the entire dissertation with emphasize on its major contributions on PSDA-based seismic design and performance assessment procedures. There are several appendices at the end of the dissertation. They describe the ground-motion database, details of model buildings, the graphical user interface (GUI) developed for the easy implementation of proposed procedures in Chapter 6, an empirical conversion relationship to estimate the maximum roof drift ratio (MRDR) from MIDR as well as a practical methodology for the rapid estimation of global pushover curves for frame buildings. The last two appendices can be used to modify the proposed PSDA-based seismic design and assessment procedures for utilizing MRDR instead of MIDR.

CHAPTER 2

A STATISTICAL STUDY ON TURKISH BUILDING STOCK, DESCRIPTION OF FRAME MODELS AND GROUND MOTION DATABASE

2.1 General

Estimating nonlinear response of structures within a probabilistic framework requires incorporation of uncertainties in the computational process that are inherent in structural properties as well as earthquake ground motion. The uncertainties related with structural properties are mainly due to the variability in structural geometry and material characteristics. When structural geometry is of concern, variation in beam and column section geometries, story heights, span lengths, discontinuities within the frames, orientation of columns, etc. significantly contribute to the randomness in structural response. The uncertainties in material response are mainly due to the randomness of material properties as well as time related and environmental factors. Consideration of uncertainty in material behavior is a challenging task as it significantly increases the number of models and analysis for accurate estimation of structural response (Ay, 2006). Accordingly, this study only considers the uncertainties related to the structural geometry. Material properties are taken as deterministic and invariant for the building models that are utilized to estimate the nonlinear structural response. In order to incorporate the uncertainties in the structural geometry, the building models utilized in this dissertation are designed on the basis of a statistical study that compiles general characteristics of the Turkish reinforced concrete (RC) buildings.

This chapter first summarizes the statistical study that covers several residential RC buildings compiled from the Bakırköy district in İstanbul. The buildings used in the statistical study are provided by the PROTA Engineering and Consultancy Inc. that is involved in many seismic retrofitting projects in Turkey. A total of 333 residential buildings are investigated within this context. Discussions on the statistical study are followed by the summary of six RC building models that are designed by using the Turkish Earthquake Code (TEC, 2007). The member dimensions of these buildings are computed

from the result of the aforementioned statistical study. This part also presents the analytical models of these 2-D frame buildings that are extracted from their 3-D representations. These buildings are utilized in the entire dissertation to develop the MIDR predictive model and the probabilistic approach for seismic design and performance assessment of frame buildings. The chapter ends with the general features of the earthquake ground-motion database utilized in this study.

2.2 Statistical Study on General Characteristics of Turkish Residential Buildings

The Bakırköy database includes both moment-resisting and shear-wall frame systems (abbreviated as MRF and SWF, respectively). Of the entire building inventory, MRF buildings constitute the majority (96%). The Bakırköy district is located in the most prone seismic zone (Zone I) according to the Turkish Seismic Zonation Map. Approximately half of the Turkish territory (42% of the country) is designated as Zone I according to this map and the building inventory compiled from Bakırköy is believed to resemble the general characteristics of Turkish building stock in Zone I locations. The distribution of the compiled building database in terms of total number of stories is given in Figure 2.1.

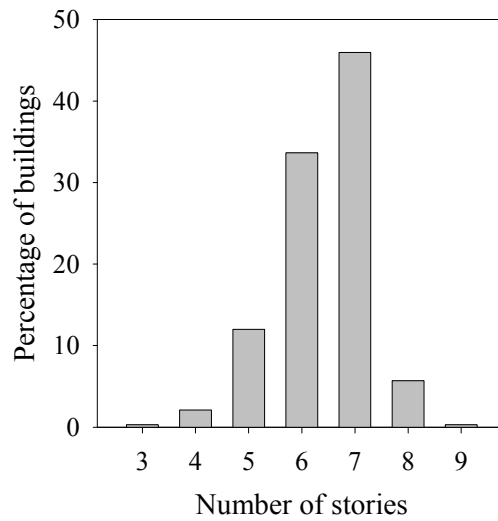


Figure 2.1 Distribution of building database in terms of total number of stories

Figure 2.1 depicts that buildings with 6 and 7 stories constitute the majority in the building database. Buildings with 3 and 9 stories are very small in percentage. They are excluded from the statistical study as they cannot be taken as representative samples of their groups. The rest of the buildings (331 buildings) are examined for their various geometrical aspects such as floor dimensions, story heights, structural member sizes, number of continuous and discontinuous frames, etc. The statistical information about these specific building properties are given in the consecutive subsections.

2.2.1 Statistics on Story Heights

Buildings are investigated for their ground-story height and story heights above the ground level (the latter group is designated as normal-story height). Mean value of the ground story height is 2.98 m regardless of story number with a standard deviation of 0.42 m. The mean of normal-story height is determined as 2.8 m. It is also independent of story number with a standard deviation of 0.1 m. Building data are also examined by binning the frames according to their story numbers but the results for mean ground-story height and mean normal-story height are approximately the same as above figures.

2.2.2 Statistics on Plan Dimensions

The general floor plan of the buildings is rectangular. This geometry is independent of the story number. Mean values and standard deviations of long and short floor plan directions (abbreviated as long-direction and short-direction herein after) in terms of story number are presented in Figure 2.2. The ratio of short-to-long directions for different story numbers are shown in Figure 2.3. Note that long- and short-direction in terms of floor plans dimension may also be the indications of strong and weak axis of the buildings.

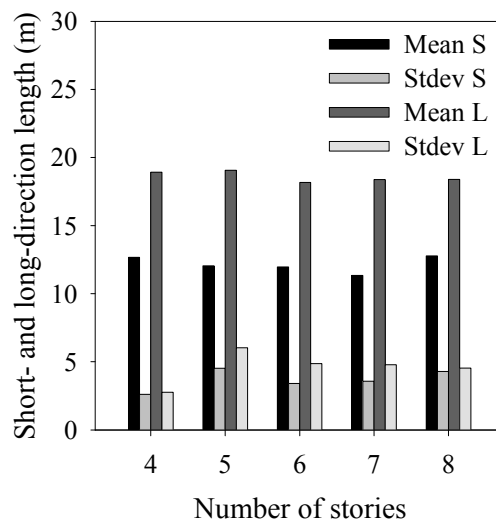


Figure 2.2 Mean values and standard deviations of short and long floor plan directions (S refers to short-direction on floor plan; L refers to long-direction on floor plan; Stdev is the standard deviation about the mean of short- or long-direction lengths)

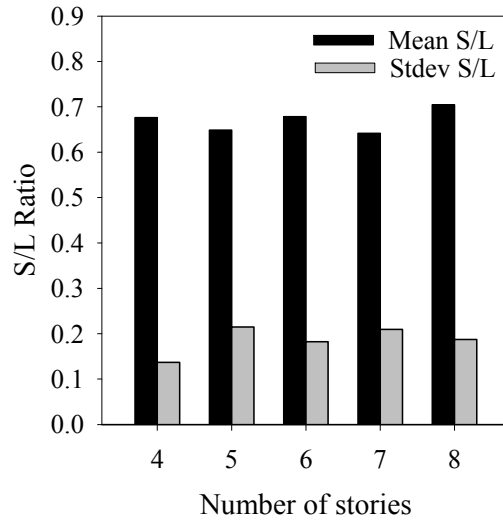


Figure 2.3 Mean values and standard deviations of short-to-long directions (S/L ratio) in terms of story number (Stdev refers to standard deviation about mean S/L)

Figures 2.2 and 2.3 suggest that planar dimensions are not influenced by the variations in story number. The mean and standard deviation values of the short- and long-direction lengths of investigated buildings are summarized in Table 2.1.

Table 2.1 Averages and corresponding standard deviations of building floor dimensions

	Mean (m)	Standard Deviation
Short-direction	11.8	3.7
Long-direction	18.4	4.9
Short/Long direction	0.66	0.2

2.2.3 Statistics on Number of Continuous Frames

One of the general characteristics of Turkish buildings is the existence of discontinuous frames. In order to simulate general Turkish residential buildings, the number of continuous and discontinuous frames in short and long directions are examined. The number of continuous frames is determined as 1428 among 301 buildings. This number is 2189 for discontinuous frames. Figure 2.4 presents a histogram showing continuous and discontinuous frames according to their orientation on the floor plan.

The number of continuous frames is also counted according to their locations on the floor plan. A continuous frame that is located in the vicinity of floor geometrical center is called as interior continuous frame. In a similar way when a continuous frame is located close to the outer edge, it is called as exterior continuous frame. This type of grouping is not done

for discontinuous frames as the focus of this study is confined to continuous frame models. The percentages of continuous frames in short- and long-directions are given in Figure 2.5. The first letters L and S in Figure 2.5 refer to continuous frames oriented in the long- and short-directions on the floor plan, respectively. The second letters I and O used in the same figure indicate interior and exterior continuous frames, respectively.

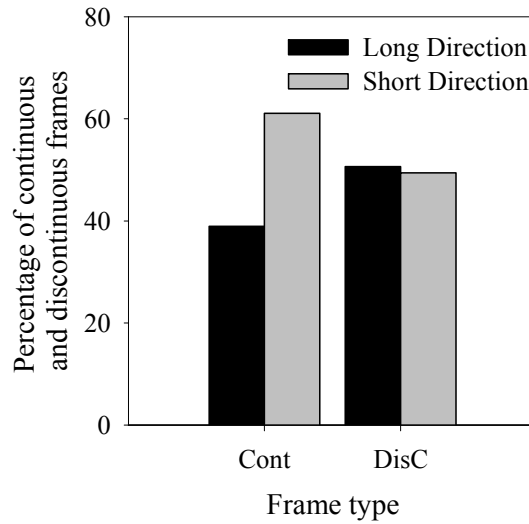


Figure 2.4 Percentages of continuous and discontinuous frames in terms of their floor plan directions (The abbreviations “Cont” and “DisC” stand for continuous and discontinuous frames, respectively)

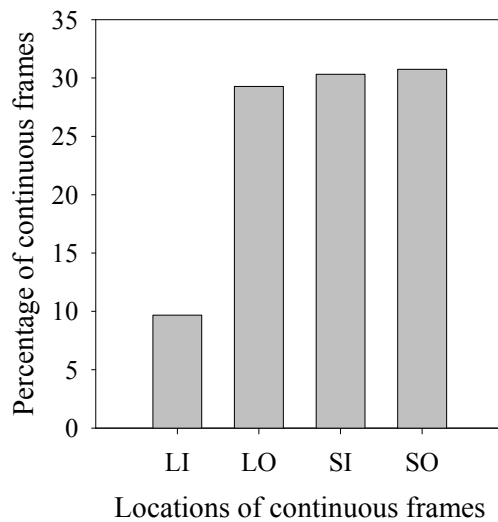


Figure 2.5 Percentages of continuous frames in short- and long-directions

2.2.4 Statistics on Span Length

Average span length as well as minimum and maximum span lengths along short- and long-directions are considered as the other important geometrical parameters and are included in the statistical study. Continuous frames in the building database are examined according to their minimum, maximum and average span lengths. The minimum (MinSL), maximum (MaxSL) and average (AveSL) span lengths for each continuous frame are extracted for this purpose. The mean statistics for these variables for the entire continuous frame inventory are listed in Table 2.2.

Table 2.2 Average span length statistics of continuous frames in short- and long-direction

	$\overline{\text{AveSL}}^*$ (m)	$\overline{\text{MinSL}}^*$ (m)	$\overline{\text{MaxSL}}^*$ (m)
Short-direction mean	3.50	2.36	4.41
Short-direction Stdev**	0.74	0.77	1.05
Long-direction mean	3.58	2.38	4.81
Long-direction Stdev**	0.61	0.66	1.04

* The horizontal bar over the abbreviations indicate the mean of all continuous frames.

** Stdev is the abbreviation for standard deviation about the mean.

2.2.5 Statistics on Geometry and Orientation of Columns

The most common geometric shape of columns for the investigated buildings is rectangle (95.7% of column sections are rectangular in the entire database). The square and circular column cross-sections constitute only 4.1% and 0.2% of the database, respectively. The longer cross-sectional dimensions of almost half of the rectangular columns are oriented along the long-direction of the floor plans. This observation indicates that the majority of the investigated buildings are stronger in the long floor plan direction. Figure 2.6 shows the percentage of columns whose longer cross-sectional dimensions are oriented either along long- or short-directions of floor plans. The last vertical bar indicates the percentage of circular and square columns in the column database.

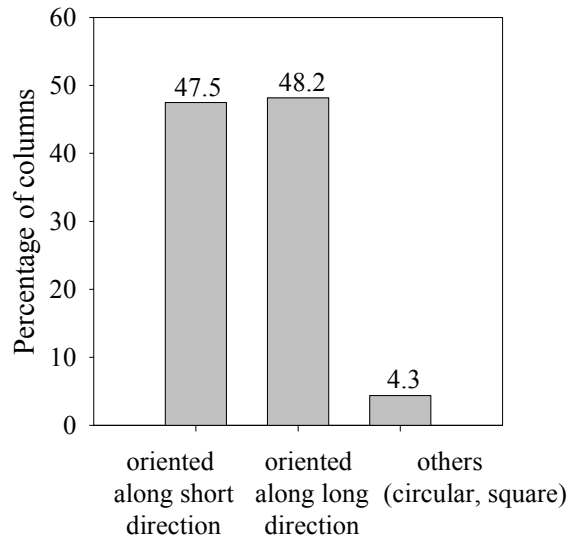


Figure 2.6 Distribution of strong directions of columns according to floor plan directions

Figure 2.7 shows story-wise variation of average columns-width dimensions (shorter cross-sectional dimensions) oriented along the short direction of floor plans. The error bars on the plots indicate the standard deviation about the computed means. Figure 2.8 describes similar statistics for column widths that are oriented in the long direction of floor plans. Figures 2.9 and 2.10 present the average values of column depths (larger cross-sectional dimension) oriented along the short and long directions of the floor plans, respectively.

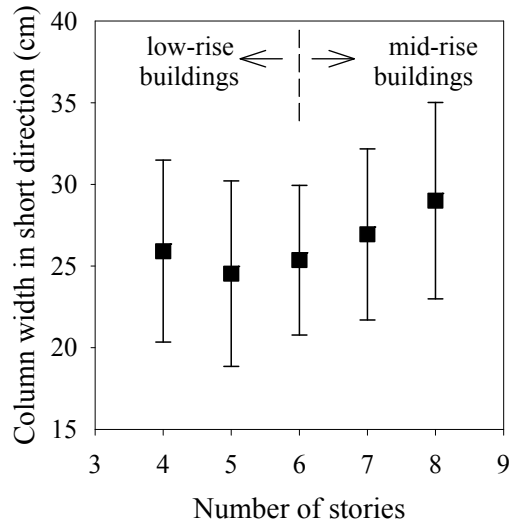


Figure 2.7 Average column width statistics in short direction of the floor plan with respect to story number

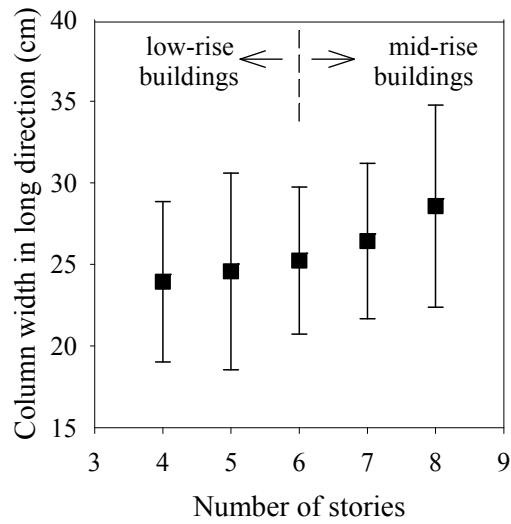


Figure 2.8 Average column width statistics in long direction of the floor plan with respect to story number

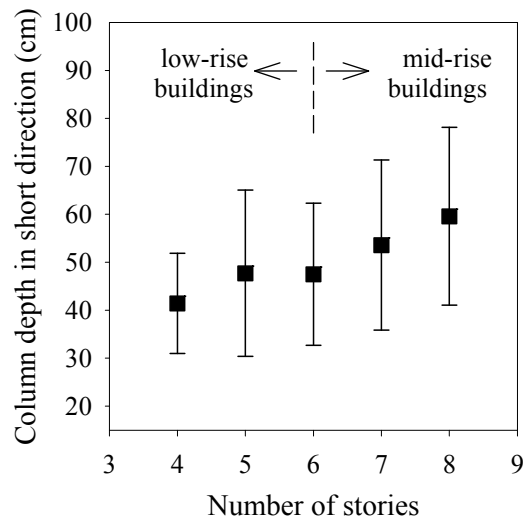


Figure 2.9 Average column depth statistics in short direction of the floor with respect to story number

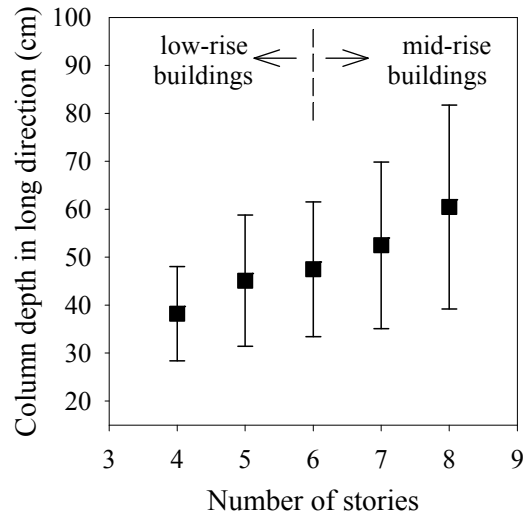


Figure 2.10 Average column depth statistics in long direction of the floor plan with respect to story number

Independent of the weak and strong axes of column cross-sections and regardless of their orientation with respect to weak or strong axes of the floor plans, the column sizes tend to increase with increasing story number. These figures also indicate that the gradient of increasing trend in the column dimensions of 6-, 7-, and 8-story buildings is uniform. The average column depth-to-width ratios along weak and strong axes of floor plans given in Figures 2.11 and 2.12 draw a similar conclusion such that the changes in column dimensions for buildings of 6 and more stories are more stable and follow a more predictable pattern. This observation leads to grouping of investigated buildings as low- and mid-rise systems assuming that the 6-story buildings constitute some type of border between these two groups. This subjective judgment (also illustrated on Figures 2.7 to 2.12) is used in the modeling of frame buildings that is described in the following sections.

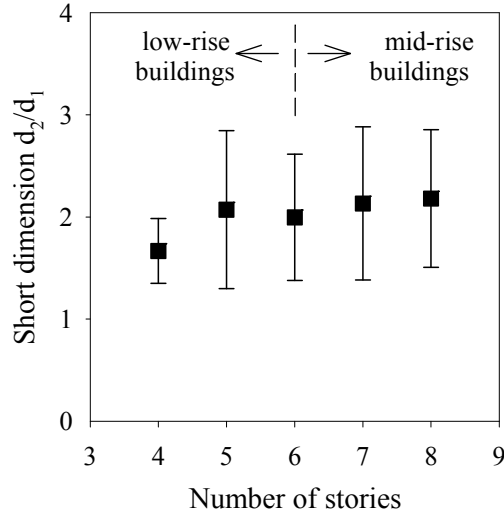


Figure 2.11 Average column depth-to-width ratio (d_2/d_1) statistics in short direction of the floor plan as a function of story number

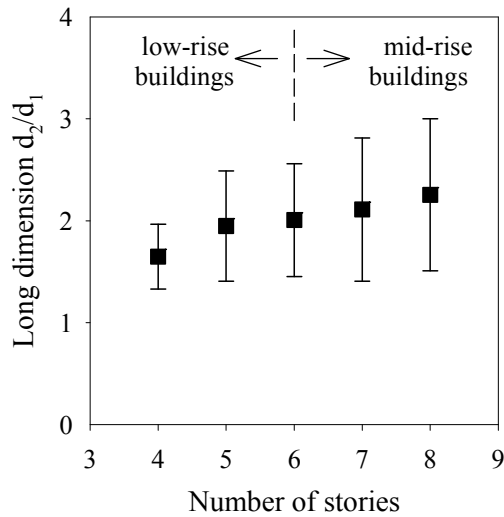


Figure 2.12 Average column depth-to-width ratio (d_2/d_1) statistics in long direction of the floor plan as a function of story number

The statistical study on the Bakırköy building inventory has also indicated the overall pattern about the variation of column dimensions along the total building height. Figure 2.13 illustrates the relative change in the mean column areas along the building height. The presented mean statistics are computed by normalizing the total column areas at each story level with the one at the ground story. The mean statistics indicate that, on average, top-story column areas are reduced by 25% with respect to ground story areas. The decrease in column areas seem to be more gradual after the 2nd stories regardless of the story number.

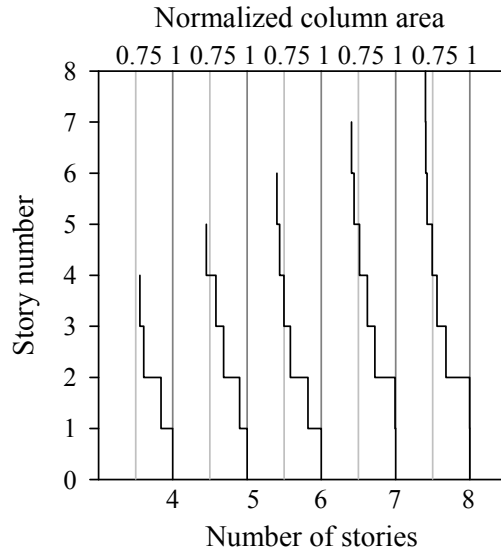


Figure 2.13 Mean column area statistics along the total building height

2.3 Description of Building Models

Three-dimensional RC buildings with 3-, 4-, 5-, 7-, 8- and 9- stories are generated from the blueprints of the Bakırköy building inventory. They are capable of reflecting the common Turkish construction practice as summarized here. The architectural features of these buildings differ from each other. Their floor plans are modified by considering the overall statistics, presented for the uncertainties in geometrical properties. The buildings are designed using the PROBINA Orion software (Prota, 2008) version 14.1 in accordance with the Turkish standards; TS 500-2000 (Turkish Standards Institute, 2000), TS 498 (Turkish Standards Institute, 1997) and Turkish Earthquake Code (TEC, 2007). The buildings are assumed to be located at a site in Zone I with Z3 (soft soil) site classification. The concrete and reinforcing steel for design are selected as C20 (concrete strength of 20MPa) and S420 (yield steel strength of 420 MPa), respectively. All models are designed for ductile behavior using $R=8$ as suggested by Turkish Earthquake Code (TEC, 2007). The effective peak acceleration for design spectrum is taken as $A_0=0.4g$ and the resulting spectral ordinates correspond to a return period of $T_R=475$ years according to the provisions in this code.

Figure 2.14 illustrates the ground-story floor plan of the 3-story building as a representative sample. The interior continuous frame designated by the rectangular box is selected as the 2-D representative frame model of the 3-story building. The floor plans of the rest of the buildings are given in Appendix A.

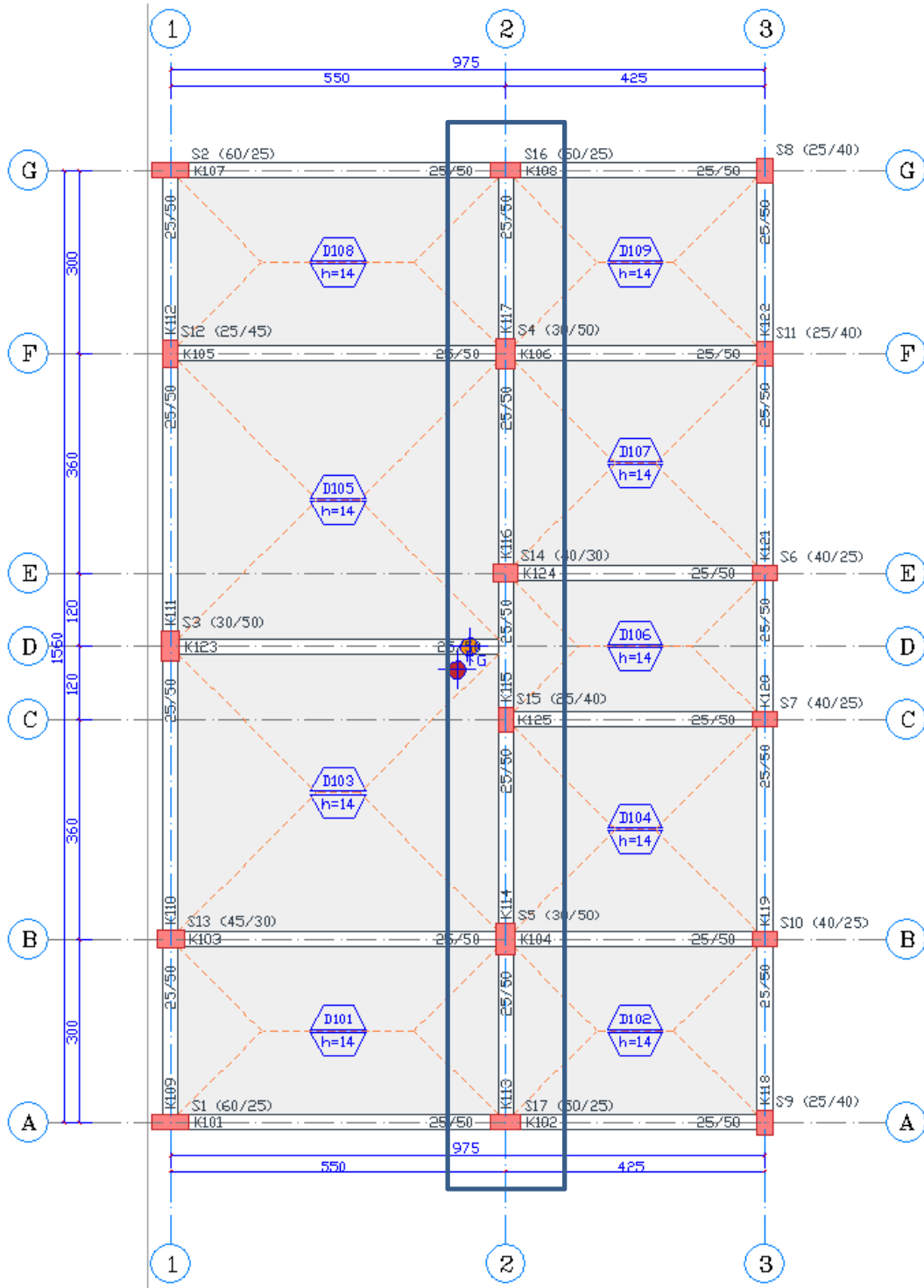


Figure 2.14 Ground-story floor plan of the 3-story building that is generated and designed using PROBINA Orion Software (Prota, 2008). The design complies with all relevant Turkish codes including Turkish Earthquake Code (TEC, 2007)

The selected 2-D frames are analytically modeled using OpenSees (2006) finite element analysis software with fiber-based nonlinear beam column elements that are capable of mimicking spread plasticity along the element. The columns are modeled with single force-based beam-column element with 5 integration points as their longitudinal reinforcement does not change along the member length. The amount of reinforcement is different at the supports and mid-span for beams. Thus, each beam member is modeled with a set of displacement-based nonlinear beam-column elements with 2 integration points. The accuracy of displacement-based beam-column element increases with finer discretization of the member. Following this point, the lengths of displacement-based beam-column elements for each beam member are adjusted such that they are close to the depth of the beam cross-section as recommended by Neuenhofer and Filippou (1997). The stress-strain relationships of concrete and steel are established with uniaxial material objects; Concrete01 and Elastic-Perfectly Plastic (EPP) material, respectively. Concrete01 material uses Kent-Scott-Park concrete model (Kent and Park, 1971; Scott et al., 1982) with degraded linear unloading and reloading stiffnesses in accordance with the work of Karsan and Jirsa (1969) without tensile strength. Figures 2.15 illustrates the basics of stress-strain relationship of Concrete01 and EPP material objects.

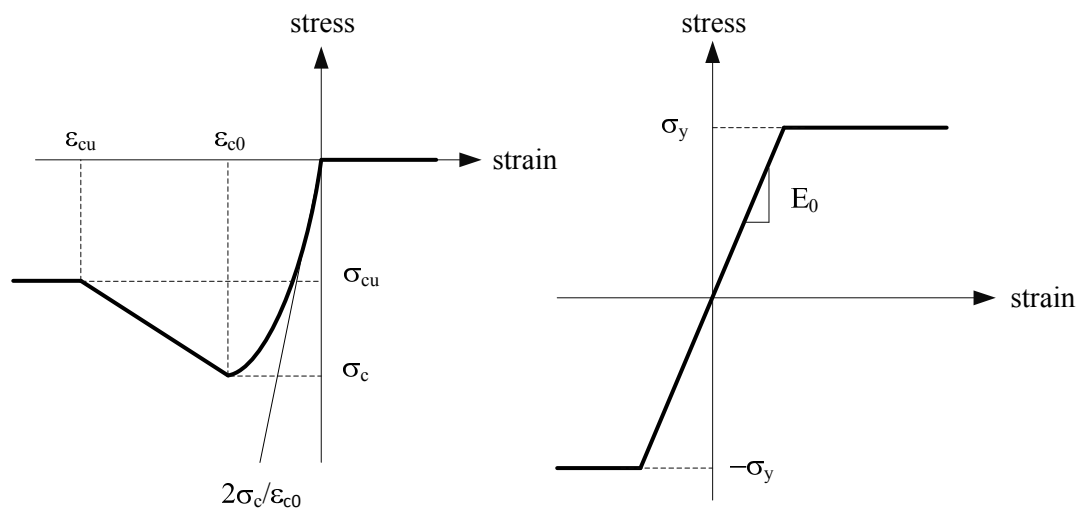


Figure 2.15 Stress-strain relationship of Concrete01 (left panel) and EPP (right panel) material objects

For each section in the analytical frame models, the unconfined concrete and confined concrete model properties are calculated according to the modified Kent and Park model (1971) using unconfined compressive strength with $\sigma_c=20$ MPa at $\epsilon_{c0}=0.002$. The EPP steel material is defined with a yield strength of 420 MPa at $\epsilon_{sy}=0.0021$ yield strain.

Seismic mass of each floor is assumed to be lumped at column-beam connections according to the tributary area concept. The viscous damping for response history analysis

is simulated by using Rayleigh damping. All structural members are assumed to have 5% stiffness proportional damping ratio.

The floor diaphragm effect is overlooked in the analytical models due to several reasons. Firstly, under the rigid diaphragm assumption, the increase in the number of constraints, may result in convergence problems in the nonlinear response history analysis. Secondly, the rigid diaphragm assumption may not be the most accurate way of modeling slab effects. A recent study by Sousa et al. (2012) concludes that rigid diaphragm modeling at each floor level can artificially increase the initial stiffness as well as maximum base shear at the ground level. They also show that rigid diaphragm models increase beam shear forces and decrease deformations. Sousa et al. (2012) recommend the use of equivalent truss elements for modeling slabs in building systems that yield a more realistic column behavior as well. Under these recent findings disregarding the rigid floor diaphragm model for the model buildings of this study is believed to increase the accuracy of their structural response under seismic action.

The analytical models of frame systems used in this dissertation are established under the modeling assumptions described in the above paragraphs. Figure 2.16 gives the analytical model of the 3-story building whereas Appendix B shows the analytical models for the rest of the frames. The frame models are described by a code that is based on story number. For example, 3S_MRF stands for the 3-story moment-resisting frame model. Table 2.3 summarizes some of the important dynamic properties of each building model. As one can infer from the listed dynamic properties, the model buildings are flexible and their modal mass contributing to the fundamental mode behavior is approximately 80% of the total mass.

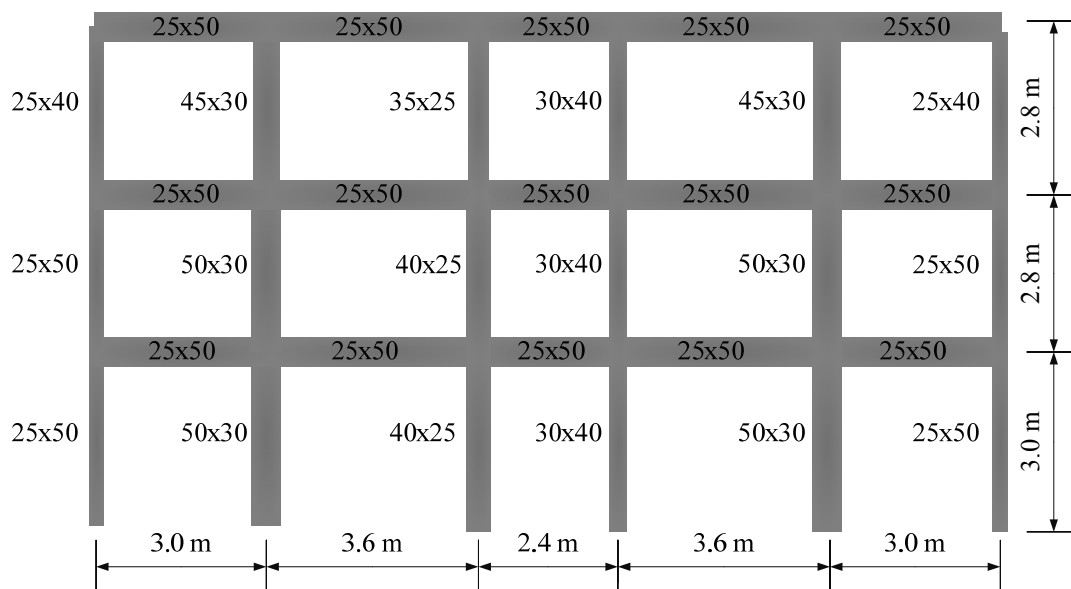


Figure 2.16 3-story model frame and its member dimensions

Table 2.3 Important dynamic features of model frames

Frame	Total Mass (t)	Fundamental Period, T_1 (s)	First-mode effective modal mass factor (α_1)
3S_MRF	251.78	0.71	0.84
4S_MRF	155.14	0.86	0.82
5S_MRF	201.65	1.05	0.78
7S_MRF	302.62	1.09	0.77
8S_MRF	494.43	1.27	0.77
9S_MRF	861.48	1.37	0.78

2.4 General Characteristics of the Ground Motion Database Used in this Study

The accelerograms utilized in this study are obtained from three sources: PEER strong-motion database (<http://peer.berkeley.edu/smcat/>), European strong-motion database (http://www.isesd.hi.is/ESD_Local/frameset.htm) and Turkish strong-motion database (<http://kyh.deprem.gov.tr/ftpe.htm>). A total of 628 ground motions recorded on NEHRP C and D site classes (BSSC, 2009) with normal, strike-slip and reverse faulting mechanism are compiled. The NEHRP C and D site classes can be classified by $V_{s,30}$ values (average shear wave velocity of the upper 30 soil profile) with $360 \text{ m/s} \leq V_{s,30} < 760 \text{ m/s}$ and $180 \text{ m/s} \leq V_{s,30} < 360 \text{ m/s}$, respectively. The moment magnitude (M_w) range of the database is $5.0 \leq M_w < 7.7$ whereas all records have Joyner-Boore distances (R_{jb} ; Joyner and Boore, 1981) that are less than 100 km. The chosen magnitude and distance range is believed to have engineering significance for seismic design and performance assessment of new and existing buildings. The important features of the ground-motion database are given in Appendix C. Figures 2.17 and 2.18 show M_w versus R_{jb} scatters in terms of style-of-faulting and site class distributions. The database distribution shows deficiencies in terms of style-of-faulting whereas site classes display a more homogenous scatter.

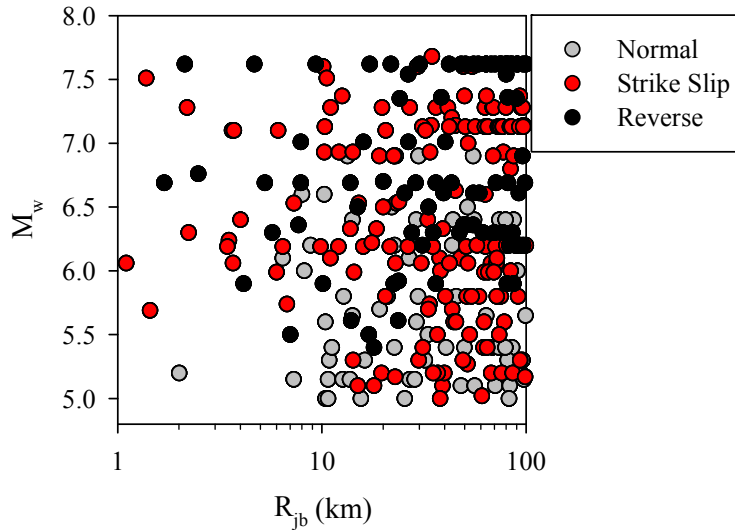


Figure 2.17 M_w versus R_{jb} distribution of the selected ground motion database in terms of style-of-faulting (i.e., normal, strike slip and reverse)

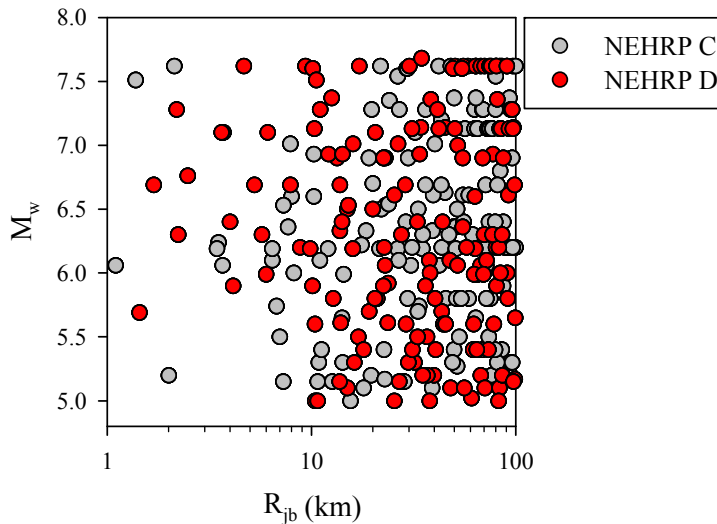


Figure 2.18 M_w versus R_{jb} distribution of the selected ground motion database in terms of NEHRP C and D site classes

Figures 2.19 and 2.20 compare the acceleration spectra of the compiled database with the code-base spectrum that is used in the design of frame models. These comparative figures portray the significance of record-to-record variability that should be considered in a probabilistic manner while assessing the level of seismic demands and resulting structural response. The small-to-moderate magnitude events in the database can be assumed to represent frequently occurring earthquakes for regions of high seismicity. Thus, the buildings that are properly designed for such regions (such as the model frames designed according to the code-based spectrum given in these plots) should sustain negligible damage when they are subjected to ground motions generated by these earthquakes. In a

similar fashion, if moderate-to-large magnitude events of the ground-motion database represent less frequent earthquakes of high seismicity regions, the code conforming buildings (again the model frames focused by this study) should not collapse or experience heavy damage. To this end, ensuring the above expected behavior from building systems require proper and physically sound approaches that can account for all sorts uncertainties involved in ground-motion intensities and structural response. The proposed MIDR predictive model as well as the presented probabilistic methodologies that make use of this model are believed to convey useful information for the evolution of such methods. The following chapters describe the development of these tools.

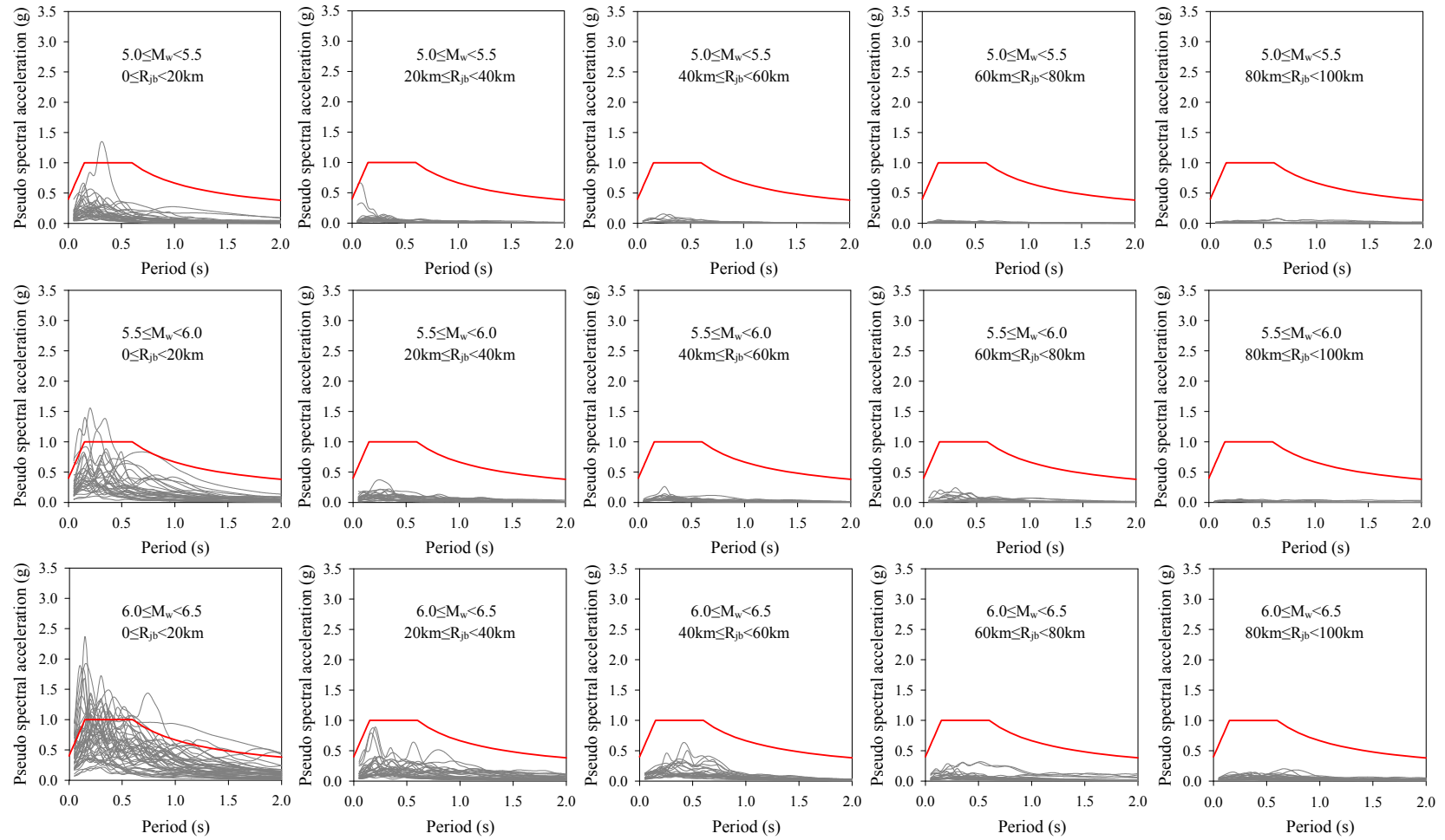


Figure 2.19 Design spectrum for $A_0=0.4g$ and Z3 site conditions (TEC07) versus acceleration response spectra of accelerograms in M_w - R_{jb} bins

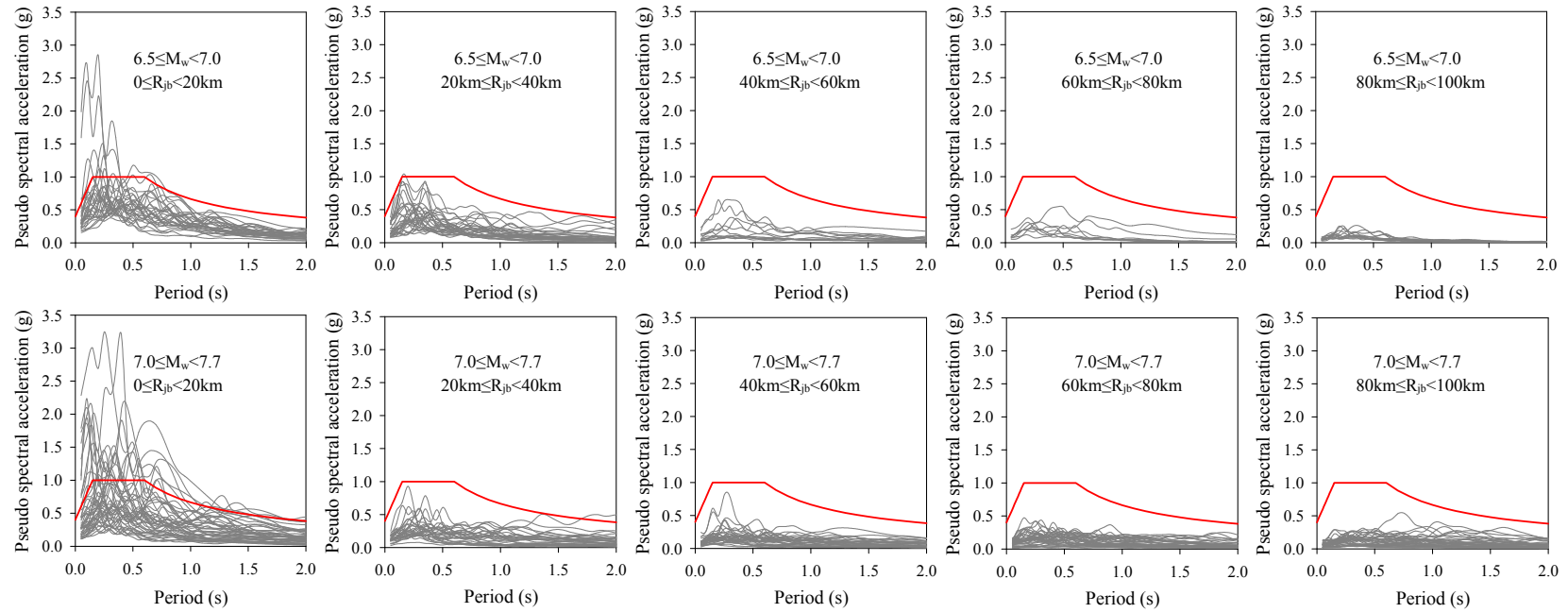


Figure 2.20 Design spectrum for $A_0=0.4\text{g}$ and Z3 site conditions (TEC07) versus acceleration response spectra of accelerograms in M_w - R_{jb} bins

CHAPTER 3

INTERPRETATIONS AND OBSERVATIONS ON NONLINEAR MDOF RESPONSE

3.1 Introduction

Under seismic action, estimating the nonlinear deformation demands in multistory buildings is of prime importance since it is directly related with structural performance. While assessing structural performance through damage states, there is a need to select a reliable demand parameter that successfully correlates with damage. Lessons from the past earthquakes have been revealed that structural and non-structural damages are mainly resulted from lateral deformation. Thus, an engineering demand parameter (EDP) such as interstory drift ratio (IDR) is a proper measure while correlating structural performance with demand. It should be noted that an engineering demand parameter is not only useful for assessing the structural performance but can also be the indication of lateral deformation capacity of the structure that is designed under target seismic demands (e.g., pseudo spectral acceleration).

One of the goals of the dissertation is to derive a predictive model (Chapter 5) for estimating maximum interstory drift ratio (MIDR) for code confirming reinforced concrete (RC) Turkish frame buildings. MIDR is an engineering demand parameter corresponding to the maximum of IDRs in a building. Thus, it draws an upper limit for IDR demands. The advantage of the proposed MIDR equation will be the assessment of lateral deformation demands on buildings in a fairly reliable manner. Eventually, such a tool can be of use for rapid performance assessment of existing buildings or preliminary design of new buildings.

In order to estimate the MIDR demands, nonlinear response history analyses (RHA) are performed using the reinforced concrete frame set that is described in Chapter 2. A total of 628 unscaled records (314 two-component horizontal accelerograms) are utilized for nonlinear response history analyses. The computation process of the demand parameters will be given in the subsequent sections of this chapter.

To develop the proposed prediction equation, it is essential to consider the crucial factors that affect the behavior of MIDR. Since variations in engineering demand parameters are closely related to the characteristics of ground motion and structure, the proposed prediction equation should combine the most prominent parameters of these components. The functional forms of ground-motion prediction equations (GMPEs) indicate that the major seismological estimator parameters that affect the ground-motion amplitudes are magnitude, source-to-site distance, depth, site class and style-of-faulting (SoF). Among these parameters magnitude and source-to-site distance terms are the key variables while addressing the source and path effects on the variation of ground motions. Several studies have revealed that site class and SoF have lesser effect on reducing dispersion in the GMPEs compared to magnitude and source-to-site distance (e.g., Bommer et al., 2003; Boore, 2004). However, they are still important while defining the ground-motion amplitudes. To this end, site class is used as the third independent explanatory variable in the MIDR predictive model to reflect the soil influence on structural behavior. Style-of-faulting is disregarded in the proposed MIDR model since the strong-motion database used in the derivation of MIDR model lacks of uniform distribution of different faulting styles (i.e., normal, strike-slip and reverse faults). These highlighted remarks will be discussed throughout the dissertation while developing the MIDR predictive model.

There are many structural parameters that can describe the nonlinear seismic behavior of structural systems. However, an efficient structural estimator parameter to be used in a simplified predictive model should be robust and easy-to-compute for accurate representation of the nonlinear structural response. To this end, the strength reduction factor, R_y is preferred as the independent structural parameter in the proposed MIDR model. It is noted that R_y is a code-based variable and it serves as a bridge between MDOF and corresponding equivalent SDOF behavior while describing EDPs. The relationship between R_y and MIDR is presented in the following chapter while discussing the response of equivalent SDOF systems of the model buildings under the chosen ground-motion database.

In this chapter, the nonlinear RHA results are investigated in global and local levels. Firstly, global engineering demands in terms of base shear versus roof displacements for each frame model are given. Later, IDR and MIDR results calculated from nonlinear RHA are presented. The variation of these local demand parameters are mainly investigated in terms of magnitude and source-to-site distance. The presented and discussed observations will be used in the subsequent chapters where the evolution of the proposed predictive model is discussed.

3.2 Critical Remarks on the Determination of Building Response Parameters

This section explains some important details while compiling the nonlinear building response parameters from nonlinear RHA. The presented discussions may be useful in

understanding the behavior of these response parameters under the influence of earthquake action.

Interstory drift ratio (IDR) is the absolute maximum lateral displacement between two consecutive stories normalized by the story height. Rigid diaphragm assumption is not used in the frame models and IDR is calculated from the column drifts rather than the average of lateral story displacements. At each time step of the nonlinear RHA and for each story level, the drift ratios (DRs) of column members are calculated by normalizing their lateral displacement differences between the top and bottom ends with the column heights. At a given time increment, the instantaneous drift ratios calculated from the columns at each story level are used to compute average instantaneous drift ratio (DR_{ave}) that is given in Eq. (3.1).

$$DR_{ave} = \frac{1}{nh} \sum_{j=1}^n \Delta_{j,i}^{top} - \Delta_{j,i}^{bottom} \quad (3.1)$$

where,

$\Delta_{j,i}^{top}$ is lateral displacement at the top end of the j^{th} column at the i^{th} story at a particular instant

$\Delta_{j,i}^{bottom}$ is lateral displacement at the bottom end of the j^{th} column at the i^{th} story at a particular instant

h is column height

n is number of columns at each story

At each story, IDR demands are calculated by taking the absolute maximum of instantaneous DR_{ave} 's over the entire length of strong-motion record. Finally, the MIDR demand for a building model under a particular accelerogram is computed by taking the maximum of IDRs. Some building models experienced numerical convergence problems or collapsed during the nonlinear RHA. The numerical instability problems as well as collapse can be associated with poor software solution algorithms and exceeding the lateral deformation because of significantly high seismic demand or second order effects. When a numerical problem occurs towards the end of the record, the nonlinear RHA is assumed to be complete and the EDPs of interest are included in the inventory. If the model collapses or non-convergence is experienced during the strong-motion part of the accelerogram, the corresponding results are discarded in this study. The computed demands in some analyses are significantly high. Some of these high demands can be attributed to secondary effects. In order to account for realistic response of models and draw reliable limits for the EDPs of concern, outliers are excluded from the overall results. Whenever the computed MIDR value is greater than 0.06 (6% of story height), the corresponding nonlinear RHA is discarded from the compiled dataset. The maximum MIDR of the two horizontal ground-motion components is taken into account because it possesses the most critical value for engineering design and assessment. When one of the horizontal components fails to

converge or the model collapses under that horizontal component, the nonlinear RHA results of the other component is considered in the statistical studies.

The investigated EDPs are presented for different magnitude and distance bins. One-way and two-way bins are utilized for scatter, median and median + standard deviation plots of the observed data. They will be shown in the following sections. The moment magnitude (M_w) interval for each bin is selected as $0.5M_w$ unit. This rule is disregarded for the last magnitude bin as the largest M_w in the database is 7.68 (1972, Sitka Alaska Earthquake). Thus, there are 5 magnitude bins for the statistical observations made on the chosen EDPs: M_w 5.0-5.5, M_w 5.5-6.0, M_w 6.0-6.5, M_w 6.5-7.0 and M_w 7.0-7.7. The distance bins have increments of 10 km. A total of 10 distance bins are established with the following ranges: 0-10 km, 10-20 km, 20-30 km, 30-40 km, 40-50 km, 50-60 km, 60-70 km, 70-80 km, 80-90 km and 90-100 km. The above properties of the magnitude and distance bins are not changed throughout the statistical observations. The number of records in each magnitude and distance bin are listed in Table 3.1 to give a better idea on the distribution of accelerograms in the ground-motion database.

The maximum base shear $(V_{base})_{max}$ and the maximum roof displacement $(\Delta_{roof})_{max}$ are considered while gathering the base shear versus roof displacement demands computed from nonlinear RHA. For each accelerogram, the maximum base shear is calculated as the absolute maximum of the base shears recorded during the analysis. Accordingly, the absolute maximum roof displacement attained during the analysis is assigned to the maximum roof displacement.

Table 3.1 Number of accelerograms in each magnitude and distance bin

Magnitude M_w	Distance (km)				
	5.0-5.5	5.5-6.0	6.0-6.5	6.5-7.0	7.0-7.7
0-10	3	7	16	6	15
10-20	14	8	7	9	8
20-30	6	7	7	11	8
30-40	7	5	8	4	7
40-50	4	5	6	2	9
50-60	2	4	6	4	7
60-70	5	5	3	2	9
70-80	4	4	7	2	10
80-90	6	2	7	3	9
90-100	5	2	4	3	10

3.3 Nonlinear Global Demands on Code Confirming MDOF Systems

The maximum base shear $(V_{\text{base}})_{\text{max}}$ versus maximum roof displacement $(\Delta_{\text{roof}})_{\text{max}}$ scatters are illustrated from Figure 3.1 to Figure 3.6 for each frame. The nonlinear static analysis (pushover analysis) curves are also plotted on these figures. The pushover curves are obtained by incrementally pushing the buildings up to 2.0 % roof drift. All model buildings can deform beyond the chosen target roof drift. Nonlinear RHA results of adjacent magnitude bins (e.g., M_w 5.0-5.5 and M_w 5.5-6.0) are given on each plot to emphasize the influence of magnitude on maximum base shear and roof displacement demands. The plots suggest that the increase in magnitude results in an increase in base shear and roof displacement demands. This is particularly clear for taller buildings (e.g., 9S_MRF). The plots also indicate a fairly good correlation between static pushover curves and $(V_{\text{base}})_{\text{max}}$ - $(\Delta_{\text{roof}})_{\text{max}}$ pairs when structures respond within the elastic limits. The match between pushover curves and nonlinear RHA results decreases with increased level of nonlinearity in building response. The maximum base shear and roof displacement pairs do not necessarily occur at the same instant. This unsynchronized behavior is particularly true when structures respond beyond their elastic limits. It is believed that the unsynchronized occurrence of $(V_{\text{base}})_{\text{max}}$ and $(\Delta_{\text{roof}})_{\text{max}}$ pairs is the major reason behind the observed deviations from the falling branches of pushover curves. The significant variation of demands within each magnitude bin shows the effect of distance: short-distance accelerograms cause larger maximum base shear and roof displacement demands for similar magnitude events. The influence of distance effect on the maximum base shear and roof displacement demands are also investigated for 10 distance bins. They are not shown as separate plots for brevity.

The other observation from the pushover (PO) curves of model buildings is the negative post-yielding slope that advocates the consideration of secondary effects by the structural analysis software (OpenSees, 2006). The influence of secondary effects come into picture during nonlinear RHA that are described to some detail in Section 3.2. The secondary effects caused failure of some structural models or excessive nonlinear MIDR demands that are disregarded in this study for defining more reliable structural response of code-confirming buildings.

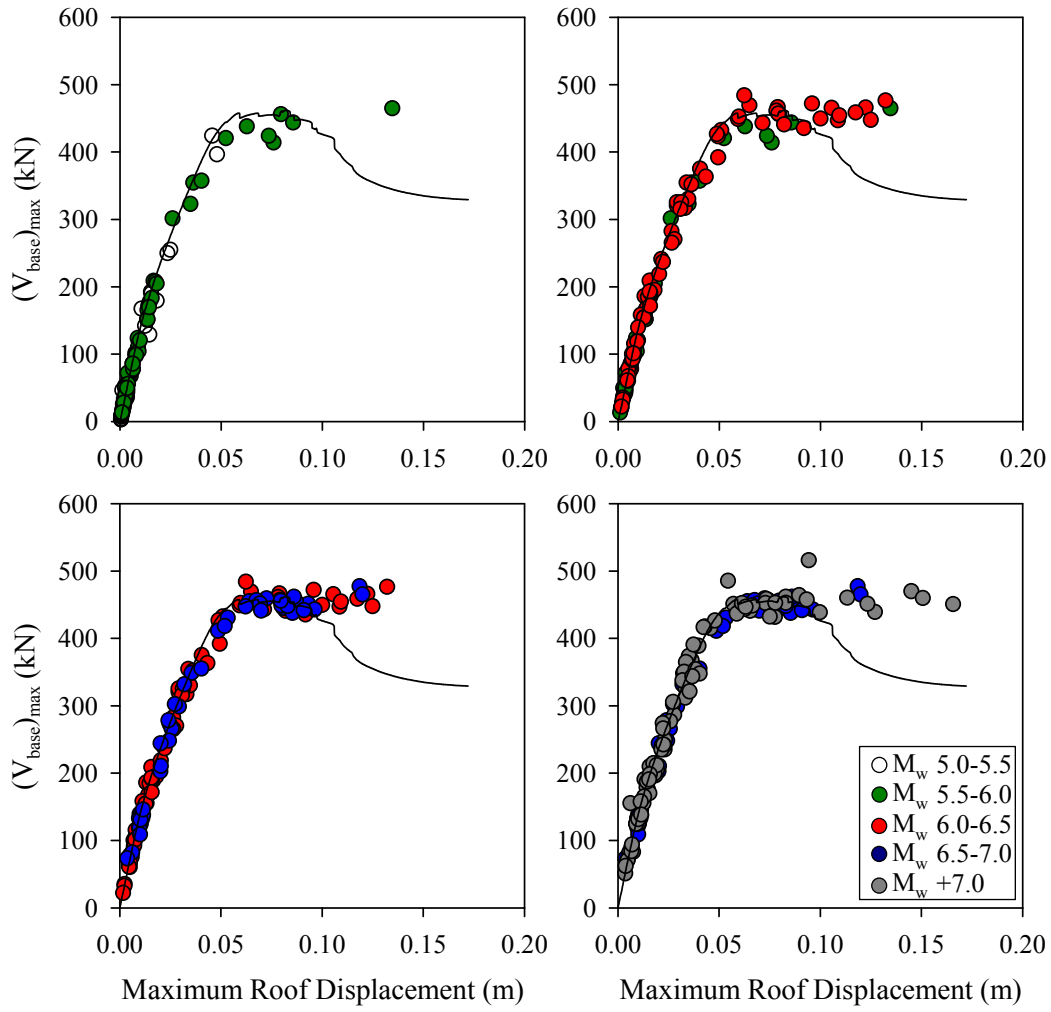


Figure 3.1 Comparison of maximum base shear $(V_{base})_{max}$ versus maximum roof displacement demands of 3-story building (3S_MRF) for adjacent magnitude bins

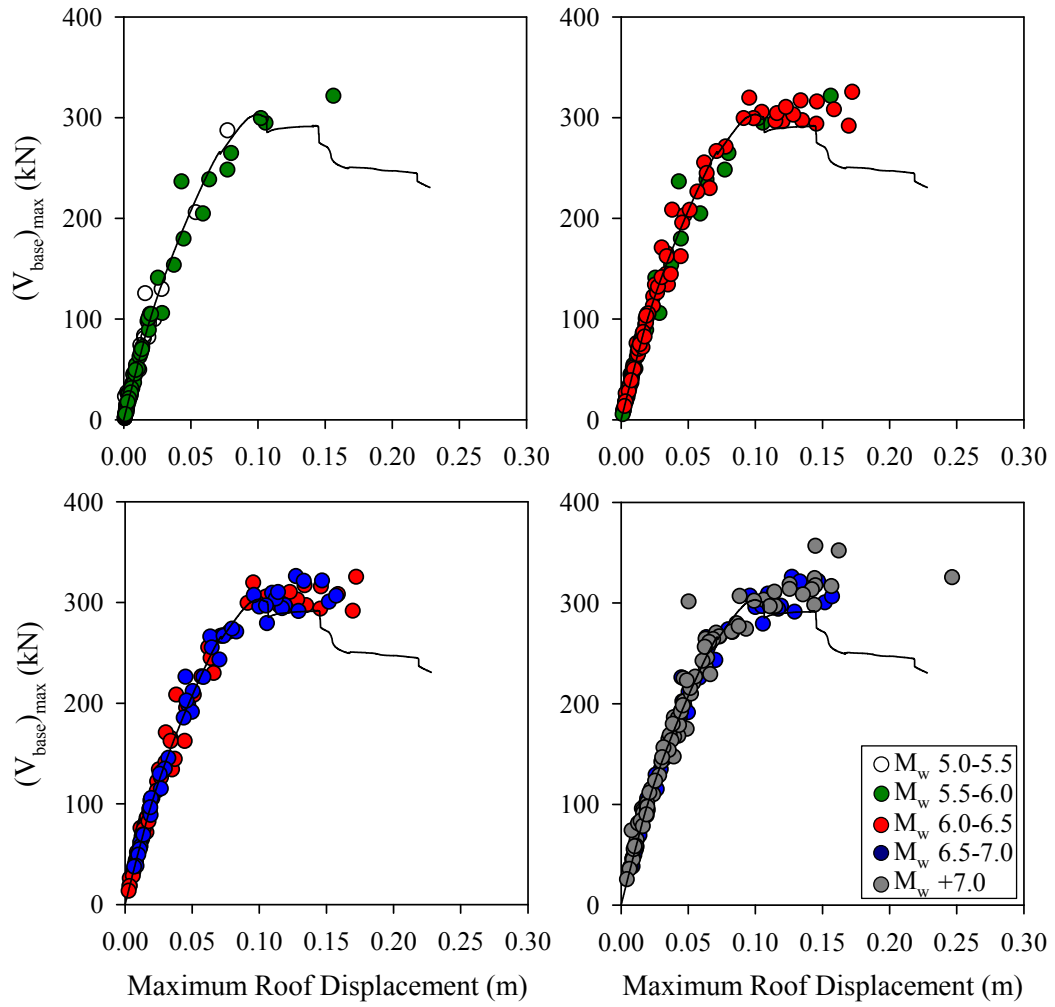


Figure 3.2 Comparison of maximum base shear $(V_{\text{base}})_{\text{max}}$ versus maximum roof displacement demands of 4-story building (4S_MRF) for adjacent magnitude bins

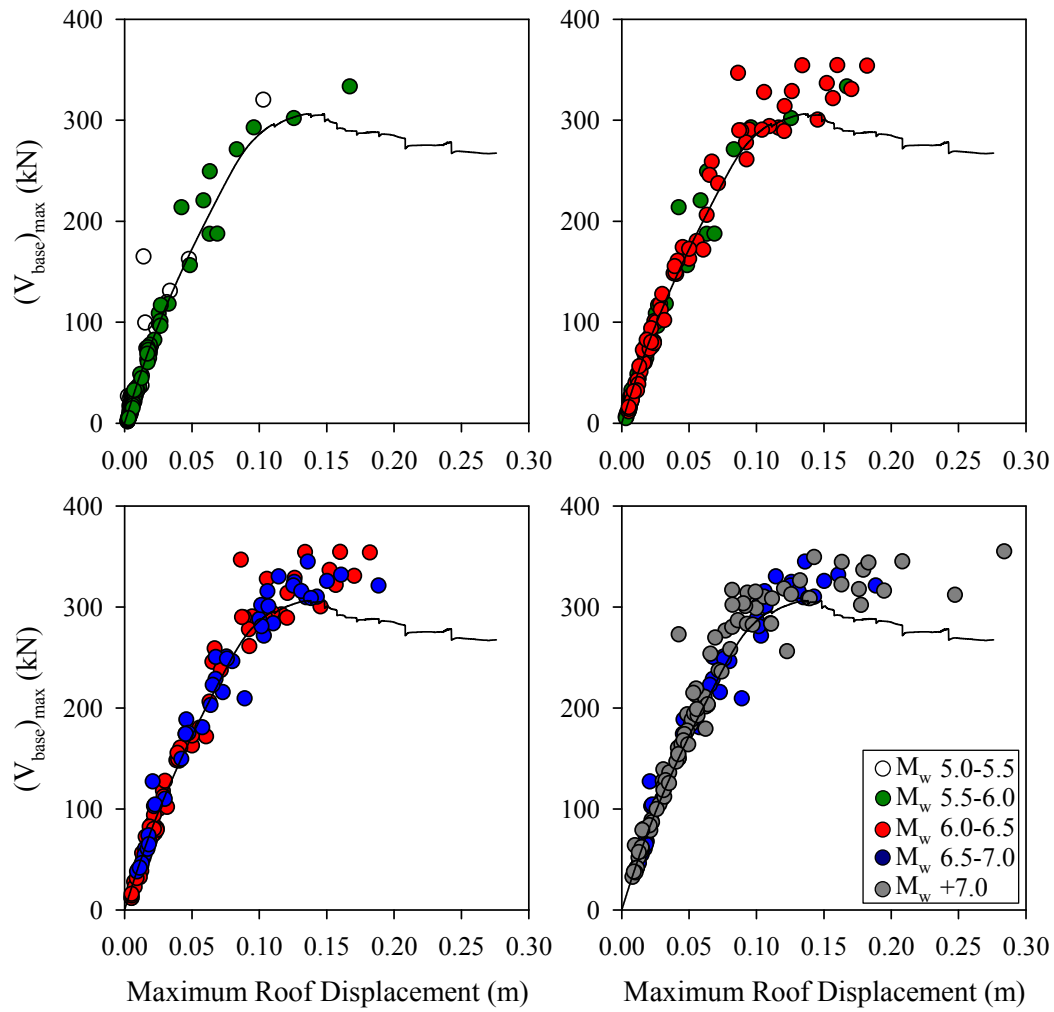


Figure 3.3 Comparison of maximum base shear $(V_{base})_{max}$ versus maximum roof displacement demands of 5-story building (5S_MRF) for adjacent magnitude bins

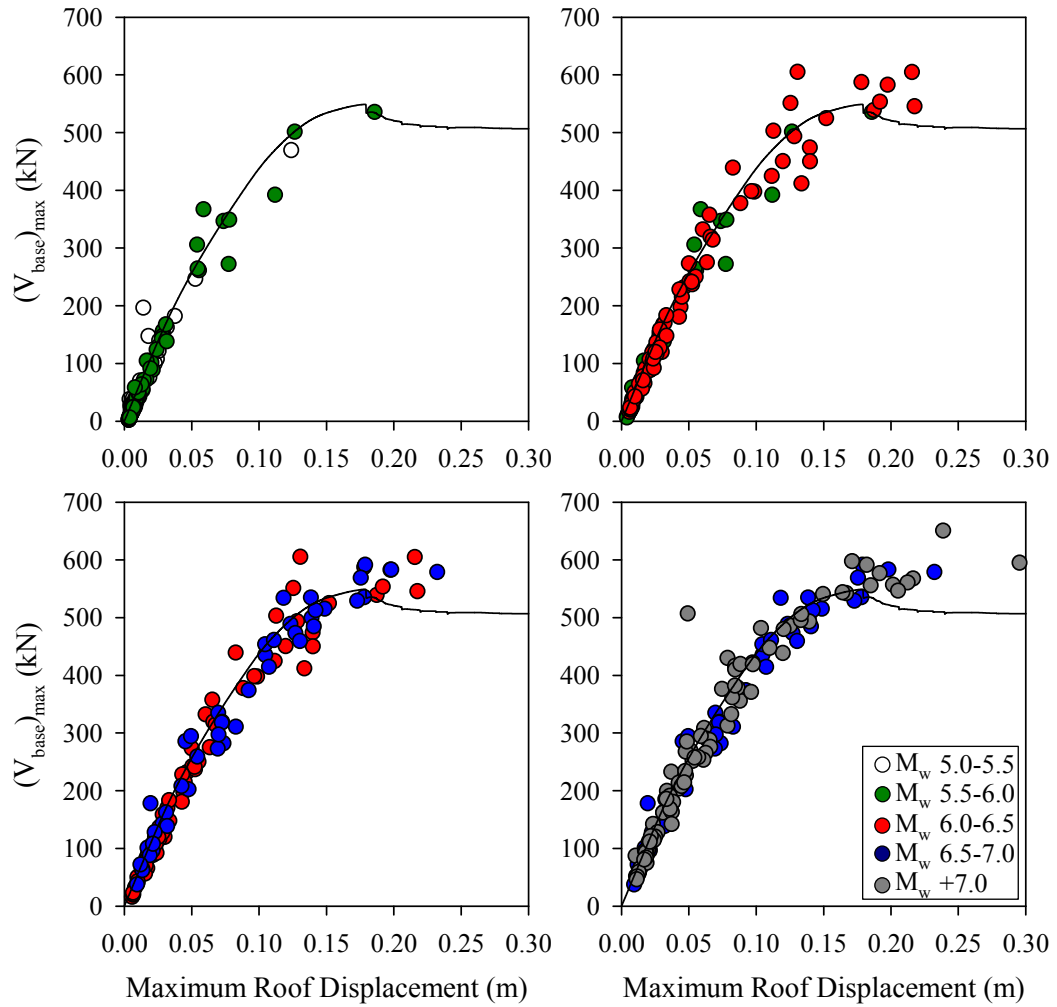


Figure 3.4 Comparison of maximum base shear $(V_{\text{base}})_{\text{max}}$ versus maximum roof displacement demands of 7-story building (7S_MRF) for adjacent magnitude bins

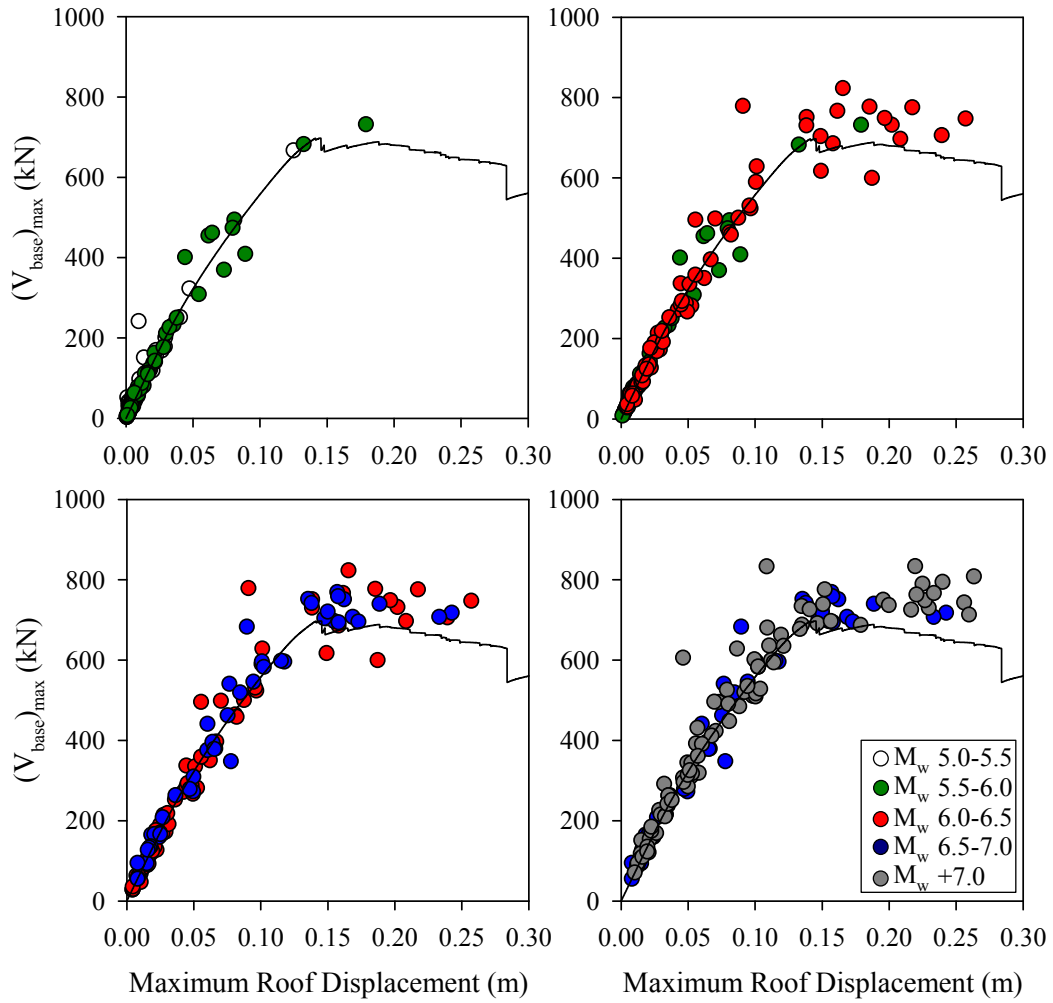


Figure 3.5 Comparison of maximum base shear $(V_{base})_{max}$ versus maximum roof displacement demands of 8-story building (8S_MRF) for adjacent magnitude bins

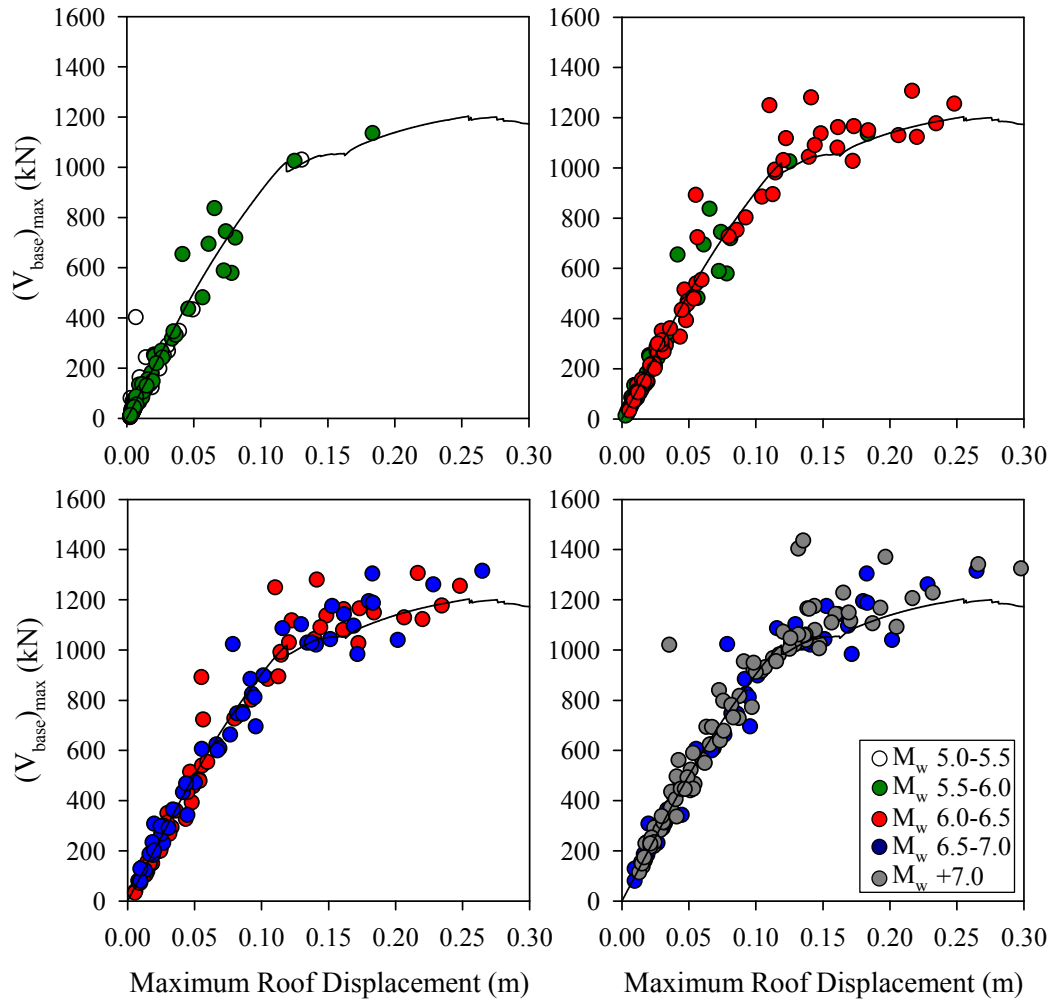


Figure 3.6 Comparison of maximum base shear $(V_{\text{base}})_{\text{max}}$ versus maximum roof displacement demands of 9-story building (9S_MRF) for adjacent magnitude bins

3.4 Nonlinear IDR and MIDR Demands on Code Confirming MDOF Systems

This section is composed of various sub-sections that show the statistical results of overall nonlinear RHA to understand the influence of some certain parameters on IDR and MIDR demands. The validity of log-normality assumption for IDR and MIDR is discussed first. This discussion is followed by the effect of various seismological parameters on the variation of IDR and MIDR. Section 3.4 ends with a short discussion about the dependence of MIDR on building fundamental period (T_1).

3.4.1 Log-normality of MIDR

The distributions of IDR and MIDR are important for the proposed prediction equation in this study. In general ground-motion parameters are assumed to be log-normally distributed (Baker and Cornell, 2006; Bommer and Abrahamson, 2006; Jayaram and Baker, 2008). Similarly MIDR demands are assumed to be log-normally distributed in several studies (Song and Ellingwood, 1999; Shome and Cornell, 1999). Recently Romão et al. (2011) expressed the suitability of log-normal distribution for MIDR for a given level of the intensity measure (IM). More specifically, Romão et al. (2011) indicated that the MIDR demands calculated from a set of ground motions scaled according to a selected IM follow log-normal distribution. Bearing on this assertion, the distributions of MIDR and IDR are verified for log-normality using Kolmogorov-Smirnov goodness-of-fit test (Ang and Tang, 1975) at a significance level of $\alpha_{sig}=5\%$. Figure 3.7 shows the Kolmogorov-Smirnov (KS) goodness-of-fit test results for MIDR obtained from the nonlinear RHA results of each model building. The log-normality of MIDR holds at 5% significance level as given in these plots.

Although Kolmogorov-Smirnov test is useful to estimate the goodness-of-fit of a sample set against a distribution, it has some limitations. The major limitation is that the central estimates of the probability distribution is selected as equal to the ones of the sample set if they are not specified. This issue leads the null distribution (probability distribution, if the null hypothesis cannot be rejected) to be dependent on the sample data. Therefore, the results of the test become conservative in terms of the probability of error. In other words, the critical values associated with the confidence levels get smaller. This fact compromises the reliability of the KS test results. In order to overcome this issue, Lilliefors (1967) presented an adapted version of KS for normal distribution that is known as Lilliefors test. According to the Lilliefors test, the critical values corresponding to the significance levels are updated using Monte Carlo methods. By making use of the Lilliefors test, the normality of the MIDR demands are recalculated. Table 3.2 summarizes the test results in terms of p values that determine how likely a null hypothesis is to be rejected or not rejected. The null hypothesis for this case is the suitability of MIDR to log-normal distribution. For a given significance level, the null hypothesis is rejected if the p-value is less than the significance

level. Thus, p-value is the measure to reject or not to reject the null hypothesis at a given significance level.

Table 3.2 p values calculated from Lilliefors test to verify the normality of logarithmic MIDR for the frame set

Frame ID	p value
3S_MRF	5.6 %
4S_MRF	1.05%
5S_MRF	1.0%
7S_MRF	2.23%
8S_MRF	0.8%
9S_MRF	0.4%

The results in Table 3.2 indicate that, only the 3-story frame MIDR results verify the normality of logarithmic MIDR at 5% significance level. For 4-, 5-, and 7- story frames, the normality of logarithmic MIDR is achieved at 1% significance level. For the rest of the frames, the significance levels are below 1%. Accordingly, one can infer that the log-normality of MIDR is not fully confirmed by Lilliefors test. In order to figure out the limits that define the deviation of MIDR demands from log-normal distribution, the logarithm of MIDR inventory is inspected by normal quantile (Q-Q) plots. Figure 3.8 illustrates the normal Q-Q plots for each frame model. The plots are given in this figure indicate that, except for the tails, MIDR can be assumed as log-normally distributed, the standard normal distributions of the logarithms of MIDR values are very close to the theoretical standard normal distribution within ± 2 standard deviation (σ) range. Under these observations, the log-normality of MIDR assumption is assumed to be sufficient for the MIDR predictive model and its implementation to the probability-based procedures described in Chapter 6.

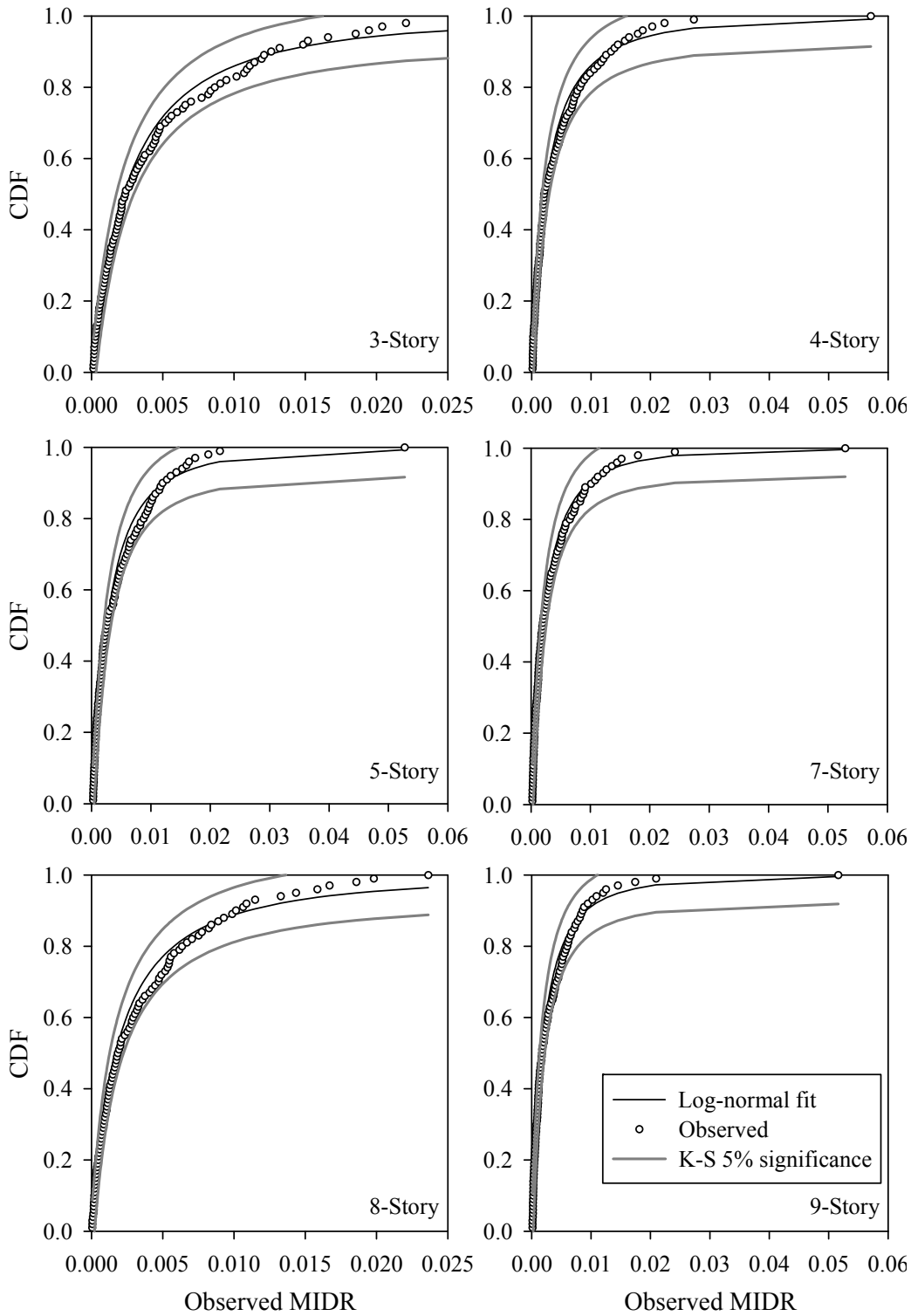


Figure 3.7 Log-normal fits on MIDR demands for the frame set and their comparison with the actual distribution of observed MIDR as well as the Kolmogorov-Smirnov goodness-of-fit test at 5% significance

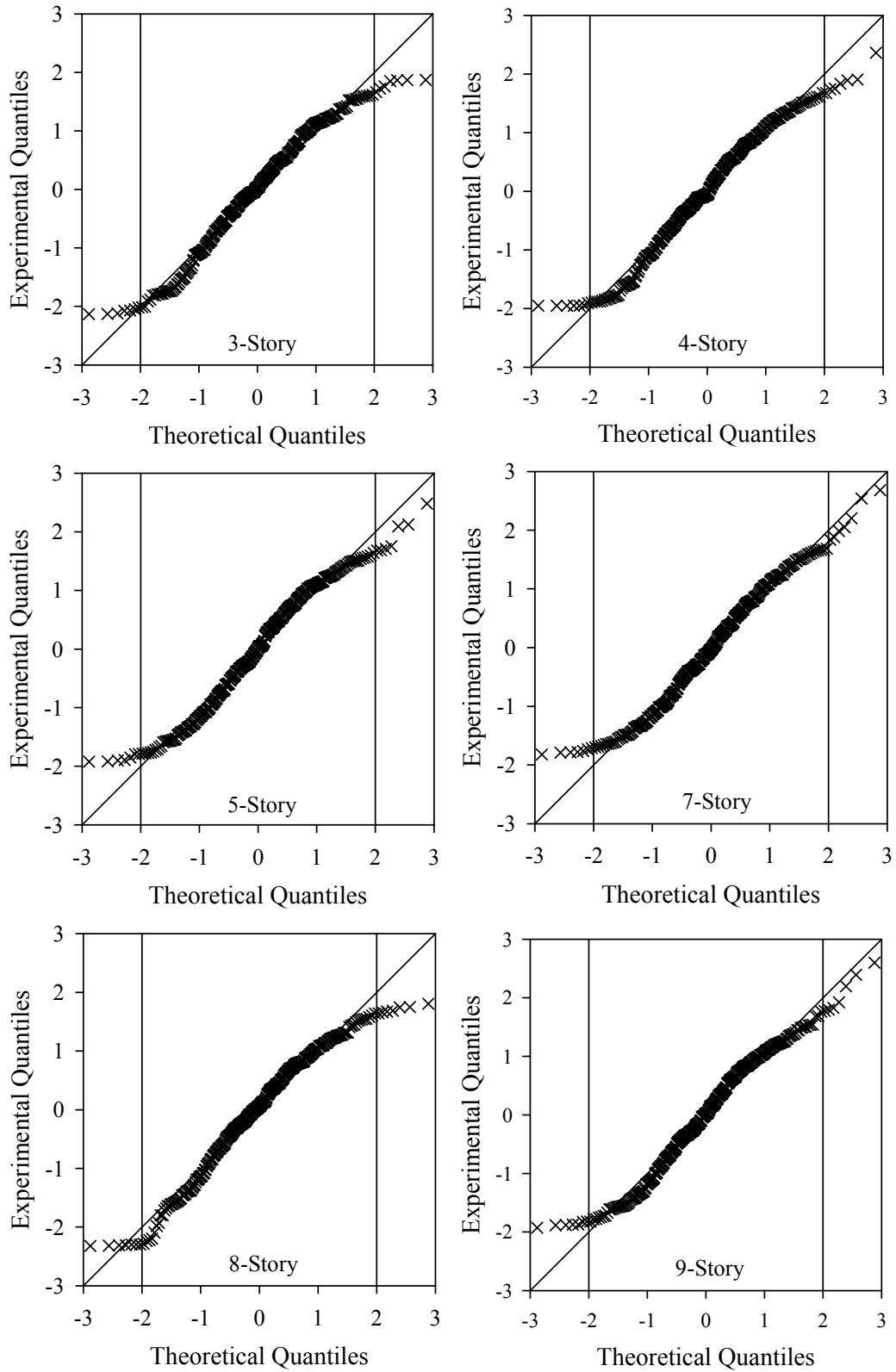


Figure 3.8 Normal Q-Q plots for the logarithmic MIDR demands for the entire frame set

3.4.2 Variation of IDR Profiles in Terms of Magnitude and Distance

The IDR variations of frame models are investigated separately in terms of magnitude and distance bins. The median IDR values of each frame are presented in Figure 3.9 calculated from different magnitude bins. In a similar manner, Figure 3.10 represents the median + σ IDR results for the same magnitude bins. Figures 3.11 and 3.12 show the median and median + σ IDR results for the previously described distance bins, respectively.

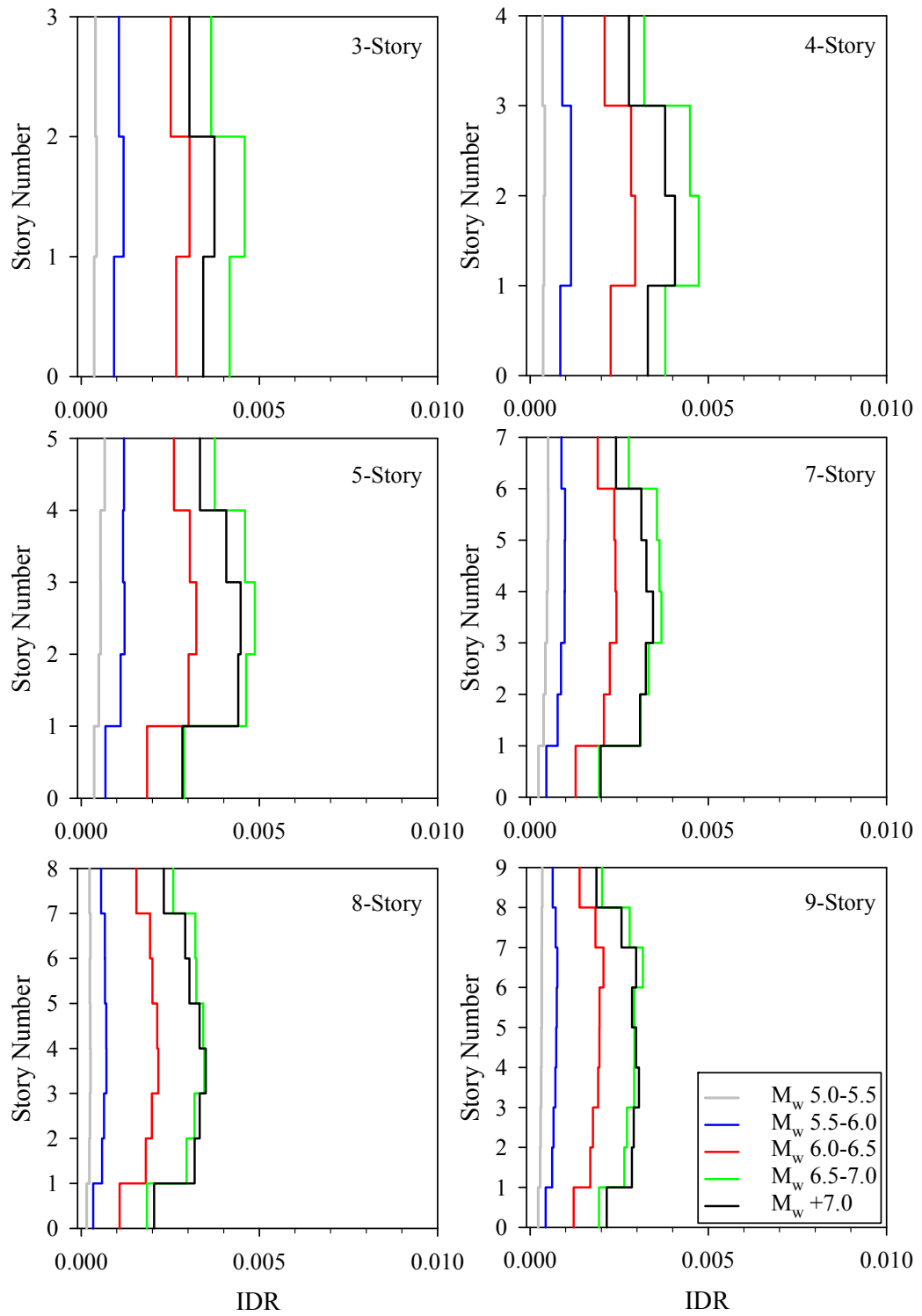


Figure 3.9 Variation of median IDR profiles along the building height for different magnitude bins

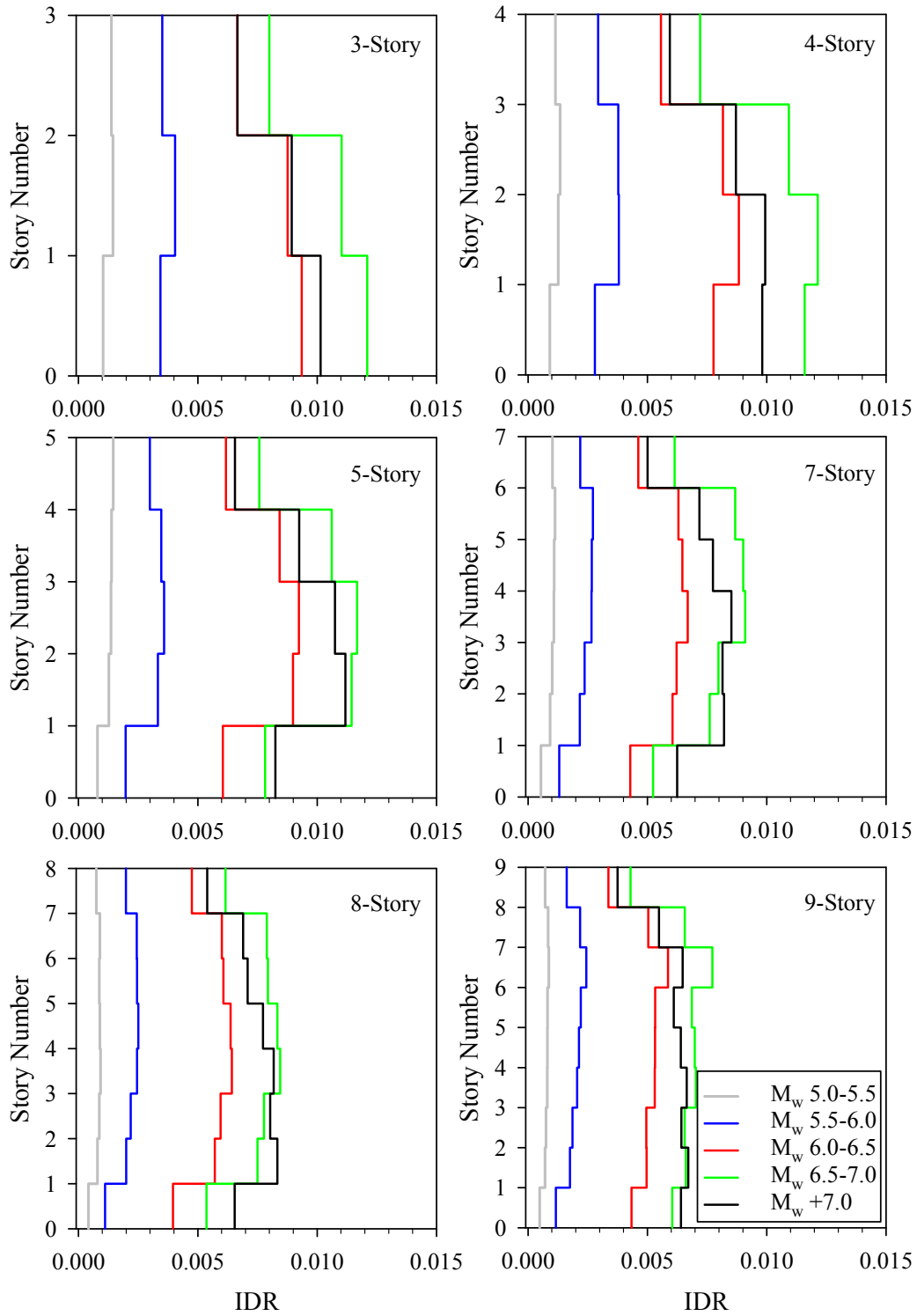


Figure 3.10 Variation of median + σ IDR profiles along the building height for different magnitude bins

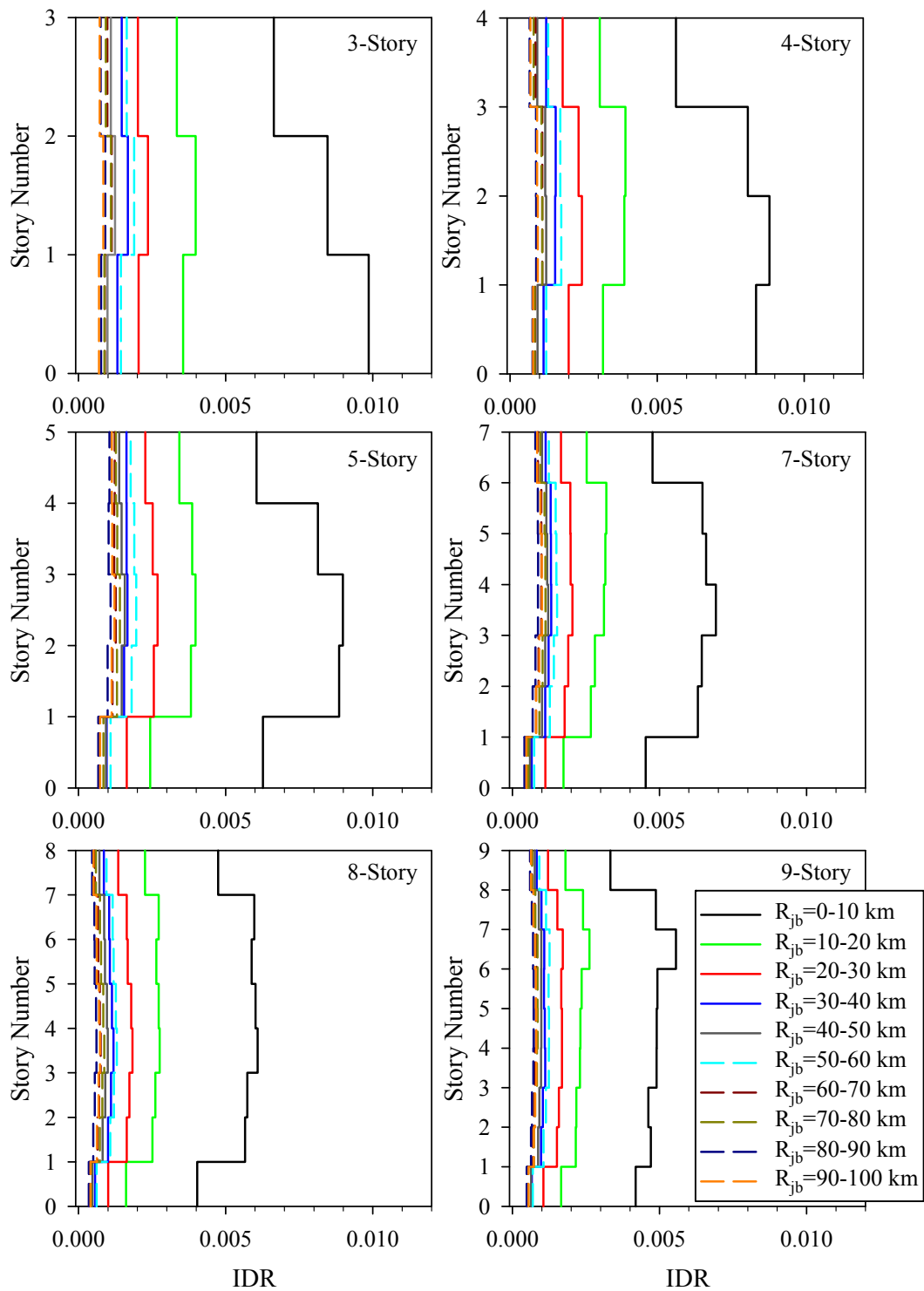


Figure 3.11 Variation of median IDR profiles along the building height for different distance bins

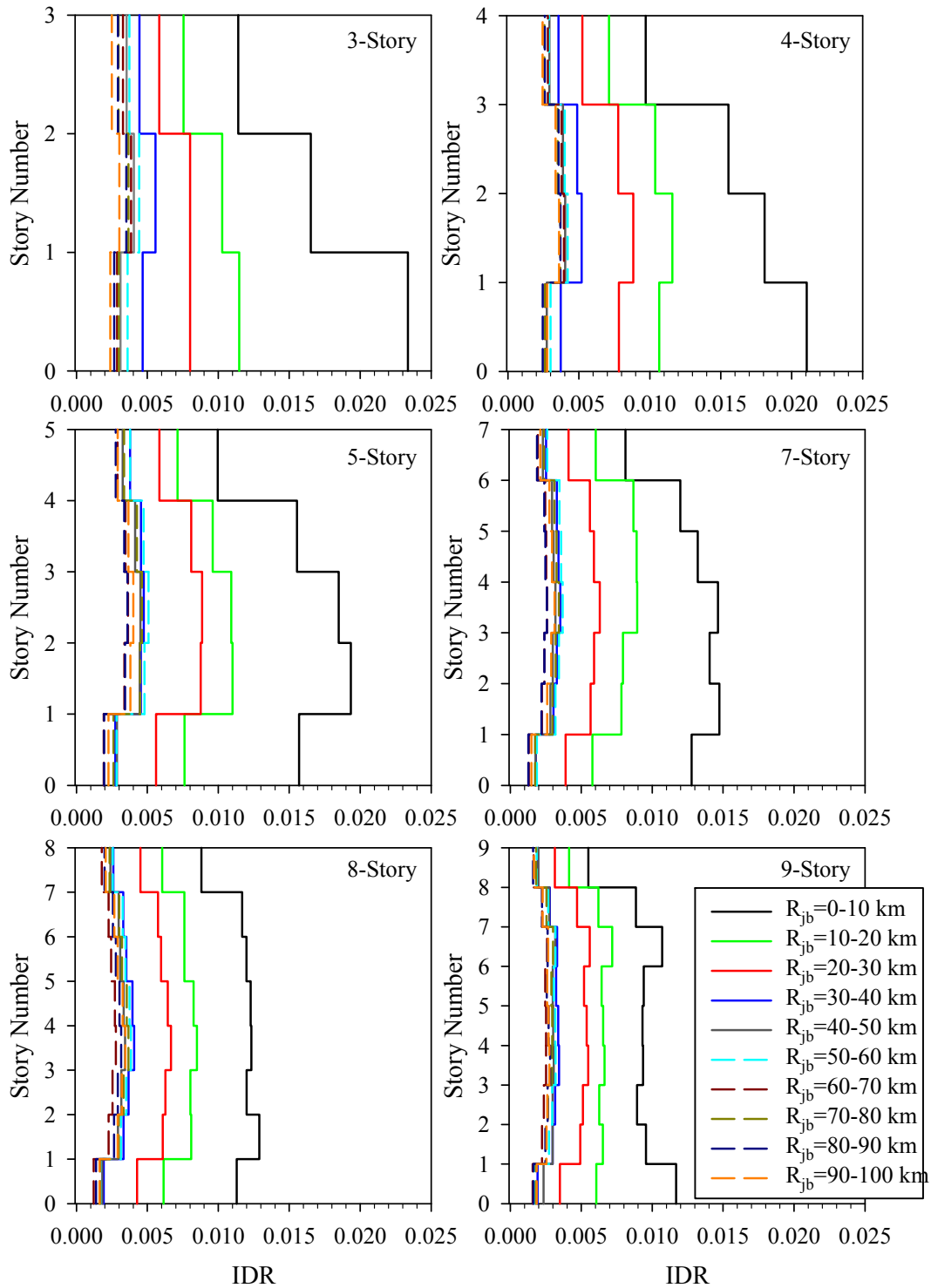


Figure 3.12 Variation of median + σ IDR profiles along the building height for different distance bins

The given plots indicate that the change in magnitude significantly affects IDR demands. As the magnitude increases, the IDR demands tend to increase as well. The median IDR values (Figure 3.9) seem to follow a gradually increasing pattern for the first three magnitude bins. This observation becomes vague for the two larger magnitude bins. The IDR results of M_w+7 bin are closer (and even smaller) to the M_w 6.5-7.0 bin. Smaller IDR values of M_w+7 bin with respect to M_w 6.5-7.0 subset are particularly valid for low-rise frames (i.e., 3S_MRF, 4S_MRF and 5S_MRF).

Unexpectedly low IDR and MIDR values computed from the 1999 Düzce Earthquake (M_w 7.1) records can be one of the reasons to explain the observed magnitude effect for the two larger magnitude bins. The MIDR versus distance (R_{jb}) scatters of the two larger magnitude bins (Figure 3.13) illustrate this fact. The MIDR values of the 1999 Düzce Earthquake that are encircled in red constitute the lower bound of these two magnitude bins when its magnitude and the proximity of its accelerograms to the source (generally less than 30 km) are of concern. The other observation from these scatter diagrams is the similarity of MIDR values computed from the larger two magnitude bins, which can explain the closer median IDR trends observed from these two magnitude groups. The majority of numerical problems (Figure 3.14a) and outliers (Figure 3.14b) that are disregarded in the statistical studies also fall into the largest magnitude bin (See discussions in Section 3.2). These peculiarities contribute to the lower MIDR and IDR demands of the largest magnitude bin as well. The overall discussions in this paragraph advocate the significance of ground-motion features as well as the interaction between structure and ground motion that should be properly considered all together while estimating the EDPs during a seismic action.

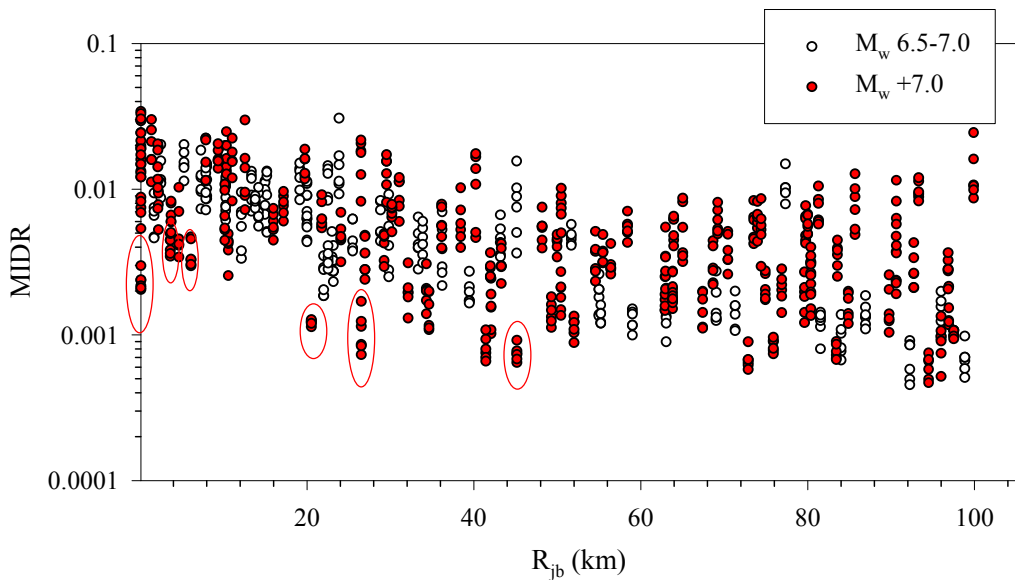


Figure 3.13 Comparison of MIDR demands between the largest two magnitude bins. The red circles enclosing some of the MIDR values from the M_w+7 bin designate the nonlinear RHA results of the 1999 Düzce Earthquake

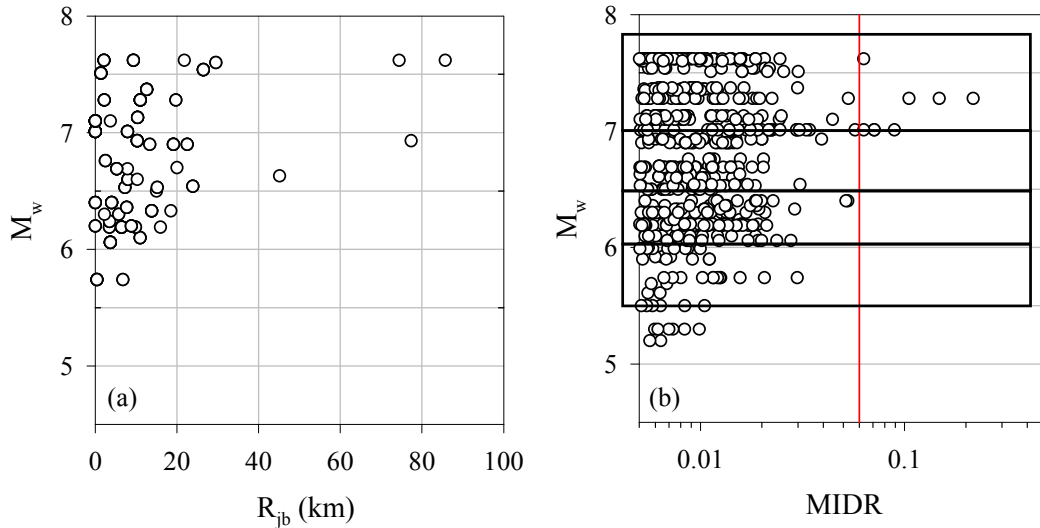


Figure 3.14 (a) Distribution of failed and not-converged records in terms of distance and magnitude (b) outlier MIDR values (scatters to the right of vertical red line) that are disregarded in the statistical analyses

The median IDR plots in Figure 3.9 also indicate a decrease in IDR demands with the increase in total number of stories. The relatively low IDR values of mid-rise frames (7S_MRF, 8S_MRF, and 9S_MRF), in particular towards larger magnitude records (the last three magnitude bins) can indicate the level of sensitivity in IDR to building height. This phenomenon can be explained by the redistribution of forces and deformations in structural systems that becomes more prominent with the increase in structural members. The results presented in this study show that the redistribution property of taller buildings is more effective as the level of inelasticity increases that is related to higher ground-motion amplitudes.

The other important observation from Figure 3.9 concerns the location of MIDR (maximum of IDRs along the building height). MIDR is generally located at stories near the mid-height of the frames except for the 9S_MRF model. The MIDR demands of 9S_MRF shift towards the upper stories that can be explained by the contribution of higher mode effects. Observations made from median IDR plots (Figure 3.9) are also valid for median + σ IDR plots (Figure 3.10) indicating the coherent and consistent behavior of this parameter.

Figures 3.11 and 3.12 that show the influence of source-to-site distance on the variation of IDR indicate a decrease in IDR demands with increasing distance. IDR demands change rapidly for the first 30 km (i.e., the first 3 distance bins). The variation of IDR as a function of distance seems to diminish at larger distances. This is particularly valid for taller buildings in the building inventory. Similar to magnitude-dependent IDR behavior, the location of MIDR is close to mid-height stories for all model buildings at all distance

ranges except for the 9S_MRF building. As in the case of magnitude-dependent behavior, MIDR demands of 9S_MRF shift towards the upper stories.

Before closing this section, the suggested IDR limits in some of the seismic design codes are discussed under the presented statistics in Figures 3.9 to 3.14. According to Eurocode 8 (CEN, 2004), the allowable interstory drift depends on the type of non-structural elements and their arrangement in the structure. Eurocode 8 (CEN, 2004) multiplies the IDRs with a reduction factor¹, v , that is recommended as 0.4 for building importance classes III¹ and IV¹ and 0.5 for building importance classes I¹ and II¹. The reduced IDRs are compared against 0.5% drift limit for buildings having brittle non-structural elements, 0.75% drift limit for buildings having ductile non-structural elements and 1.0% drift limit for buildings having non-structural elements that do not interact with other structural or non-structural elements. The maximum MIDR limit in the Turkish Earthquake Code (TEC, 2007) is 2% for reinforced concrete structures. According to the ASCE/SEI 7-10 (ASCE, 2010), the drift ratio limit varies between 0.7% and 2.5% depending on the structural type and seismic use group. In the case of moment resisting RC frame structures, the limitation in ASCE/SEI 7-10 (ASCE, 2010) are set to 1.0%, 1.5% and 2.0% for seismic use groups IV², III² and I-II², respectively. According to this code, regular buildings are assigned to seismic use group II and have drift limitation up to 2.0%.

The interstory drift provisions in these codes draw similar upper limits for IDR. A 2% interstory drift can be interpreted as the upper limit of IDR for ductile reinforced concrete systems considering the damage-control (Life Safety) limit state. This limit seems to be higher than the median and median + one standard deviation IDR demands computed from nonlinear RHA. This observation agrees with Priestley et al. (2007) where the authors state that most code-complying buildings, particularly frame buildings, will not reach the structural damage-control limit state under severe seismic action. The code-based drift limits also place emphasis on the structural type and usage purpose of structures regardless of the seismicity in the region of concern. In other words, the design checks of two similar type buildings, one designed for high seismic demands and the other designed for relatively lower seismic demands are done with the same drift limit. Different levels of

¹ According to Eurocode 8 (CEN, 2004) the reduction factor, v , takes into account the lower return period of the seismic action related with the damage limitation requirement. The importance classes I and II comprise of ordinary buildings and buildings of minor importance for public safety, whereas the importance classes III and IV refer to buildings whose seismic resistance and integrity during earthquakes is important in terms of post-earthquake consequences and civil protection (schools, hospitals, fire stations, power plants, etc.).

² According to ASCE/SEI 7-10 (2010), all structures are assigned to a seismic group depending on the type of use. Seismic use group I comprises of structures that represent a low risk to human life, whereas seismic use group III refers to the structures that have a substantial risk on the public safety and economy. Structures containing toxic or explosive substances where their quantity exceeds a threshold are assigned to seismic group III. Structures that are designated as essential facilities and required to maintain functionality and those containing substantial quantities of hazardous substances are assigned to seismic group IV. All buildings and other structures that are not listed in other categories are assigned to seismic group II.

design ground motions for those buildings will result in different member sizes and the same code-based drift limitation would not reflect the modern seismic design philosophy that aims at tailoring the structural behavior and capacity specific to the level of design ground motion demand. Thus, the code-based drift limits should consistently reflect the target annual exceedance rate of ground-motion intensity used for design. The proposed MIDR expression that is described in the following chapters is believed to constitute a useful tool to comply with this objective of modern seismic design philosophy. Chapter 6 presents a set of probability-based seismic design and performance assessment procedures that make use of the MIDR expression. These procedures are believed to be consistent with the modern design and performance assessment concepts.

3.4.3 Dependence of MIDR on Style-of-Faulting

The amplitudes of ground-motion intensity measures (e.g., PGA, PSA, PGV etc.) are affected from different faulting mechanisms and the new ground-motion prediction equations consider the style-of-faulting (SoF) effect in their functional forms. This subsection investigates the dependency of MIDR on SoF.

Figure 3.15 shows the variation of entire MIDR values as a function of distance and magnitude for normal, reverse and strike-slip faulting mechanisms. The scatter plots suggest the existence of SoF influence on MIDR. However, the nonuniform distribution of SoF in terms of magnitude and distance in the ground-motion dataset (see details in Chapter 2) as well as the interaction between ground motion and building response requires a statistical quantification about the significance of SoF on MIDR. This is achieved through ANOVA tests in this dissertation. The ANOVA test provides information about similarity of sample means (or medians under log-normal distribution) of several groups. The null hypothesis in ANOVA is the similarity of sample means among the bins. The p-value, which is the major statistical output of ANOVA test, is the probability that shows the strength of rejecting the null hypothesis at a given significance level. (The significance level is usually selected as 5% in such statistical tests). A p-value closer to zero indicates a higher probability of rejecting null hypothesis. In other words, a large p-value means the increased likelihood of fail-to-rejection of null hypothesis.

The ANOVA tests are done by grouping the MIDR inventory into several magnitude and distance bins. The magnitude bins used in ANOVA tests are ones that are defined in the beginning of this chapter. The distance bins are established with a distance increment of 20 km. This way a sufficient number of MIDR data is retained in each magnitude-distance bin pair for reliable ANOVA test. The null hypothesis, as indicated previously, is the similarity of sample MIDR means for each magnitude-distance bin pair in terms of different faulting mechanisms. Figures 3.16, 3.17 and 3.18 show the ANOVA test results of the model frames for normal-strike slip, normal-reverse and strike slip-reverse faulting mechanisms, respectively. The significance level is considered as 5% in the test results. These figures display several panels and each panel corresponds to ANOVA test results of a specific

magnitude-distance bin pair. The ordinates of the scatter show logarithms of mean MIDR values. Each data pair, on these panels, from left to right constitutes the mean MIDR values of 3-, 4-, 5-, 7-, 8- and 9-story frames, respectively. The square and circular points in each data pair correspond to logarithmic mean MIDR of normal and strike-slip (Figure 3.16), normal and reverse (Figure 3.17) and strike-slip and reverse (Figure 3.18) accelerograms, respectively. If data pairs are given as solid symbols, differences between the compared sample means are insignificant at 5% significance level. When the sample mean differences are significant at 5% significance level, the data pairs are given as hollow symbols. The numbers at the top of each scatter plot indicate the number of records used for calculating the logarithmic mean MIDR in each data pair. For some M_w - R_{jb} bin pairs, scatter plots are not given as the number of data is not meaningful to run ANOVA tests.

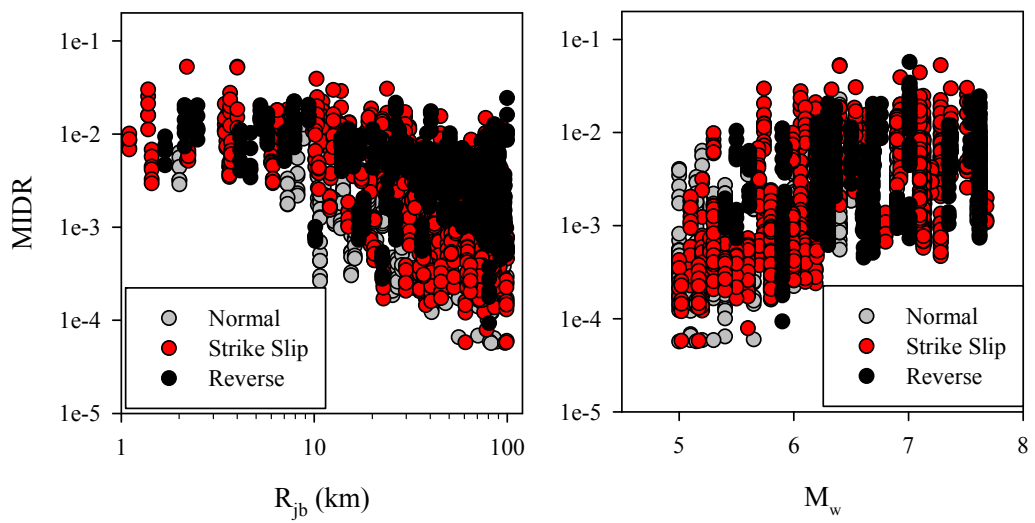


Figure 3.15 Influence of SoF on MIDR

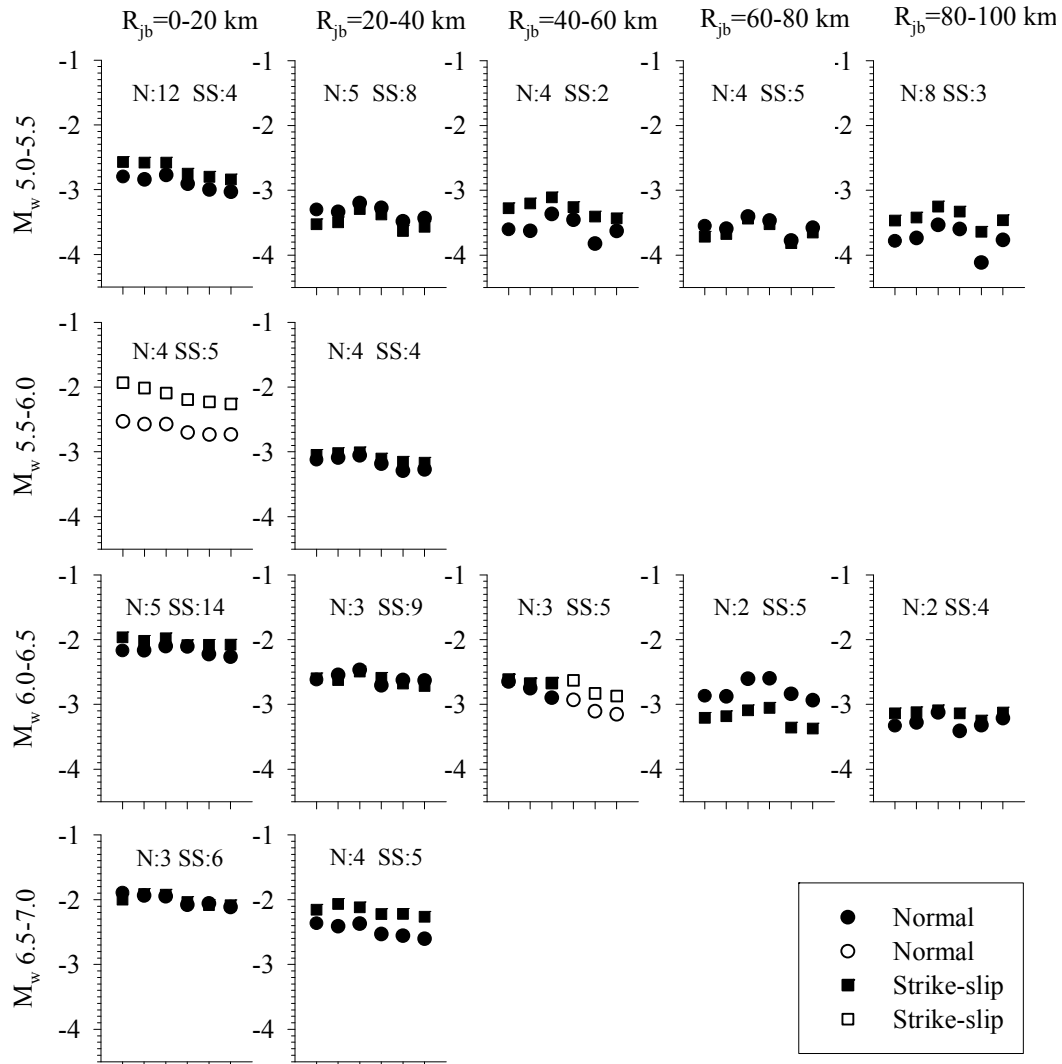


Figure 3.16 Scatter plots of each M_w - R_{jb} bin where ANOVA tests are performed to assess the influence of normal (N) and strike slip (SS) faulting on MIDR demands computed from each model frame

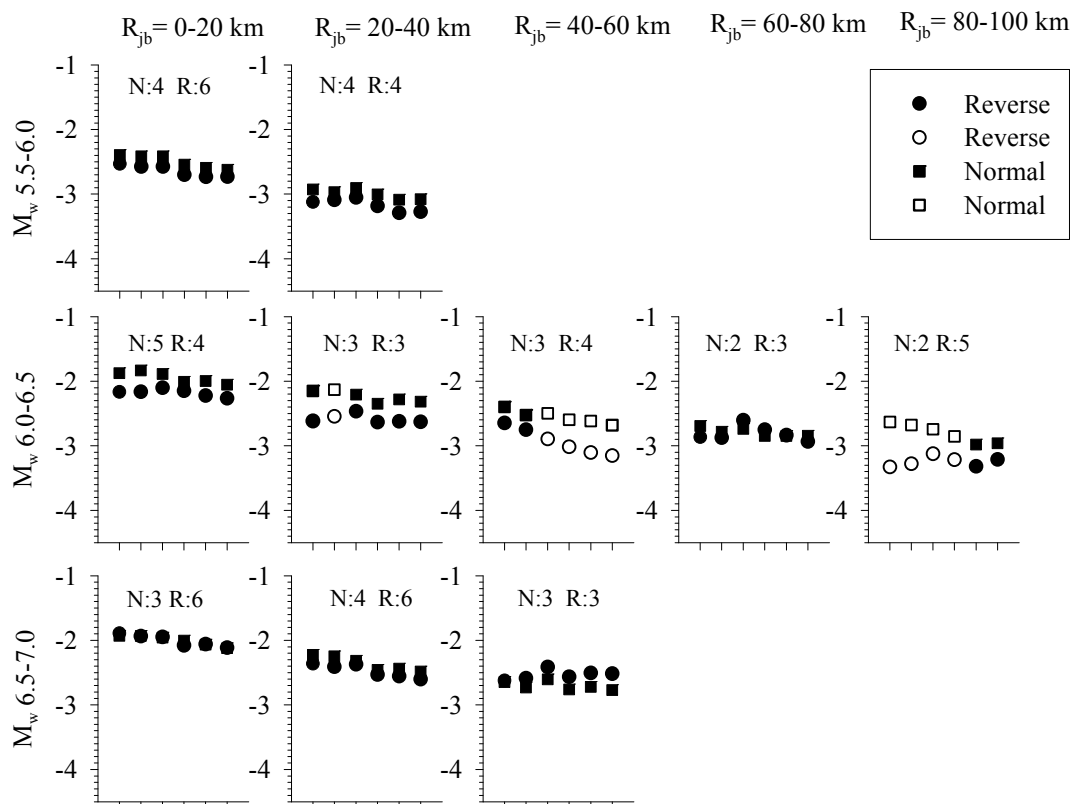


Figure 3.17 Scatter plots of each M_w - R_{jb} bin where ANOVA tests are performed to assess the influence of normal (N) and reverse (R) faulting on MIDR demands computed from each model frame

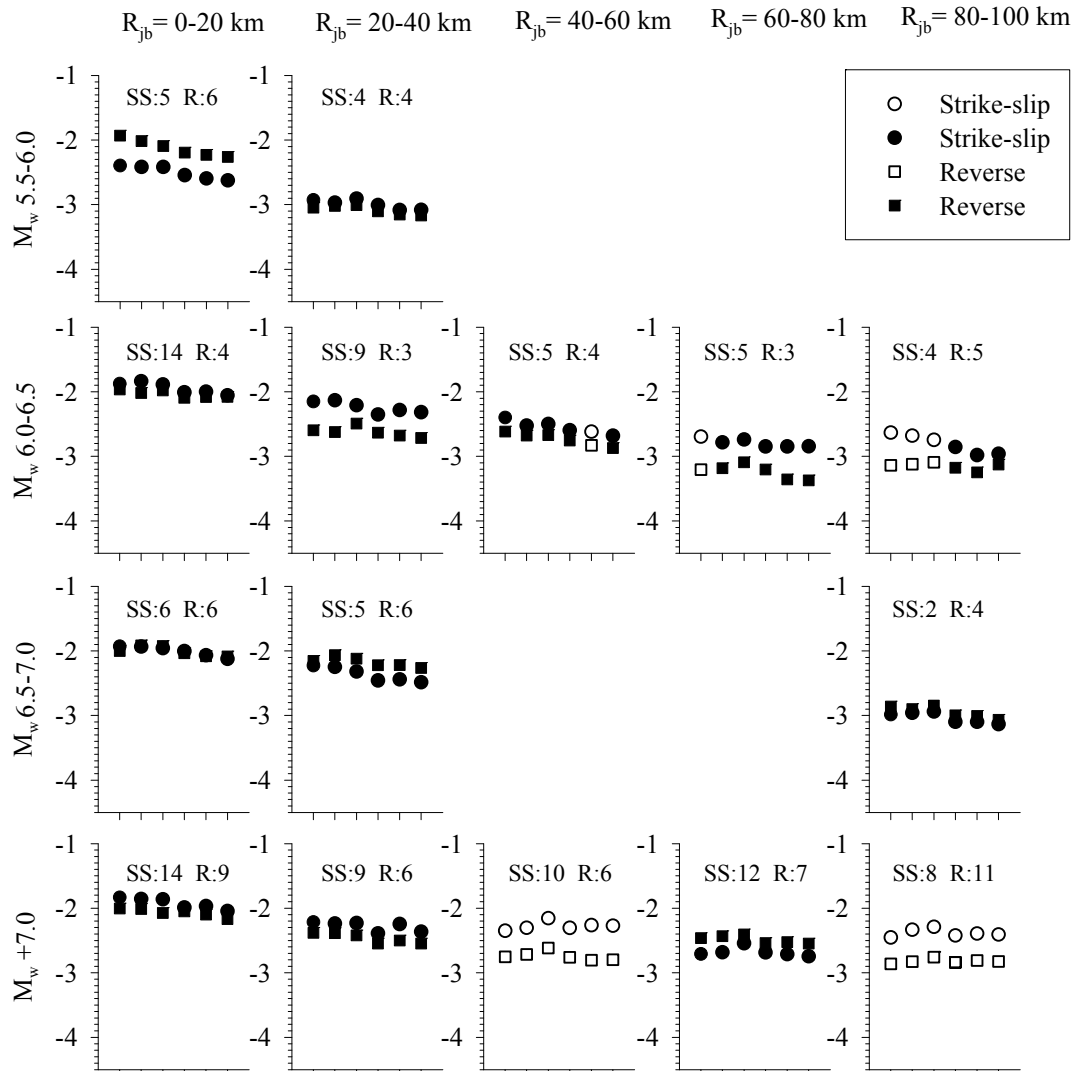


Figure 3.18 Scatter plots of each M_w - R_{jb} bin where ANOVA tests are performed to assess the influence of strike-slip (SS) and reverse (R) faulting on MIDR demands computed from each model frame

The ANOVA tests show that SoF effect is visible only for a few number of magnitude-distance bin pairs compared to the entire number of tests. These results suggest a weak dependence of MIDR on SoF. The lack of data in several magnitude-distance bins as well as the nonuniform distribution of the data in terms of SoF may cast doubts about the reliability of the conclusion derived from ANOVA tests. For the sake of simplicity, the predictive model presented in this study disregards the influence of SoF on MIDR estimations and this simplification may result in a slight bias in the estimated MIDR values. This bias is accepted as tolerable and disregarding SoF effects on MIDR is considered as the limitation of the proposed empirical model.

3.4.4 Dependence of MIDR on Soft and Stiff Site Conditions

The ground-motion dataset used in this dissertation consists of recordings from NEHRP C ($360\text{m/s} \leq V_{s,30} < 760\text{m/s}$) and NEHRP D ($180\text{m/s} \leq V_{s,30} < 360\text{m/s}$) site classes as discussed in Chapter 2. These site classes grossly correspond to Z2 and Z3 soil conditions in the Turkish Earthquake Code (TEC, 2007). The absence of other site conditions, such as rock sites with $V_{s,30} \geq 760\text{m/s}$, in the database may result in limited observations about the actual soil influence on MIDR. However, the site classes encompassed by the database represent the most frequent soil conditions for many engineered buildings. The scatters in Figure 3.19 show the variation of MIDR for the site classes considered in this study. Figure 3.19a shows this variation as a function of distance whereas Figure 3.19b gives the same information in terms of magnitude. The MIDR data pertaining to NEHRP C and D sites are shown in different color codes on these panels. The plots indicate that MIDR values are not very sensitive to the soil behavior of NEHRP C and D site classes as their magnitude- and distance-dependent trends are similar to each other without showing a significant quantitative variation. In other words, there is no clear separation of MIDR demands between NEHRP C and D site classes. Similar to the previous section, ANOVA tests are done to see the sensitivity of MIDR on site classes. The same magnitude-distance bin pairs and the same illustration format is used as explained in Section 3.4.3 for the current ANOVA tests. The only difference is the grouping of MIDR values: for the current analysis logarithmic means of MIDR values are given for NEHRP C and NEHRP D site classes. The ANOVA test results given in Figure 3.20 do not exhibit a strong evidence for speculating on the dominance of soil behavior (NEHRP C and D site classes) on MIDR amplitudes. However, when compared to ANOVA statistics for SoF, the site class seems to play a more dominant role in the MIDR amplitudes as there are more magnitude-distance bin pairs that show the significance of site class effect on sample mean MIDR values. Moreover, the distribution of data in terms of site class for the selected magnitude and distance bin pairs seem to be more uniform.

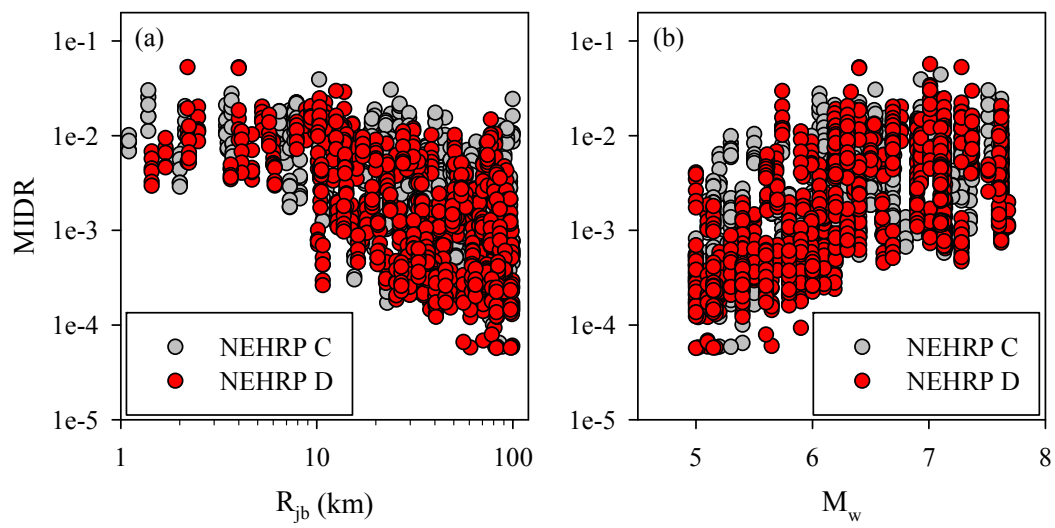


Figure 3.19 Variation of MIDR as functions of (a) distance and (b) magnitude bins for different site classes

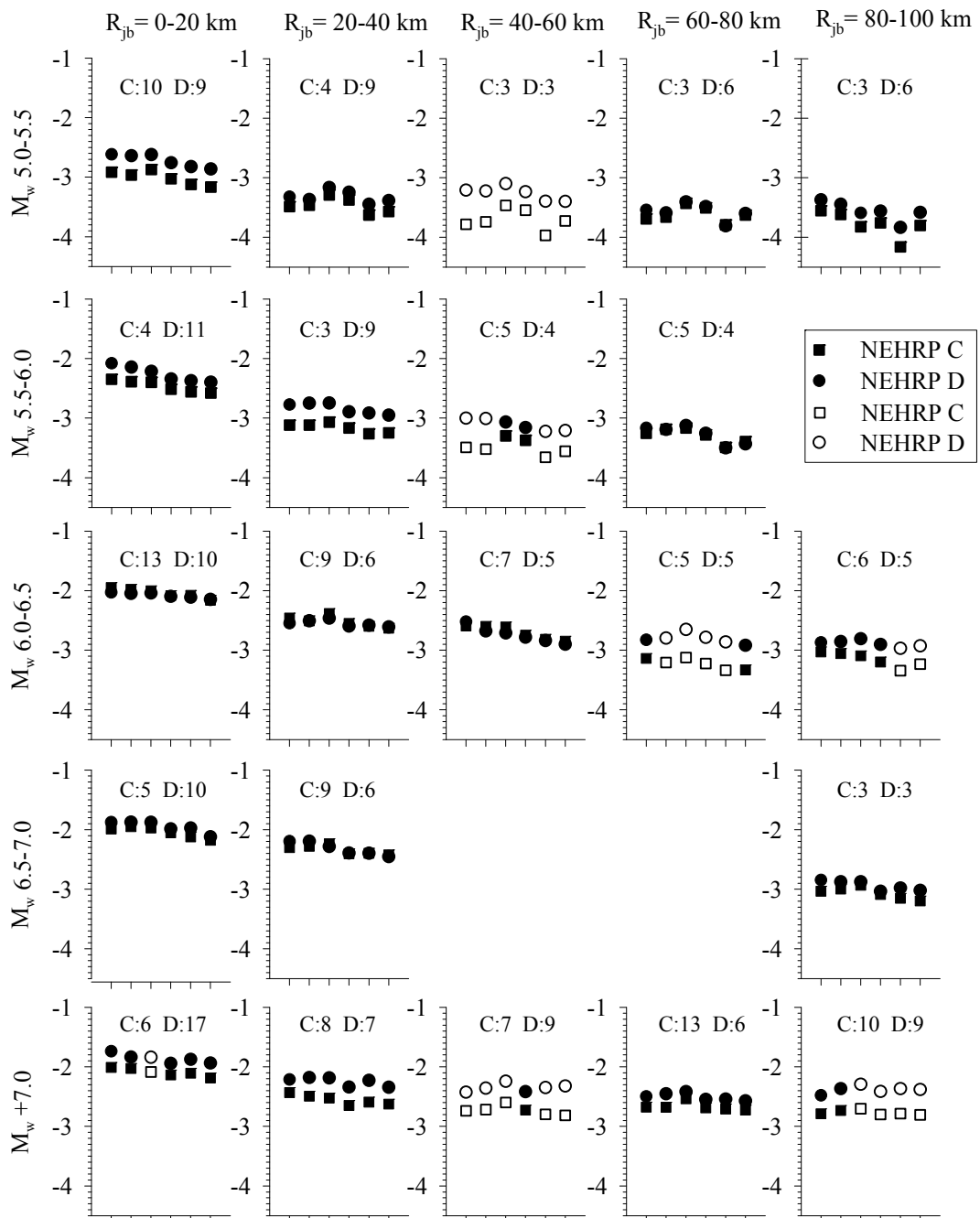


Figure 3.20 Scatter plots of each M_w - R_{jb} bin where ANOVA tests are performed to assess the influence of NEHRP C and NEHRP D site class on MIDR demands computed from each model frame

3.4.5 Variation of MIDR with Distance and Magnitude

The significance of magnitude and distance on IDR is discussed in Section 3.4.2 that also includes some limited information on MIDR. This section provides broader information about the sensitivity of MIDR on magnitude and distance. MIDR scatters are studied individually for two adjacent magnitude or distance bins to understand the effects of these seismological parameters on MIDR variation. Scatter plots in terms of consecutive magnitude bins are shown between Figures 3.21 and 3.26. Figures 3.27 to 3.32 show similar MIDR scatters for consecutive distance bins. Each figure displays the MIDR scatters for a particular building model. Each scatter plot contains trend lines that show the general behavior of MIDR for the two adjacent magnitude or distance bins.

Scatters that are plotted as a function of distance for consecutive magnitude bins (Figure 3.21 - Figure 3.26) indicate a decrease in MIDR with increasing distance. The distance-dependent decrease in MIDR is significant for small magnitudes (first two panels in Figures 3.21 to 3.26). The decay in MIDR with increasing distance is still apparent for larger magnitude bins but the distance influence is relatively weaker in these cases (last two panels in Figures 3.21 to 3.26). The closer trend lines in the last 2 panels of these figures are the major evidences to this observation. The MIDR values of M_w 6.5-7.0 bin are slightly larger than those computed from M_w +7 bin. The possible reasons behind this observation are explained in Section 3.4.2 while discussing the observed IDR behavior and will not be repeated here for brevity.

Similar observations to those that are discussed in the above paragraph can also be made for magnitude-dependent MIDR scatters that are shown by different distance bins between Figures 3.27 and 3.32. These figures indicate that the magnitude-dependent decay in MIDR is more gradual for $M_w > 6.0$. This observation is more visible for distances less than $R_{jb}=50$ km. As the source-to-site distance (R_{jb}) attains values greater than 50 km the gradient of magnitude-dependent decay in MIDR becomes similar for the entire magnitude interval.

The dependency of MIDR on magnitude and distance shows similarities with the influence of these seismological parameters on ground-motion intensity measures (e.g., PGA, PGV, PSA etc). This fact once again emphasizes the importance of proposed predictive model as it combines the seismological features of ground motions and structural properties.

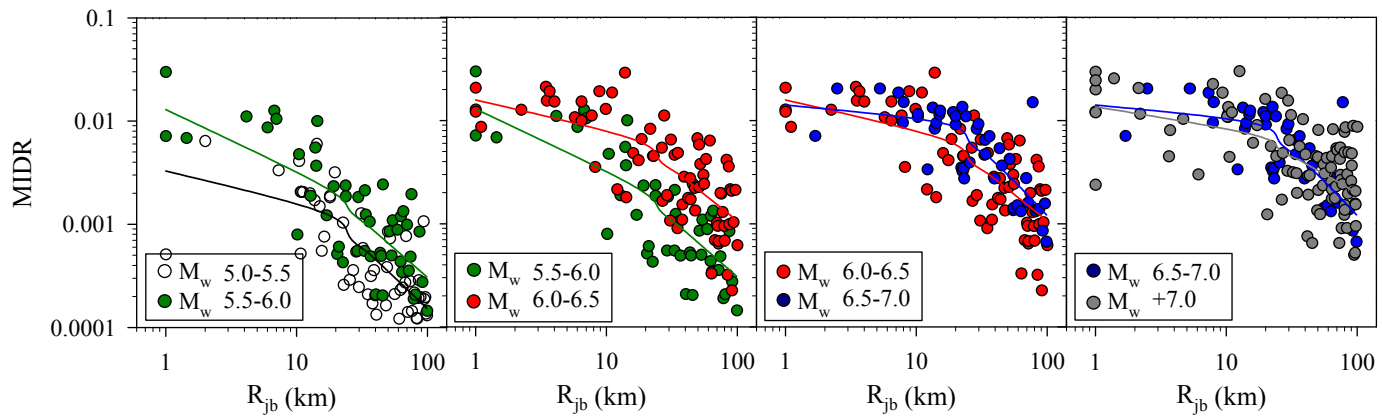


Figure 3.21 Comparison of MIDR demands on 3-story model for adjacent magnitude bins

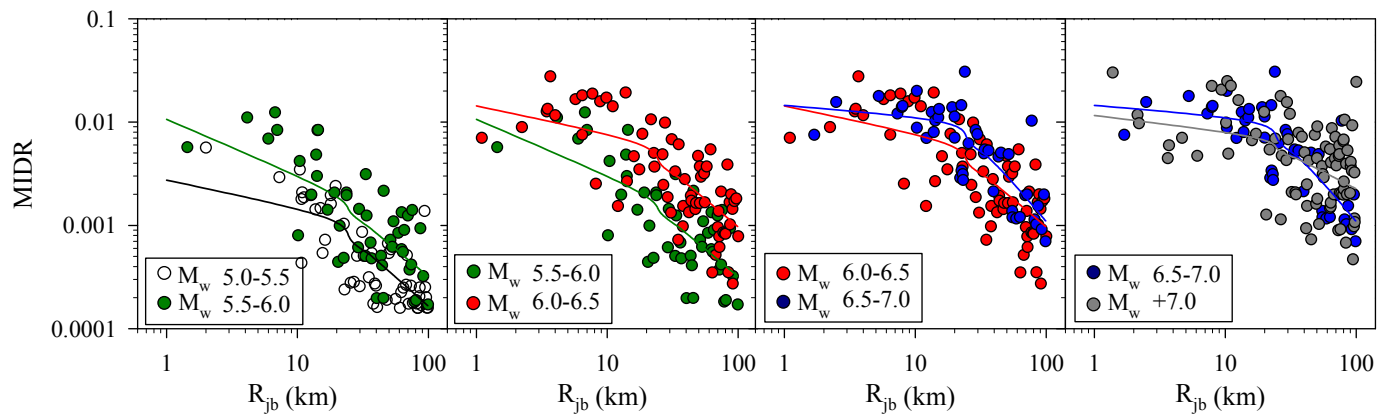


Figure 3.22 Comparison of MIDR demands on 4-story model for adjacent magnitude bins

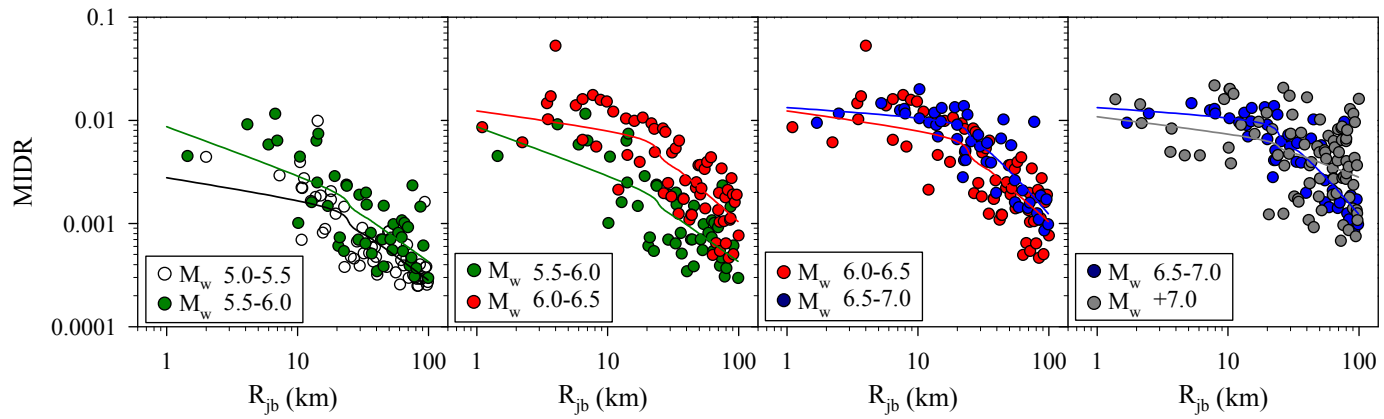


Figure 3.23 Comparison of MIDR demands on 5-story model for adjacent magnitude bins

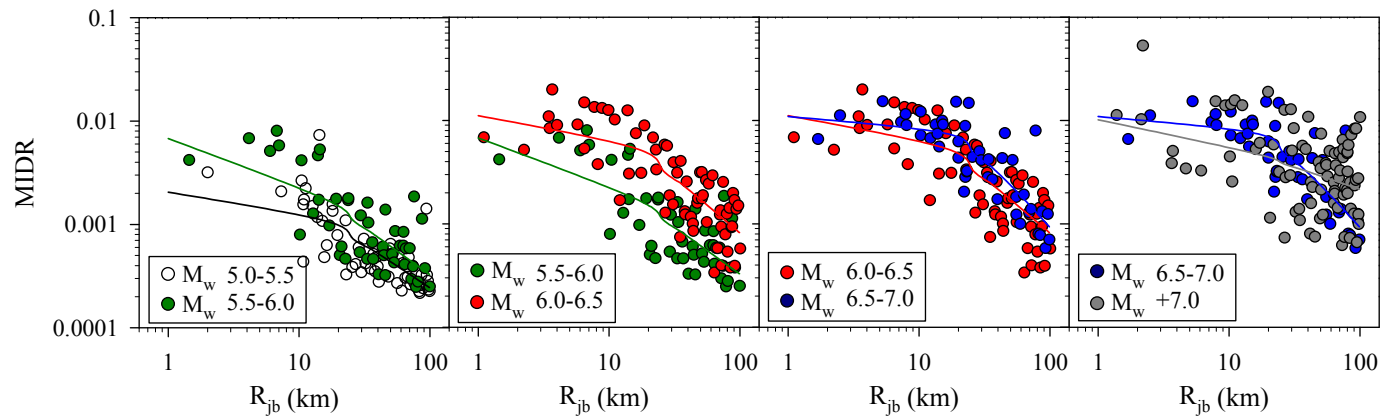


Figure 3.24 Comparison of MIDR demands on 7-story model for adjacent magnitude bins

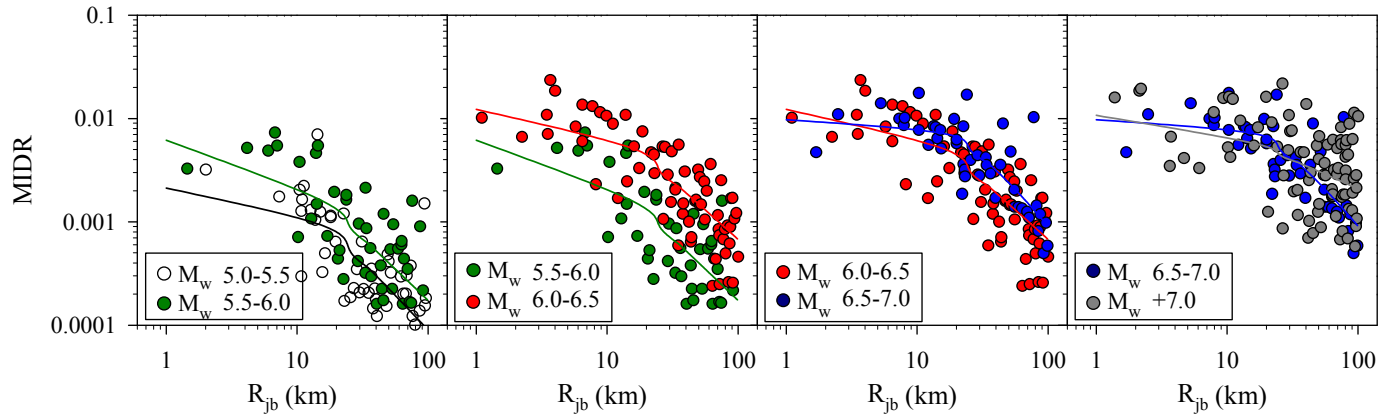


Figure 3.25 Comparison of MIDR demands on 8-story model for adjacent magnitude bins

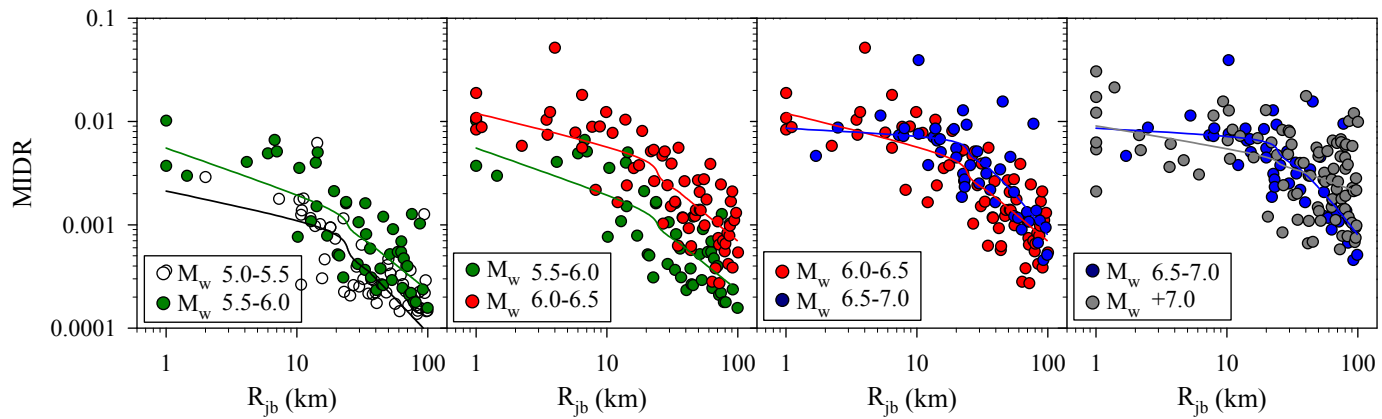


Figure 3.26 Comparison of MIDR demands on 9-story model for adjacent magnitude bins

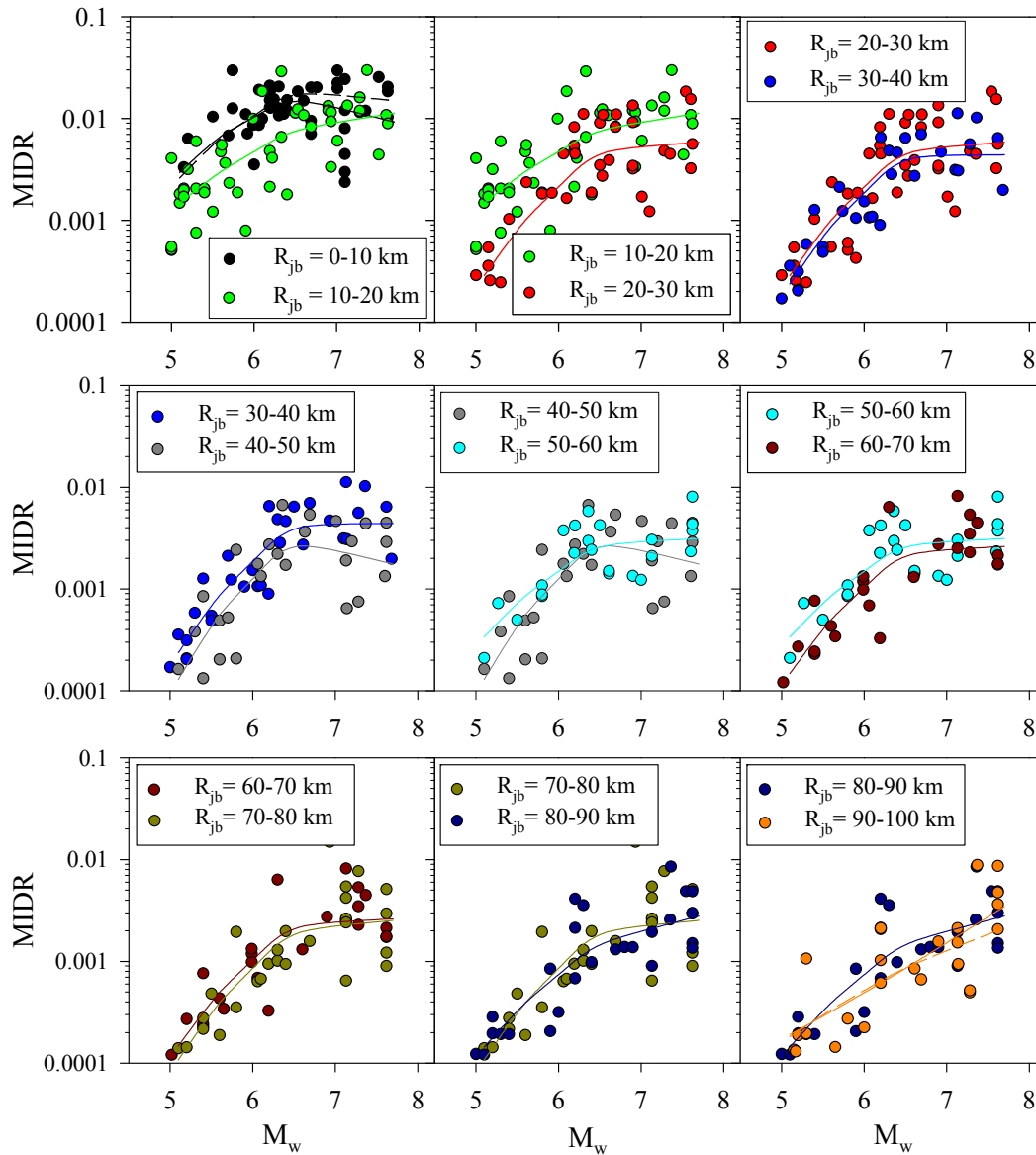


Figure 3.27 Comparison of MIDR demands on 3-story model for adjacent distance bins

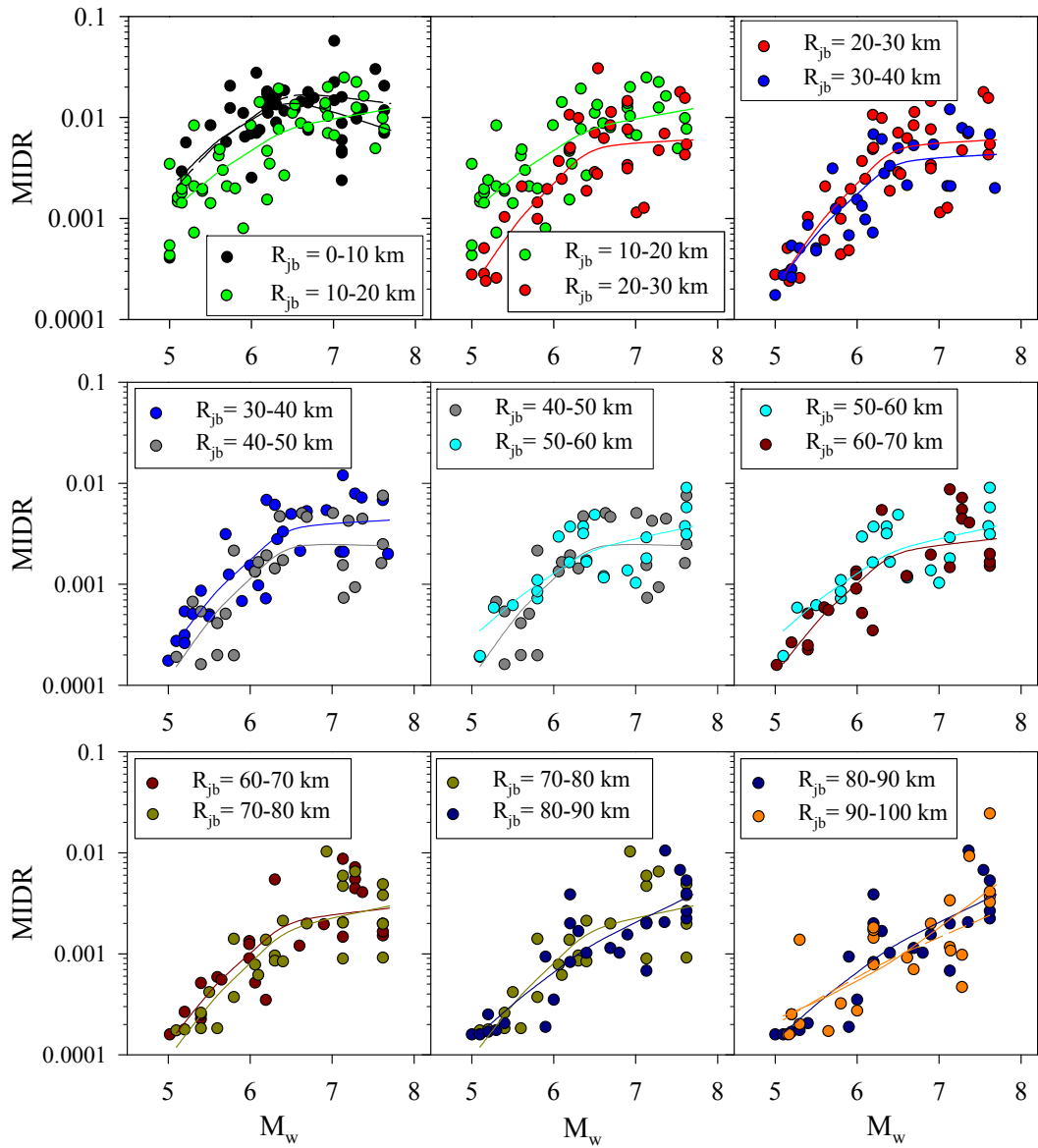


Figure 3.28 Comparison of MIDR demands on 4-story model for adjacent distance bins

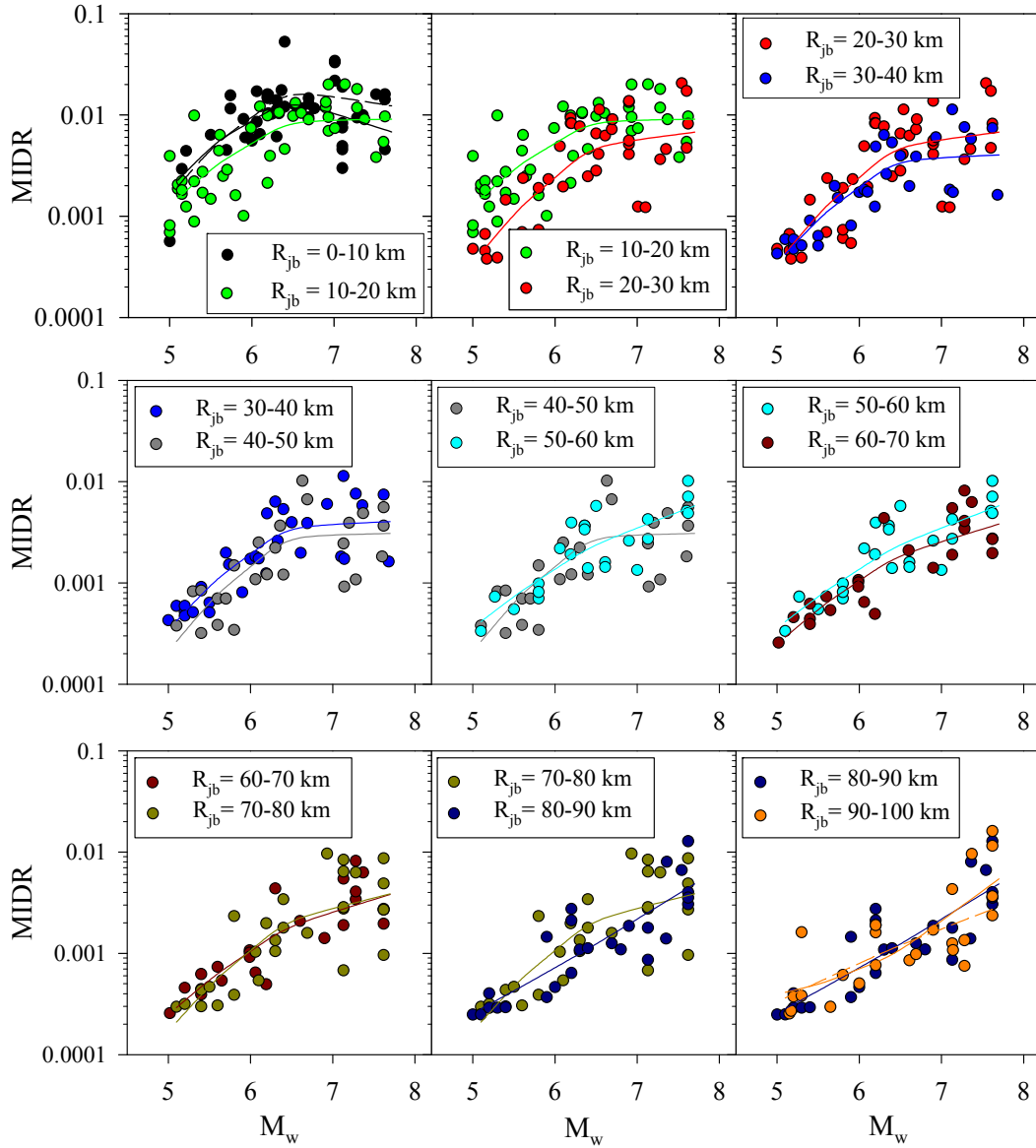


Figure 3.29 Comparison of MIDR demands on 5-story model for adjacent distance bins

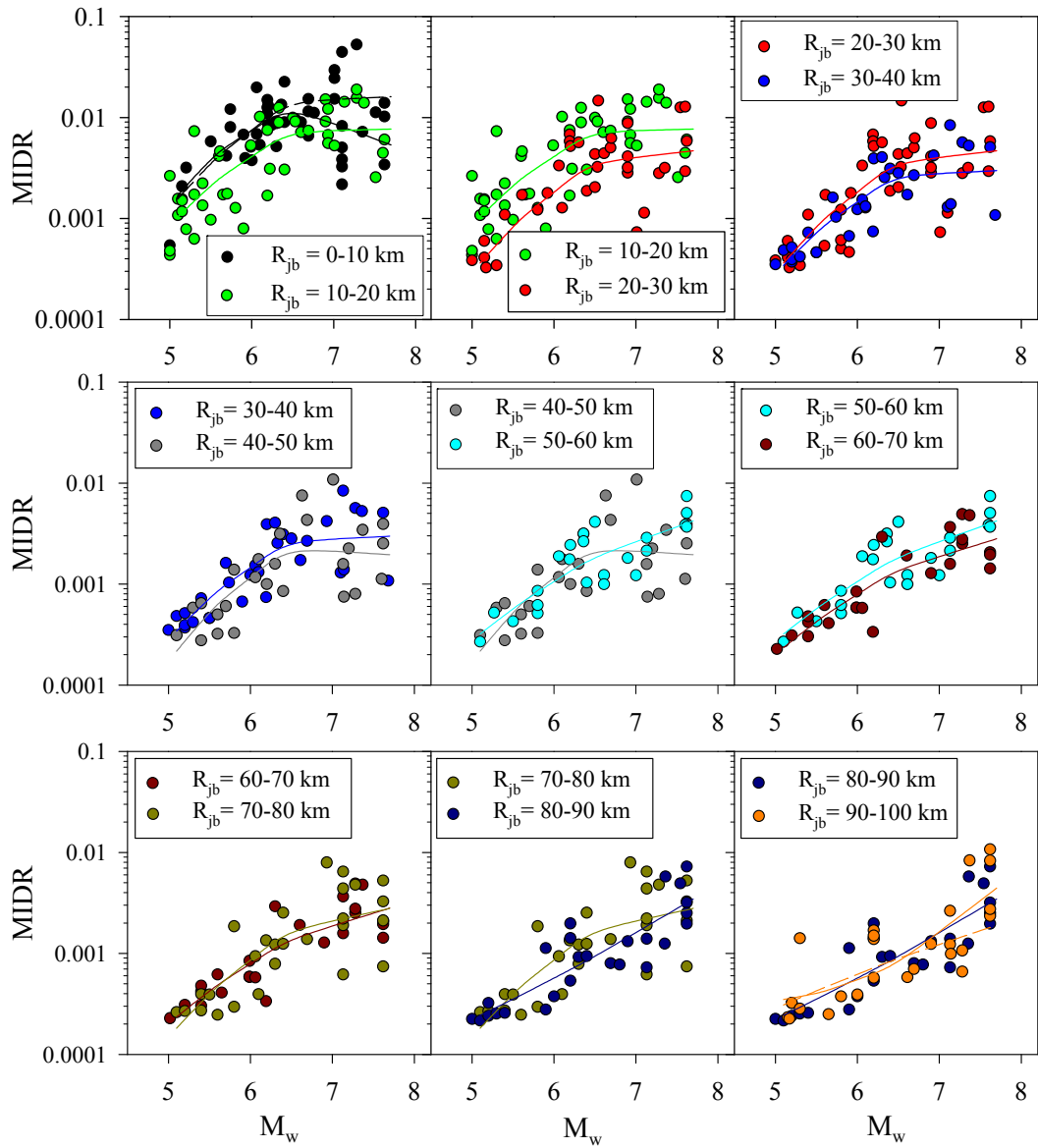


Figure 3.30 Comparison of MIDR demands on 7-story model for adjacent distance bins

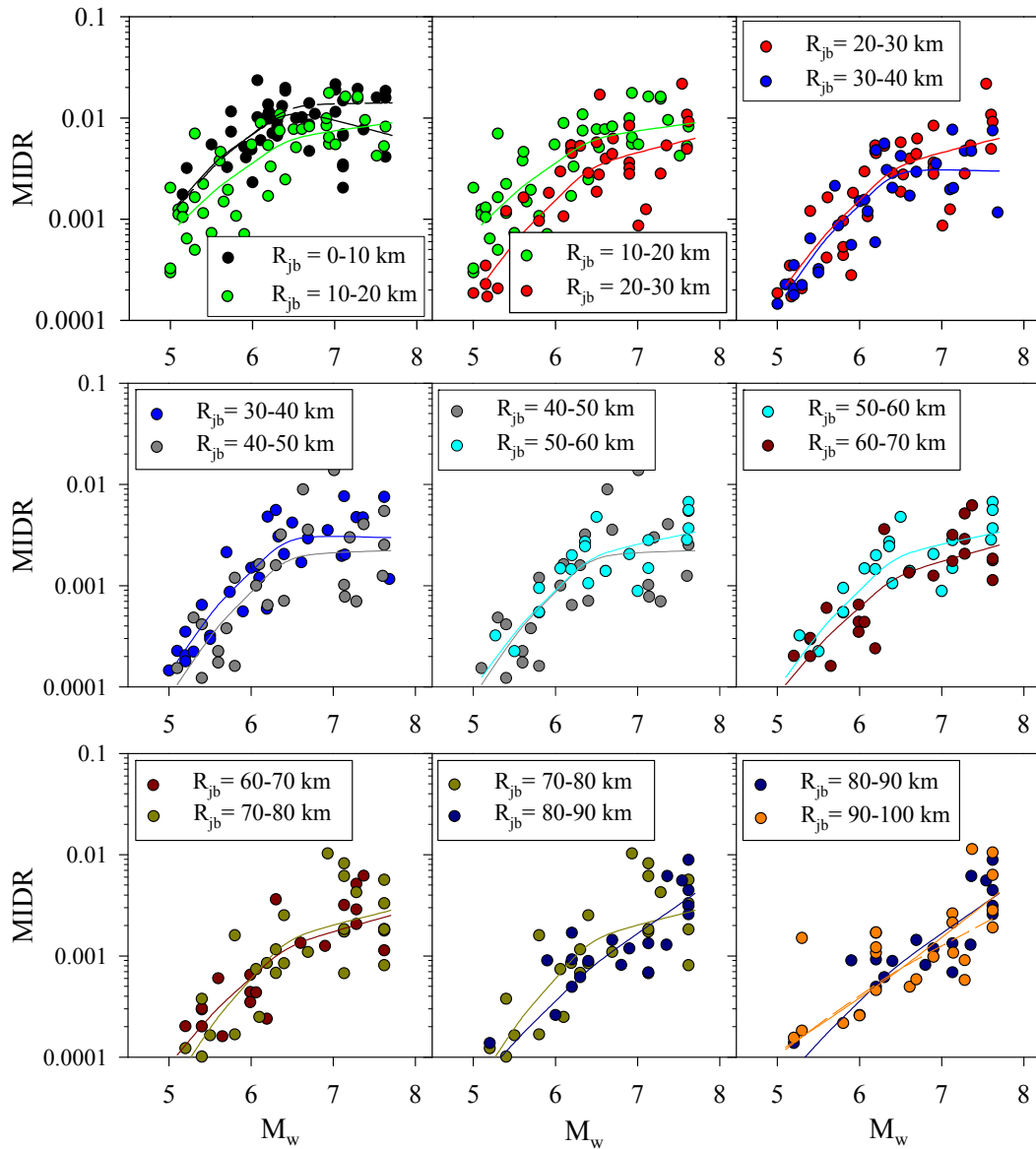


Figure 3.31 Comparison of MIDR demands on 8-story model for adjacent distance bins

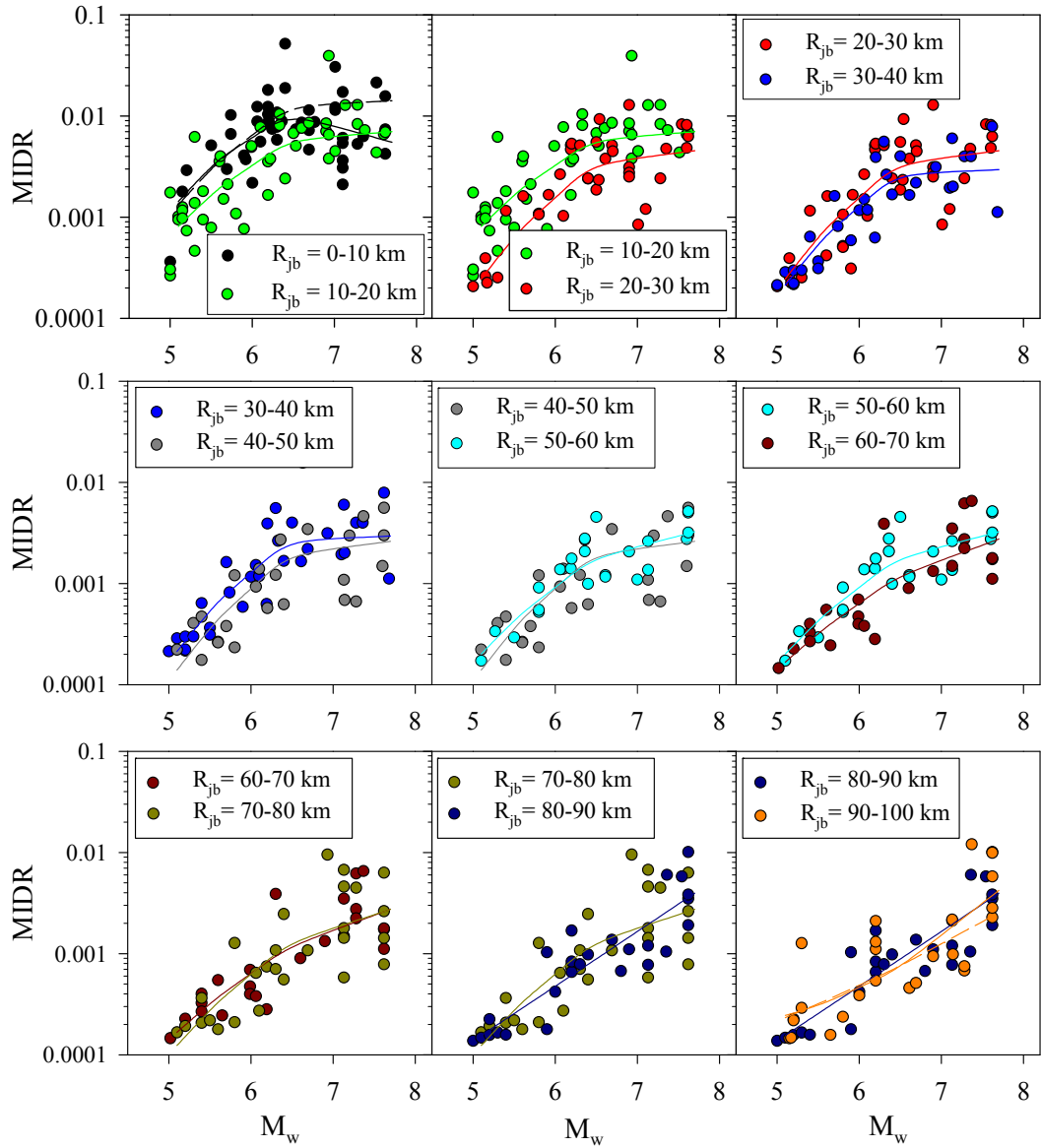


Figure 3.32 Comparison of MIDR demands on 9-story model for adjacent distance bins

3.4.6 Dependence of MIDR on Fundamental Period and Story Number

The MIDR demands of model frames are presented in terms of their fundamental period (T_1) and total height in Figures 3.33a and 3.33b, respectively. The solid squares on these figures correspond to median (logarithmic mean) MIDR values for each frame model. The logarithmic standard deviation of MIDR results for each building is indicated under the corresponding scatter column. Figure 3.33 shows that median MIDR values tend to decrease with increasing fundamental period and story height. However, the variation of MIDR with the changes in building period and height seems to be negligible for the building models considered in this dissertation. Thus, one may assume that MIDR is independent of building fundamental period and height as long as the dynamic response of considered buildings is of concern in this study. The similarity in dispersion statistics fortifies this remark.

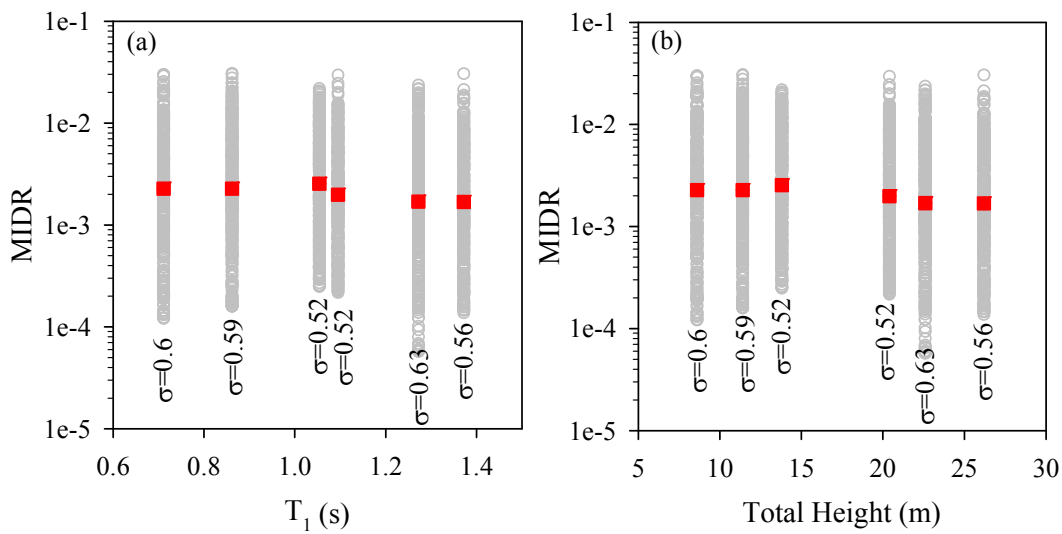


Figure 3.33 Dependency of MIDR on (a) fundamental period and (b) total height. The solid squares represent the median values of each frame model. The MIDR logarithmic standard deviations (σ) of each model are also given on these plots.

In order to provide a quantitative measure about the dependence of MIDR on T_1 and story number ANOVA tests are implemented using the nonlinear RHA results in hand. The ANOVA results that are computed for different magnitude and distance bins are given in Tables 3.3 and 3.4, respectively. The p-value statistics listed in these tables are mostly above 0.05 and would suggest the insensitivity of MIDR on building fundamental period for the building type and period range covered in this study. This observation is used while developing the proposed predictive model. In other words, only one specific expression for estimating MIDR is developed instead of multiple equations that account for the variations in story number or fundamental period.

Table 3.3 Results of ANOVA and F-Tests in terms of magnitude sub-bins (grey shaded cells show the results where null-hypothesis, independency of MIDR on T_1 and building height, cannot be rejected)

M_w	p value ANOVA (All frames)	3S-4S*	4S-5S*	5S-7S*	7S-8S*	8S-9S*
		p value F test				
5-5.5	0.33	0.33	0.34	0.01	0.47	0.13
5.5-6	0.22	0.04	0.07	0.03	0.35	0.20
6-6.5	0.31	0.34	0.05	0.00	0.34	0.00
6.5-7	0.16	0.19	0.02	0.16	0.29	0.01
7-7.7	0.14	0.19	0.02	0.06	0.30	0.00

* S stands for story

Table 3.4 Results of ANOVA and F-Tests in terms of distance sub-bins (grey shaded cells show the results where null-hypothesis cannot be rejected)

R_{JB} (km)	p value ANOVA	3S-4S*	4S-5S*	5S-7S*	7S-8S*	8S-9S*
		p value F test				
0-10	0.01	0.22	0.09	0.00	0.30	0.00
10-20	0.30	0.18	0.09	0.42	0.30	0.01
20-30	0.31	0.04	0.05	0.04	0.09	0.00
30-40	0.14	0.29	0.15	0.10	0.49	0.30
40-50	0.91	0.39	0.12	0.03	0.08	0.03
50-60	0.29	0.33	0.32	0.07	0.27	0.17
60-70	0.63	0.45	0.31	0.03	0.28	0.49
70-80	0.94	0.07	0.35	0.08	0.07	0.31
80-90	0.93	0.16	0.19	0.01	0.18	0.40
90-100	0.94	0.00	0.13	0.05	0.36	0.28

* S stands for story

3.4.7 Overall Statistics of MIDR for Magnitude and Distance Influence

Confined to the building models and ground-motion database of this study, observations about the independency of MIDR on fundamental period imply the use of entire nonlinear RHA results to produce more compact statistics on the magnitude and distance influence of MIDR demands. Figures 3.34 and 3.35 present two-way statistical plots for different

magnitude and distance bin pairs using the entire MIDR inventory. The scatters in Figure 3.34 and Figure 3.35 certify the previous observations that are made from the statistics of each building model. The increase in magnitude decreases the distance-dependent decay rate in MIDR that can be observed in Figure 3.34. This figure also shows the insensitivity of MIDR for large magnitude and short distance records. The scatters in Figure 3.35 that show the magnitude-dependent MIDR variation for different distance bins emphasize this observation from another perspective. These plots suggest that MIDR changes gradually for $M_w > 6.0$ for distances up to 40 km. For smaller magnitude events and for larger distances (distances greater than 50 km), the observed changes in MIDR demands are very rapid. In general the magnitude scaling of MIDR can be represented by a 2nd order polynomial. The distance scaling of MIDR requires a magnitude-dependent slope. These conclusions will be used while establishing the functional form of the proposed MIDR predictive model.

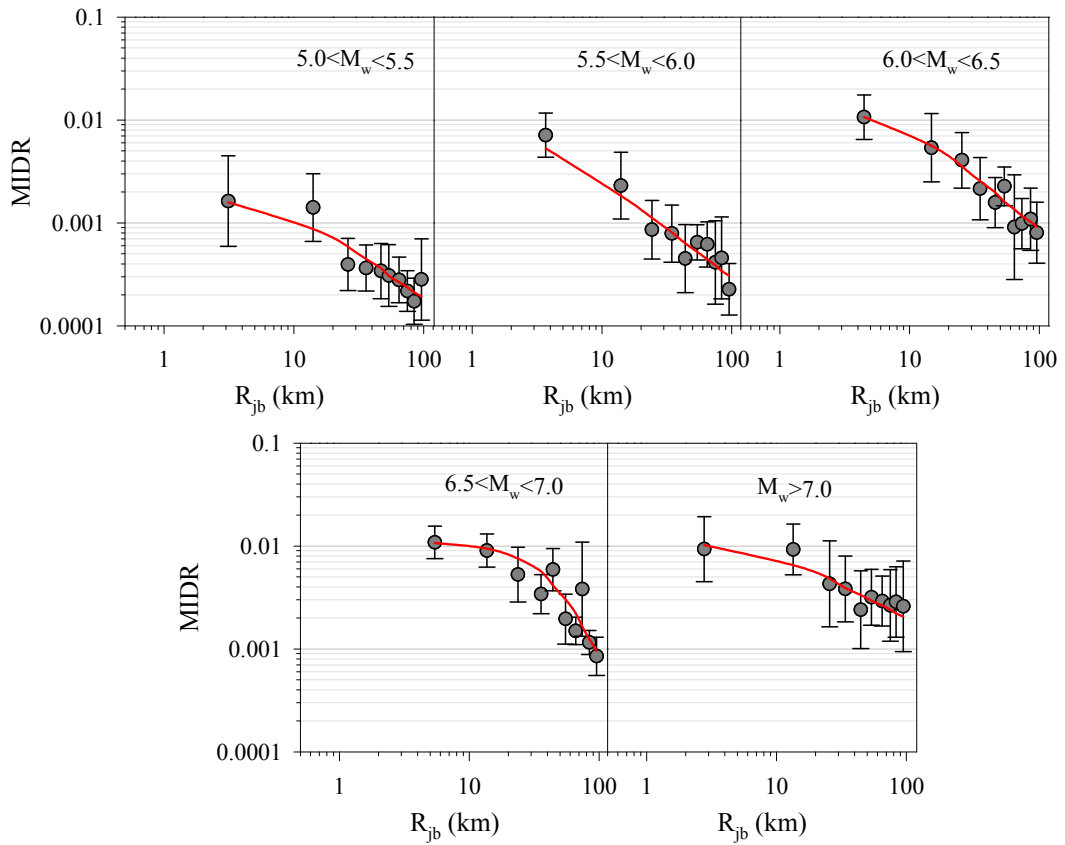


Figure 3.34 Variation of median MIDR together with ± 1 standard deviation error bars against distance for different magnitude bins. The solid lines are nonlinear fits to show the overall trend in MIDR variation

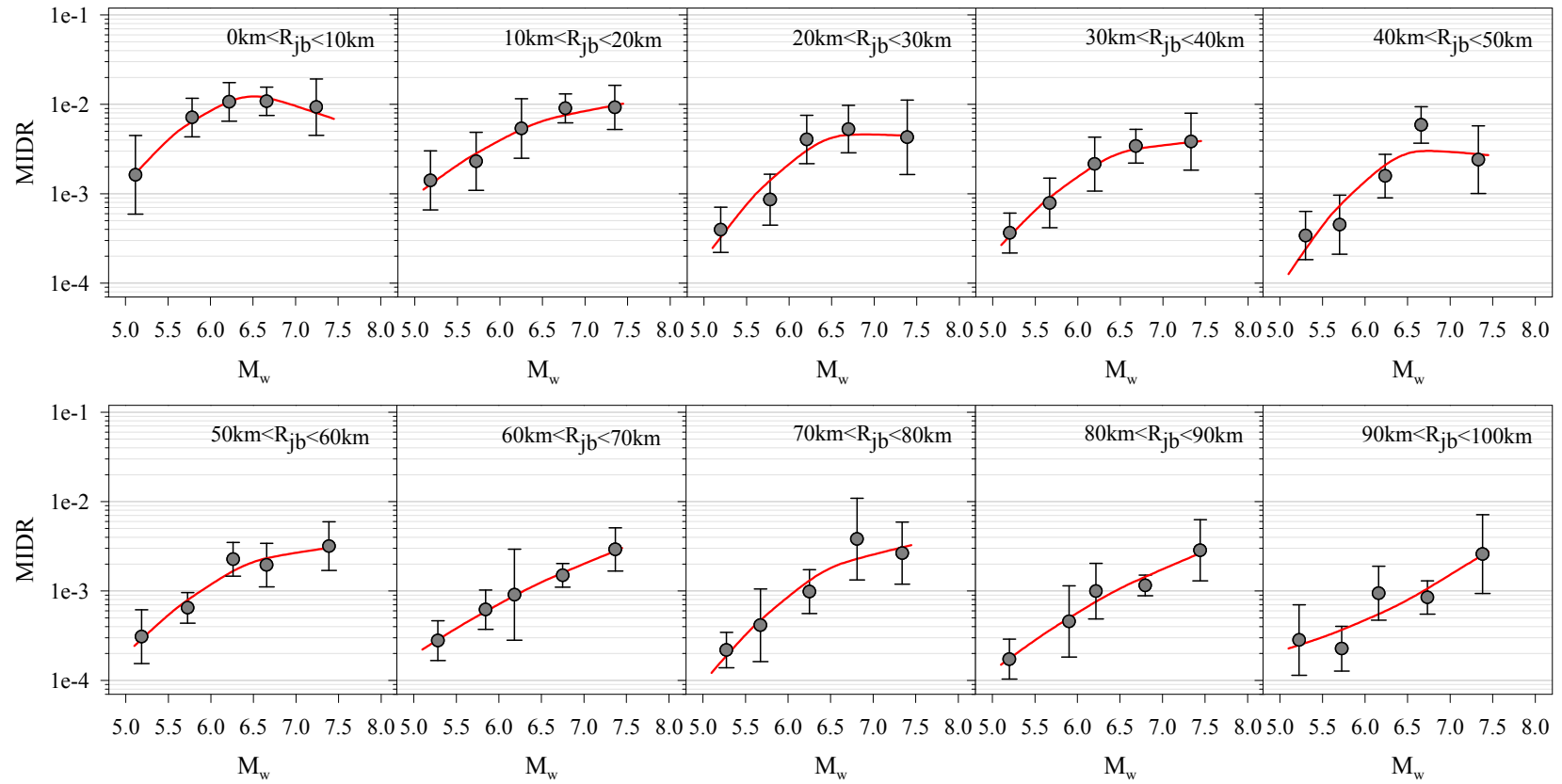


Figure 3.35 Variation of median MIDR together with ± 1 standard deviation error bars against magnitude for different distance bins. The solid lines are nonlinear fits to show the overall trend in MIDR variation

CHAPTER 4

INTERPRETATIONS AND OBSERVATIONS ON NONLINEAR SDOF RESPONSE

4.1 Introduction

Nonlinear response history analysis is accepted as the most accurate way of determining seismic performance of structures. To this end, the proposed predictive model for MIDR is based on the nonlinear RHA results of MDOF models as indicated in the previous chapter. This approach enabled this study to mimic the behavior of subject EDP as close as possible to reality. As the proposed predictive model aims at capturing the nonlinear structural behavior with a simple but robust structural feature; the idealized equivalent SDOF representations of model buildings are obtained. The structural parameter selected for this purpose is strength reduction factor, R_y that is defined as the elastic to yield lateral strength ratio of the idealized equivalent SDOF system of the building model. The idealized SDOF systems are subjected to nonlinear RHA to understand the behavior of chosen structural parameter against MIDR as well as magnitude and distance. These observations are used in the subsequent chapters while describing the predictive model as well as the probabilistic procedure used for computing the annual exceedance rate of MIDR under a certain earthquake scenario.

This chapter first describes the detailed analysis to obtain the most accurate representation of the equivalent SDOF systems of the model buildings. The most efficient idealization method is achieved from a set of alternative nonlinear static procedures (NSPs). Comparisons between MDOF and SDOF responses in linear and nonlinear response domains are used to define the most suitable idealization method for equivalent SDOF systems. The rest of the chapter discusses the correlation between R_y and MIDR demands and variation of R_y as a function of magnitude and distance. The observations from this chapter as well as those discussed in the previous chapter will shape the predictive model that is discussed in the subsequent parts of the thesis.

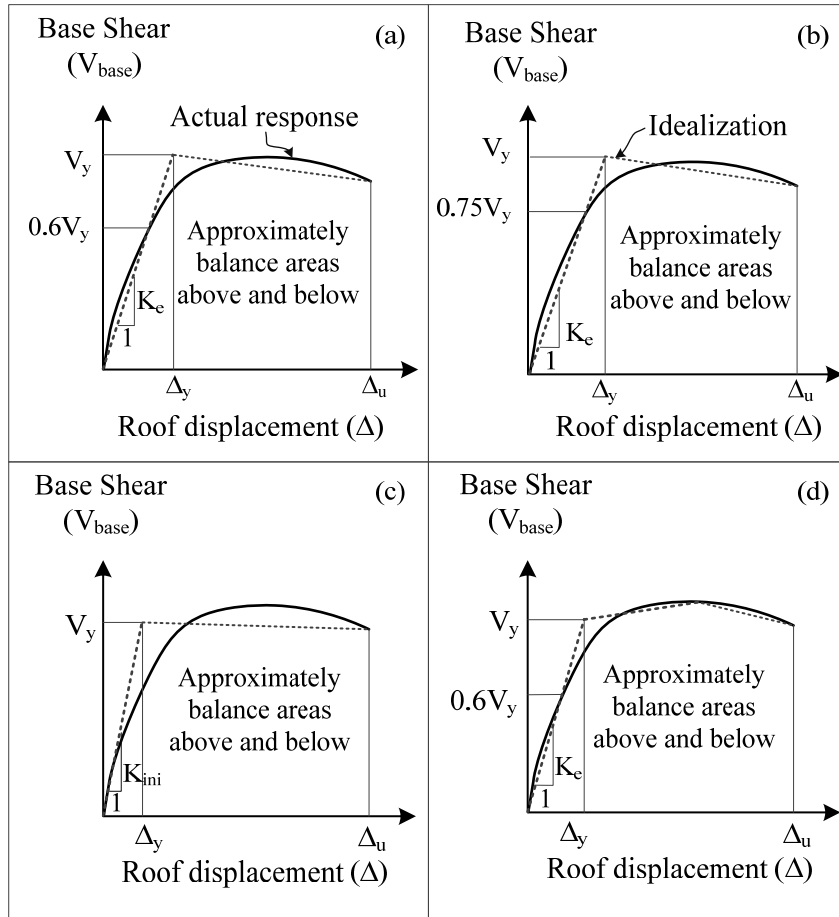
4.2 Identification of the Most Proper Nonlinear Static Procedure

4.2.1 Alternative Nonlinear Static Procedures (NSPs)

Pushover (PO) curves for each model building are obtained by applying a first mode compatible lateral loading pattern, computed through the normalization of first mode shape by story masses with incremental steps. The target roof-drift is set for 2.0% but the frame models can deform beyond this roof drift. The idealizations of PO curves obtained from pushover analysis are done using 3 code-based methods [FEMA-356, (FEMA, 2000); ATC-40, (ATC, 1996); ASCE/SEI 41-06, (ASCE, 2007)]. An alternative approach is also tested by modifying the 60% yield base shear ($0.6V_y$) rule of the FEMA-356 document (see details in the following paragraph). Except for the ASCE/SEI 41-06 procedure, the other 3 methods are based on bi-linear idealization of PO curves. The PO curves are idealized using a tri-linear model in ASCE/SEI 41-06 to simulate strength degradation effects.

According to FEMA-356, the bi-linearization is done in such a way that 60% of yield base shear force (V_y) intersects the pushover curve while keeping the areas under the idealized and original curves the same. This method is modified in an alternative approach by replacing the 60% V_y limit to 75% V_y (designated as “modified FEMA-356” herein after). The slope of the elastic part of bi-linear model is kept the same as the initial stiffness of the pushover curve in ATC-40. Similar to other two methods, equal area rule should be satisfied in ATC-40.

Analogous to FEMA-356, the ASCE/SEI 41-06 method requires the idealized model to intersect the pushover curve at 60% of V_y . A second line is defined with positive post-yield slope while keeping the areas under the idealized and original curves the same. A third line is then introduced to simulate the degrading part of the pushover curve that intersects the 2nd line. Figure 4.1 illustrates the conceptual differences of NSPs investigated in this study. The idealized models are presented together with the actual pushover curves in Figure 4.2. The properties of the idealized pushover curves for each frame model are listed in Table 4.1.



where K_{ini} : Initial lateral stiffness
 K_e : Effective lateral stiffness
 V_y : Yield base shear
 Δ_y : Yield roof displacement
 Δ_u : Ultimate roof displacement

Figure 4.1 Illustrative sketch of idealized PO curves for (a) FEMA-356 (FEMA, 2000), (b) modified FEMA-356, (c) ATC-40 (ATC, 1996) and (d) ASCE/SEI 41-06 (ASCE, 2007)

Table 4.1 Properties of idealized pushover curves

Frame ID	Idealization Method	Idealized Yield Base Shear Force V_y (kN)*	Idealized Yield Roof Displacement Δ_y (m)*	Idealized Yield Base Shear Coefficient (V_y /Total Weight)*	Idealized Yield Roof Drift Ratio (%)*
3S_MRF	FEMA-356	461.03	0.0418	0.187	0.49
	Modified FEMA-356	471.14	0.0472	0.191	0.55
	ATC-40	447.73	0.0349	0.181	0.41
	ASCE/SEI-41	414.21	0.0360	0.168	0.42
4S_MRF	FEMA-356	304.65	0.0703	0.200	0.62
	Modified FEMA-356	313.38	0.0791	0.206	0.69
	ATC-40	291.05	0.0566	0.191	0.50
	ASCE/SEI-41	278.65	0.0625	0.183	0.55
5S_MRF	FEMA-356	300.81	0.0883	0.152	0.64
	Modified FEMA-356	309.17	0.0968	0.156	0.70
	ATC-40	280.76	0.0673	0.142	0.49
	ASCE/SEI-41	270.73	0.0775	0.137	0.56
7S_MRF	FEMA-356	519.18	0.1063	0.175	0.52
	Modified FEMA-356	533.09	0.1179	0.180	0.58
	ATC-40	498.83	0.0898	0.168	0.44
	ASCE/SEI-41	441.55	0.0867	0.149	0.42
8S_MRF	FEMA-356	684.58	0.1122	0.141	0.50
	Modified FEMA-356	695.81	0.1221	0.143	0.54
	ATC-40	669.50	0.0986	0.138	0.44
	ASCE/SEI-41	640.30	0.1032	0.132	0.46
9S_MRF	FEMA-356	1143.02	0.1183	0.135	0.45
	Modified FEMA-356	1179.58	0.1296	0.140	0.49
	ATC-40	1125.00	0.1125	0.133	0.43
	ASCE/SEI-41	969.18	0.0980	0.115	0.37

*See Figure 4.1 for explanations of these parameters.

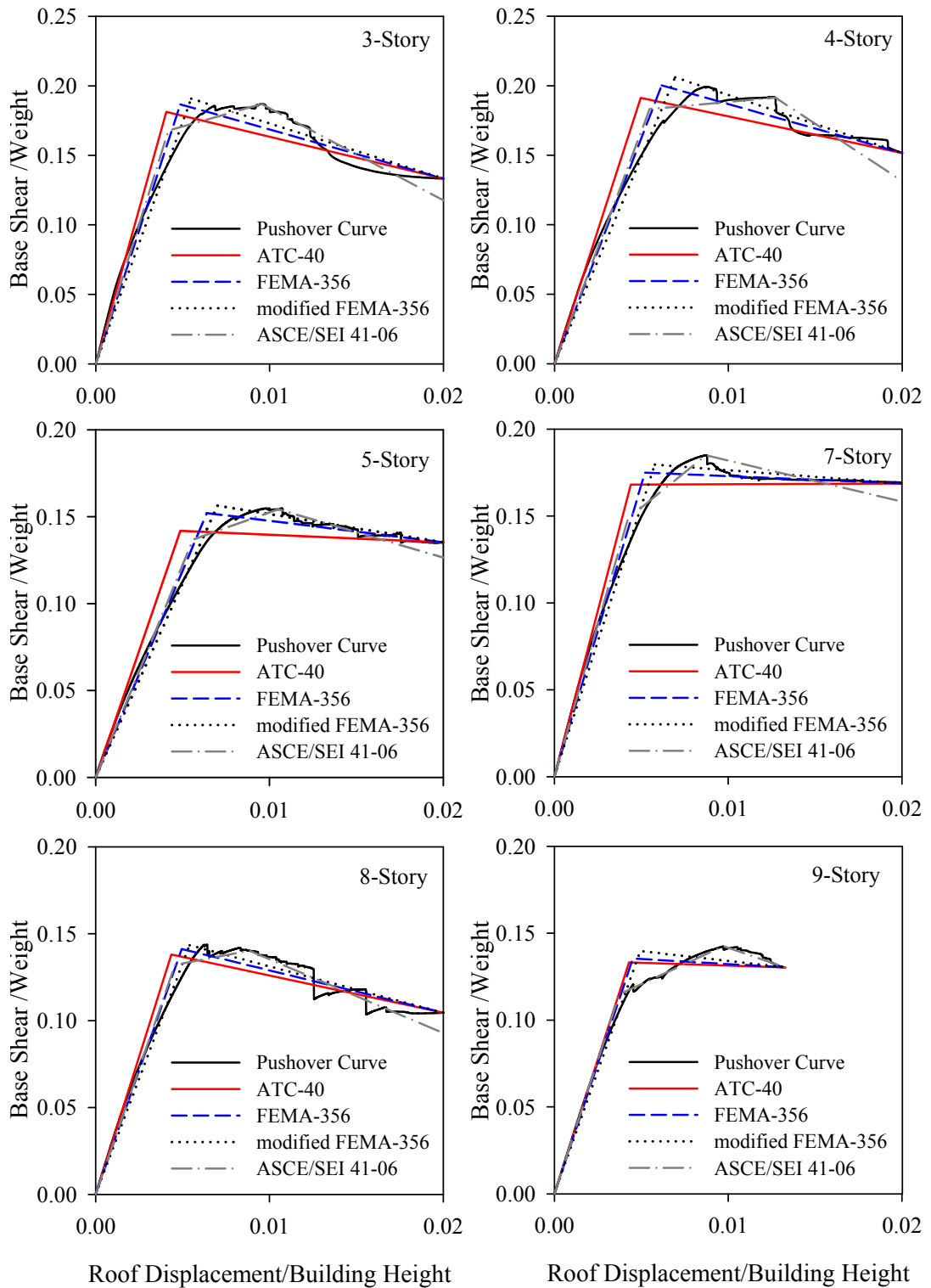


Figure 4.2 Pushover curves of model buildings together with their idealizations. The base shear values are normalized by the total building weight whereas roof displacement are normalized by building height.

4.2.2 Conversion of Idealized Pushover Curves to SDOF Format

The idealized pushover curves are converted to acceleration-displacement response spectrum (ADRS) format. This process is implemented by following the methodology developed by Freeman et al. (1975). The coordinates of capacity curves in ADRS formats are calculated using Eqs. (4.1) and (4.2).

$$PSA = \frac{V}{\alpha_1 M} \quad (4.1)$$

$$S_d = \frac{\Delta}{\Gamma_1 \phi_{1,r}} \quad (4.2)$$

where,

- PSA is pseudo spectral acceleration (m/s^2)
- V is base shear force (kN)
- M is total mass of the building (t)
- α_1 is first-mode effective modal mass factor
- Δ is roof displacement (m)
- Γ_1 is first-mode modal participation factor
- $\phi_{1,r}$ is first-mode modal amplitude at the roof

The above equations directly assume first-mode dominance in structural behavior. The force-displacement relation of equivalent SDOF response is illustrated in Figure 4.3. The effective stiffness and period of equivalent SDOF model can be calculated using Eqs. (4.3) and (4.4), respectively.

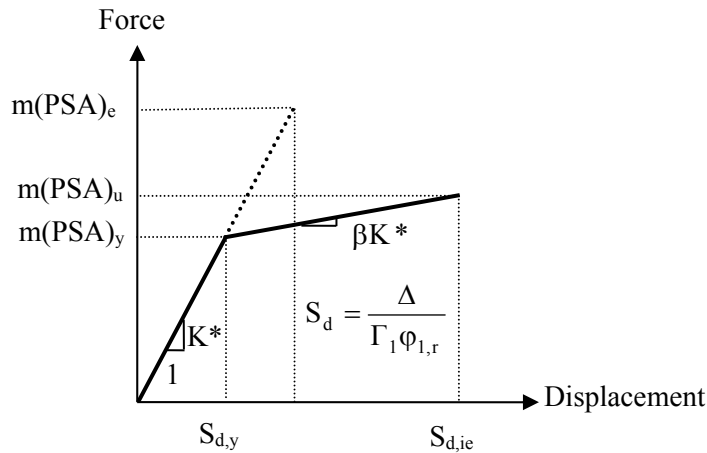


Figure 4.3 Force-displacement relation of equivalent SDOF models

$$K^* = \frac{m(PSA)_y}{S_{d,y}} \quad (4.3)$$

$$T_{\text{eff}} = 2\pi \sqrt{\frac{S_{d,y}}{(PSA)_y}} \quad (4.4)$$

where,

- K^* is effective stiffness of equivalent SDOF system
- $m(PSA)_y$ is yield base shear force of equivalent SDOF system
- $m(PSA)_e$ is elastic base shear force of equivalent SDOF system
- $m(PSA)_u$ is ultimate base shear force of equivalent SDOF system
- $S_{d,y}$ is yield displacement of equivalent SDOF system
- T_{eff} is effective period of equivalent SDOF model
- m is mass of equivalent SDOF system ($=\alpha_1 M$)

4.2.3 Comparisons of Nonlinear Static Procedures

Inelastic roof displacement demands calculated from nonlinear RHA of MDOF models are compared with inelastic spectral displacements ($S_{d,ie}$) obtained from nonlinear RHA of equivalent SDOF systems. The ratios of inelastic spectral displacements to roof displacement demands $(\Delta_{\text{roof}})_{\text{max}}$ computed for each alternative idealization are used to evaluate their performance. The ratios are computed using Eq. (4.5). The product $S_{d,ie}$ and $\Gamma\phi_{1,r}$ in the numerator theoretically represents the nonlinear roof displacement obtained from equivalent SDOF response. Inherently, this approach assumes first-mode dominant structural behavior. Since equivalent SDOF results modified for MDOF response are expected to approximate the actual inelastic roof displacements, the ratios closer to $C=1$ would give an overall idea about the accuracy of each idealization method. The results of alternative idealization methods are illustrated in Figure 4.4.

$$C = \frac{S_{d,ie} \Gamma_1 \phi_{1,r}}{(\Delta_{\text{roof}})_{\text{max}}} \quad (4.5)$$

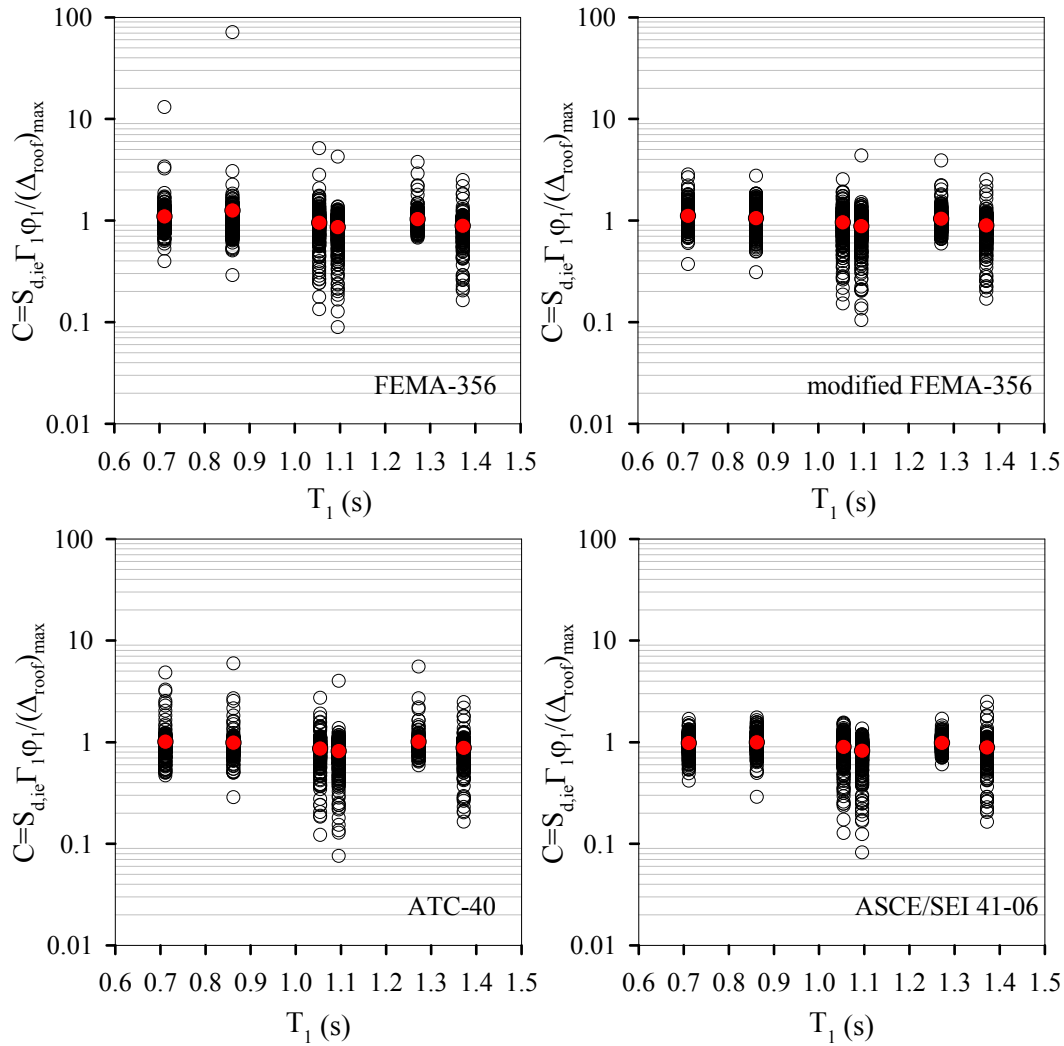


Figure 4.4 Roof displacement ratios calculated from nonlinear RHA of equivalent SDOF and MDOF models of 3-, 4-, 5-, 7-, 8- and 9- story frames. The red solid circles represent the mean value of each group.

Although the average of C values for all alternative idealization methods is close to unity in Figure 4.4, their dispersion about $C=1$ differs. The cumulative density functions (CDF) of C ratios shown in Figure 4.5 justify this argument. The vertical dashed lines on each panel are used to mark the probability of C ratios falling between 0.9 and 1.1. A higher probability would advocate lesser dispersion about $C=1$. The corresponding probability for each alternative idealization method is also given on the panels. The comparisons among these probability values indicate that bilinear idealization of ATC-40 method results in the highest probability. Thus, nonlinear SDOF analyses that are based on the ATC-40 bilinear idealization would mimic the actual roof displacements better than the other evaluated methods. Therefore bilinear PO curve idealizations that are based on ATC-40 method are considered to be the most appropriate ones for the purposes of this study.

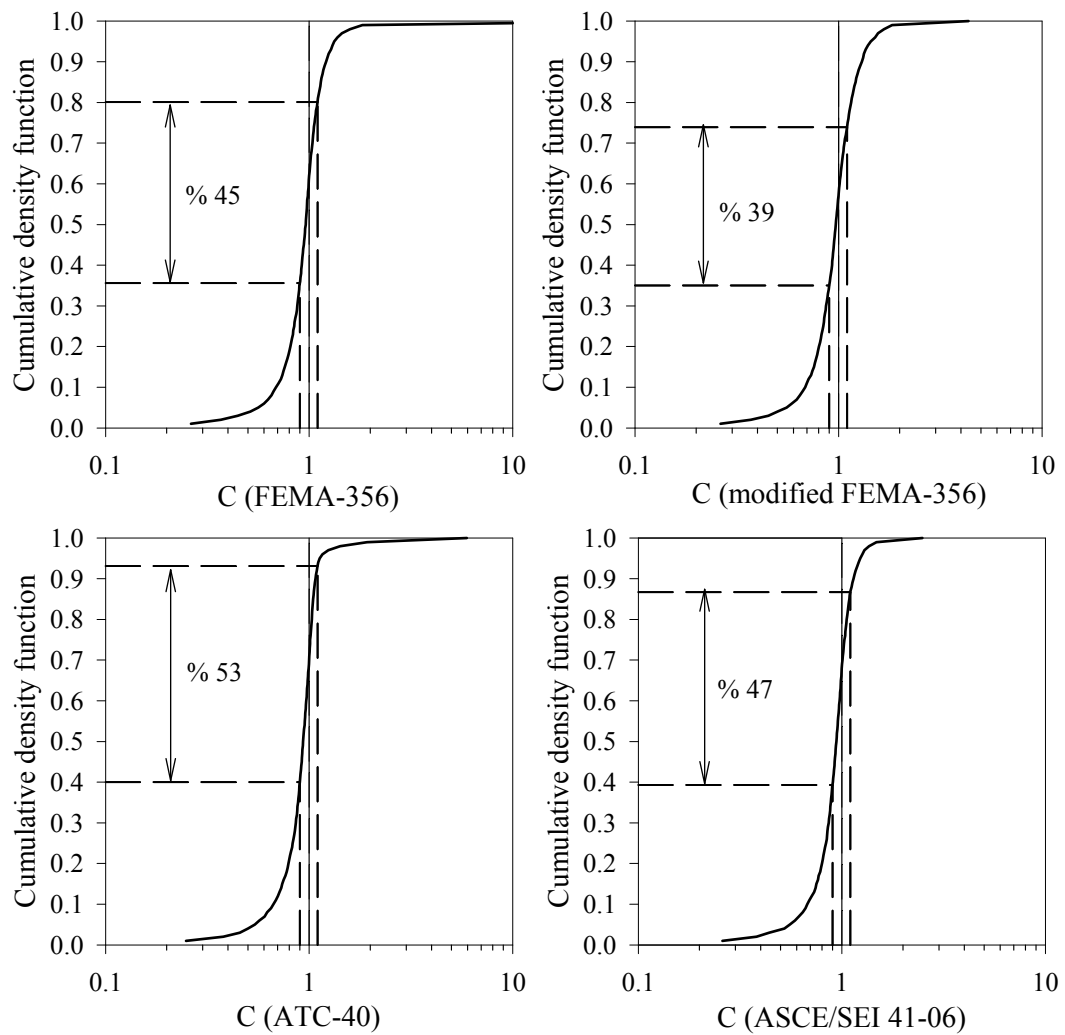


Figure 4.5 The cumulative probability densities of C values computed from each idealization method.

Idealized equivalent SDOF systems are used for running linear RHA. The elastic pseudo spectral accelerations (PSA_e) computed from these analyses are used together with the previously defined yields pseudo spectral accelerations (PSA_y) from bilinear idealizations to compute strength reduction factor, (R_y) for each case. Eq. (4.6) shows the definition of R_y used in this study.

$$R_y = \frac{PSA_e}{PSA_y} \quad (4.6)$$

4.3 Observations on R_y : Effects of Various Parameters on R_y

This section describes the probability distribution of R_y , its dependency on building period and height and its correlation with MIDR. The observations presented in this section will be used in the following chapter while describing the MIDR predictive model since R_y is selected as the definitive structural estimator parameter in the proposed predictive equation.

4.3.1 Log-normality of R_y

The log-normality assumption of R_y values gathered from nonlinear RHA of equivalent SDOF systems (representing 6 frame models) are tested at a significance level of 5% using Kolmogorov-Smirnov (KS) goodness-of-fit test (Ang and Tang, 1975). Figure 4.6 shows the scatter plots of observed data together with log-normal fits and upper and lower bounds according to this testing method. The provided statistics advocate the reliability of log-normality assumption for R_y distribution. However, as indicated in the section 3.4.1, this goodness-of-fit test produces unconservative results if the probability distribution (log-normal distribution in this case) parameters (i.e., mean and standard deviation) are obtained from the sample data set. In order to overcome this limitation, Lilliefors test (Lilliefors, 1967) is also applied to the computed R_y values in order to test the normality of the logarithmic R_y demands. The p-value statistics computed from Lilliefors test for each frame are below 1% significance level. These results indicate that the R_y distribution fail to satisfy log-normality at 5% significance level. The R_y distribution is further investigated using Q-Q plots. Figure 4.7 illustrates normal quantiles of logarithms of R_y values against theoretical normal distribution. As one can infer from the plots, the tails of the quantiles beyond $\pm 2 \sigma$ deviate from normal distribution. In other words, logarithms of R_y values follow normal distribution fairly well within $\pm 2 \sigma$ range. This behavior is considered within the tolerance limits of this study and R_y is accepted as a log-normal variate for the purposes of this study.

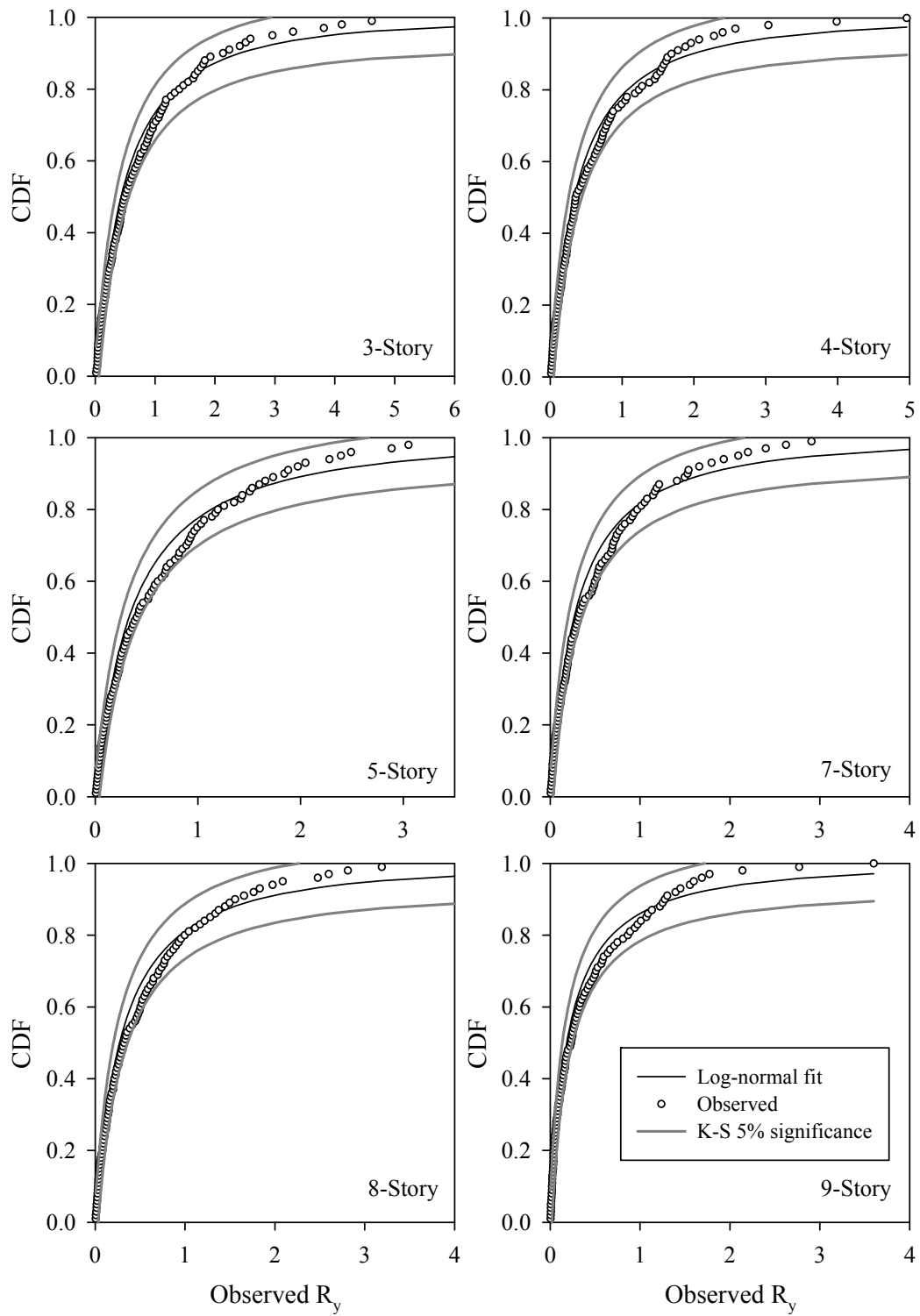


Figure 4.6 Kolmogorov-Smirnov goodness-of-fit results for the log-normality assumption of R_y -distribution

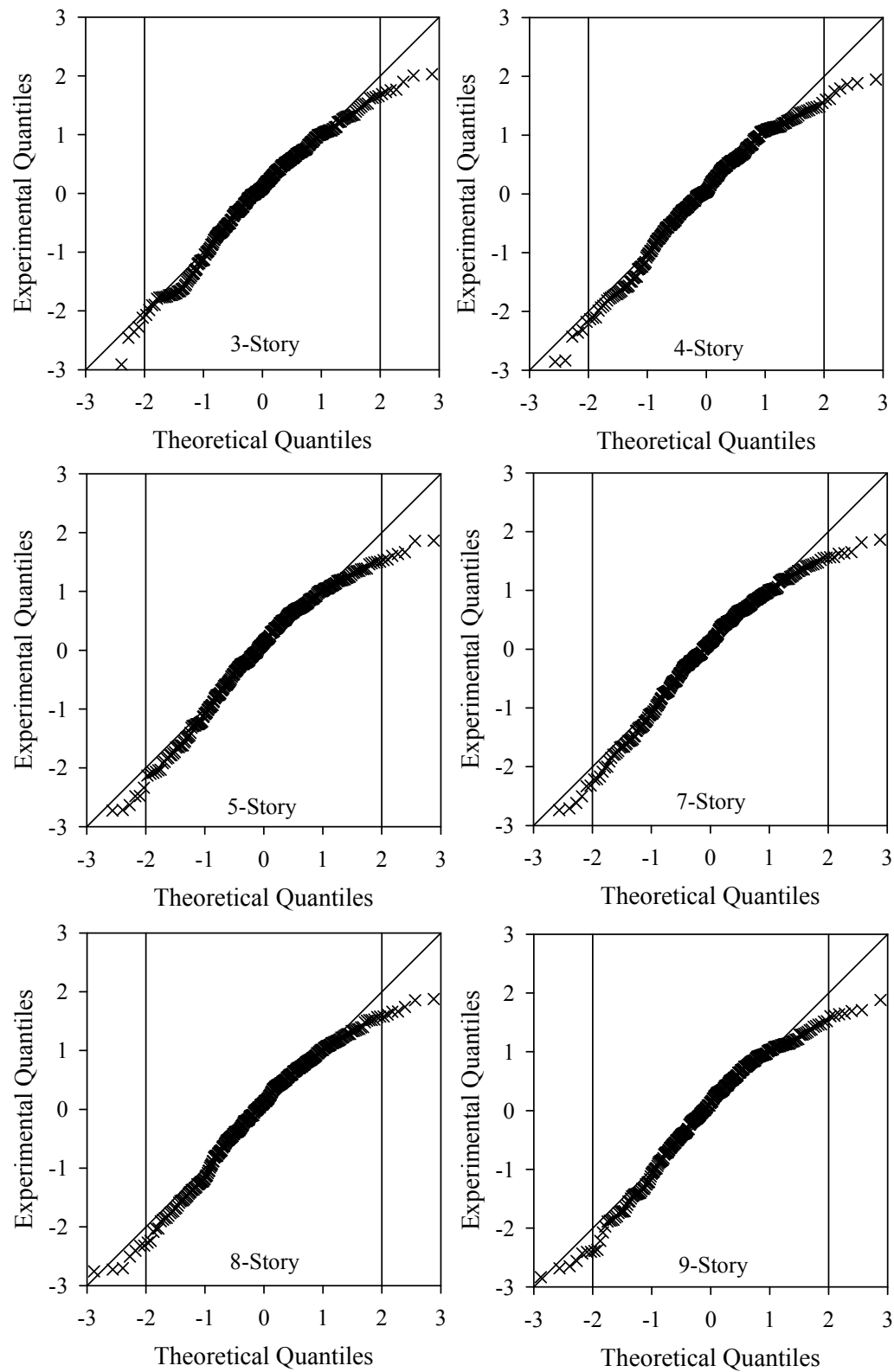


Figure 4.7 Q-Q plots of the logarithms of R_y values for the frame set used in this study

4.3.2 Dependence of R_y on Fundamental period and Story Number

Figure 4.8 shows the variation of R_y in terms of fundamental period, T_1 (left panel) and total building height, (right panel) under the entire nonlinear RHA of equivalent SDOF systems. The red squares indicate the median R_y values of each equivalent SDOF model. The plots indicate similar R_y -distributions regardless of the variations in fundamental period and total building height. These observations are similar to those of MIDR distributions as discussed in Section 3.4.6. In fact, ANOVA tests to quantitatively measure the period and building height dependency of R_y yield fail-to-reject results for the null hypothesis. These statistics are not given here for brevity.

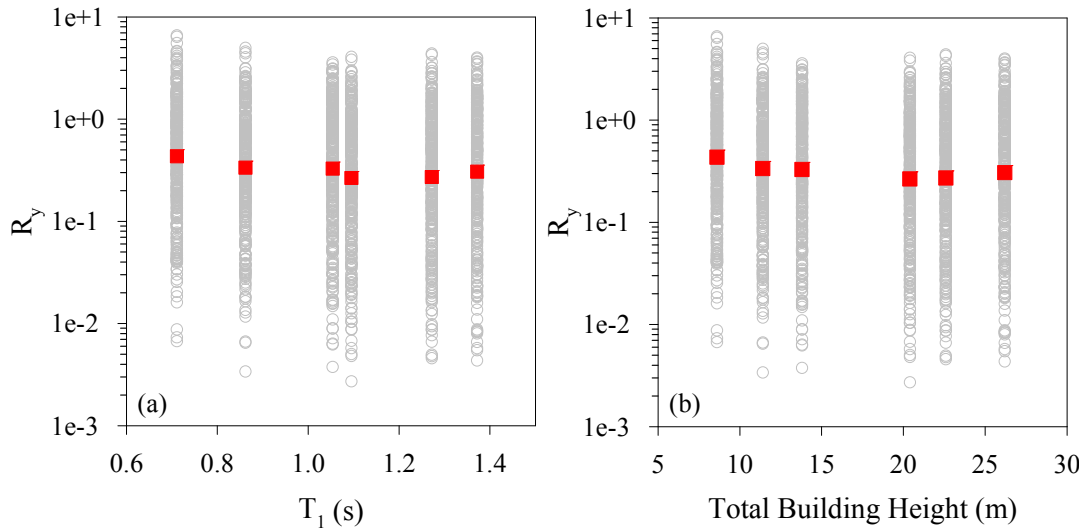


Figure 4.8 Dependence of R_y on (a) fundamental period and (b) total building height

4.3.3 Relationship between MIDR and R_y

Figure 4.9 shows the relationship between R_y and MIDR for the entire dataset. There is a fairly good correlation between R_y and MIDR for $R_y \geq 0.05$. This agreement diminishes towards very small R_y values (i.e., $R_y < 0.05$). It is believed that the dominance of gravitational loads over seismic loads is the reason behind the almost steady MIDR values against decreasing strength reduction factors for $R_y < 0.05$. In other words, the small-magnitude and far-source recordings that result in negligible seismic demands do not govern the lateral deformation shape of buildings. Instead, gravitational loads dominate the structural behavior for such recordings. This fact results in the observed pattern for R_y that is presented in Figure 4.9.

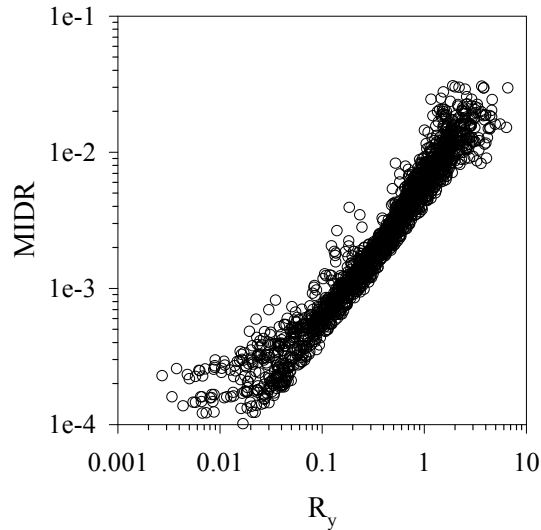


Figure 4.9 Dependence of MIDR on R_y using entire database

Figures 4.10 and 4.11 show the relationship between R_y and MIDR for different magnitude and distance bins, respectively. The red lines in each scatter plot describe the power relationship between R_y and MIDR in terms of predefined magnitude (Figure 4.10) and distance (Figure 4.11) intervals. The power relationship given in these figures explains the correlation between R_y and MIDR in a fairly good manner. These figures indicate that the MIDR versus R_y trends improve with increasing magnitude and decreasing distance. The presented power-law pattern between MIDR and R_y is used in the following chapter while estimating the variation of MIDR for different R_y values.

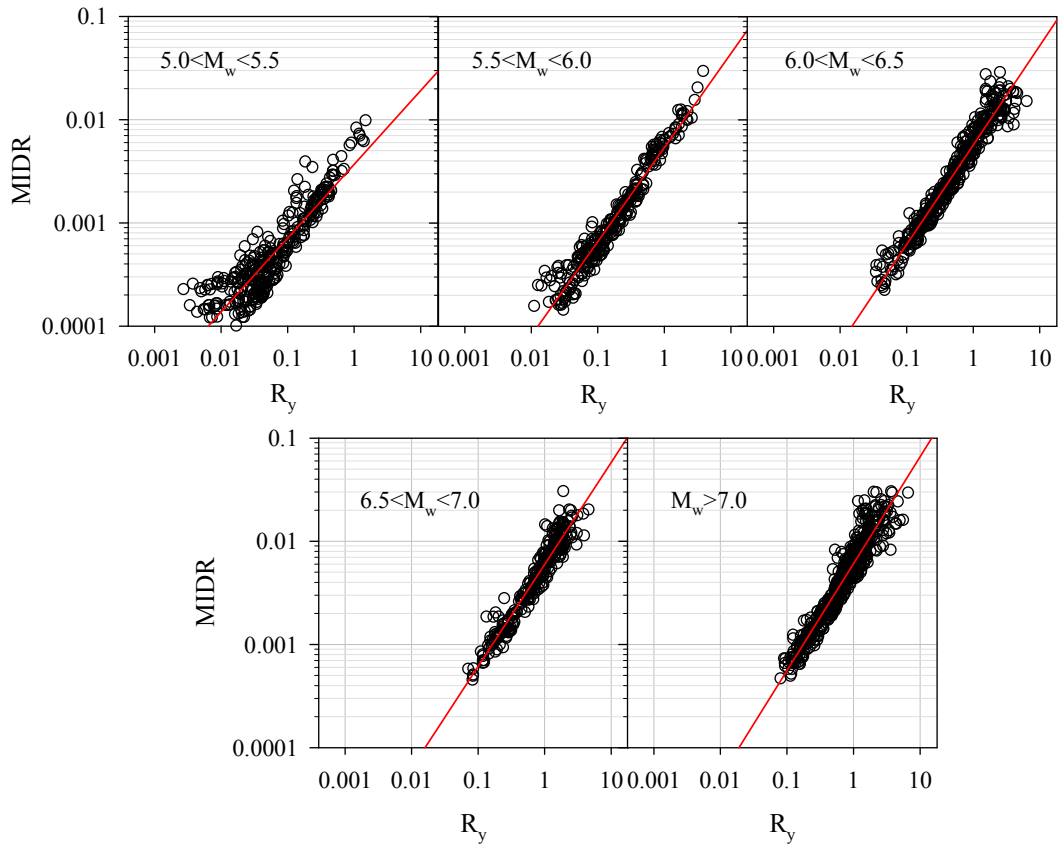


Figure 4.10 Variation of MIDR as a function of R_y for different magnitude bins

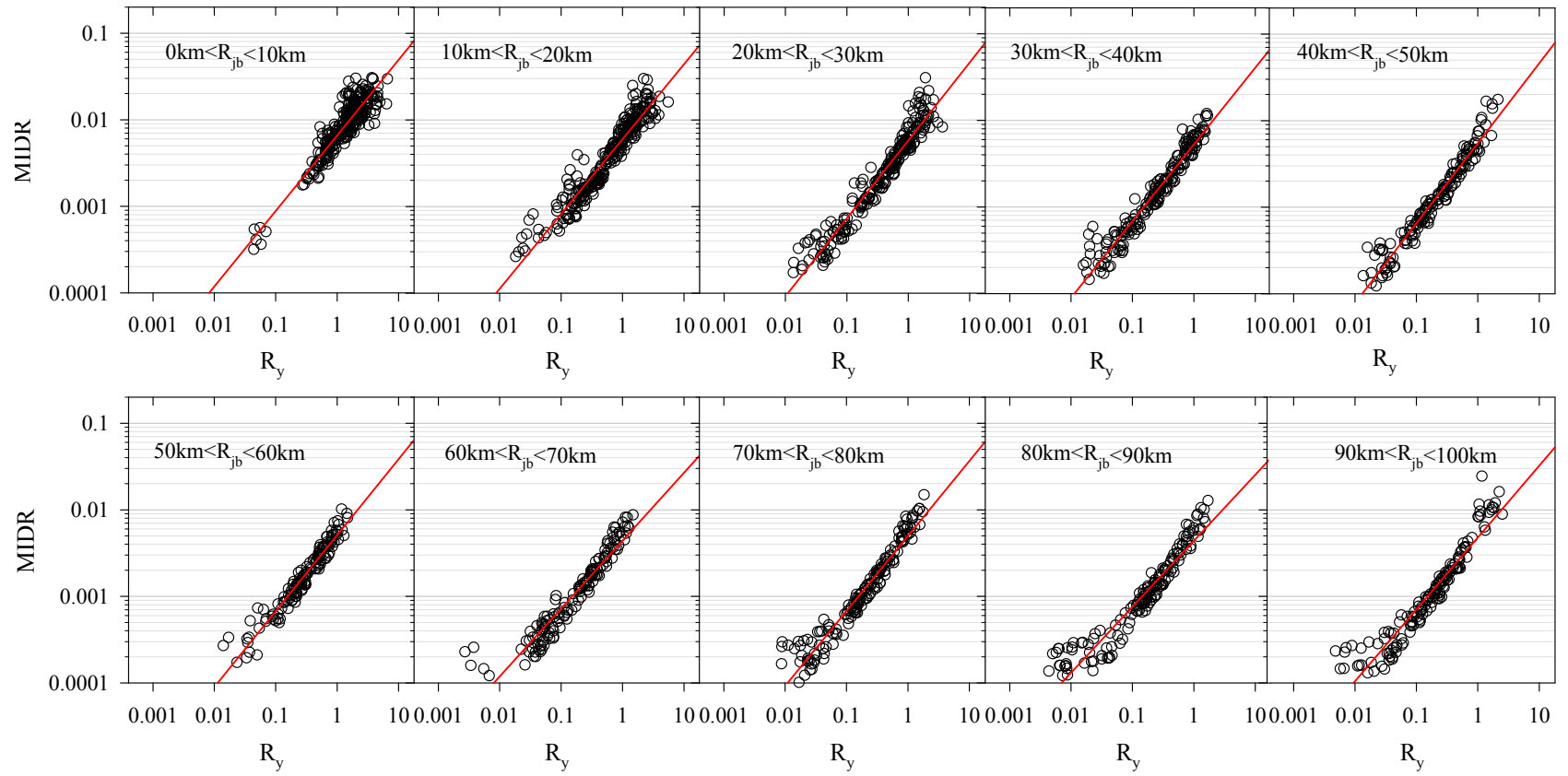


Figure 4.11 Variation of MIDR as a function of R_y for different distance bins

4.4 Further Discussions on Strength Reduction Factor

Significant number of linear and nonlinear RHA of equivalent SDOF systems as well as the strength reduction factors computed from idealized pushover curves of model buildings enable this study to evaluate the strength reduction factors provided in Turkish Earthquake Code (TEC, 2007). The building models are designed for the most seismic prone zone (Zone 1; Turkish Seismic Zonation Map) as discussed in Chapter 2. Following the seismic provisions in Turkish Earthquake Code (TEC, 2007), the structural behavior factor, $R=8$ is selected to achieve ductile moment resisting frame behavior. Note that this factor is called as response modification factor and designated as R in ASCE/SEI 7-10 (ASCE, 2010) and termed as behavior factor and designated as q in Eurocode 8 (CEN, 2004). Figure 4.12 shows the elastic spectral ordinates of the entire strong-motion dataset in ADRS format together with the unreduced target design spectrum (TEC, 2007) for residential buildings. The spectral curves given in this figure indicate the lesser demand of actual ground-motions for most cases with respect to the code-based design spectrum. This picture is expected as the ground-motion database spans recordings from a broad magnitude and distance range. The small magnitude and distant recordings as well as some of the large-magnitude and short-distance ground-motions would never reach the intensities dictated by the code (see discussions in Chapter 3 about the aleatory variability in ground motions). As shortly discussed in the last section of Chapter 2, even if a building is located in the most seismic prone zone, the seismic activity would be similar to that of presented in Figure 4.12 such that ground motions that would shake the building during its entire life span would barely reach to the corresponding intensities of code-based design spectrum. Therefore, the performance of buildings is not necessarily assessed under design level ground motions but, depending on the objectives of the project, they can also be verified under different scenario earthquakes. The proposed predictive model for MIDR is of use for such purposes as presented in Chapter 6.

Figure 4.13 shows the reduced code-based spectrum (for $R=8$) and the idealized capacities of model buildings that are computed from the ATC-40 (ATC, 1996) methodology. The immediate observation from this figure is the excessive capacity of the model buildings with respect to the reduced spectral values that are used in their design. Relatively low R_y values computed from nonlinear RHA of equivalent SDOF systems (see Figure 4.6) is due to the high capacities of building models that are presented in this figure. The overstrength that is based on the material properties and distribution of stresses and strains among structural members (redundancy) plays an important role on the observed excessive capacity of buildings models (SEAOC, Blue Book, 1999). The overstrength concept is introduced in Figure 4.14. The strength parameters V_E , V_S and V_M represent the elastic, reduced (target) and capacity strength due to overstrength, respectively. The relationship between V_E , V_S and V_M are given in Eq. (4.7).

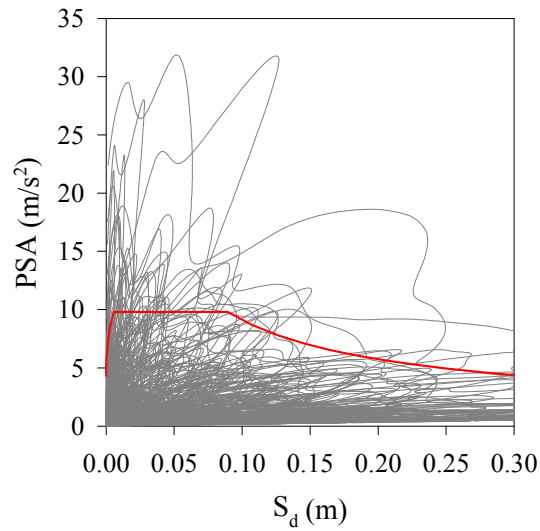


Figure 4.12 Unreduced design spectrum together with the elastic response spectra of the ground-motion dataset

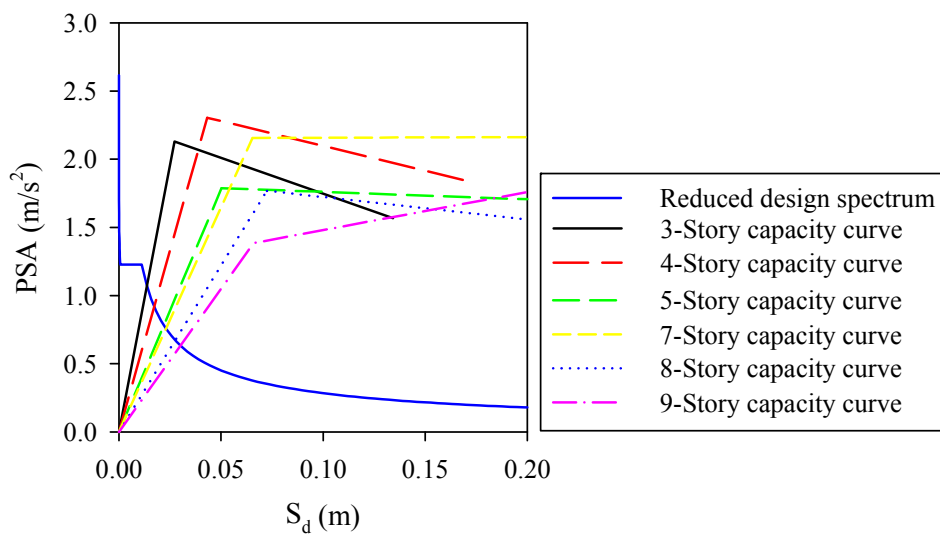


Figure 4.13 Reduced design spectrum for $R = 8$ together with the idealized capacities of the model buildings in ADRS format

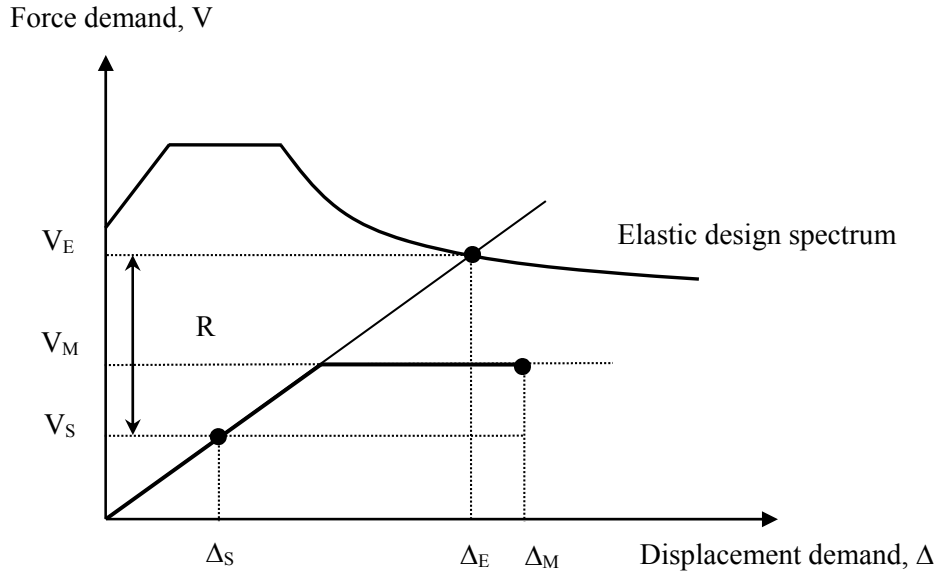


Figure 4.14 Comparison of elastic demand and general force versus displacement demands of structures

$$R = \frac{V_E}{V_S} = \frac{V_E}{V_M} \frac{V_M}{V_S} = R_y \Omega \quad (4.7)$$

In Eq. (4.7) V_E/V_M is called R_y from herein and it is the ratio of elastic spectral demand and yield capacity of equivalent SDOF system obtained from pushover analysis. The overstrength factor, Ω , is the ratio of yield strength capacity of equivalent SDOF system and reduced strength used in the design process. Based on the actual capacity of the frames and the design spectrum used in design process, the calculated R_y , and Ω are listed in Table 4.2. The overstrength factors vary between 2 and 2.9 that are generally in agreement with ASCE 7-10 (2010) provision where Ω value is provided as 3 for this building type (i.e. special moment resisting frame). These early results can be of particular use for the future revisions in Turkish Earthquake Code (TEC, 2007) for describing overstrength factors for ductile moment resisting frames. The limited observations of this study suggests an overstrength factor of $\Omega = 2.5$ for ductile moment resisting RC frames designed by the detailing requirements provided in the Turkish Earthquake Code (TEC, 2007). It is believed that $\Omega = 2.5$ is a reasonable compromise for the presented overstrength values in Table 4.2. If similar studies are conducted for other types of RC frame behavior, the overstrength reduction factor definitions in the future versions of Turkish Earthquake Code will be complete. Note that strength reduction factors computed from the linear and nonlinear RHA of equivalent SDOF systems in this study correspond to R_y that will be used in the derivation of MIDR predictive model.

Table 4.2 R_y and Ω values calculated using equivalent SDOF models

Frame ID	R_y	Ω
3S_MRF	4.02	1.99
4S_MRF	3.19	2.51
5S_MRF	3.50	2.29
7S_MRF	2.81	2.84
8S_MRF	3.04	2.63
9S_MRF	3.65	2.19

CHAPTER 5

A PREDICTIVE MODEL FOR ESTIMATING NONLINEAR MIDR DEMANDS ON MOMENT RESISTING FRAME SYSTEMS

5.1 Introduction

In the previous chapters the behavior of MIDR in terms of some seismological parameters as well as strength reduction factor, R_y , is studied in a detailed manner. MIDR, as an EDP, is an important indicator of structural performance (as well as structural capacity) under seismic demands (e.g. Algan, 1982; Sözen, 1983; Moehle, 1984, 1994; Qi and Moehle, 1991; Mayes, 1995; Heaton et al., 1995; Gülkan and Sözen, 1999; Bozorgnia and Bertero, 2001; Gülkan and Akkar, 2002; Ghobarah, 2004). This fact is considered in many modern seismic design codes and MIDR is used to define seismic performance level against different limit states. The Turkish Earthquake Code, (TEC, 2007) defines the MIDR demands for three limit states as an attempt to assess seismic performance of reinforced concrete building structures. The provisions of TEC (2007) first examine the building performance in terms of MIDR demands and then analyze the local seismic behavior at the member level. Buildings that are failed to meet the MIDR demands for a pre-determined target limit state (or target performance level) are considered as non-conforming buildings. Similarly, ASCE/SEI 41-06 (ASCE, 2007) limits the drift demands for three limit states. The major difference between TEC (2007) and ASCE/SEI 41-06 (ASCE, 2007) is that ASCE/SEI 41-06 defines different drift limits for concrete frames, concrete walls etc. at each limit state.

The above discussions emphasize the accurate computation of MIDR demands on buildings for consistent seismic performance assessment. The level of accuracy in MIDR is closely related to the implemented methodology for its calculation (i.e., from very simple procedures to complicated ones). The most accurate way of estimating MIDR demands is constructing the MDOF models of buildings and conducting nonlinear RHA. However, the complexity of time consuming nonlinear RHA often leads the analysts to prefer approximate solutions. This is particularly true if the seismic performance analysis

concerns a large group of buildings. To this end, practical methodologies with sufficient accuracy in MIDR demand calculations become important in many seismic engineering applications (e.g., seismic rehabilitation and retrofitting projects).

At the design stage of new structures, TEC (2007) provides a design spectrum with an exceedance probability of 10% in 50 years at the PGA level. The drift demands are checked at the end of the design process against the imposed drift limit as a consequence of force-based design (FBD). For RC buildings, TEC (2007) defines the interstory drift limit as 2% that can be considered as a performance state between operational and life safety performance levels. This approach implies a margin of safety in terms of MIDR at the life safety performance level. This drift limit can also be interpreted as a performance level corresponding to damage control limit state expected to be somewhere between immediate occupancy and life safety performance levels (Priestley, 2000). Thus, code-confirming buildings are expected to perform between these limit states under design earthquakes. However, seismic performance of buildings differs significantly due to inherent uncertainties in structural capacity and ground motions. Therefore, one can infer that expected performance and protection against seismic action is not fully achieved through the concepts dictated by FBD. Recent codes try to overcome the handicaps of FBD through modifications in design after displacement checks. Accordingly, if the design fails to satisfy the imposed displacement limits, it is modified and sometimes re-iteration is required to comply with the displacement criterion. Although this approach is still considered as force-based design in New Zealand and Europe, it is accepted as displacement-based design in the United States (Priestley, 2000). Nevertheless, a reliable structural design based on FBD is subjected to several iterations and modifications at the design level. As this approach (with all of its drawbacks) will be kept as the backbone of seismic design process, predicting the drift demands with reasonable accuracy can lead to prior information at the preliminary design stage of new buildings, which may increase the efficiency of iterations during design.

The first part of this chapter evaluates some empirical MIDR predictive models that are capable of representing the common code approach while estimating MIDR demands. The second part describes the proposed MIDR expression under the observations made from the functional behavior of the evaluated models as well as those of Chapters 3 and 4. The evaluation of the proposed model is given in the last part of this chapter together with its limitations.

5.2 Estimation of MIDR Demands Using Approximate Methods

Three MIDR predictive models by Miranda (1999), Akkar et al. (2005) and Medina and Krawinkler (2005) are utilized to compute approximate nonlinear MIDR demands. These methods modify spectral displacement (S_d) with different parameters to compute MIDR. Thus, the methods only differ in MIDR to S_d ratio. Estimation of MIDR demands via

spectral information is parallel with the general code-based approach. This fact constitutes one of the corner stones behind the derivation of the procedures evaluated in this chapter. Although few MIDR models are selected for verification, the proponents of these models are among the researchers who contributed significantly in MIDR demand estimations in the literature. The observations from the evaluations of these models will lead to useful information for the development of the proposed MIDR predictive model.

5.2.1 MIDR Predictive Model by Miranda (1999)

Miranda (1999) makes use of the continuum model presented by Heidebrecht and Stafford Smith (1973) to estimate the lateral deformation demands on frame systems. The general form of the approximate model by Miranda (1999) is given in Eq. (5.1).

$$\text{IDR}_{\max} = \beta_1 \beta_2 \beta_3 \beta_4 \frac{S_d}{H} \quad (5.1)$$

where,

$\beta_1, \beta_2, \beta_3, \beta_4$ are modification factors

S_d is elastic spectral displacement

H is total height of the building

The proposed equation adjusts the SDOF response (spectral displacement, S_d) to modify MDOF behavior through β_1 and β_2 parameters. The first parameter (β_1) represents the approximate modal participation factor whereas β_2 describes the ratio between elastic MIDR and elastic maximum roof drift ratio (MRDR). The third parameter (β_3), calculated from empirical expressions, modifies elastic demands for inelastic demands. In a similar fashion, the last parameter (β_4) considers the combined effects of inelasticity, number of stories and mechanisms in the post-elastic range. The detailed information on these parameters will be given in the following paragraphs.

The mathematical background of β_1 and β_2 is based on the continuum model presented by Heidebrecht and Stafford Smith (1973) that uses a fourth-order differential equation. The continuum model approximates the lateral displacement profiles of buildings that deform either under flexural- or shear-beam modes. Miranda (1999) expresses, the lateral displacement of the continuum model for a set of lateral loads distributed along the total height, H . Eqs. (5.2) give the lateral deformation profile of the continuum model when subjected to different shapes of laterally distributed loading.

$$u(z) = \frac{W_{\max} H^4}{EI(1 - e^{-a})} \left[C_1 \sinh \alpha \frac{z}{H} + C_2 \cosh \alpha \frac{z}{H} + C_3 e^{-az/H} + C_4 \left(\frac{z}{H} \right)^2 + C_5 \frac{z}{H} + C_6 \right] \quad (5.2.a)$$

$$\alpha = \sqrt{\frac{GA}{EI}} \quad (5.2.b)$$

$$C_1 = \frac{\alpha^2 e^{-a} - a^2 e^{-a} - a^3 + a\alpha^2 - \alpha^2}{a\alpha^3(a^2 - \alpha^2)}, \quad (5.2.c)$$

$$C_2 = \frac{a^2 e^{-a} - \alpha^2 e^{-a} + a^3 - a\alpha^2 + \alpha^2}{a\alpha^3(a^2 - \alpha^2)} \frac{\sinh\alpha}{\cosh\alpha} + \frac{\alpha^2 e^{-a} + a^2 - \alpha^2}{\alpha^4(a^2 - \alpha^2)} \frac{1}{\cosh\alpha}, \quad (5.2.d)$$

$$C_3 = \frac{-1}{a^2(a^2 - \alpha^2)}, \quad C_4 = \frac{-1}{2a^2}, \quad C_5 = \frac{a^2 e^{-a} - \alpha^2 e^{-a} + a^3 - a\alpha^2}{a\alpha^2(a^2 - \alpha^2)}, \quad (5.2.e)$$

$$C_6 = \frac{\alpha^2 e^{-a} - a^2 e^{-a} - a^3 + a\alpha^2 - \alpha^2}{a\alpha^3(a^2 - \alpha^2)} \frac{\sinh\alpha}{\cosh\alpha} + \frac{-1}{a^2(a^2 - \alpha^2)} - \frac{\alpha^2 e^{-a} + a^2 - \alpha^2}{\alpha^4(a^2 - \alpha^2)} \frac{1}{\cosh\alpha} \quad (5.2.f)$$

where,

W_{\max} is the intensity of the distributed load at the roof

H is total height of the continuum model

GA is total shear stiffness of the frame

EI is total flexural stiffness of the frame

α is a control parameter that accounts for the contributions of flexural and shear deformations in the simplified continuum model. $\alpha=0$ implies pure flexural beam and $\alpha=\infty$ corresponds to shear beam.

“ a ” is dimensionless control parameter to consider the shape of the lateral load. When this parameter takes values close to zero, the shape of lateral loading pattern becomes triangular. The lateral loading pattern is uniform when “ a ” goes to infinity.

The parameter α is calculated using the equation proposed by Eroğlu and Akkar (2011) while evaluating this approximate method. Eroğlu and Akkar (2011) define a story dependent α as this parameter varies along the building height. Thus, using the methodology proposed in Eroğlu and Akkar (2011), the story-dependent α variation is computed for each model building and an average α value is assigned to each model in order the Miranda (1999) methodology to render a better performance in lateral displacement profiles. The methodology proposed by Eroğlu and Akkar (2011) is presented in Appendix F. The parameter a is taken as 0.01 that corresponds to triangular lateral loading in order to approximate the first mode shapes of model frames. The modal participation factor, β_1 , is computed from Eqs. (5.3) and (5.4) for each model building. Given a building model, the mode shape of the continuum model at the height corresponding to the j^{th} floor level (i.e., ψ_j) is computed by normalizing its lateral deformation ($u(z_j)$) with the top displacement ($u(H)$) as given in Eq. (5.4). The parameter, β_1 , for each model building is then computed by using Eq. (5.3) from the discrete model displacements resulting from Eq. (5.4). “ N ” represents the total number of stories of each building model in Eq. (5.3).

$$\beta_1 = \frac{\sum_{j=1}^N \psi_j}{\sum_{j=1}^N \psi_j^2} \quad (5.3)$$

$$\Psi_j = \frac{u(z_j)}{u(H)} \quad (5.4)$$

In a similar fashion, Eq. (5.5) is used to compute β_2 that is specific to each model building. As described in detail in the previous paragraph, the lateral deformation profile, $u(z)$, of the continuum model corresponding to each building is computed and its derivative with respect to height ($du(z)/dz$) is multiplied with the total height-to-top displacement ratio of the continuum model (i.e., $H/u(H)$). The maximum of this product as given in Eq. (5.5) is the elastic MIDR to MRDR ratio. Table 5.1 lists the α , β_1 and β_2 parameters computed for each model building used in this study. The computed α values indicate that model buildings deform under flexural and shear actions but flexural behavior is more dominant for all buildings. The elastic MIDR values are approximately 50% larger than the elastic roof displacement ratios according to the listed β_2 values in Table 5.1.

$$\beta_2 = \max \left[\frac{du(z)}{dz} \frac{H}{u(H)} \right] \quad (5.5)$$

Table 5.1 The list of α , β_1 and β_2 parameters for each model building

Frame Name	α	β_1	β_2
3S_MRF	0.88	1.29	1.45
4S_MRF	0.74	1.33	1.46
5S_MRF	0.57	1.36	1.45
7S_MRF	0.68	1.40	1.51
8S_MRF	0.65	1.41	1.51
9S_MRF	0.74	1.42	1.52

The other parameters β_3 and β_4 are calculated empirically using Eqs. (5.6) and (5.7), respectively.

$$\beta_3 = \left[1 + \left(\frac{1}{\mu_{\text{SDOF}}} - 1 \right) \exp(-12T\mu_{\text{SDOF}}^{-0.8}) \right]^{-1} \quad (5.6)$$

$$\beta_4 = 1 + \frac{\mu_{\text{story}}}{30} + \frac{N}{200} \quad (5.7)$$

where,

μ_{SDOF} is displacement ductility ratio of the equivalent SDOF system

μ_{story} is maximum story displacement ductility ratio

N is number of stories

T_1 is fundamental period of the building in seconds

Note that Eqs. (5.6) and (5.7) require prior information about μ_{SDOF} and μ_{story} that can be obtained after running nonlinear static analysis as well as nonlinear SDOF and MDOF response history analyses. The accurate estimation of μ_{SDOF} can only be achieved after several intermediate steps: (a) computation of global pushover curve (roof displacement versus base shear) (b) conversion of global pushover curve to ADRS format (c) bilinear idealization of ADRS curve and (d) computation of SDOF nonlinear response history analysis under a specific ground motion (or a set of ground-motions that match the target performance level). The computation of μ_{story} is more cumbersome as it requires story-based pushover curves and MDOF nonlinear RHA. These points suggest the difficulties in the implementation of the Miranda (1999) model. As the required information already exists in the nonlinear RHA inventory, the MIDR estimates of this procedure are included in the comparative analysis of alternative MIDR predictive models.

The computation of μ_{SDOF} for each model is done as described in the above paragraph because the equivalent SDOF systems of model buildings as well as the corresponding results of nonlinear SDOF RHA are available. In a similar manner μ_{story} is computed from the story-based pushover curves and nonlinear MDOF RHA. The story-based PO curves are used to define the yield story displacement. The maximum story displacement computed from nonlinear RHA is normalized by the yield story displacement to obtain μ_{story} along the total building height.

Figure 5.1 shows the general variations of β_3 (left panel) and β_4 (right panel) parameters in terms of fundamental period (T_1) and number of stories (N). The plots show that the ductility-dependent trends in β_3 and β_4 do not change significantly for the period and story number ranges of interest in this study (i.e., $0.71\text{s} \leq T_1 \leq 1.38\text{s}$ and $3 \leq N \leq 9$). This observation once again justifies the remarks made in section 3.4.6: the sensitivity of MIDR to fundamental period and story number can be overlooked for low-to-mid rise buildings.

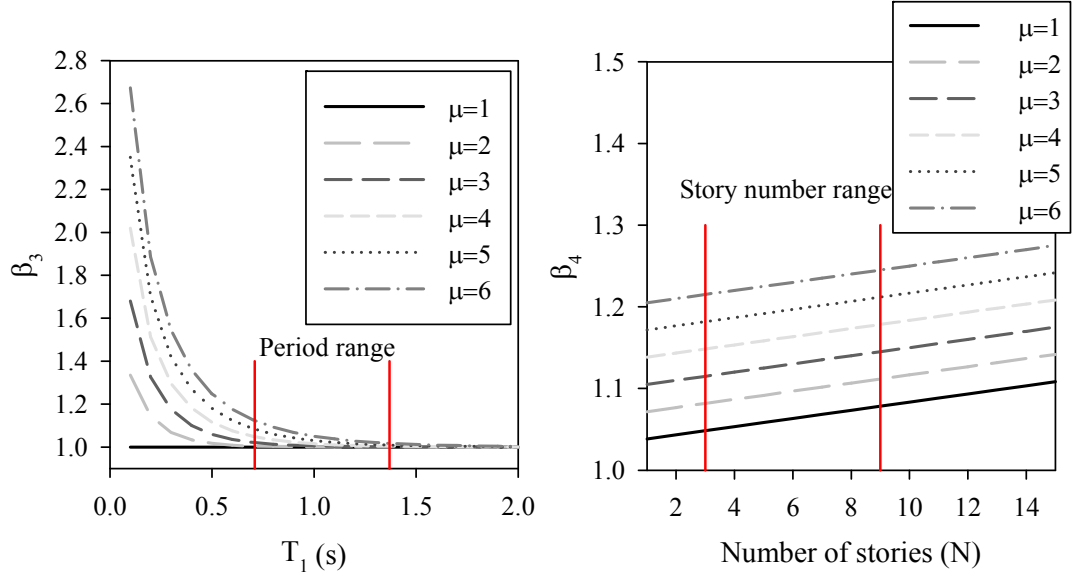


Figure 5.1 Overall variations of β_3 and β_4

The MIDR estimation ($MIDR_{\text{predicted}}$) computed from Miranda (1999) are evaluated by using the MIDR values ($MIDR_{\text{observed}}$) of nonlinear RHA (discussed in Chapter 3). An error term is introduced for this purpose as given in Eq. (5.8). Error terms greater than unity indicate overprediction of MIDR values by Miranda (1999). The mean error and standard deviation of the error are calculated using Eqs. (5.9) and (5.10), respectively. The total number of data used in the comparisons is designated by n in these expressions.

$$E = \frac{MIDR_{\text{predicted}}}{MIDR_{\text{observed}}} \quad (5.8)$$

$$\bar{E} = \frac{1}{n} \sum_{k=1}^n E_k \quad (5.9)$$

$$\sigma_E = \sqrt{\frac{1}{n-1} \sum_{k=1}^n (E_k - \bar{E})^2} \quad (5.10)$$

Figure 5.2 illustrates the error scatters of Miranda (1999) in terms of strength reduction factor, R_y . The R_y values are computed for each model as described in Section 4.2.3. Note that these R_y values are actual strength reduction factors and do not incorporate overstrength factor. The particular reason behind the use of R_y is to observe the performance of Miranda (1999) for structures behaving in the linear and nonlinear range.

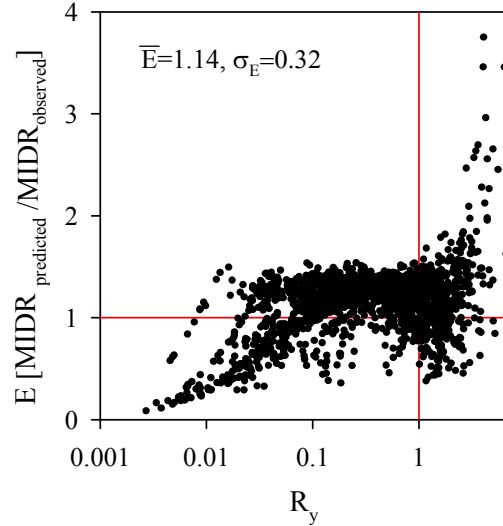


Figure 5.2 Error scatters of inelastic MIDR predictions against R_y for the Miranda (1999) procedure

One can infer from Figure 5.2 that predictions diverge significantly as R_y attains very small and large values. Miranda (1999) tends to overestimate MIDR values with increasing R_y (in particular when the models respond in the post-elastic range; $R_y > 1$). This trend reverses and the method significantly underestimates the MIDR values for very small R_y values. The poor performance of Miranda (1999), even for structures responding in the elastic range can be attributed to the use of complicated modification factors that are derived from continuum model idealization. The limited accuracy of β_3 and β_4 factors that depend on μ_{SDOF} or μ_{story} can also play a role on the observed performance of this method.

The MIDR estimations of Miranda (1999) are also investigated using the residual analysis. The residuals of the estimated MIDR demands are calculated using Eq. (5.11) and they are plotted in terms of moment magnitude (M_w) and source-to-site distance (R_{jb}).

$$\text{Residual} = \log(\text{MIDR}_{\text{observed}} / \text{MIDR}_{\text{predicted}}) \quad (5.11)$$

The residual plots for Miranda (1999) are given in Figure 5.3. The scatter plots also show the average residuals computed for different magnitude and distance bins. The magnitude bins are established with a magnitude interval of 0.5 units. This interval is selected as 20 km for distance bins. The average residual trends indicate a strong dependency of magnitude for the MIDR predictions by Miranda (1999). The distance dependency of MIDR estimations is not as strong as magnitude but it is still apparent for some particular distance intervals.

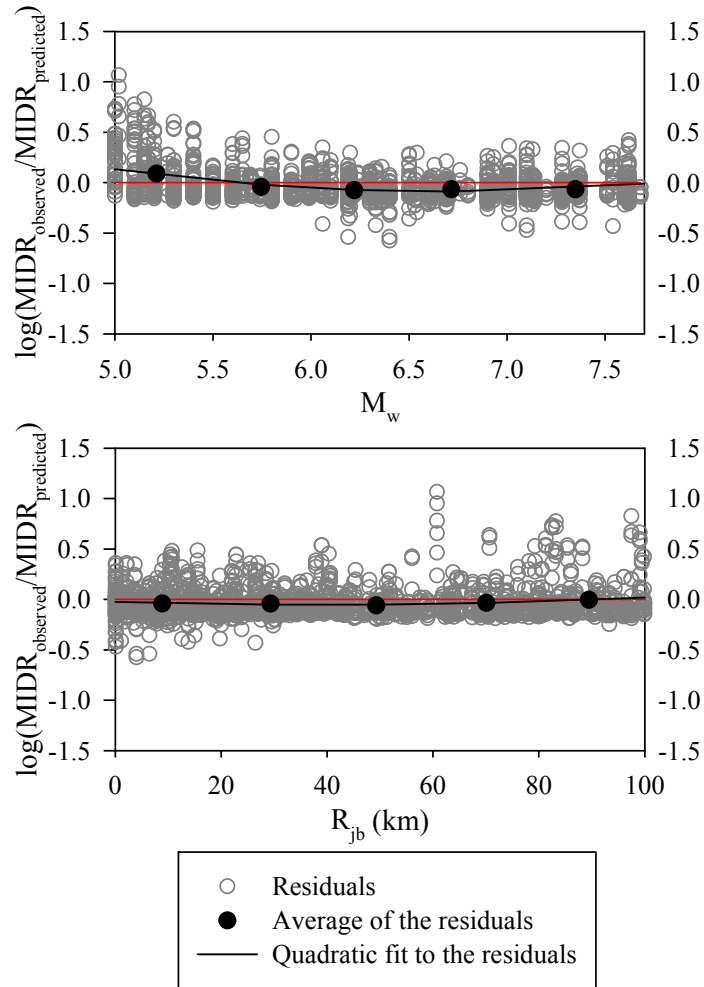


Figure 5.3 Residual scatters of the MIDR predictions from Miranda (1999) in terms of M_w and R_{jb}

The unbiased estimations of a predictive model in terms of important seismological parameters requires a random distribution of residuals about zero for each one of these variables. The discussions in Chapter 3 emphasize the significance of magnitude and distance on MIDR variation. As depicted from Figure 5.3, the Miranda (1999) predictive model results are biased in terms of magnitude and distance as the trend lines fitted on residuals deviate from zero line, which can be considered as the violation of their randomness. The biased MIDR estimations of Miranda (1999) can be considered as an important drawback for the performance of this method. The dependency of Miranda (1999) on magnitude and distance also violates the sufficiency principle of Luco and Cornell (2007). These authors define a predictive model as sufficient when its estimations are independent of magnitude and distance. The Miranda (1999) procedure does not include a measure of uncertainty to account for the likely variations in MIDR estimations due to record-to-record variability (aleatory variability). This measure of uncertainty is

generally referred to as standard deviation in the predictive models and the lack of such parameter in Miranda (1999) reduces its efficiency for MIDR estimations.

5.2.2 MIDR Predictive Model by Akkar et al. (2005)

Akkar et al. (2005) model computes elastic MIDR by modifying the ground story drift ratio expression for shear frames ($GSDR_{sh}$) presented by Gülkan and Akkar (2002). The approximate model of Akkar et al. (2005) is presented by a set of expressions in Eq. (5.12).

$$\begin{aligned} MIDR(T, \zeta, \rho) &= \gamma_1(\rho, T) \gamma_2(\rho, T) GSDR_{sh}(T, \zeta) \\ \gamma_1(\rho, T) &= c_1(\rho) + \frac{c_2(\rho)}{T}, \quad \gamma_2(\rho, T) = e^{(c_3(\rho) - c_4(\rho)/T)} \\ GSDR_{sh} &= 1.27 \sin\left(\frac{\pi h}{2H}\right) \frac{S_d(T, \zeta)}{h}, \quad c_1(\rho) = \frac{1}{1 + 0.35 / \rho^{0.65}}, \\ c_2(\rho) &= \frac{1}{8 + 25\rho^{0.4}}, \quad c_3(\rho) = \frac{1}{2\rho + 1}, \quad c_4(\rho) = \frac{0.07}{\rho^{0.25}} \end{aligned} \quad (5.12)$$

where,

- T_1 is fundamental period of the building in seconds
- h is story height in meters
- H is total building height in meters
- ζ is damping ratio
- ρ is beam-to-column stiffness ratio (Blume, 1968)

In their study, Gülkan and Akkar (2002) express $GSDR_{sh}$ as a function of elastic spectral displacement (S_d). Thus, S_d constitutes the basis of MIDR estimations. In order to convert $GSDR_{sh}$ to MIDR, two modification factors are utilized by Akkar et al. (2005) that account for general frame behavior and the relation between maximum interstory drift ratio (MIDR) and ground story drift ratio (GSDR). As the method is limited to elastic building behavior, Metin (2006) suggested to use inelastic spectral displacement ($S_{d,ie}$) to account for post-elastic building response. Metin (2006) also stated that implementation of $S_{d,ie}$ instead of S_d results in better performance of the Akkar et al. (2005) method for buildings responding beyond their elastic capacities. Needless to say the accuracy of $S_{d,ie}$ (i.e., whether it is estimated from an approximate method or computed from nonlinear SDOF RHA) plays a positive role in the performance of this method. Bearing on the comments of Metin (2006), the Akkar et al. (2005) expression is used with $S_{d,ie}$ values computed from the equivalent SDOF nonlinear RHA results. The procedure for computing equivalent SDOF systems of building models and nonlinear SDOF RHA to compute $S_{d,ie}$ are discussed extensively in Chapter 4 and in the previous section.

The γ_1 and γ_2 parameters of Akkar et al. (2005) are calculated as a function of beam-to-column stiffness ratio, ρ , and fundamental period, T_1 . Akkar et al. (2005) evaluate their MIDR equation for a frame set with fundamental periods and beam-to-column stiffness

ratios, varying between 0.2-2.0 s and 0.125-∞, respectively. In order to give a better insight into this procedure, the combined effect of γ_1 and γ_2 parameters is investigated. Figure 5.4 illustrates the variation of $\gamma_1*\gamma_2$ as a function of ρ for the fundamental periods of each model frame. The product of these terms will be designated as γ_3 hereafter for the sake of simplicity.

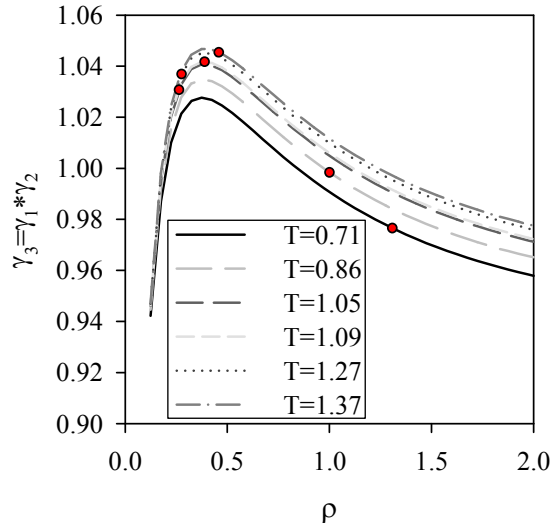


Figure 5.4 Variation of γ_3 in terms of ρ together with real estimations for each frame

Figure 5.4 indicates a rapid increase of γ_3 for ρ values up to 0.3. The increasing trend is followed by a rapid decay after this corner ρ value. As fundamental period (T_1) increases, γ_3 term tends to increase but this behavior is more apparent towards larger ρ values and for fundamental periods $T_1 \leq 1.05$ s. The γ_3 values computed for each model frame are also shown by solid circles on this figure and they vary between 0.98-1.045. Although γ_3 values seem to change with fundamental period, the difference between the maximum and minimum γ_3 (9-story and 3-story frames, respectively) is approximately 7%. Moreover, within the ρ values of model buildings the maximum amplification in γ_3 due to variations in fundamental period (T_1) is only 2%. This observation advocates that for the model frames of interest, γ_3 is not very sensitive to the fundamental period and MIDR estimations mainly differ due to the changes in $S_{d,ie}$ results.

A similar evaluation procedure is applied as in the case of Miranda (1999) while assessing the performance of Akkar et al. (2005) procedure. The error scatter plot in terms of strength reduction factor, R_y is shown in Figure 5.5. The mean error and standard deviation of error for the Akkar et al. (2005) model are also given on the figure. The performance of the model, both in terms of error trends as well \bar{E} and σ_E is comparable to Miranda (1999).

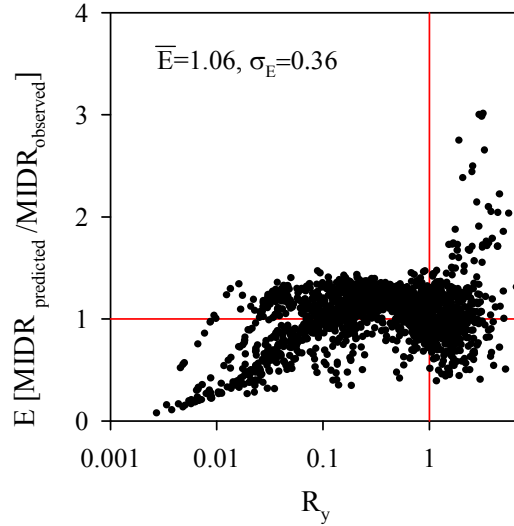


Figure 5.5 Error scatters of inelastic MIDR predictions according to Akkar et al. (2005) procedure

The residual plots of the MIDR estimations for Akkar et al. (2005) in terms of magnitude and distance are given in Figure 5.6. The format of residuals in Figure 5.6 is the same as of Figure 5.3. The observed trends in Figure 5.5 are also very similar to those shown in Figure 5.3. The distance-dependent residual trends by Akkar et al. (2005) are slightly better than the ones observed from the Miranda (1999) method. The presented residual trends of Akkar et al. (2005) also suggests that this procedure would estimate biased MIDR in terms of magnitude and distance, which casts doubts about the sufficiency of the model.

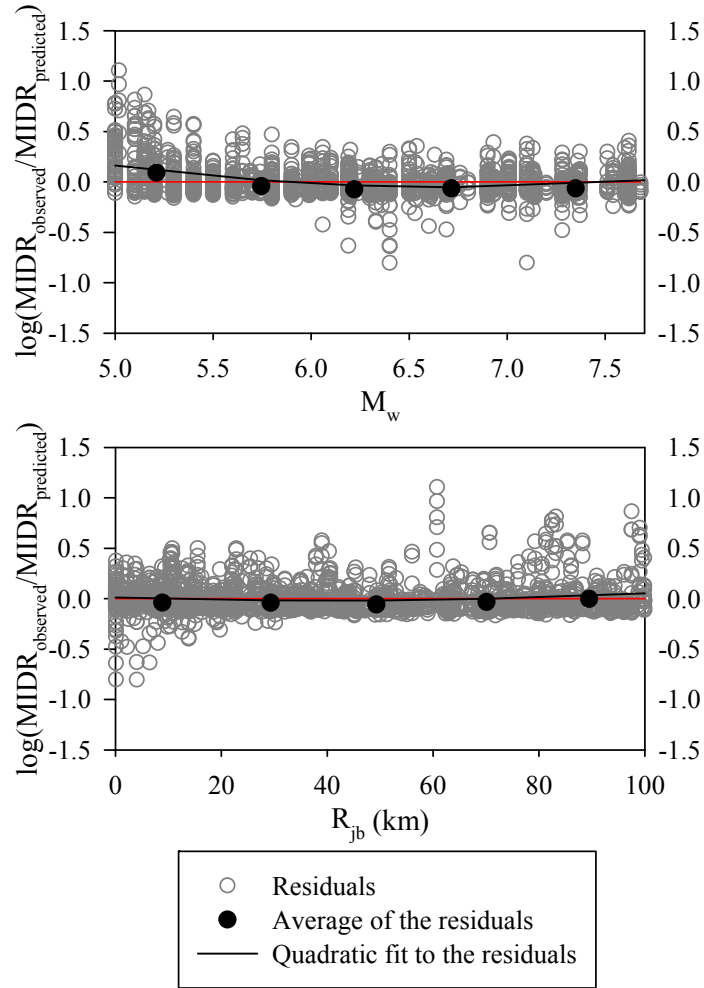


Figure 5.6 Residual scatters of the MIDR estimations by Akkar et al. (2005) in terms of M_w (upper panel) and R_{jb} (lower panel)

5.2.3 MIDR Predictive Model by Medina and Krawinkler (2005)

Similar to the previous models, this procedure is based on the modification of S_d by two parameters that account for conversions from SDOF to MDOF response and MRDR to MIDR demands. The MIDR expression by Medina and Krawinkler (2005) is given in Eq. (5.13).

$$\theta_{s,max} = (0.46 + 0.9T_1) \frac{\Gamma_1 S_d(T_1)}{H} \quad (5.13)$$

where,

$\theta_{s,max}$ is median maximum interstory drift ratio

T_1 is fundamental period (s)

Γ_1 is first mode participation factor

S_d is elastic spectral displacement (m)
 H is total building height (m)

This empirical equation produces median maximum interstory drift ratios for flexible structural systems with fundamental periods of $0.2N$ where N is the number of stories. The fundamental periods of low-rise frames (3-, 4-, and 5-story frames) utilized in this study are close to $0.2N$ (and even slightly higher) and they are between $0.1N$ and $0.2N$ for mid-rise frames (7-, 8-, and 9-story frames). The model buildings are assumed to comply with the flexibility condition of Medina and Krawinkler (2005). The median MIDR estimates for the model frames recomputed by inserting Γ_1 and S_d values into Eq. (5.13) that are already available from the modal analyses and equivalent SDOF RHA described in the previous chapters.

Figure 5.7 illustrates error scatters of the Medina and Krawinkler (2005) model against strength reduction factor, R_y . As in the case of previous model evaluations, the mean error and standard deviation of error are also indicated on the figure.

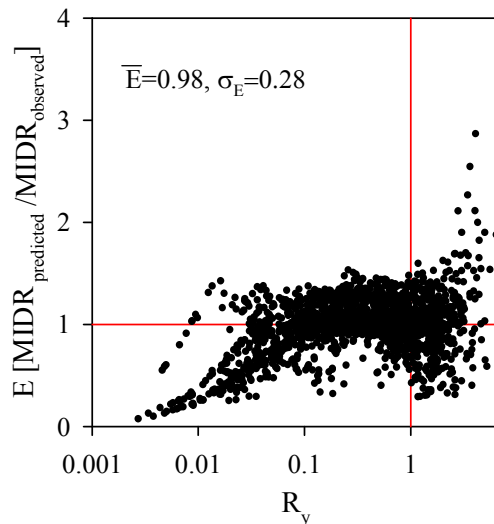


Figure 5.7 Error scatters of MIDR estimates for Medina and Krawinkler (2005)

In brief, the error trends as well as the error statistics (\bar{E} and σ) are very similar to the observations made for the other two MIDR equations. The residual plots given in Figure 5.8 to understand the level of bias in the MIDR estimations of Medina and Krawinkler (2005) also depict a similar picture as of the other two empirical models. Observations from the residual plots of Medina and Krawinkler (2005) once again confirm that this model would yield biased MIDR estimations for magnitude and distance.

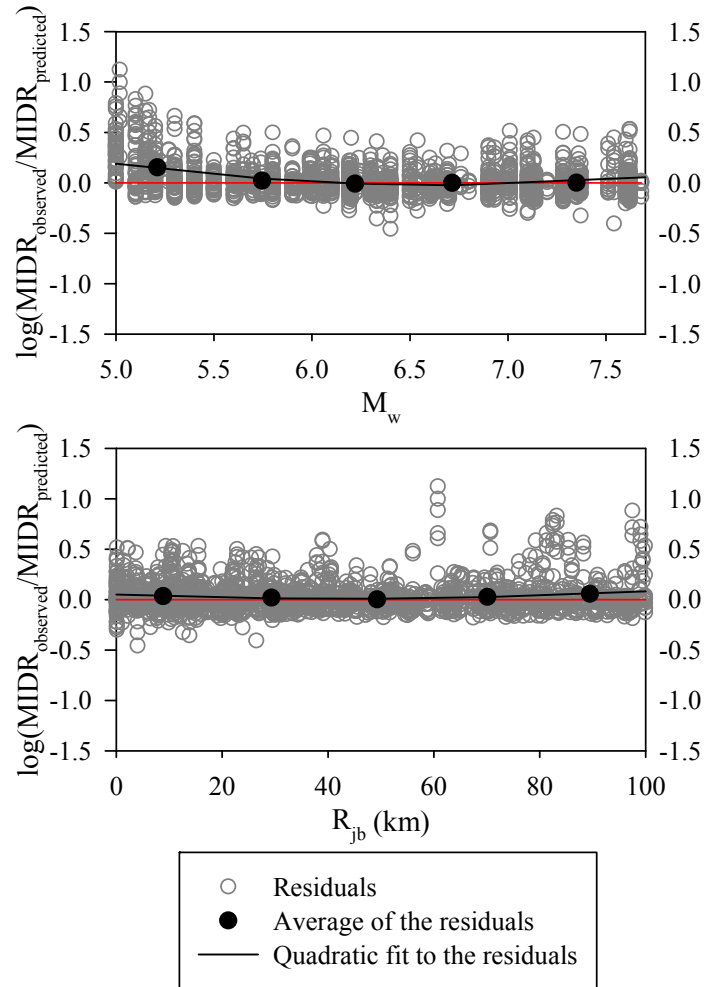


Figure 5.8 Residual scatters of the MIDR estimations of Medina and Krawinkler (2005) in terms of M_w (upper panel) and R_{jb} (lower panel)

5.3 A Summary of Important Observations on MIDR from Alternative MIDR Predictive Models

Observations made from the evaluation of three approximate methods are summarized in the following lines before presenting the proposed MIDR expression in this dissertation.

1. For code complying moment resisting RC frames, the MIDR demands are not sensitive to the variations of fundamental period for the building models considered in this dissertation. This fact is already justified by the nonlinear RHA results in Chapter 3 as well as by the approximate expressions of Akkar et al. (2005) and Miranda (1999) in this chapter.

2. MIDR is well correlated with R_y (strength reduction factor) both in the elastic ($R_y \leq 1$) and inelastic ($R_y > 1$) region. The good correlation between MIDR and R_y suggests that strength reduction factor is a proper structural estimator of MIDR demands. However, the verified MIDR models cannot properly address the significance of the relation between strength reduction factor and MIDR as presented via error plots.
3. The equation by Akkar et al. (2005) reveals that beam-to-column stiffness index, ρ , is also effective on MIDR demands. Miranda (1999) uses a similar parameter, α , to account for the general frame response to estimate the MIDR demands.
4. The influence of magnitude and source-to-site distance cannot be overlooked in MIDR variation. The approximate MIDR models evaluated in this chapter fail to estimate unbiased MIDR demands in terms of magnitude and distance. A proper MIDR predictive model should account for the variations in magnitude and distance in a reliable manner. The record-to-record variability (aleatory variability) in MIDR estimations is also disregarded by the approximate MIDR methods evaluated in this chapter. The aleatory variability should be mapped on MIDR estimations and one way of considering record-to-record variability is introducing the standard deviation (σ) term as part of the MIDR predictive model. Such a term does not exist in the methods evaluated here.
5. The evaluated approximate models aim at estimating MIDR primarily from SDOF response (spectral information) that is modified by some specific factors to represent MDOF behavior. The evaluations showed that the use of many auxiliary expressions to estimate MIDR reduces the performance of the model. A better alternative can be the direct estimation of MIDR by using the most important structural and seismological estimators that have direct impact on the MIDR variation. Moreover regressions that are directly done on MIDR values obtained from nonlinear RHA would increase the performance (reliability) of the approximate empirical model.

5.4 The Predictive Model for MIDR

Based on the observations summarized in the previous section of MIDR and the correlation of MIDR with structural and ground-motion parameters, the predictive model for this EDP is developed as a function of magnitude (M_w), source-to-site distance (R_{jb}), site conditions, strength reduction factor (R_y). The proposed predictive model for MIDR is selected among several functional forms considering the success and stability of the model in predicting nonlinear MIDR demands. The functional form of MIDR is given in Eq. (5.14). The predictive model produces median MIDR (logarithmic mean) estimations and considers

the aleatory variability (record-to-record variability) with the standard deviation (sigma) term, $\sigma_{\log_{10}(\text{MIDR})}$.

$$\log_{10}(\text{MIDR}) = b_1 + b_2 M_w + (b_3 + b_4 M_w) \log_{10}(D) + b_6 \log_{10}(F) + b_8 S_1 + b_9 S_2 + \sigma_{\log_{10}(\text{MIDR})} \quad (5.14)$$

$$D = \sqrt{R_{jb}^2 + b_5^2}$$

$$F = \sqrt{R_y^2 + b_7^2}$$

where,

b_1 to b_9 are regression constants

M_w is moment magnitude

R_{jb} is Joyner and Boore distance

R_y is strength reduction factor (see section 4.4)

$S_1=1$ for soft soil (NEHRP D) and 0 otherwise

$S_2=1$ for stiff soil (NEHRP C) and 0 otherwise

The functional form given by Eq. (5.14) contains a linear magnitude scaling term ($b_1+b_2M_w$). The distance scaling term is also linear with a magnitude-dependent slope $[(b_3+b_4M_w)\log_{10}D]$ to account for the influence of magnitude on the MIDR variation with increasing or decreasing distance. The expressions used to define magnitude and distance scaling are developed by considering the magnitude and distance-dependent variation of MIDR as discussed in Chapter 3. The influence of structural parameter, R_y , is described in by $b_6\log_{10}(F)$ term that is also identified from the relationships between MIDR versus R_y . The relationship between MIDR versus R_y is given in Chapter 4. The influence of site class (either NEHRP C or NEHRP D due to the limitation of the strong-motion database) is defined by the dummy site variables S_1 and S_2 in Eq. (5.14) that take values of unity when the MIDR is estimated for NEHRP D ($S_1=1$) and NEHRP C ($S_2=1$) site classes. Thus, the proposed MIDR predictive model does not account for the nonlinear soil effects on the median MIDR estimations.

The regressions are done by using the one-stage maximum likelihood method of Joyner and Boore (1993). The regression method computes the coefficients by considering the functional forms of each estimator parameter obtained from observations. The uncertainties involved in the functional forms of each estimator parameter is accounted for by this regression technique and it is reflected on the computed standard deviation. The regression constants of the predictive model are given in Table 5.2.

Table 5.2 Equation constants of the MIDR predictive model

b_1	b_2	b_3	b_4	b_5	b_6
-1.0461	0.00543	-0.29536	0.02325	7.22157	0.92186
b_7	b_8	b_9	σ_1	σ_2	
0.02929	-1.01252	-1.04103	0.1167	0.0259	

The dispersion about median MIDR is presented by standard deviation, $\sigma_{\log_{10}(\text{MIDR})}$, that considers the inter-event (σ_2) and intra-event (σ_1) variability. The inter-event variability defines the variations due to specific source features of earthquakes. The intra-event variability accounts for the variations of path and site effects within an earthquake. The intra-event standard deviation given for the proposed MIDR model also considers the variation of total story number (or fundamental period) since each building model is assumed as a separate site collocated closely to the recording station while running the regressions. The total standard deviation expression is given in Eq. (5.15) and it is calculated as 0.1195.

$$\sigma_{\log_{10}(\text{MIDR})} = \sqrt{\sigma_1^2 + \sigma_2^2} \quad (5.15)$$

5.5 Evaluation of the Predictive Model

The performance of the proposed model is investigated by considering the conventional residual analysis plots. These are given in Figure 5.9 and they show the variation of total residuals in terms of magnitude (M_w) and source-to-site distance (R_{jb}). The format of these plots is similar to those presented while evaluating the other approximate MIDR expressions. The plots depict that MIDR estimations are unbiased in terms of magnitude and distance, which complies with the efficiency condition described by Luco and Cornell (2007). It should also be noted that the dispersion of residual scatters are less when compared to the observations made for the other approximate methods. This is not surprising as the proposed MIDR model is directly derived from the ground-motion database used for the residual analysis.

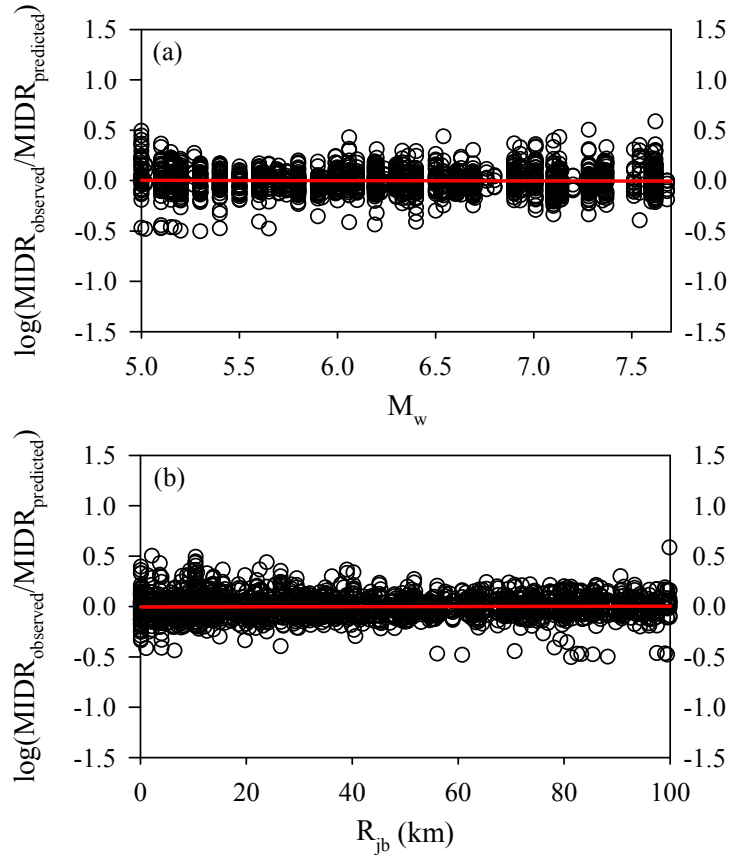


Figure 5.9 Residual plots of the predictive model in terms of (a) M_w and (b) R_{jb} . The overall trends of the residuals are shown with red lines; a 2nd order fit on the residual scatters

The left panel on Figure 5.10 compares the predicted and observed MIDR demands in terms of strength reduction factor, R_y . The scatters of the proposed model show not only the median estimations (grey circles) but also median ± 1 standard deviation estimations (light grey lines) in order to illustrate how the proposed model can handle the uncertainty in MIDR estimations due to record-to-record variability. The observed MIDR values are demonstrated by red circles. As it can be inferred from the left panel of Figure 5.10, the observed and estimated MIDR demands follow very similar patterns with the variations in R_y . As the level of nonlinearity increases (high R_y values), the performance of the proposed model decreases that is also shown quantitatively by the difference statistics given in the middle panel. The difference statistics are calculated by subtracting the estimated MIDR values from the observed ones. Only median MIDR estimates are used to compute these statistics. Although the difference statistics diverge from zero for large R_y , their values are very small indicating the insignificance of error introduced by the proposed model on MIDR estimations. The error statistics of the proposed model computed from Eq. (5.8) are given on the right panel in Figure 5.10. These statistics also depict lower performance of the proposed model towards higher nonlinearity as the dispersive character of error scatters

are more prominent towards larger R_y . However, the overall performance of the proposed model can still be considered as sufficient when the behavior of the same statistics are compared with those of other 3 alternative procedures presented in the previous section.

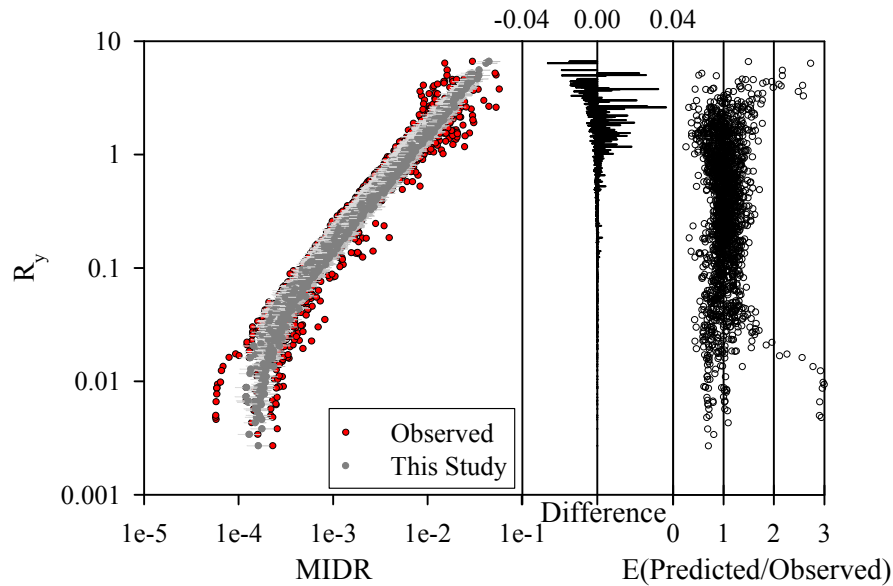


Figure 5.10 Comparison of predicted and observed MIDR scatters together with difference and error scatter diagrams for strength reduction factor

When the constant MIDR limits imposed by several seismic design codes for design and performance assessment procedures are of concern, the importance of proposed predictive model becomes more apparent. As it is tried to be emphasized in the entire dissertation not only the structural parameters but also the seismicity of a given region control the variation of EDPs. Direct estimation of engineering demand parameters from the consideration of seismological and structural parameters would result in more realistic design and performance assessment procedures for the future updates of seismic design provisions.

Figures 5.11 and 5.12 show the variation of median MIDR demands in terms of distance and magnitude, respectively. Each panel on these figures presents the median MIDR demands for different strength reduction factors (R_y). As noted in the previous chapter, the strength reduction factor used by the predictive model disregards the overstrength due to inherent redistribution feature of structural systems. Therefore, if one wants to evaluate the presented results by considering the code-based structural behavior factors the given R values should be modified by the overstrength factor Ω . The overstrength factors computed for the building models used in this dissertation are already presented in Chapter 4. The soil condition chosen for these plots is NEHRP site class C ($360\text{m/s} \leq V_{s,30} < 760\text{m/s}$). The panels clearly indicate the level of sensitivity of MIDR on magnitude, distance and nonlinear structural behavior. The increase in magnitude and level of nonlinearity amplifies the MIDR demands. Median MIDR estimations decrease with increasing distance. The predictive model enables the estimation of MIDR from the variation of these

seismological and structural estimator parameters. This feature is particularly useful for the probabilistic seismic performance and damage assessment of structural systems by using MIDR as the major EDP.

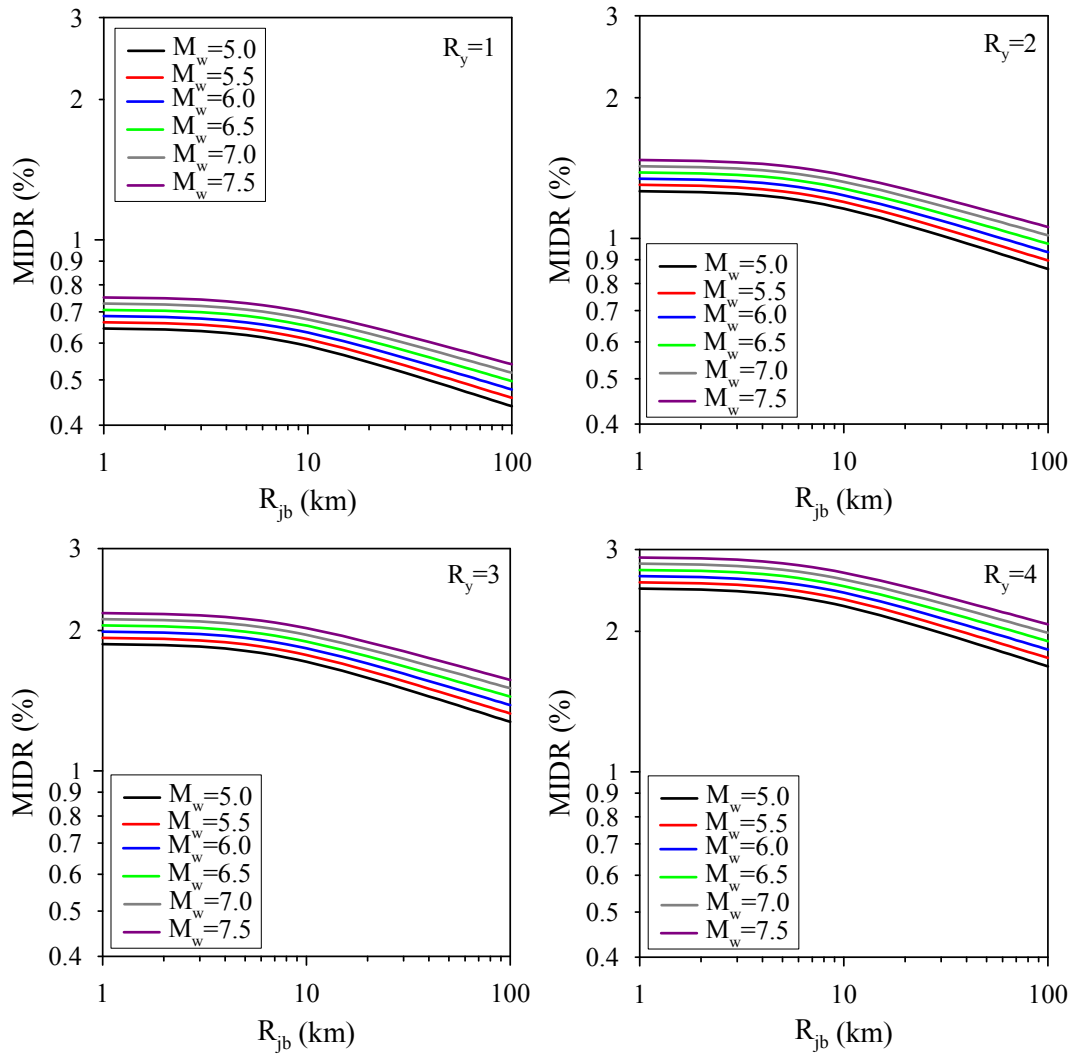


Figure 5.11 Variation of median MIDR estimations with R_{jb} for $R_y=1$ (top, left panel), $R_y=2$ (top, right panel), $R_y=3$ (bottom, left panel) and $R_y=4$ (bottom, right panel)

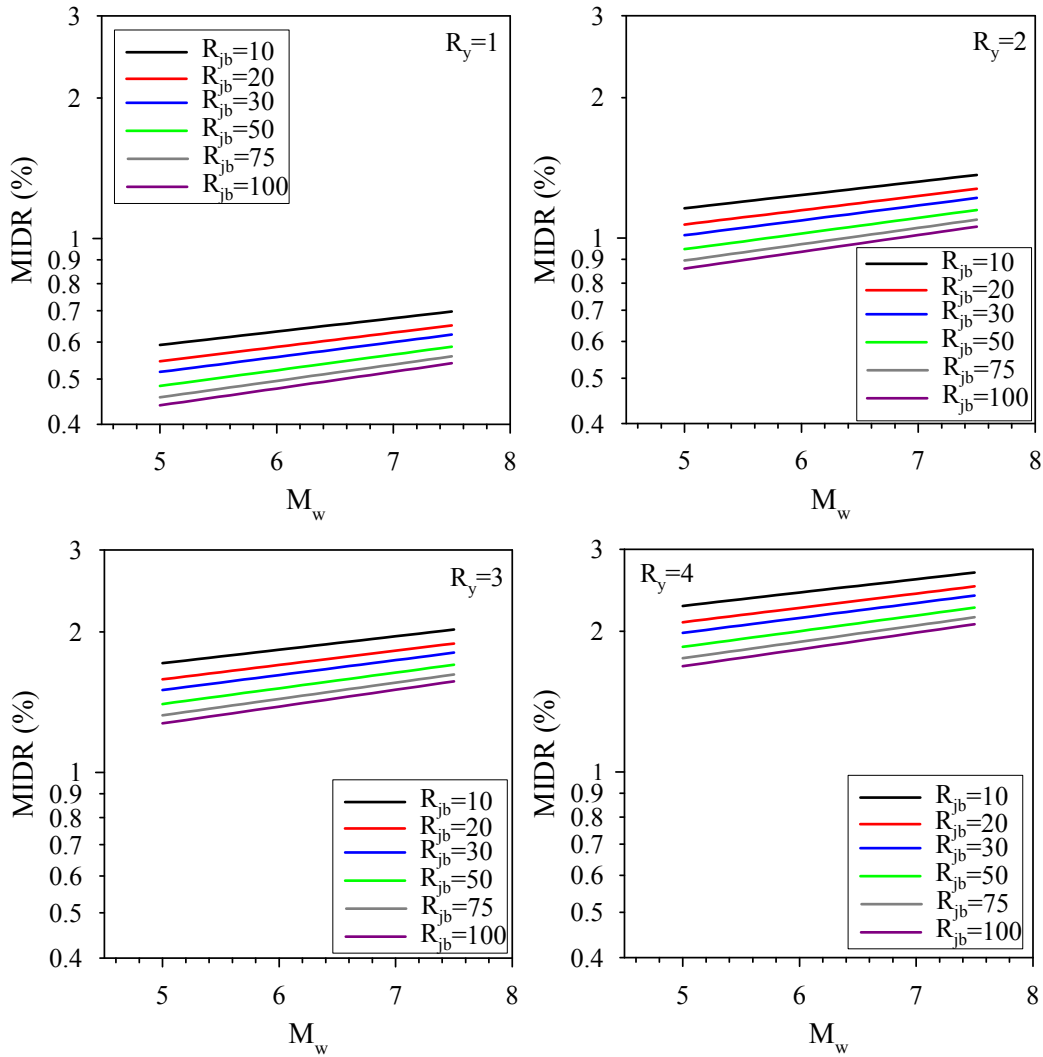


Figure 5.12 Variation of median MIDR estimations with M_w for $R_y=1$ (top, left panel), $R_y=2$ (top, right panel), $R_y=3$ (bottom, left panel) and $R_y=4$ (bottom, right panel)

The last figure of this chapter (Figure 5.13) shows the influence of aleatory variability on MIDR estimations. This figure presents the magnitude-dependent variation of median ± 1 sigma MIDR values for a stiff-soil site (NEHRP C) located $R_{jb}=10$ km from the causative fault. The strength reduction factor is chosen as $R_y=4$ for the fictitious RC moment resisting frame. This plot once again emphasizes the significance of record-to-record variability and level of seismicity on the MIDR values. Disregarding these parameters and approaching the problem in a deterministic manner would overlook the current engineering needs for reliable MIDR estimations.

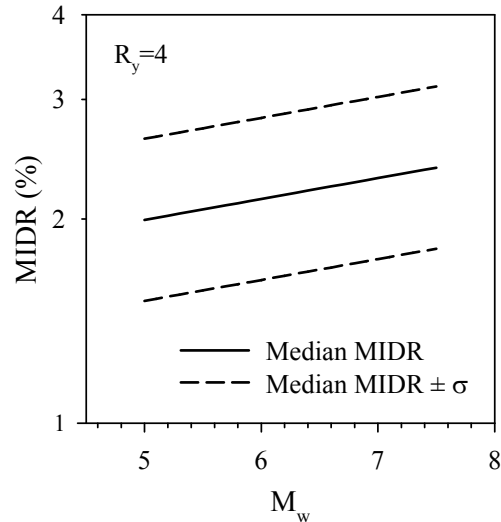


Figure 5.13 Variation of median and median $\pm \sigma$ MIDR estimations with M_w for $R_y=4$ and NEHRP C site class

5.6 Limitations and General Features of the Proposed MIDR Model

The overall features of the MIDR predictive model as well as its capabilities and assumptions made during its development are listed below.

- The predictive model is developed for code complying low- and mid-rise (3 to 9 story) RC buildings. The period range of the frames vary between $\sim 0.7s$ and $1.4s$. Further studies are necessary to assess the performance of the proposed model for high-rise and stiffer buildings. Due to the limitations of 2-D modeling, torsional effects are not included in the study. Moreover the model is developed assuming that the buildings are dominated by first-mode behavior.
- The magnitude range of the MIDR model is $5.0 \leq M_w < 7.7$. The source-to-site distance (R_{jb}) is confined to $R_{jb} \leq 100$ km. To this end, the proposed predictive model addresses both near and far distance as well as small and large magnitude events of engineering interest.
- The ground-motion set is a composition of accelerograms that are recorded on stiff (NEHRP C) and soft (NEHRP D) site classes. The range of applicability of the MIDR model is between 180 m/s and 760 m/s in terms of $V_{s,30}$. Although this shear-wave velocity range covers the soil conditions of most engineered structures, the MIDR demands for buildings located on rock sites should be integrated in future studies related to this model.

- The proposed model is capable of estimating nonlinear MIDR demands for code-complying moment resisting frames.

CHAPTER 6

USE OF MIDR PREDICTIVE MODEL IN PROBABILITY-BASED DESIGN AND SEISMIC PERFORMANCE ASSESMENT

6.1 Introduction

Seismic performance of buildings is of prime importance when future earthquakes are of concern. This fact urges the implementation of rational seismic design and assessment methodologies to ensure the safe and reliable response of existing and new buildings against seismic action. Quantification of seismic reliability of structures has always been a challenging task for the structural engineers due to randomness and uncertainties involved in the earthquake phenomenon and nonlinear structural response. The structural and earthquake related peculiarities need to be considered within a probabilistic framework to quantify the unknowns of nature as well as man-made structures. This issue has motivated many researchers to continuously improve the design and assessment methodologies in earthquake engineering (e.g., Bertero and Bertero, 2000; Cornell and Krawinkler, 2000; Moehle and Deierlein, 2004; Priestley et al., 2007). The major outcome of these efforts is the so-called performance-based earthquake engineering (PBEE) that constitutes the framework of next generation seismic design guidelines.

Although, the PBEE methods can differ in terms of their area of application, they require the implementation of probabilistic approaches in seismic demand, damage, loss and decision related analyses. This way, the uncertainties at each stage are incorporated for their proper quantification. The challenge in PBEE methodologies, however, is the integration of their simplified, nevertheless reliable, versions in seismic design codes. Accordingly, this chapter provides a set of useful procedures for probabilistic quantification of nonlinear structural demands that can be of use for the design and seismic performance assessment of low- and mid-rise RC frame buildings in Turkey. The proposed methods are inspired by the probabilistic seismic demand analysis (PSDA) of Bazzurro (1998) that aims at expressing the probabilistic estimation of earthquake induced structural displacement. The first chapter discusses different PSDA approaches that have conceptual differences in combining seismic

effects and structural response. The PSDA approach of this chapter is based on the structure-specific EDP attenuation equation that is introduced in Chapter 5. In this sense, the source of proposed design and assessment methodologies rests on probabilistic techniques and combines the proposed MIDR predictive model with probabilistic seismic hazard assessment methodology. The proposed methods do not intend to replace the current design and assessment procedures in the codes. They can be used as substitutes for the drift-related provisions to account for the uncertainties in the level of seismicity and structural response that have been frequently emphasized in the main body of this dissertation. The chapter starts with addressing the theoretical background of the proposed design and seismic performance assessment methodologies. The rest of the chapter provides case studies to describe their implementation and discusses how they can incorporate the uncertainties involved in seismic demands and structural response.

6.2 Use of Probabilistic Concepts Together with the MIDR Predictive Model

The determination of annual probability (or rate) of exceeding some level of MIDR under future earthquakes can be computed by using the probabilistic seismic hazard assessment (PSHA) concept introduced by Cornell (1968). Using the total probability theorem, PSHA convolves the occurrence probabilities of earthquakes and exceedance probability of the ground-motion intensity parameter by considering the probability distributions of earthquakes, source-to-site distances associated with potential seismic sources and ground-motion intensity parameter conditioned on magnitude, distance, etc. The probability distributions essentially describe the uncertainties involved in each one of these terms and the final product is the quantification of annual exceedance rate (or probability) of the ground-motion intensity parameter for a certain threshold level. The details of PSHA can be found in any text book. (e.g., Reiter, 1990; Thenhaus and Campbell, 2003; McGuire, 2004) or benchmark papers (e.g., Cornell, 1968; Cornell, 1971; McGuire, 1995) and will not be repeated here for brevity.

The MIDR predictive model can be considered as a probability distribution that describes the exceedance probability of MIDR conditioned on M_w , (moment magnitude), R_{jb} (source-to-site distance), SC (site class) and R_y (strength reduction factor). If one uses the conditional probability, the conditional exceedance of MIDR can be described by Eq. (6.1).

$$P(\text{MIDR} > x |_{M_w, R_{jb}, SC, R_y}) = \frac{P(\text{MIDR} > x \cap M_w = m_w \cap R_{jb} = r_{jb} \cap SC = s \cap R_y = r_y)}{P(M_w = m_w \cap R_{jb} = r_{jb} \cap SC = s \cap R_y = r_y)} \quad (6.1)$$

In the above expression the capital letters designate the random variables whereas small letters are the corresponding values. Eq. (6.2) reads Eq. (6.1) in another format:

$$P(\text{MIDR} > x \cap M_w = m_w \cap R_{jb} = r_{jb} \cap \text{SC} = s \cap R_y = r_y) = P(\text{MIDR} > x |_{M_w, R_{jb}, \text{SC}, R_y}) \times P(M_w = m_w \cap R_{jb} = r_{jb} \cap \text{SC} = s \cap R_y = r_y) \quad (6.2)$$

If random variables SC and R_y are predefined, their probabilities are unity. Under this condition Eq. (6.2) reduces to;

$$P(\text{MIDR} > x \cap M_w = m_w \cap R_{jb} = r_{jb}) = P(\text{MIDR} > x |_{M_w, R_{jb}}) \times P(M_w = m_w \cap R_{jb} = r_{jb}) \quad (6.3)$$

Eq. (6.3) can further be simplified by removing the intersection terms from the left-hand side (just for brevity) and using conditional probability for the last term on the right-hand side.

$$P(\text{MIDR} > x) = P(\text{MIDR} > x |_{M_w, R_{jb}}) \times P(M_w) \times P(R_{jb} | M_w) \quad (6.4)$$

Eq. (6.4) indicates that the exceedance probability of MIDR is the product of exceedance probability of MIDR conditioned on M_w and R_{jb} , the occurrence probability of magnitude given an event and the occurrence probability of R_{jb} conditioned on the magnitude of given event provided that SC and R_y are already known.

Following the above theoretical information and using the total probability theorem the exceedance probability of MIDR for a certain threshold level given occurrence of an earthquake is described in Eq. (6.5).

$$P(\text{MIDR} > x) = \int_{(m_w)_{\min}}^{(m_w)_{\max}} \int_0^{(r_{jb})_{\max}} P(\text{MIDR} > x |_{M_w, R_{jb}}) f_{M_w}(m_w) f_{R_{jb}|M_w}(r_{jb}, m_w) dm_w dr_{jb} \quad (6.5)$$

where $P(\text{MIDR} > x |_{M_w, R_{jb}})$ comes from the MIDR predictive model, $f_{M_w}(m_w)$ and $f_{R_{jb}|M_w}(r_{jb}, m_w)$ are the probability density functions for magnitude and source-to-site distance conditioned on M_w . The integration operation adds up the conditional probabilities of exceedance associated with all magnitudes and distances. In other words, the probability functions of magnitude $f_{M_w}(m_w)$ and distance $f_{R_{jb}|M_w}(r_{jb}, m_w)$ yield the occurrence probabilities of magnitudes and distances within $(m_w)_{\min} \leq m_w \leq (m_w)_{\max}$ and $r_{jb} \leq (r_{jb})_{\max}$, respectively. The conditional probability $P(\text{MIDR} > x |_{M_w, R_{jb}})$ yields the exceedance probability of MIDR for a certain value of x conditioned on magnitudes and distances within the ranges of $(m_w)_{\min} \leq m_w \leq (m_w)_{\max}$ and $r_{jb} \leq (r_{jb})_{\max}$. The latter two probabilities computed from $f_{M_w}(m_w)$ and $f_{R_{jb}|M_w}(r_{jb}, m_w)$ can be considered as weighting factors of $P(\text{MIDR} > x |_{M_w, R_{jb}})$. In general $f_{M_w}(m_w)$ is described either by truncated Gutenberg-Richter magnitude recurrence law (McGuire, 2004) or characteristic model (Schwartz and

Coppersmith, 1984). The probability density $f_{R_{jb}|M_w}(r_{jb}, m_w)$ is computed by assuming that earthquakes will occur with equal probability at any location on the seismic source associated with an empirical relationship that combines rupture dimensions and size of earthquake (e.g., Wells and Coppersmith, 1994; Leonard, 2010).

The conditional probability $P(\text{MIDR} > x |_{M_w, R_{jb}})$ is computed by assuming that MIDR predictive model is the probability distribution of the random variable MIDR. One can describe this point by rewriting the functional from of the MIDR predictive model as;

$$\log_{10}(\text{MIDR}) = \log_{10} \overline{\text{MIDR}}(M, R_{jb}, SC, R_y) + \varepsilon \sigma_{\log_{10}(\text{MIDR})} \quad (6.6)$$

The terms $\log_{10} \overline{\text{MIDR}}(M, R_{jb}, SC, R_y)$ and $\sigma_{\log_{10}(\text{MIDR})}$ are the outputs of MIDR model; they are the estimated mean and standard deviation of $\log_{10} \text{MIDR}$, respectively. The logarithmic mean $\log_{10} \overline{\text{MIDR}}$, is a function of moment magnitude (M_w), Joyner and Boore source-to-site distance (R_{jb}), site class (SC) and strength reduction factor (R_y). The term ε refers to number of standard deviations above and below mean MIDR estimation and describes the aleatory variability on MIDR together with the standard deviation, $\sigma_{\log_{10}(\text{MIDR})}$ as shown in Eq. (6.6). Since the distribution of MIDR can be assumed as log-normal (see discussions in Chapter 3) and since the randomness of R_y and SC is waived for simplification purposes, $P(\text{MIDR} > x |_{M_w, R_{jb}})$ can be described by the expression given in Eq. (6.7).

$$P(\text{MIDR} > x |_{M_w, R_{jb}}) = 1 - \Phi \left[\frac{\log_{10} x - \log_{10} \overline{\text{MIDR}}}{\sigma_{\log_{10}(\text{MIDR})}} \right] \quad (6.7)$$

where $\Phi \left[\frac{\log_{10} x - \log_{10} \overline{\text{MIDR}}}{\sigma_{\log_{10}(\text{MIDR})}} \right]$ is the standard normal cumulative distribution function

because the logarithm of any log-normal variate is normally distributed. The visual description of Eq. (6.7) is given in Figure 6.1. As one can infer from this illustrative sketch, the MIDR exceedance probability for the threshold value x decreases (shaded areas) with increasing distance, which is expected from the discussions given in Chapter 5. Note that the strength reduction factor, R_y and soil conditions are assumed to be known in the entire derivations. These parameters will be treated as deterministic throughout this study in order not to complicate the integral expression given in Eq. (6.5). Moreover, the proposed design and assessment procedures do not require the consideration of this parameter as a random variable.

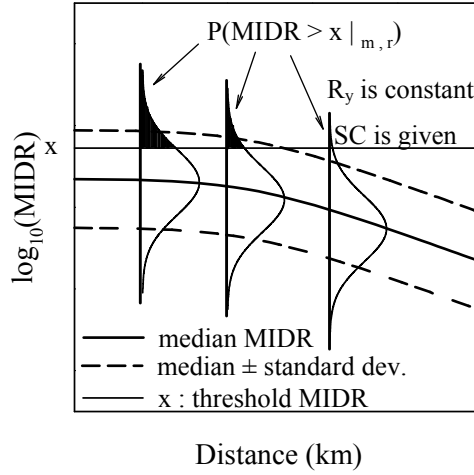


Figure 6.1 Illustration of $P(\text{MIDR} > x | M_w, R_{jb})$ for constant strength reduction factor and known site class. The site class is assumed as homogenous in the location of interest in this illustrative example (Modified from Baker, 2008).

Eq. (6.5) is a probability of exceedance given an earthquake and does not include any information about how often earthquakes occur on the source of interest. A simple modification to Eq. (6.5) is necessary to compute the rate of $\text{MIDR} > x$. This is given in Eq. (6.8).

$$\lambda(\text{MIDR} > x) = \lambda(M_w > (m_w)_{\min}) \int_{(m_w)_{\min}}^{(m_w)_{\max}} \int_0^{(r_{jb})_{\max}} P(\text{MIDR} > x | M_w, R_{jb}) f_{M_w}(m_w) f_{R_{jb}|M_w}(r_{jb}, m_w) dm_w dr_{jb} \quad (6.8)$$

where $\lambda(M_w > (m_w)_{\min})$ is the rate of occurrence of earthquakes greater than $(m_w)_{\min}$ from source and $\lambda(\text{MIDR} > x)$ is the rate of $\text{MIDR} > x$. When one considers multiple seismic sources contributing to $\lambda(\text{MIDR} > x)$, Eq. (6.8) turns out to be the sum of the rates of $\text{MIDR} > x$ from each individual source.

$$\lambda(\text{MIDR} > x) = \sum_{i=1}^{n_{\text{source}}} \lambda(M_w > (m_w)_{\min i}) \int_{(m_w)_{\min}}^{(m_w)_{\max}} \int_0^{(r_{jb})_{\max}} P(\text{MIDR} > x | M_w, R_{jb}) f_{M_w, i}(m_w) f_{R_{jb}|M_w, i}(r_{jb}, m_w) dm_w dr_{jb} \quad (6.9)$$

In Eq. (6.9), n_{source} is the number of sources, $f_{M_w, i}(m_w)$ and $f_{R_{jb}|M_w, i}(r_{jb})$ denote the probability density functions for source i . Figure 6.2 shows the schematic illustration of entire process given in Eq. (6.9). As the above calculations are generally performed by computers, the practical approach is to discretize the continuous distribution of $f_{M_w, i}(m_w)$ and $f_{R_{jb}|M_w, i}(r_{jb})$ into n_m and n_r intervals, respectively. The discretized format of Eq. (6.9) is given in the following line.

$$\lambda(\text{MIDR} > x) = \sum_{i=1}^{n_{\text{source}}} \lambda(M_w > (m_w)_{\min,i}) \sum_{j=1}^{n_m} \sum_{k=1}^{n_r} P(\text{MIDR} > x |_{M_{w,j} R_{j,b,k}}) P(M_w = m_{w,i}) P(R_{j,b} = r_{j,b,k})_i$$

(6.10)

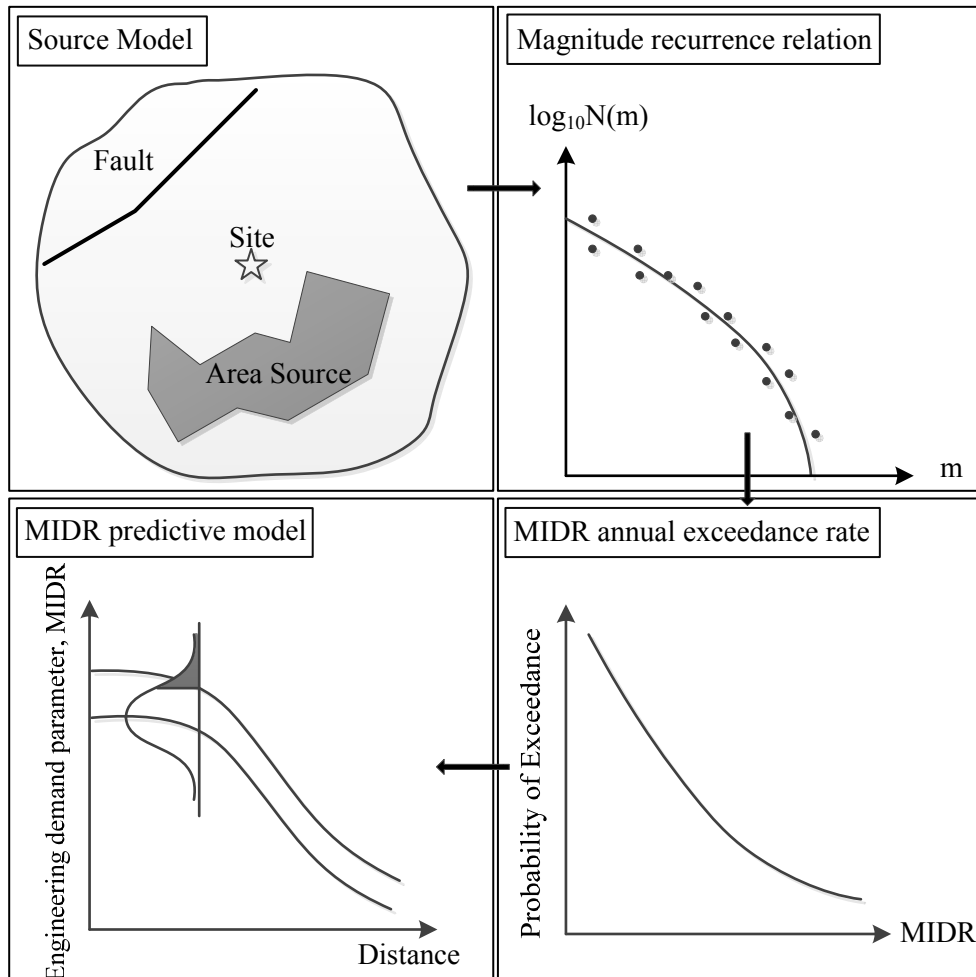


Figure 6.2 Schematic illustration of the proposed probabilistic concept

The discretized form to compute annual exceedance rates of MIDR is done by a computer program that is associated with a graphical interface. Appendix D describes the general features of this software. The annual MIDR exceedance rates computed from Eq. (6.10) can be transformed into probabilities for a certain exposure time assuming that earthquake process and resulting MIDR are Poissonian. This simplifying assumption is questionable as earthquake and the resulting EDPs cannot be independent of previous events. However, Poissonian assumption is common in many PSHA related applications and is used in this study for practicality reasons.

6.3 Proposed Probability-based Design and Seismic Performance Assessment Procedures

The entire body of this dissertation has focused on the significance of seismicity level, randomness in earthquakes and complicated structural response against earthquakes while estimating MIDR. The current codes do not account for these factors while defining MIDR levels for different seismic performance levels. In general, the drift limits are provided as constants regardless of the level of seismicity (see the discussion in Section 3.4). Moreover, MIDR is implicitly related with spectral quantities (SDOF information) by seismic codes that seems to result in inaccurate MIDR estimations as discussed in Chapter 5. The uncertainties involved due to record-to-record variability as well as building response are also overlooked in the drift limit descriptions for different performance levels. All of these deficiencies are believed to be addressed by the design and performance assessment procedures described in the following lines.

The proposed design process is itemized in the following steps:

1. Assume R (usually varies between 4 and 8 in seismic design codes).
2. Given the region of interest, compute uniform hazard spectrum, UHS, (or its envelope) for the design return period dictated by the seismic design code (e.g., 475 years return period – 10% exceedance probability in 50 years exposure time–by Turkish Earthquake Code).
3. Design the building using vertical and lateral earthquake loads by implementing the detailing provisions of the code.
4. Compute the yield capacity of the building from nonlinear static procedures (ATC-40 method is the preferred method in this study as discussed in Chapter 4).
5. Compute R_y by comparing the yield capacity and elastic spectral ordinate obtained from the uniform hazard spectrum (or its envelope) at the fundamental period.

6. Compute the MIDR annual exceedance rate curve for the calculated R_y using the theory described in Section 6.2. Note that the seismic hazard and MIDR annual exceedance rates are entirely consistent as the uniform hazard spectrum (or the corresponding envelope) and MIDR exceedance rates are computed from the same seismic sources.
7. For the predefined annual exceedance rate (or return period) used for the derivation of uniform hazard spectrum for design, find the MIDR value from MIDR annual exceedance rate curve computed for R_y (call it as $MIDR_{performance}$). Note that this step is also entirely consistent if both PSHA and probabilistic MIDR annual exceedance rates follow Poissonian process.
8. From the pushover inventory identify the damage state of the building at $MIDR_{performance}$. Usually newly designed buildings are expected to comply with the Life Safety (LS) performance level with a margin of safety level under design ground motions. The expected building damage state of this performance level is described in many building design provisions (e.g., clause 7.8 in the Turkish Earthquake Code).
9. Check if the building damage state complies with the code required performance at $MIDR_{performance}$. If this check is failed, reduce R by unity and reiterate the procedure starting from Step 3.

Note that the above procedure is hybrid in the sense that it follows the conventional code-based design approach but the final performance checks are done with the $MIDR_{performance}$ computed from the design method described in this study. The consistency between the level of seismicity while determining the dimensions and detailing of the building and the MIDR value that is expected to occur for the same hazard level is the strength of this procedure. If followed, the resulting design surmounts the deficiencies summarized in the first paragraph of this section. Figure 6.3 illustrates the proposed design concept schematically. Depending on the importance of the building, the above procedure can also be implemented for collapse prevention seismic performance level that is generally described for a return period of 2475 years ground motion (i.e., 2% exceedance probability in 50 years exposure time).

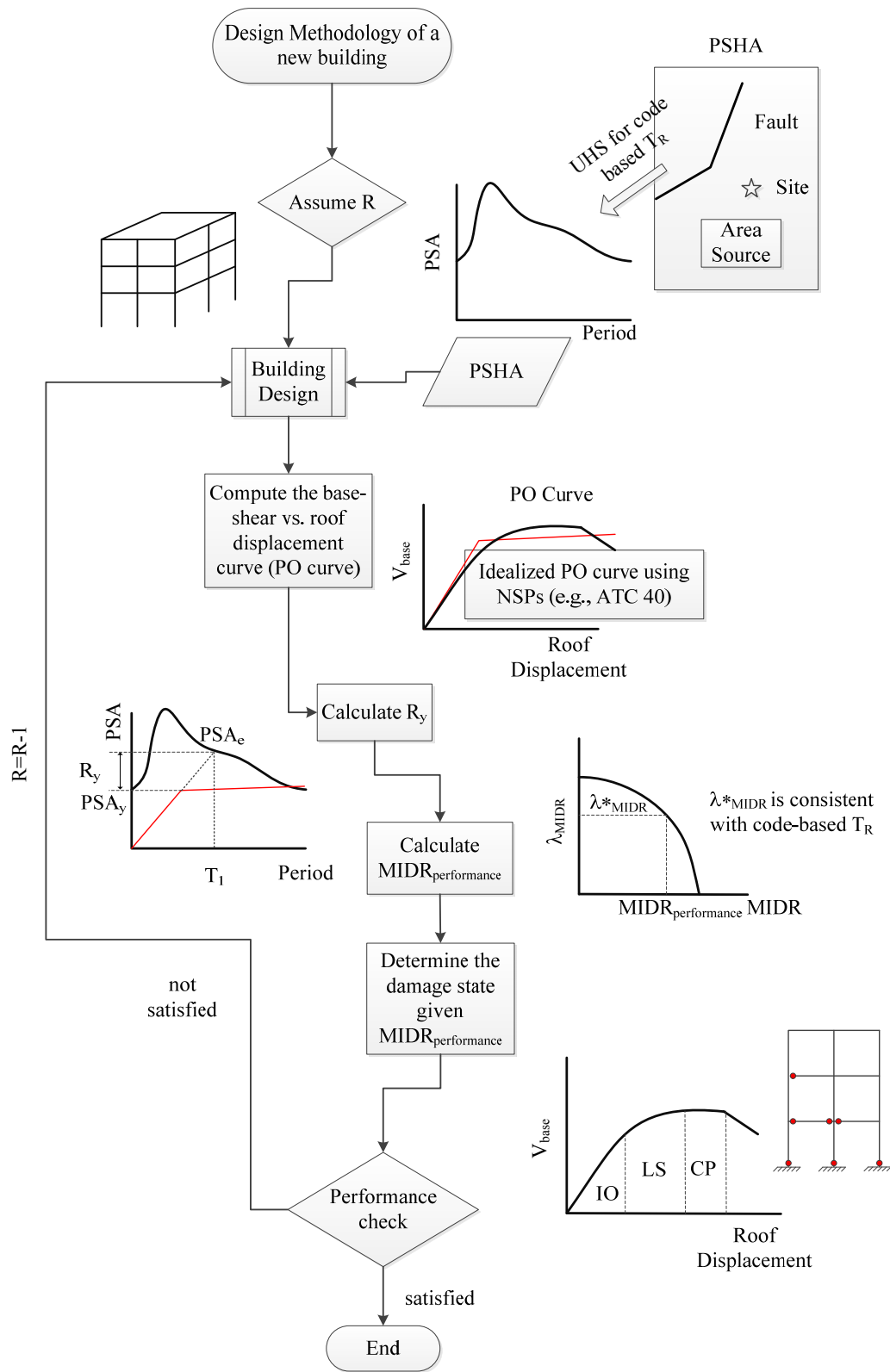


Figure 6.3 Schematic illustration of the proposed seismic design procedure

The proposed seismic performance assessment procedure shows similarities with the above design approach. The steps that should be followed for this case are given below.

1. Given a building, compute its capacity from nonlinear static pushover analysis (ATC-40 method can be used here as in the case of design methodology).
2. Compute R_y by comparing the building capacity curve and uniform hazard spectrum, UHS, (or its envelope) computed for the target seismic performance level (e.g., immediate occupancy, life safety or collapse prevention). For example, the Turkish Earthquake Code requires uniform hazard spectrum of 475 years return period (i.e., 10% exceedance probability in 50 years) for life safety performance level.
3. For the given target performance level compute MIDR annual exceedance rate curve for R_y using the methodology described in Section 6.2. Extract the MIDR value that corresponds to the annual exceedance rate at the target performance level (call this MIDR as $MIDR_{performance}$ as in the case of design method).
4. Identify the damage state of the building using the pushover inventory at $MIDR_{performance}$. If the building damage state complies with the code driven requirements for the target seismic performance level, the building capacity can be assumed as sufficient. The opposite means that the building fails to satisfy code requirements at that target performance level.

The above seismic performance assessment procedure is illustrated in Figure 6.4. Additional practical approaches are brought into the design and assessment procedures proposed in this study. A simple relationship is developed between nonlinear MIDR and MRDR EDPs by using the nonlinear RHA of this study. Eq. (6.11) presents this simple relationship and Appendix E briefly describes its derivation.

$$\log_{10}(MRDR) = 0.995\log_{10}(MIDR) - 0.135 \quad (6.11)$$

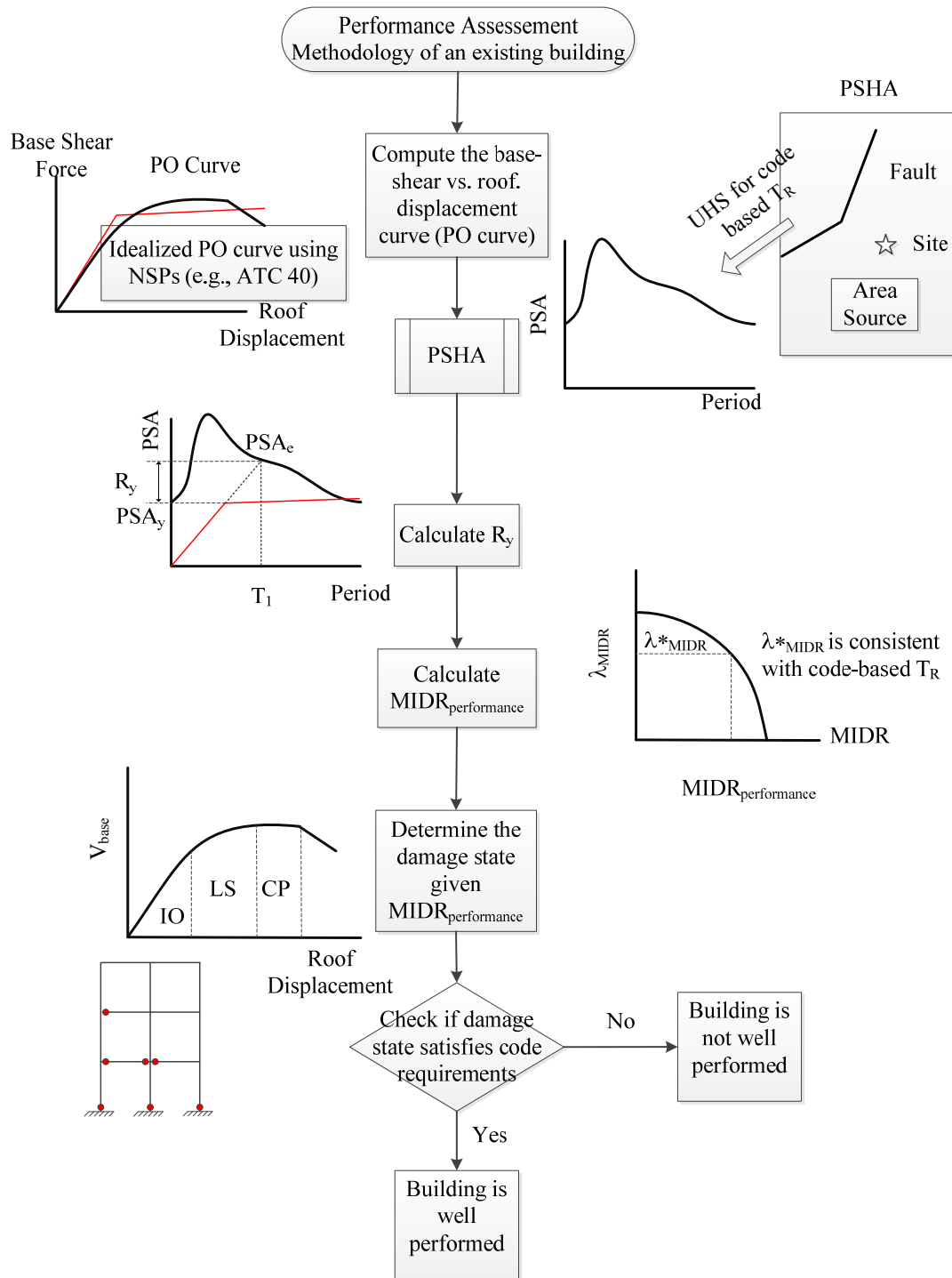


Figure 6.4 Schematic illustration of the proposed seismic performance assessment procedure

Eq. (6.11) can be used to convert MIDR annual exceedance rates into MRDR annual exceedance rates by modifying the results of MIDR predictive model for MRDR. Inherently, the conversion from MIDR to MRDR modifies the aleatory variability in MRDR estimations. This should be accounted for while modifying the MIDR predictive model for MRDR. The new standard deviation that should be used in the MRDR estimations is given in Eq. (6.12).

$$\sigma_{\log_{10}(\text{MRDR})} = \sqrt{0.995^2 \sigma_{\log_{10}(\text{MIDR})}^2} \quad (6.12)$$

Substitution of Eqs. (6.11) and (6.12) into the logarithmic mean estimations of Eq. (5.17) would result in the computation of annual exceedance rates of MIDR. These expressions are given in Eqs. (6.13).

$$\log_{10}(\overline{\text{MRDR}}) = 0.995 \log_{10}(\overline{\text{MIDR}}) - 0.135 ; \sigma_{\log_{10}(\text{MRDR})} = \sqrt{0.995^2 \sigma_{\log_{10}(\text{MIDR})}^2} \quad (6.13a)$$

$$P(\text{MRDR} > x |_{M_w, R_{jb}}) = 1 - \Phi \left[\frac{\log_{10} x - \log_{10} \overline{\text{MRDR}}}{\sigma_{\log_{10}(\text{MRDR})}} \right] \quad (6.13b)$$

$$\lambda(\text{MRDR} > x) = \sum_{i=1}^{n_{\text{source}}} \lambda(M_w > (m_w)_{\text{min}i}) \sum_{j=1}^{n_m} \sum_{k=1}^{n_r} P(\text{MRDR} > x |_{M_{w,j} R_{j,b,k}}) \times P(M_w = m_{w,j}) P(R_{j,b} = r_{j,b,k})_i \quad (6.13c)$$

Note that the first and second expressions in Eq. (6.12a) modify the logarithmic mean and standard deviation of MIDR for MRDR. Eq. (6.12b) assumes that MRDR is also a log-normal variate and Eq. (6.12c) is the modified annual exceedance rate expression for MRDR (modified from Eq. (6.10)). If this new format is used instead of MIDR, the global capacity curves can be estimated from many approximate procedures such as the one developed in this study that is given in Appendix F in detail. The use of such approximations for global capacity curves would certainly increase the speed of calculations in the proposed design and assessment methods. One should note that upon the implementation of above modification, the code-based MIDR limits given during the implementation of proposed procedures should be replaced with the corresponding MRDR limitations. The rest of the chapter presents case studies about the implementations of proposed design and performance assessment procedures.

6.4 Case studies for the Proposed Seismic Design Procedure

Case studies for design consider two locations in Turkey with different levels of seismic activity. The first location is in the province of Ankara with coordinates 40.0749⁰N and 32.5849⁰E. This place is designated as Zone IV (the lowest seismic prone zone) according to Turkish Seismic Zonation Map. The second location is chosen as the central part of the Düzce City (40.9N, 31.15E) that is identified as the most seismic prone region (Zone I) according to the same seismic zonation map. The reinforced concrete buildings to be

designed for these two locations are residential buildings with 6 stories. The seismic design regulations of Turkish Earthquake Code (TEC, 2007) are followed in the design stage that require design spectral ordinates of $T_R=475$ years (10% exceedance probability in 50 years assuming that seismic activity is Poissonian).

The design spectra for the case studies are computed from site-specific PSHA studies. The PSHA for the city of Düzce considers the seismic activity of the Düzce fault segment of the North Anatolian Fault zone as well as the background seismicity of 60 km x 60 km square framing around the central part of the Düzce city. The other fault segments of the North Anatolian Fault do not fall into this square so their likely effect on the city of Düzce are disregarded in PSHA. The Düzce fault is modeled as a fault plane with dimensions of 65 km x 25 km. The strike and dip angles of this fault are chosen as 264° and 64° , respectively based on the study by Umutlu et al. (2004). The fault is assumed to be located between the coordinates of $40.77^{\circ}\text{N}-31.45^{\circ}\text{E}$ and $40.67^{\circ}\text{N}-30.69^{\circ}\text{E}$. The average slip rate of the Düzce fault and the shear rigidity of the crust are taken as 10mm/year and 3.10^{11} dyne/cm² respectively. The mechanism of the fault is taken as strike-slip. The magnitude recurrence relationship of the fault is assumed to follow truncated normal distribution. The characteristic magnitude of the Düzce fault is calculated as M_w 7.2 using the empirical relationship provided by Wells and Coppersmith (1994). This value is close to the magnitude of the latest 1999 Bolu-Kaynaşlı earthquake (M_w 7.12) that occurred on the same fault segment. The standard deviation of truncated normal distribution is chosen as 0.2 and this distribution is assumed to be bounded by ± 2 sigma around characteristic magnitude. The background seismicity is represented by the truncated Gutenberg-Richter magnitude recurrence relationship with a beta value of 1.88. The minimum activity rate is calculated as 0.67 from the background seismicity. The minimum and maximum magnitudes for the background seismicity are taken as M_w 4.0 and M_w 6.4, respectively.

The PSHA for the city of Ankara considers three-linear segments of the North Anatolian Fault located on the north of Ankara. The region chosen for the background seismicity encloses these fault segments and the city of Ankara that is located in the center of background area. The three-linear NAF segment assumed to be located between the coordinates of $40.497^{\circ}\text{N}-37.081^{\circ}\text{E}$, $41.11^{\circ}\text{N}-35.341^{\circ}\text{E}$, $41.129^{\circ}\text{N}-34.225^{\circ}\text{E}$ and $40.395^{\circ}\text{N}-29.625^{\circ}\text{E}$. The faulting mechanism of the NAF segments is taken as strike-slip with a dip angle of 90° . The average slip rate of the NAF segments and the shear rigidity of the crust are taken as 20 mm/year and 3.10^{11} dyne/cm² respectively. Characteristic earthquake recurrence law (Schwartz and Coppersmith, 1984) is used to represent the occurrence rates of earthquakes on the considered fault segments. The characteristic magnitudes of the fault segments are assumed to vary uniformly between M_w 7.0 and M_w 7.6 in this model. The minimum magnitude considered on the faults is taken as M_w 4.0. The slope for the exponential part of the characteristic magnitude recurrence model is $\beta = 2.1$. The magnitude recurrence law for the background seismicity is represented by truncated Gutenberg-Richter relationship with minimum and maximum magnitudes of M_w 4 and M_w 6.8, respectively. $\beta=1.3$ and minimum activity rate is 0.12 for the background magnitude recurrence model.

These background seismicity parameters are computed from the earthquake catalog survey. It should be noted that the, PSHA for these two distinct locations is carried out by using the Akkar and Bommer (2010) ground-motion prediction equation (GMPE) as it is capable of representing the seismological features of the selected regions.

Figure 6.5 shows the uniform hazard spectra (UHS) computed from PSHA for these two locations for stiff soil conditions (Z_2 ; $V_{s,30}=400$ m/s). The computed UHS for $T_R=475$ years are compared with the design spectrum envelopes provided by the Turkish Earthquake Code (TEC, 2007). The comparisons indicate that the code-based spectra and site-specific spectra are comparable; the site-specific spectra are slightly conservative with respect to the code-based spectra towards shorter periods. The conservative spectral ordinates of site-specific spectra are more noticeable for the Ankara case. Nevertheless, the spectral accelerations of UHS and the code-based spectra are very similar to each other for both cases at the fundamental periods of the buildings (see Table 6.1 for the spectral accelerations at fundamental periods). Thus, the overall structural features of the designed buildings would be the same even if the code spectra were used in these case studies.

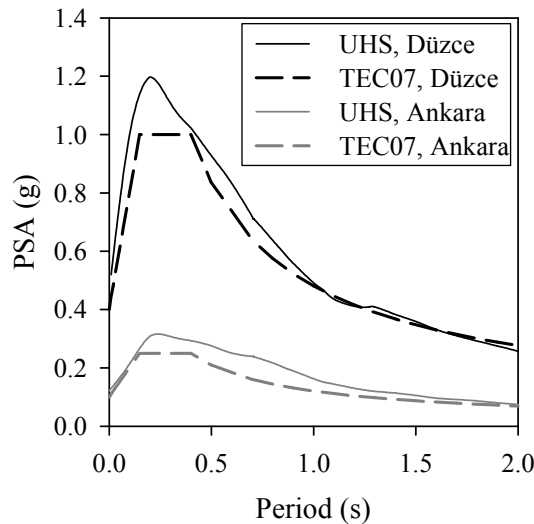


Figure 6.5 UHS versus TEC07 design spectra for $T_R=475$ years for the Düzce and Ankara case studies

The preliminary designs of the buildings are done under the guidance of statistical studies presented in Chapter 2. In other words, the cross-sectional dimensions of structural members, floor plan dimensions, story heights and reduction in the lateral stiffness over the building heights follow the statistics given in Chapter 2. The chosen floor plans do not contain any discontinuous frames in order not to complicate the design process. Figure 6.6 shows the floor plans and RC frames designed under the detailing requirements of the Turkish Earthquake Code (TEC, 2007). The vertical loads for design are taken from the relevant Turkish standards: (TS 500-2000 (Turkish Standards Institute, 2000), TS 498 (Turkish Standards Institute, 1997) and Turkish Earthquake Code (TEC, 2007). The

representative earthquake lateral loads are computed from the site-specific UHS for $T_R=475$ years. The major dynamic features and material properties of the residential buildings are given in Table 6.1. The buildings comply with the reinforcement details of ductile behavior according to Turkish Earthquake Code (TEC, 2007). The maximum interstory drift checks indicate 0.64% (for Ankara) and 1.7% (for Düzce) under the design load combinations dictated by the code. These values are below the allowed MIDR limit (2%) required by TEC (2007).

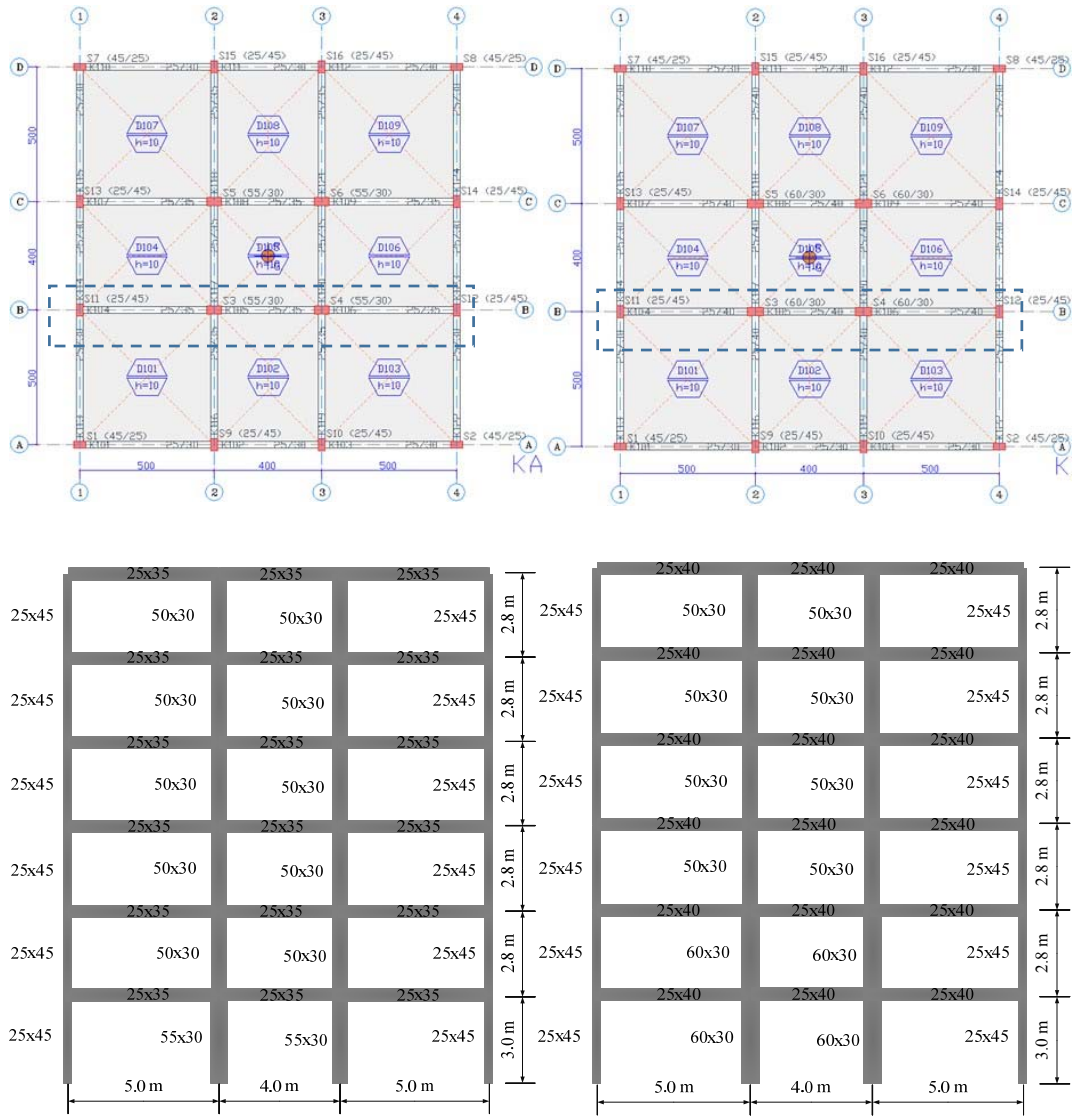


Figure 6.6 Typical floor plans and the cross-sectional views of 2D frames that are designed for the Ankara and Düzce case studies. The dashed rectangular boxes show the frames designed for each case.

Table 6.1 Important dynamic and material properties of the buildings designed in the cities of Ankara and Düzce

Location	Total mass (t)	Fundamental period (T_1)	Effective modal mass factor (α_1)	R	Steel ¹	Concrete ²	PSA _{UHS} (T_1) ³	PSA _{TEC07} (T_1) ⁴	PSA _y (T_1) ⁵	R _y ⁶	MIDR performance
Ankara	175	1.28	0.79	8	S420	C20	0.12g	0.097g	0.16g	0.8	0.8%
Düzce	193	1.23	0.79	8	S420	C20	0.4g	0.4g	0.2g	2.05	2.1%

¹ Steel grade S420 corresponds to steel yield strength of 420 MPa

² Concrete grade C20 corresponds to concrete compressive strength of 20 MPa

³ Pseudo spectral acceleration at the fundamental period obtained from UHS

⁴ Pseudo spectral acceleration at the fundamental period obtained from the Turkish Earthquake Code (TEC, 2007) design spectrum

⁵ Yield pseudo spectral accelerations of the frames

⁶ Strength reduction factor calculated from UHS

The global capacities of the buildings are computed from the nonlinear static procedure described in ATC-40 (ATC, 1996). They are given in ADRS format in Figure 6.7. The left panel on Figure 6.7 compares idealized PO curve and elastic response spectrum for the building located in Ankara whereas the panel on the right shows the same comparison for the building in the city of Düzce. The comparisons between the idealized PO curves and elastic spectra yield R_y values that are computed as the ratio between pseudo elastic (PSA_e) and yield pseudo (PSA_y) spectral accelerations of the buildings. This information is also given in Table 6.1. The computed R_y for the building in Ankara is less than unity ($R_y=0.8$), which indicates that the code requirements result in overdesign for the lowest seismic prone zone. The seismic design loads for this particular case seem to be insignificant and the imposed minimum cross-section dimensions by the code result in excessive lateral capacity for the designed building. The maximum interstory drift check given in the previous paragraph also certifies the overdesign (or excessive lateral capacity) of this building. The R_y value for the residential building in Düzce is computed as $R_y=2.05$ indicating an overstrength factor of $\Omega=4$ that is slightly above the corresponding values listed in Table 4.2 in Chapter 4.

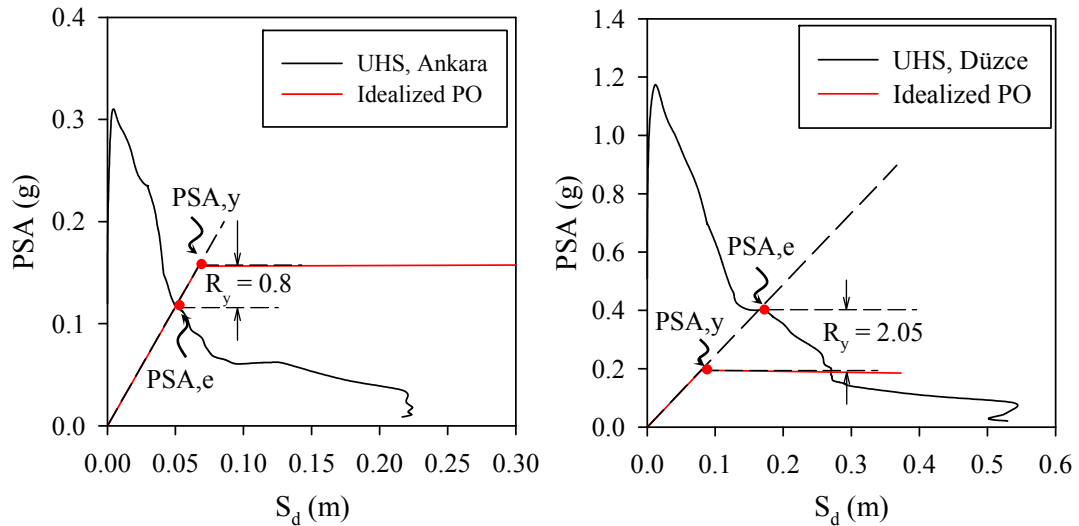


Figure 6.7 Comparisons of idealized PO curves and UHS utilized for design in ADRS format

Figure 6.8 shows the MIDR annual exceedance rates for the buildings designed in the selected locations of Ankara and Düzce. These curves are computed from Eq. (6.10) utilizing the seismic sources employed in the calculation of UHS. The computer software given in Appendix D is used in the computations. The use of same seismic sources in the computation of probability-based MIDR values warrant an internal consistency between the seismic demands (spectral ordinates) and engineering demand parameter (MIDR in this case) that is used to verify the efficiency of final design. As MIDR values are assumed to follow Poissonian process, the computed MIDR annual exceedance rate that is the reciprocal of target return period ($=1/T_R = 1/475 \approx 2.1 \times 10^{-3}$) also represents an exceedance probability of

10% in 50 years time in the proposed approach. Thus, the probabilistic MIDR demands computed for the R_y values of each building are fully compatible in terms of verifying the expected performance levels of the designed buildings under future design ground motions. The left and right panels in Figure 6.8 are two different ways of showing the MIDR annual exceedance rates. The probabilistic MIDR curves on the left panel have a format similar to those used in PSHA. The vertical axis shows the annual exceedance rates with the changes in MIDR given in abscissa. The MIDR curves on the right panel reveals the same information, but this time the MIDR variation is described with the changes in return period, T_R , along the horizontal axis that replaces the annual exceedance rates. It is believed that the right panel plot shows the sensitivity of MIDR to the level of target hazard more clearly in terms of engineering perspective. Both panels also describe the estimated MIDR levels for the subject annual exceedance rate (or return period) for the designed buildings in Ankara and Düzce.

The MIDR values computed from the proposed procedure indicate that the future ground motion spectral intensities with an exceedance probability of 10% in 50 years time barely cause structural damage for the building located in Ankara. The estimated MIDR at this target hazard level is 0.8% (also shown on Figure 6.8) that is below the immediate occupancy damage state limit given by the Turkish Earthquake Code (TEC, 2007; Chapter 7, Table 7.6). The estimated MIDR value for the Ankara case is also well below the required MIDR limit (2%) used for controlling the lateral deformation limits after design (TEC, 2007; Chapter 2; Clause 2.10.1). The estimated MIDR demand for $T_R=475$ years is 2.1% for the building in the city of Düzce. This value suggests that the structural damage experienced by the building would be in between the immediate occupancy and life safety damage states (TEC, 2007; Chapter 7, Table 7.6). However, the estimated probabilistic MIDR for the Düzce case is slightly above the 2% MIDR limit imposed for controlling the lateral deformations (TEC, 2007; Chapter 2, Clause 2.10.1). These case studies suggest that MIDR values that are derived within a probabilistic framework with a realistic consideration of regional seismic activity and design ground-motion demands (i.e., consistency between the likelihoods of seismic and engineering demand parameters) would yield more reliable and useful information about the performance of newly designed buildings for future earthquakes.

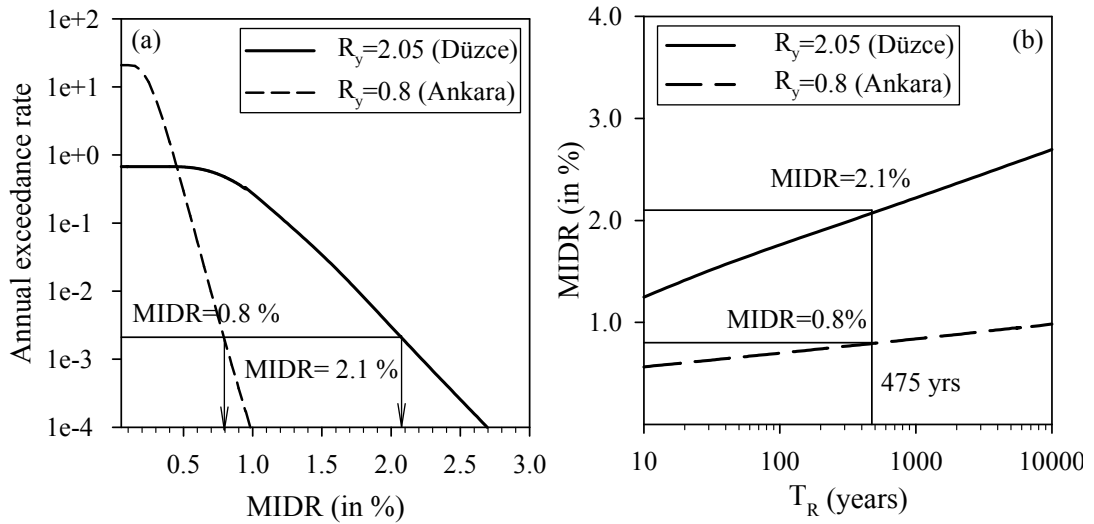


Figure 6.8 MIDR curves for the Düzce and Ankara case studies in terms of (a) annual exceedance rate (b) return period

6.5 Case Studies for the Proposed Seismic Performance Assessment Procedure

The proposed seismic performance assessment procedure is presented by considering the 3-, 5-, and 8-story frame models that are described in Chapter 2. These buildings are designed for the most seismic prone zone (Zone I) according to the Turkish Seismic Zonation Map. To this end, the case studies consider the PSHA results conducted for the city of Düzce for the description of seismic demands. The Düzce PSHA, as discussed in the previous section is repeated for soft soil conditions (Z3; TEC, 2007) because the subject frames are designed for this site class. For completeness, the proposed seismic performance assessment procedure is also repeated by using the code-based design spectrum that describes seismic demands for Zone I and Z3 soil conditions. Figure 6.9 compares the UHS and code-based design spectrum for $T_R=475$ years that are used for the case studies presented in this section. The spectral ordinates of these spectra differ in the short period range but towards longer periods, the two spectra yield very similar spectral acceleration values.

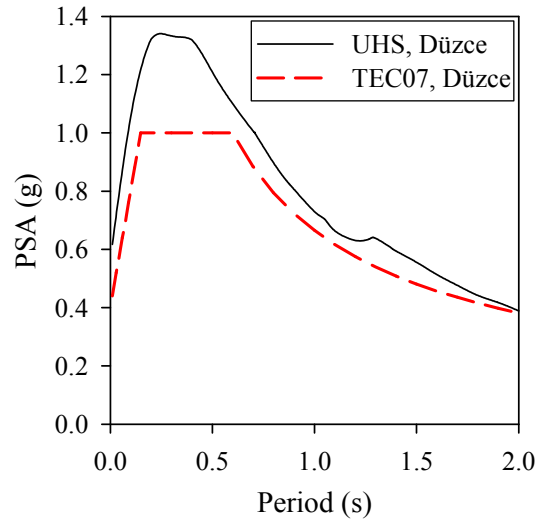


Figure 6.9 UHS versus TEC07 design spectra for $T_R=475$ years for Düzce case study

The global pushover and their idealized forms for the subject buildings are already given in Chapter 3 and they will not be repeated here to prevent repetition. The bilinear idealization of the global capacity curves are done by ATC-40 (ATC, 1996) that is the preferred method in this dissertation. Figure 6.10 shows the idealized pushover curves together with the UHS and code-based spectra in ADRS format. The idealized PO curves and the elastic spectra are used to compute R_y for each building model. R_y values computed from UHS are also illustrated in this figure. The other R_y values that are computed from the code-based spectrum are not shown on Figure 6.10 in order not to crowd the picture. The entire R_y values as well as the other important parameters used in the seismic performance assessment of the frames are given in the Table 6.2.

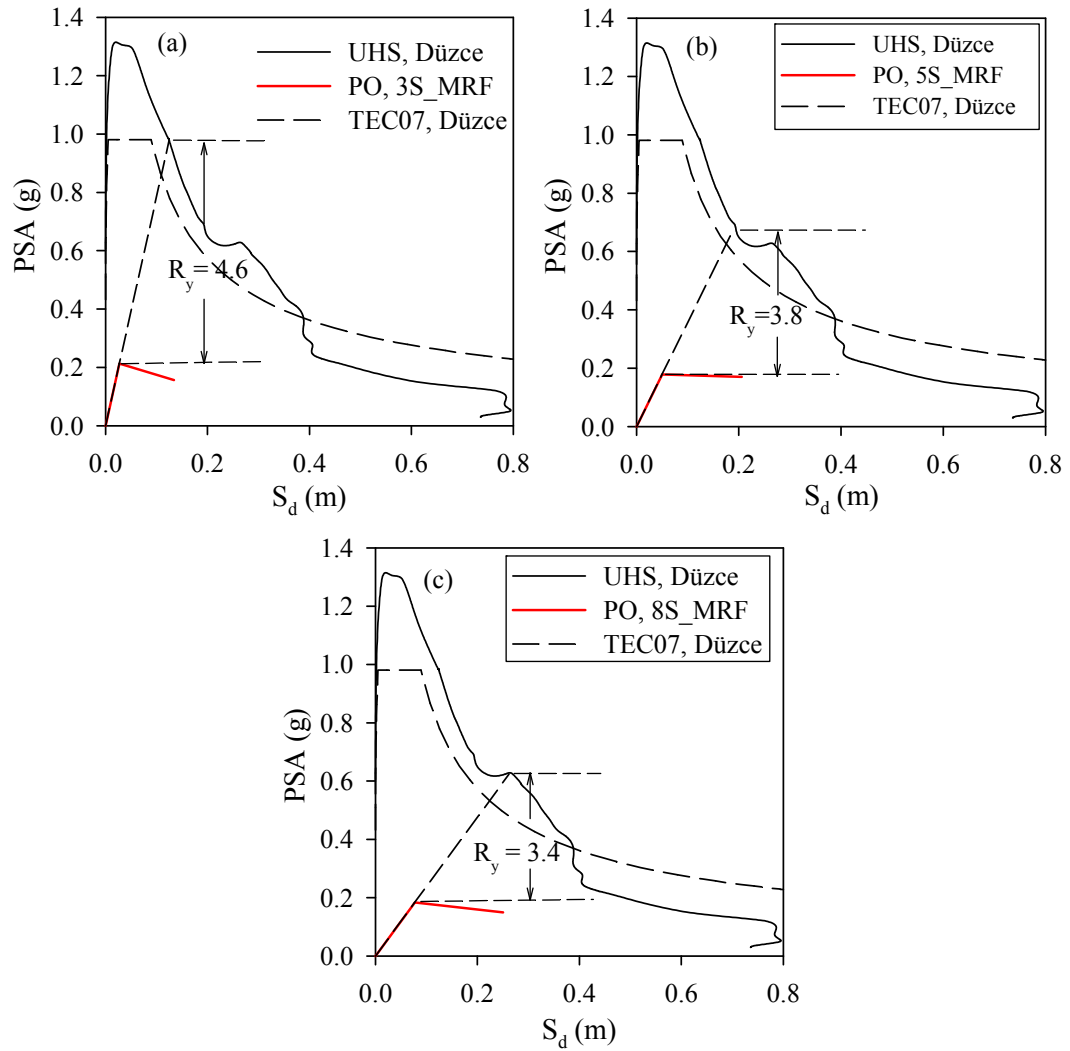


Figure 6.10 Comparison of idealized PO curves of (a) 3S_MRF, (b) 5S_MRF, (c) 8S_MRF with UHS and code-based design spectrum for Düzce in ADRS format

Table 6.2 Important dynamic and structural parameters of 3-, 5- and 8-story frames

Frame ID	Total mass (t)	Fundamental period (T_1)	Effective modal mass factor (α_i)	R	Steel	Concrete	$PSA_{UHS}(T_1)$	$PSA_{TEC07}(T_1)$	$PSA_y(T_1)$	R_y UHS	R_y TEC07	MIDR performance
3S_MRF	251.78	0.71	0.84	8	S420	C20	0.87g	0.98g	0.21g	4.6	4.0	4.65%
5S_MRF	201.65	1.05	0.78	8	S420	C20	0.69g	0.64g	0.18g	3.8	3.5	3.9%
8S_MRF	494.43	1.27	0.77	8	S420	C20	0.64g	0.54g	0.19g	3.4	2.9	3.53%

Figure 6.11 shows the probability-based MIDR versus return period curves computed for the R_y values obtained from UHS. The R_y values of code-based spectrum for the model buildings are close to those of UHS so they are not plotted on this figure. The estimated $MIDR_{performance}$ levels for $T_R=475$ years for the three frames are also given in Figure 6.11. This information together with the $MIDR_{performance}$ estimations for the code-based spectral demands are listed in Table 6.2 as well. The estimated MIDR levels are above 3% for both UHS and code-based spectrum as depicted from Figure 6.11 and Table 6.2. This observation indicates that these buildings would experience structural damage beyond the life safety damage state per provisions described in Turkish Earthquake Code (TEC, 2007). The life safety damage state limit is defined as 3% by this code (Clause 7.5.3 and Table 7.6 in the Turkish Earthquake Code). As a matter of fact the 475-years MIDR estimations of the proposed procedure suggest a near-collapse or collapse state for the 3- and 5-story buildings independent from the spectra used to define seismic demands. This situation is illustrated in Figure 6.12 with the plastic hinge formation of the subject buildings when site-specific UHS are considered. The plastic hinge patterns given in this figure clearly suggest a severe structural damage for all 3 buildings. These plastic hinging patterns show almost the same distributions when the code-based design spectrum is of concern.

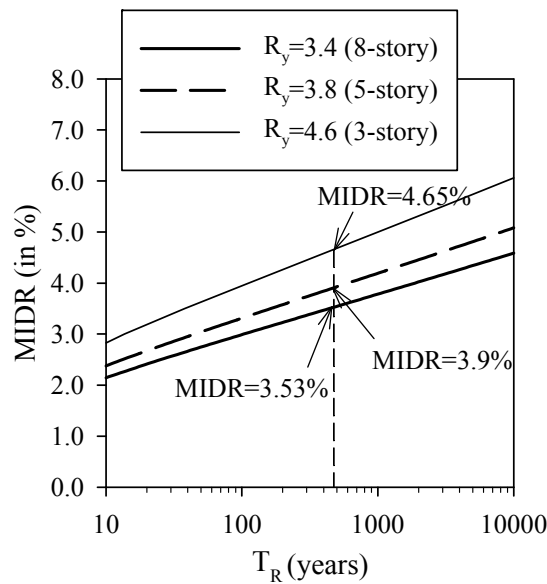


Figure 6.11 Estimated $MIDR_{performance}$ levels for the three frames

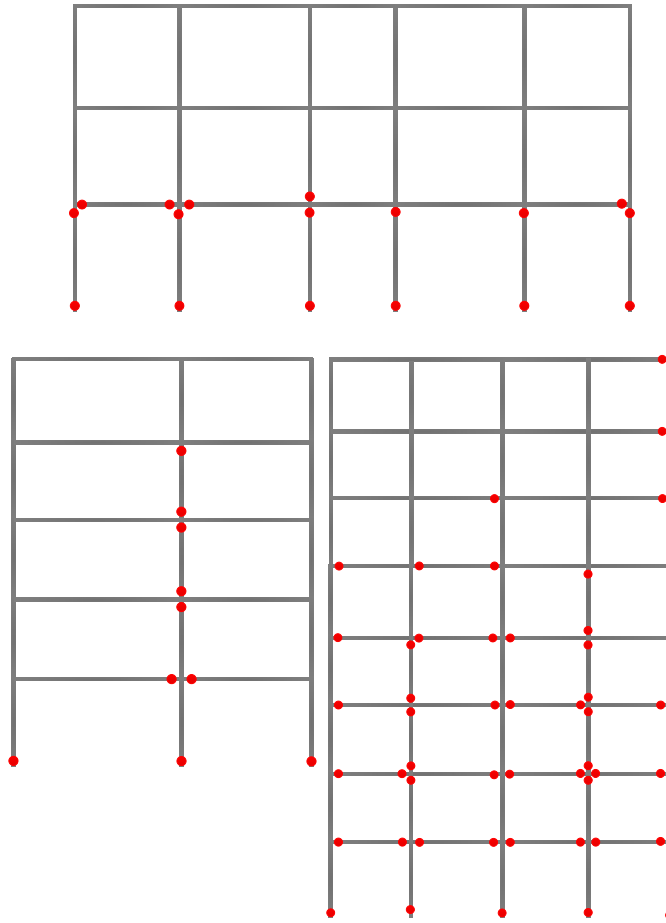


Figure 6.12 Plastic hinge pattern at the estimated $MIDR_{performance}$ for frames 3S_MRF, 5S_MRF and 8S_MRF

The above observations once again indicate the significance of seismic activity and consistency between the seismic and engineering demand parameter definitions at the target hazard level while assessing the seismic performance of structural systems. It is believed that the proposed seismic performance assessment procedure emphasizes these points in a fairly well manner. Note that the considered buildings are code-conforming and satisfy the maximum interstory drift limits for lateral deformations imposed by the Turkish Earthquake Code (TEC, 2007). As discussed in the previous section and various parts of the dissertation these code based limits do not account for the seismic activity in the region of interest. This conceptual deficiency results in incomplete information about the expected structural response under future earthquakes in view of the peculiarities involved in structural behavior and ground-motion intensity.

6.6 Addressing the Uncertainties Inherent in Ground Motions and Structural Response by the Proposed Probability Based Procedure

The subject model buildings of the previous section are used to study the limitations of the proposed seismic performance assessment procedure in capturing the uncertainty in MIDR at different annual exceedance rates due to random nature of ground motions, nonlinear structural response and other unexpected situations such as the variations in soil conditions. To this end, these buildings are assumed to be located on stiff sites (Z2 site class according to TEC, 2007) although they are designed for Z3 soil conditions. The location of buildings is also changed from the central part of the city of Düzce to the town of Konuralp; a district towards the north of Düzce province. These two modifications are believed to address the uncertainties involved in soil conditions as well as the target hazard levels that can be faced while assessing the seismic performance of existing buildings. Nonlinear RHA are conducted using the model buildings for a set of accelerograms that are scaled for different hazard levels (return periods) computed for the location of interest. The MIDR values of nonlinear RHA are then compared with the probabilistic MIDR estimations of the proposed seismic performance assessment procedure to understand its limitations in terms of addressing the uncertainties discussed in this paragraph. The following lines describe the steps followed to achieve this objective.

The probabilistic seismic hazard assessment is carried out once again for the above modifications with the seismic source characteristics described for the Düzce case study in Section 6.4. The same ground-motion prediction equation is used in the repeated PSHA for consistency. The PSHA is conducted for four different return periods; $T_R=225$ years, 475 years, 600 years and 975 years to better observe how the above mentioned uncertainties are handled by the probability-based MIDR estimations. Figure 6.13 displays the computed UHS for the selected return periods. Deaggregation of PSHA results for these return periods through the consideration of fundamental periods of model buildings yield the mode magnitude, source-to-site distance and epsilon values that are listed in Table 6.3. This table depicts that the most contributing earthquake scenarios do not change in terms of mode magnitude and source-to-site distance. They only vary with the changes in return period: smaller fractions of standard deviations are imposed for more frequent ground motion amplitudes.

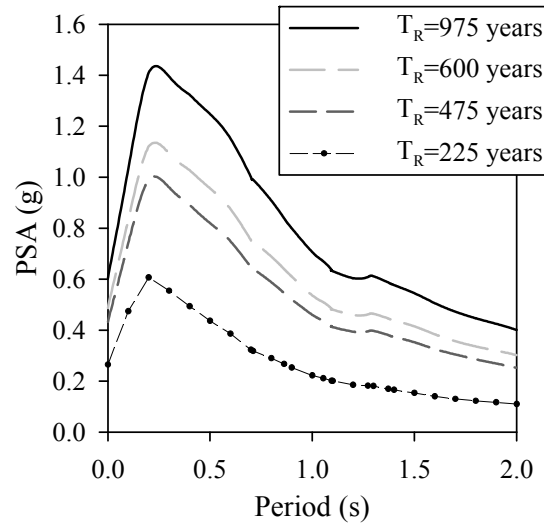


Figure 6.13 UHS for different return periods for the case studies of Section 6.6

Table 6.3 Properties of dominating earthquake scenario and corresponding target spectral acceleration

	3-Story Frame				5-Story Frame				8-Story Frame			
T_R (years)	225	475	600	975	225	475	600	975	225	475	600	975
M_w	7.25	7.25	7.25	7.25	7.25	7.25	7.25	7.25	7.25	7.25	7.25	7.25
R_{jb} (km)	16.25	16.25	16.25	16.25	16.25	16.25	16.25	16.25	16.25	16.25	16.25	16.25
ε	-0.5	0.3	0.5	0.9	-0.7	0.3	0.5	0.9	-0.7	0.3	0.5	0.9
PSA(g) UHS	0.32	0.64	0.75	1.00	0.21	0.43	0.51	0.67	0.18	0.39	0.46	0.61

The most contributing earthquake scenarios for each return period and for each model building are used to compute the conditional mean spectrum (CMS; Baker, 2011) of each particular case. The conditional mean spectra are then utilized for selecting and scaling of ground-motion records from the candidate accelerograms listed in Table 6.4. The ground-motion records listed in Table 6.4 are compiled from the PEER-NGA ground-motion database (http://peer.berkeley.edu/peer_ground_motion_database). These accelerograms consist of two horizontal components, and their magnitudes are within ± 0.25 magnitude range of the mode magnitude computed from deaggregation analyses. The soil conditions of the accelerograms are either Z2 (NEHRP C) or Z3 (NEHRP D) and their style-of-faulting is exclusively strike-slip. The source-to-site distances (R_{jb}) are generally close to the mode distance obtained from the deaggregation analyses although there are some exceptional recordings with distances approximately 2 to 3 times of mode distance. The overall features

of the compiled candidate ground-motion dataset comply with the record selection criteria proposed by Stewart et al. (2001).

Table 6.4 Major seismological properties of the candidate ground-motion set

Records Number	M_w	R_{jb} (km)	Site Class	Fault Type*
PEER1787	7.13	10.35	NEHRP C	SS
PEER1794	7.13	31.06	NEHRP C	SS
PEER1836	7.13	42.06	NEHRP C	SS
PEER1614	7.14	11.46	NEHRP C	SS
PEER1616	7.14	23.41	NEHRP C	SS
PEER1618	7.14	8.03	NEHRP C	SS
PEER0864	7.28	11.03	NEHRP C	SS
PEER0838	7.28	34.86	NEHRP C	SS
PEER0881	7.28	17.32	NEHRP D	SS
PEER0015	7.36	38.42	NEHRP C	SS
PEER1633	7.37	12.56	NEHRP C	SS
PEER1636	7.37	49.97	NEHRP D	SS
PEER1148	7.51	10.56	NEHRP C	SS
PEER1162	7.51	31.74	NEHRP C	SS
PEER1166	7.51	30.74	NEHRP D	SS

* SS stands for strike-slip faulting mechanism

For each T_R -building-CMS combination the above candidate ground-motion dataset is subjected to stripe scaling (Jalayer et al., 2007) that scales each accelerogram to the CMS spectral ordinate at the fundamental period. The scaled accelerograms are ranked through the sum of squared errors (SSE) statistical measure to identify a suite of 7 scaled accelerograms having the most similar spectral shapes to the considered CMS within the period interval of $0.2T_1 \leq T < 2T_1$ (Baker, 2011). The suits of accelerograms assembled for the entire T_R -building-CMS combination are given in Table 6.5. Figures 6.14 to 6.16 show the pseudo acceleration response spectra of scaled accelerograms, their average and target CMS for each T_R -building-CMS combination. The plots in these figures depict that the target CMS and average spectrum of scaled accelerograms almost overlap with each other within the period range of $0.2T_1 \leq T < 2T_1$ (designated by blue dashed lines). This observation suggests the implemented scaling procedure.

Table 6.5 Final list of accelerograms that are used in nonlinear RHAs

Frame ID	Return Period (years)	Record Number						
3S_MRF	225	PEER1148	PEER1636	PEER1794	PEER1633	PEER1836	PEER0015	PEER1162
	475	PEER1148	PEER0881	PEER1794	PEER1633	PEER0838	PEER0015	PEER1616
	600	PEER1148	PEER0881	PEER1794	PEER1633	PEER0838	PEER0015	PEER1616
	975	PEER1148	PEER0881	PEER1794	PEER0864	PEER0838	PEER0015	PEER1616
5S_MRF	225	PEER1148	PEER0881	PEER1162	PEER1633	PEER1836	PEER0015	PEER1616
	475	PEER1148	PEER0881	PEER1162	PEER1633	PEER0864	PEER0015	PEER1616
	600	PEER1148	PEER0881	PEER1162	PEER1633	PEER0864	PEER0015	PEER1616
	975	PEER1148	PEER0838	PEER1162	PEER1787	PEER0864	PEER0015	PEER1616
8S_MRF	225	PEER1148	PEER0838	PEER1162	PEER1836	PEER1614	PEER0015	PEER1636
	475	PEER1148	PEER0838	PEER1162	PEER0881	PEER1166	PEER0015	PEER1616
	600	PEER1148	PEER0838	PEER1162	PEER0881	PEER1166	PEER0015	PEER1616
	975	PEER1148	PEER0838	PEER1162	PEER0881	PEER1166	PEER0015	PEER1616

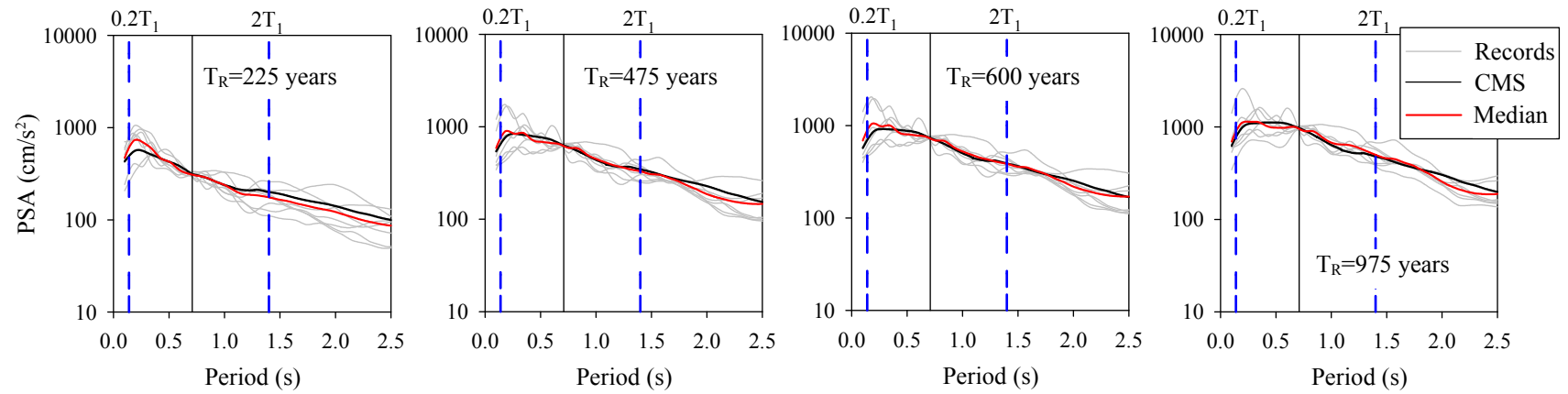


Figure 6.14 Pseudo acceleration response spectra of scaled accelerograms of 3-story building for CMS computed for different return periods

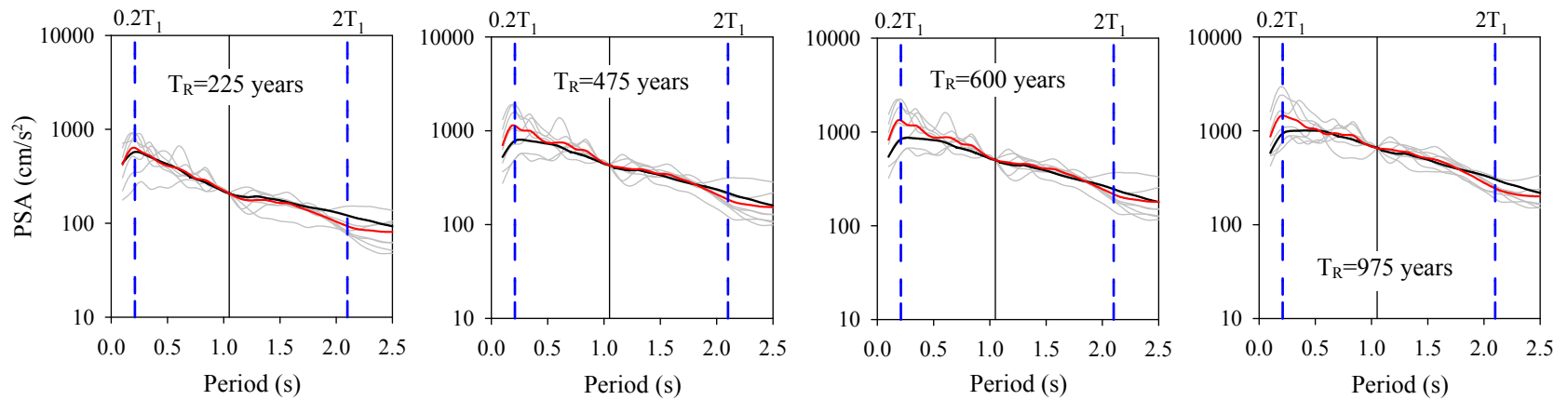


Figure 6.15 Pseudo acceleration response spectra of scaled accelerograms of 5-story building for CMS computed for different return periods

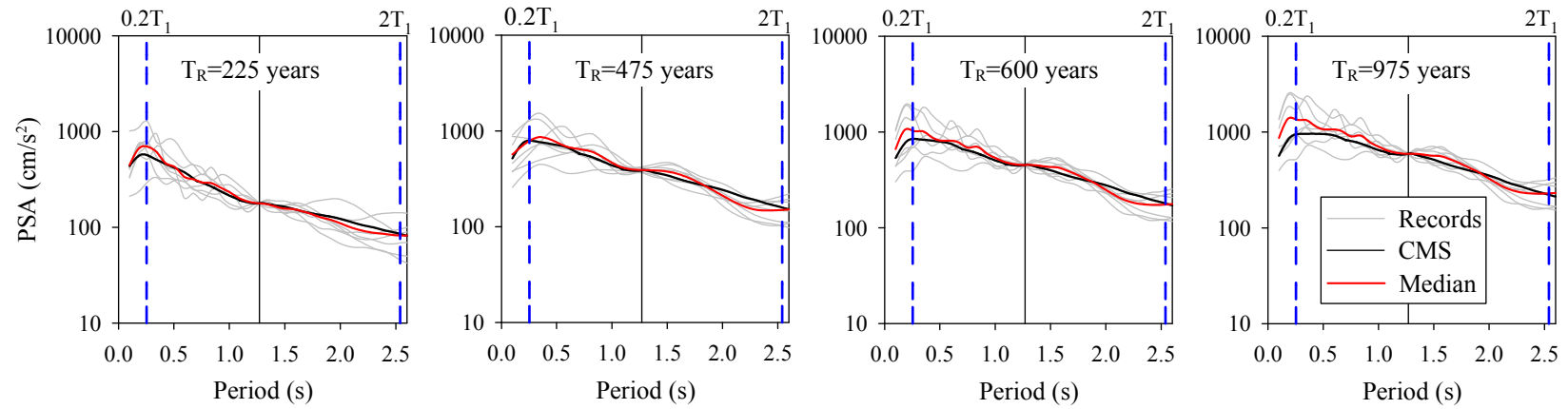


Figure 6.16 Pseudo acceleration response spectra of scaled accelerograms of 8-story building for CMS computed for different return periods

The scaled ground motions for each T_R -building-CMS combination are used in the nonlinear RHA to compute the MIDR values. The MIDR values from nonlinear RHA are compared with the probability-based MIDR curves computed from the proposed seismic performance assessment procedure. The R_y values required for the computation of probability-based MIDR curves are obtained by comparing the idealized pushover curve of model buildings with the corresponding CMS in ADRS format. This step is identical to the ones that are already presented in Figures 6.7 and 6.10. The only difference between the current case and the others is the use of CMS instead of UHS. Note that the spectral acceleration at the fundamental building period is the same for CMS and UHS due to the definition of CMS. Thus, CMS or UHS that represent the same return periods would yield the same R_y value. The use of CMS in this section is for proper selection and scaling of ground-motion records as this spectrum type results in a more realistic representation of ground-motion demand for the most contributing earthquake scenario (Baker, 2011; Baker and Cornell, 2006). Figures 6.17 to 6.19 compare the probability-based MIDR curves from the proposed procedure with the MIDR scatters computed from nonlinear RHA for each building. The outlier MIDR values ($MIDR > 6\%$) obtained from nonlinear RHA are excluded from the comparison. It is believed that such big MIDR values cannot be experienced by actual frame buildings. Moreover this study disregards such outliers in the derivation of MIDR predictive model that constitutes the backbone of the proposed seismic performance assessment procedure (see the relevant discussions in Chapter 3).

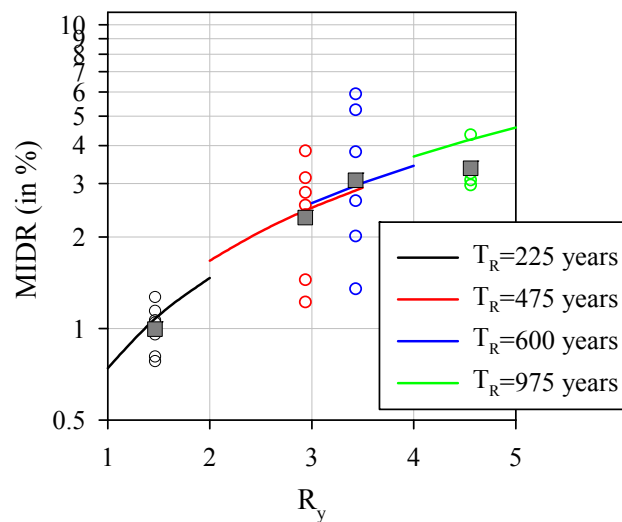


Figure 6.17 Probabilistic MIDR curves computed for distinct R_y values that correspond to different target hazard levels (or return periods) for 3-story model building. Their comparisons with the corresponding MIDR values of nonlinear RHA that are obtained from the scaled accelerogram of the same target hazard levels. The median MIDR for each scatter group is designated by solid square in these plots

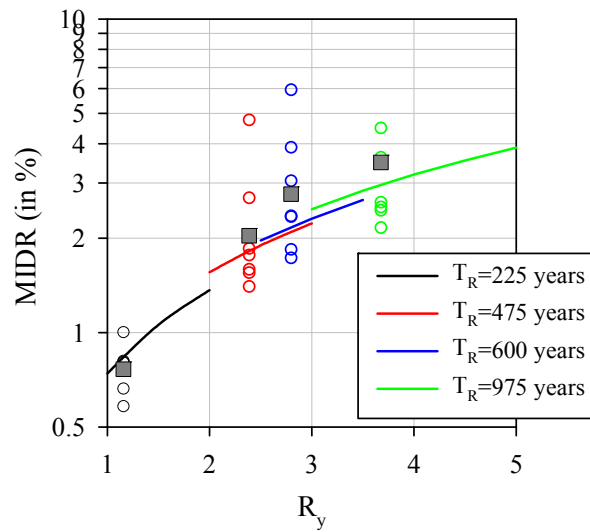


Figure 6.18 Probabilistic MIDR curves computed for distinct R_y values that correspond to different target hazard levels (or return periods) for 5-story model building. Their comparisons with the corresponding MIDR values of nonlinear RHA that are obtained from the scaled accelerogram of the same target hazard levels. The median MIDR for each scatter group is designated by solid square in these plots

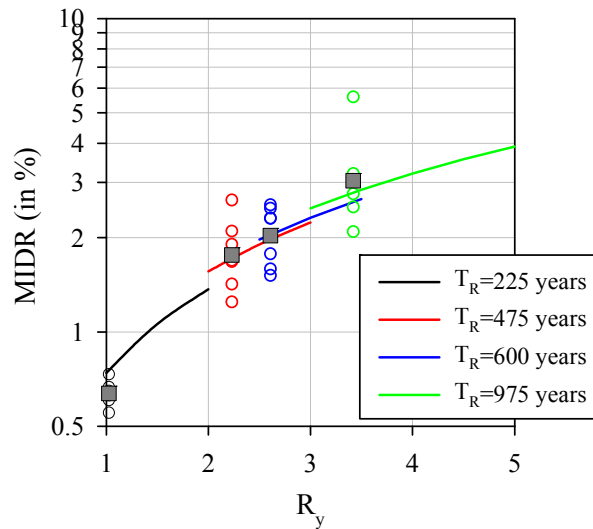


Figure 6.19 Probabilistic MIDR curves computed for distinct R_y values that correspond to different target hazard levels (or return periods) for 8-story model building. Their comparisons with the corresponding MIDR values of nonlinear RHA that are obtained from the scaled accelerogram of the same target hazard levels. The median MIDR for each scatter group is designated by solid square in these plots

The comparative plots indicate that given a hazard level (i.e., return period) the probability-based MIDR estimations (shown as solid lines on the plots) that correspond to predefined T_R -building-CMS combinations agree well with the median values of pertinent nonlinear RHA MIDR scatters (shown as vertical stripes on the figures). However, the MIDR scatters of nonlinear RHA show dispersive behavior about their median and inherently this variation cannot be captured by the probability-based MIDR estimations. This observation may suggest a more rigorous modelling of MIDR predictive model by incorporating other important structural features. Such a model update in the functional form of MIDR predictive model requires additional studies to identify the other robust structural parameters to improve the MIDR estimations. The other alternative is the derivation of similar predictive models by using other functional forms with different estimator parameters and different strong motion databases so that the modeling uncertainty can be reduced with logic-tree applications (similar to PSHA) to compute different fractiles of probabilistic MIDR estimations. Nevertheless, the close proximity of median values of MIDR scatters and probability-based MIDR estimations still makes the proposed procedure as a useful tool to guide the experts for defining more realistic MIDR demands that consider seismic activity and nonlinear building behavior.

CHAPTER 7

SUMMARY AND CONCLUSIONS

7.1 Summary

This dissertation proposed two probability-based methodologies that can be utilized for seismic design of new buildings and seismic performance assessment of existing buildings. The methodologies are developed for code-confirming reinforced concrete frame type typical low-rise and mid-rise Turkish buildings as an auxiliary tool for the design and assessment procedures provided by the Turkish Earthquake Code (TEC, 2007). The main objective of the proposed methodologies is realistic quantification of nonlinear structural demands using a probabilistic framework that accounts for the level of seismicity, record-to-record variability and uncertainties in structural response. To this end, the proposed methodologies utilize probabilistic seismic demand analysis (PSDA) that aims at estimating earthquake induced structural displacements in a probabilistic manner. Among three alternative PSDA approaches, the proposed methodologies are based on a structure-specific attenuation relationship for a selected engineering demand parameter (EDP; maximum interstory drift ratio, MIDR). This approach is originally proposed by Shome and Cornell (1999) that suggests an EDP predictive model as a function of seismological parameters such as magnitude, source-to-site distance. In this dissertation, Shome and Cornell's proposition is further improved by implementing a structural parameter (strength reduction factor, R_y) to the structure-specific MIDR predictive model in order to account for structural response uncertainties in a more rational way. This study selects MIDR as the decisive EDP due its success in correlating structural as well as non-structural damage. As PSDA constitutes the core of the proposed methodologies, the key product is the estimation of annual exceedance rates of MIDR demands at predefined levels. This way, for a given annual exceedance rate (or return period), the corresponding target MIDR demand is estimated probabilistically. The estimated MIDR demands are utilized to assess seismic performance of buildings. The proposed methodologies make use of nonlinear static analysis results to determine damage states of structural members at the target MIDR demand. Damage states and performance level of buildings are determined by following the performance assessment rules given in the Turkish Earthquake Code (TEC, 2007).

Under the main objectives of this study, a statistical study is carried out first to investigate general characteristics of Turkish building stock using the blueprints of 333 RC residential buildings from the Bakırköy district in İstanbul. Within the scope of the statistical study, the buildings are examined for their various geometrical aspects such as floor dimensions, story heights, member sizes, number of continuous and discontinuous frames and decrease in column area with story numbers. From the compiled building inventory, 6 floor plans are selected and modified on the basis of the statistical results. A total of 6 reinforced concrete (RC) buildings are designed with story numbers varying between 3 and 9 in accordance with the Turkish standards; TS 500-2000 (Turkish Standards Institute, 2000), TS 498 (Turkish Standards Institute, 1997) and Turkish Earthquake Code (TEC, 2007). The buildings are assumed to be located at a site in seismic Zone I with Z3 soil classification (TEC; 2007). From each building, a representative continuous frame is selected for nonlinear response history analysis (RHA) conducted throughout this study.

The selected frames are analytically modelled and nonlinear RHA are conducted using a total of 628 ground motions (314 two-component horizontal accelerograms). A total of 3768 nonlinear RHA are carried out and the maximum MIDR of two horizontal ground-motion components is taken into account. When one of the horizontal component results a collapse of building at the early stages of analysis or gives an outlier result above 6% of MIDR demand, the results of the other component is considered in the study. Log-normality of MIDR demands is examined using several goodness-of-fit tests. The MIDR demands are investigated in terms of magnitude and distance bins and for each considered parameter (i.e., moment magnitude, M_w ; source-to-site distance, R_{jb} ; site class, NEHRP C and D; style-of-faulting, SoF; fundamental period, T_1 and number of stories). The analysis of variance (ANOVA) tests are carried out to investigate the significance of these parameters on MIDR demands.

Nonlinear static analyses are conducted using the entire frame set by applying first mode compatible invariant lateral load pattern. By making use of pushover curves, the multi-degree-of-freedom (MDOF) models are converted to equivalent single-degree-of-freedom (SDOF) systems using several idealization methods (i.e., ATC-40, 1996; FEMA-356, 2000; ASCE/SEI 41-06, 2007). On the basis of statistical analysis results, ATC-40 idealization method is considered as the most accurate NSP in terms of strength reduction factor compared to other methods and the R_y results based on ATC-40 are utilized in the development of MIDR model. The log-normality assumption of R_y is also examined using goodness-of-fit tests. The influence of fundamental period and number of stories on R_y demands is quantified using ANOVA tests. The correlation between R_y values and MIDR demands is investigated in detail. The overstrength factors of the frames are estimated by comparing the idealized capacity curves and code-based design spectrum.

In order to emphasize the conceptual differences between the current approximate MIDR expressions and the one proposed in this study, three approximate methods that use spectral ordinates for MIDR estimations (i.e., Miranda, 1999; Akkar et al., 2005; Medina

and Krawinkler, 2005) are investigated in a comparative study using nonlinear RHA results. Under the light of observations made from their performances, the MIDR predictive model is developed on the basis of regression analysis using one-stage maximum likelihood method of Joyner and Boore (1993). The MIDR predictive model that is developed as a function of M_w , R_{jb} , stiff and soft site conditions (NEHRP C and D) and R_y produces the median MIDR estimations and considers aleatory variability with a standard deviation term. In this sense, the proposed MIDR predictive model differs significantly from other approximate methods as the functional form enables its use in probability based approaches.

The MIDR predictive model is implemented into the PSDA for constant R_y and predefined site class by making use of the total probability theorem. The proposed methodologies first calculate the uniform hazard spectrum (UHS) for the return period of concern considering the seismic sources in the proximity of the building. In case of a new building, the design methodology recommends to follow the instructions given in the Turkish Earthquake Code (TEC, 2007) in the design process of buildings. The pushover (PO) curve of the designed building is then calculated and idealized following a nonlinear static procedure (NSP). By making use of the UHS for the given site, the strength reduction factor, R_y is estimated according to the yield acceleration of the idealized PO curve. The target MIDR demand is then calculated for the same return period by conducting PSDA considering the same seismic sources, site conditions and R_y . The proposed methodologies determine the damage states of structural members using pushover analysis results at the step where target MIDR demand is first reached at a story. For assessing the seismic performance of existing buildings, the proposed procedures recommend to follow the performance assessment rules of the Turkish Earthquake Code (TEC, 2007) by making use of target MIDR to identify the damage states of structural members individually. The global performance is then determined considering the damage states of the structural members and the minimum performance levels for the given return period. Based on the nonlinear RHA results, a simple relationship is also presented between MIDR and maximum roof drift ratio (MRDR). On this basis of this relationship, using the total probability theorem an MRDR expression is also presented as an alternative for its use in the design and performance assessment.

The final part of the thesis presents the application of the proposed methodologies on new and existing buildings for code-complying frames with two case studies. The efficiency of the proposed seismic assessment methodology is examined through a comparative study that is carried out using 3-, 5- and 8- story frames. The MIDR demands of the selected frames are calculated using the proposed methodology and nonlinear RHA using 7 ground motions that are selected and scaled using conditional mean spectrum (CMS) at 4 return period levels (i.e., 225, 475, 600, 975 years). Under the observations made on the results, the physical limitations of the proposed methodologies are highlighted and future needs are discussed.

7.2 Conclusions and Contributions

The main conclusions drawn in this dissertation are given below.

- i. The collected results from nonlinear RHA indicate the significance of seismicity level, randomness of earthquakes and uncertainties in structural response. This observation indicates that one should account for these factors in order to evaluate nonlinear structural response in a reliable manner.
- ii. The influence of magnitude and source-to-site distance is significant on MIDR results. It is shown that the approximate MIDR models investigated in this study produce biased results as they do not account for these seismological parameters. In this sense, the sufficiency requirement defined by Luco et al. (2007) is not met by these approximate methods. On the other hand, the proposed MIDR predictive model is capable of producing unbiased results as it is based on the important seismological estimator parameters as well as the structural response parameter R_y .
- iii. MIDR is well correlated with strength reduction factor, R_y . Although conversion of backbone curve (PO curve) to bilinear representation is straightforward for first mode dominant structures, selecting the most suitable linearization method is essential as this study recommends the use of ATC-40 (ATC, 1996) method.
- iv. Confined to the period and story number ranges covered by the frame models utilized in this study, the influence of period and number of stories on the MIDR demands is insignificant. Site class effect is visible on MIDR demands. The MIDR results indicate that in general soft sites produce larger MIDR demands compared to stiff sites. The ANOVA tests indicate that one cannot overlook this parameter when estimating nonlinear structural demands. Style-of-faulting (SoF) seems to be insignificant on MIDR demands that is concluded from the ANOVA tests. However, this observation may have reservations as the compiled strong-motion database lacks of a uniform SoF distribution in the magnitude and distance ranges considered in this study.
- v. The proposed methodologies enable to quantify seismic performance of new and existing buildings in a more realistic way by considering the level of seismicity, record-to-record variability and uncertainties in structural response. In this sense, the proposed methodologies significantly differ from the current nonlinear static procedures (NSPs) that estimate target MDOF demands (i.e., roof displacement) using equivalent single-degree-of-freedom (SDOF) system approximation. Firstly, the direct estimation of EDP (MIDR in this case) from seismological and structural parameters eliminates the intensity-measure (spectral quantities or peak ground acceleration and velocity) based relationship between seismic hazard and target structural demands. Moreover, the MIDR estimations from the proposed approach minimizes the errors incorporated by SDOF approximation as well. Secondly, the proposed methodologies

consider uncertainties in structural response and record-to-record variability that are inherently overlooked by NSPs.

- vi. Although nonlinear response history analysis (RHA) yields more accurate results compared to NSPs, it is challenging as it requires proper knowledge on ground motion selection and scaling. The selection of target spectrum (e.g., UHS, CMS) as well as the ground motion selection and scaling method significantly affect the level of record-to-record variability incorporated in the results. In this sense, the proposed methodologies present a simpler way when compared to RHA for estimating nonlinear structural demands. It also improves the reliability of results by properly accounting for record-to-record variability as well as uncertainties in structural response.
- vii. The case studies show that the frame models that are assumed to be located at high seismic regions (Zone I according to the Turkish Earthquake Code) are subjected to large MIDR demands. Although these frames are designed in accordance with the Turkish Earthquake Code (TEC, 2007), none of them conforms the expected performance level (i.e., life safety) under a proper designing. This observation indicates that the design approach of the Turkish Earthquake Code (TEC, 2007) that accounts for deterministic MIDR limits can lead to unsafe design. This remedy for such deficiencies can be putting more emphasis on probability based design process that can convey reliable information on the seismic performance of buildings.
- viii. This study proposes a relationship between MIDR and MRDR. This relationship is utilized to construct a second PSDA methodology on the basis of MRDR. As the main focus of this dissertation is MIDR rather than MRDR, the performance of MRDR based methodology is not examined in a detailed manner. In this sense, MRDR based seismic performance is subject to further studies.
- ix. This study also presents a software to conduct PSDA using the proposed MIDR predictive model. The developed software given in Appendix D has a graphical user interface (GUI) that enables estimating annual exceedance curve for MIDR in a simple way. The PSDA software is open to improvements and implementations of new features and believed to be helpful for researchers working on this area.

7.3 Limitations and Future Work

The proposed MIDR predictive model can be utilized for code-complying typical RC Turkish buildings with number of stories 3-9 and period range of $0.7s < T_1 < 1.4s$. The ground motion library utilized in this study is limited to magnitudes $5.0 \leq M_w < 7.7$, source-to-site distances $0 \leq R_{jb} < 100$ km and site classes NEHRP C and D. The application of the proposed methodologies outside the defined fundamental period, total story number range as well as other site conditions (e.g., rock, very soft) is subject to further studies. The

proposed MIDR predictive model is based on three important seismological parameters (i.e., moment magnitude, M_w ; source-to-site distance, R_{jb} ; and site class) and single structural parameters (i.e., strength reduction factor, R_y). The predictive model can be improved by incorporating other seismological and structural estimator parameters. The number of predictive models can be increased by considering different functional forms, different building types and strong-motion databases. Moreover, regional and structural-type dependent predictive models can improve the accuracy and applicability of this model. These improvements and numerical accuracy of the MIDR predictive models will help to reduce the modeling uncertainty with logic-tree applications. This way for a given annual exceedance rate, PSDA will provide several MIDR values that can be represented by a probability distribution (e.g., normal, lognormal). This information can lead to estimation of target MIDR demands for different fractiles. Accordingly, one can design buildings considering the response above central estimations (e.g., 86% percentile) of MIDR that is particularly important for important buildings. The proposed methodologies can also be extended to probabilistic seismic damage and loss analysis. This way, quantitative knowledge on structural performance, damage and loss is provided for the given level of seismic risk. This information is helpful to building owners or stakeholders to make rational decisions on the expected performance of buildings.

REFERENCES

Akka, S., Yazgan, U., and Gulkan, P., (2005). Drift estimates in frame buildings subjected to near-fault ground motions, *Journal of Structural Engineering-ASCE*, Vol. 131(7), 1014-1024.

Akka, S., and Bommer, J.J., (2010). Empirical equations for the prediction of PGA, PGV, and spectral accelerations in Europe, the Mediterranean Region, and the Middle East, *Seismological Research Letters*, Vol. 81 (2), 195-206.

Akka, S., Douglas, J., Di Alessandro, C., Campbell, K., Somerville, P., Cotton, F., Silva, W., and Baker, J., (2012). Defining a consistent strategy to model ground-motion parameters for the GEM-PEER Global GMPEs Project. *15th World Conference on Earthquake Engineering*, Lisbon, Portugal.

Akka, S., and Özen, Ö., (2005). Effect of peak ground velocity on deformation demands for SDOF systems, *Earthquake Engineering and Structural Dynamics*, Vol. 34 (13), 1551-1571.

Algan, B. B., (1982). Drift and damage considerations in earthquake resistant design of reinforced concrete buildings, Ph.D. Thesis, Department of Civil Engineering, University of Illinois, Urbana, Illinois, 480 pp.

American Society of Civil Engineers (ASCE), (2007). ASCE/SEI 41-06 Seismic Rehabilitation of Existing Buildings, Reston, VA, 411 pp.

American Society of Civil Engineers (ASCE), (2010). ASCE/SEI 7-10, Minimum design loads for buildings and other structures, Reston, VA, 247 pp.

Ang, A. H.-S., and Tang, W. H., (1975). Probability concepts in engineering planning and design, Vol 1, New York, Wiley.

Applied Technology Council, ATC (1996). ATC-40, Seismic evaluation and retrofit of concrete buildings, Report No: SSC 96-01, Redwood City, CA.

Applied Technology Council, ATC (2004). FEMA-440 Improvement of Nonlinear Static Seismic Analysis Procedures, ATC-55 Project Report, prepared by the Applied Technology Council for the Federal Emergency Management Agency, Washington, DC.

Aslani, H., and Miranda, E., (2005). Probability-based seismic response analysis, *Engineering Structures*, Vol. 27(8), 1151-1163.

Ay, B. Ö., (2006). Fragility Based Assessment of Low-Rise and Mid-Rise Reinforced Concrete Frame Buildings in Turkey, M.Sc. Thesis, Department of Civil Engineering Middle East Technical University, Ankara, 145 pp.

Baker, J. W., and Cornell, C. A., (2004). Choice of a vector of ground motion intensity measures for seismic demand hazard analysis, *Proceedings of the 13th World Conference on earthquake Engineering, Vancouver, B.C., Canada*, on CD-ROM.

Baker, J. W., and Cornell, C. A., (2005). A vector-valued ground motion intensity measure consisting of spectral acceleration and epsilon, *Earthquake Engineering and Structural Dynamics*, Vol. 34 (10), 1193-1217.

Baker J. W., and Cornell C. A., (2006). Spectral shape, record selection and epsilon, *Earthquake Engineering and Structural Dynamics*, Vol. 35(9), 1077-1095.

Baker J. W., (2008). An introduction to Probabilistic Seismic Hazard Analysis (PSHA), Version 1.3.

Baker, J.W., (2011). Conditional Mean Spectrum: Tool for ground-motion selection, *Journal of Structural Engineering (ASCE)*, Vol. 137 (3), 322-331.

Bazzurro, P., and Cornell, C. A., (1994). Seismic hazard analysis of nonlinear structures. I: Methodology, *Journal of Structural Engineering (ASCE)*, Vol. 120(11), 3320-3344.

Bazzurro, P., (1998). Probabilistic seismic demand analysis. Stanford University, Stanford, CA, Ph.D. Thesis, 329 pp.

Bertero, R. D., and Bertero, V. V., (2000). Application of a comprehensive approach for the performance-based earthquake-resistant design buildings, *12th World Conference on Earthquake Engineering*, Auckland.

Blume, J. A., (1968). Dynamic characteristics of multi-story buildings. *J. Struct. Div. ASCE*, 94(2), 377-402.

Bommer, J. J., Douglas, J., and Strasser, F. O., (2003). Style-of-Faulting in Ground-Motion Prediction Equations, *Bulletin of Earthquake Engineering*, Vol. 1(2), 171-203.

Bommer, J. J., and Abrahamson, N. A., (2006). Why do modern probabilistic seismic-hazard analyses often lead to increased hazard estimates?, *Bulletin of the Seismological Society of America*, Vol. 96(6), 1967-1977.

Boore, D. M., (2004). Can site response be predicted?, *Journal of Earthquake Engineering*, Vol. (8), 1-41.

Borzi B., Pinho, R., and Crowley, H. (2008). Simplified pushover-based vulnerability analysis for large-scale assessment of RC buildings, *Engineering Structures*, Vol. 30(3), 804-820.

Bozorgnia, Y., and Bertero, V. V., (2001). Improved shaking and damage parameters for post-earthquake applications, *Proceedings of the SMIP01 Seminar on Utilization of Strong-Motion Data*, Los Angeles, California, September 12, 1-22.

Bradley, B.A. and Dhakal, R.P., (2008). Error estimation of closed-form solution for annual rate of structural collapse. *Earthquake Engineering and Structural Dynamics*, Vol. 37(15), 1721-1737.

Building Seismic Safety Council (BSSC), (2009). FEMA P-750, NEHRP recommended provisions for seismic regulations for new buildings and other structures, Washington, DC.

Chopra, A.K., and Chintanapakdee, C. (2001). Drift spectrum versus modal analysis of structural response to near-fault ground motions, *Earthquake Spectra*, Vol. 17(2), 221-234.

Collins, K. R., Wen, Y. K., and Foutch, D. A., (1996). Dual-level seismic design: A reliability-based methodology, *Earthquake Engineering & Structural Dynamics*, Vol. 25(12), 1433-1467.

Cordova, P.P., Deierlein, G.G., Mehanny, S.S.F. and Cornell, CA., (2000). Development of a two-parameter seismic intensity measure and probabilistic assessment procedure, *The Second U.S.-Japan Workshop on Performance-Based Earthquake Engineering Methodology for Reinforced Concrete Building Structures*, Sapporo, Hokkaido, Japan.

Cornell, C. A., (1968). Engineering seismic risk analysis, *Bulletin of the Seismological Society of America*, Vol. 58(5), 1583-1606.

Cornell, C. A., (1971). Probabilistic analysis of damage to structures under seismic load, *Dynamic Waves in Civil Engineering*, J. Wiley and Sons, N.Y.

Cornell, C. A., (1996). Calculating building seismic performance reliability; A basis for multi-level design norms, *Proc. Eleventh World Conference on Earthquake Engineering*, Acapulco, Mexico.

Cornell, C.A., and Krawinkler, H., (2000). Progress and challenges in seismic performance assessment. PEER Center News, 3 (2) <http://peer.berkeley.edu/news/2000spring/performance.html> (accessed March 2013).

Dym, C. L., and Williams, H. E. (2007). Estimating fundamental frequencies of tall buildings, *Journal of Structural Engineering*, Vol. 133(10), 1479-1483.

Erdik, M., and Durukal E., (2003). Damage to and Vulnerability of Industrial Facilities in the 1999 Kocaeli, Turkey Earthquake. Building Safer Cities: The Future of Disaster Risk, A. Kreimer, M. Arnold, A. Carlin, Editors, Disaster Management Series No.3, The World Bank, Washington, 289-291.

Eroğlu, T., and Akkar, S., (2011). Lateral stiffness estimation in frames and its implementation to continuum models for linear and nonlinear static analysis, *Bulletin of Earthquake Engineering*, Vol. 9(4), 1097-1114.

European Committee for Standardization (CEN), (2004). Eurocode 8: Design of structures for earthquake resistance-Part 1: General rules, seismic actions and rules for buildings, EN1998-1, Brussels.

Federal Emergency Management Agency, (2000). Prestandard and Commentary for the Seismic Rehabilitation of Buildings, FEMA-356, American Society of Civil Engineers, Reston, Virginia.

Freeman S.A., Nicoletti J.P., and Tyrell J.V., (1975). Evaluations of Existing Buildings for Seismic Risk: A case study of Puget Sound Naval Shipyard, Bremerton. Proceedings of First U.S. NCEE, EERI, Berkeley, Washington, 113-122.

Gengshu, T., Pi, Y.-L., Bradford, M.A., and Tin-Loi, F. (2008). Buckling and second-order effects in dual shear-flexural systems. *Journal of Structural Engineering*, Vol. 134(11), 1726-1732.

Ghobarah, A., (2004). On drift limits associated with different damage levels, *Performance-Based Seismic Design Concepts and Implementation, Proceedings of an International Workshop*, Bled, Slovenia, June 28-July 1 (Editors, Peter Fajfar and Helmut Krawinkler), PEER Report, 2004/05, 321-333.

Goulet, C. A., Haselton, C. B., Mitrani-Reiser, J., Beck, J. L., Deierlein, G. G., Porter, K. A., and Stewart, J. P., (2007). Evaluation of the seismic performance of a code-conforming reinforced-concrete frame building-from seismic hazard to collapse safety and economic losses, *Earthquake Engng. Struct. Dyn.*, Vol. 36(13), 1973-1997.

- Gupta, A., and Krawinkler, H., (1999). Seismic demands for performance evaluation of steel moment resisting frame structures, *John A. Blume Earthquake Engineering Center Rep. No. 132*, Department of Civil and Environmental Engineering, Stanford University, Stanford, California, 368 pp.
- Gülkan, P., and Sözen, M.A. (1999). Procedure for determining seismic vulnerability of building structures, *ACI Structural Journal*, Vol. 96(3), 336-342.
- Gülkan, P., and Akkar, S., (2002). A simple replacment for the drift spectrum, *Engineering Structures*, Vol. 24(11), 1477-1484.
- Han, S. W., and Wen, Y. K., (1997). Method of reliability-based seismic design. I: Equivalent nonlinear systems, *Journal of Structural Engineering*, Vol. 123(3), 256-263.
- Heaton, T. H., Hall, J. F., Wald, D. J., and Halling, M. W., (1995). Response of Highrise and Base-Isolated Buildings to a Hypothetical M_w 7.0 Blind Thrust Earthquake, *Science*, New Series, Vol. 267(5195), 206-211.
- Heidebrecht, A.C., and Stafford Smith, B., (1973). Approximate analysis of tall wall-frame structures, *Journal of Structural Division, ASCE*, Vol. 99(2), 199-221.
- Heidebrecht, A.C., and Rutenberg, A., (2000). Applications of drift spectra in seismic design, *Proceedings of the 12th World Conference on Earthquake Engineering*, Auckland, New Zealand, Paper No. 209.
- Hosseini, M., and Imagh-e-Naiini, M. R. (1999). A quick method for estimating the lateral stiffness of building systems. *The Structural Design of Tall Buildings*, Vol. 8(3), 247-260.
- Inoue, T., and Cornell, C. A., (1990). Seismic Hazard Analysis of Multi-Degree-of-Freedom Structures, Reliability of Marine Structures Program, Report No. RMS-8, Dept. of Civil and Environmental Engineering, Stanford University, California.
- Iwan, W.D., (1997). Drift spectrum: Measure of demand for earthquake ground motions, *Journal of Structural Engineering, ASCE*, Vol. 123(4), 397-404.
- Jalayer, F., (2003). Direct probabilistic seismic analysis: Implementing non-linear dynamic assessments, Ph.D. Thesis, Stanford University, Stanford, California, 243 pp.
- Jalayer, F., Franchin, P., and Pinto, P.E., (2007). A scalar damage measure for seismic reliability analysis of RC frames, *Earthquake Engineering and Structural Dynamics*, Vol. 36 (13), 2059-2079.

Jayaram, N., and Baker, J. W., (2008). Statistical tests of the joint distribution of spectral acceleration values, *Bulletin of the Seismological Society of America*, Vol. 98(5), 2231-2243.

Jayaram, N., Lin, T., and Baker, J. W., (2011). A computationally efficient ground-motion selection algorithm for matching a target response spectrum mean and variance, *Earthquake Spectra*, Vol. 27(3), 797-815.

Joyner, W.B., and Boore, D.M., (1981). Peak horizontal acceleration and velocity from strong-motion records including records from the 1979 Imperial Valley, California, Earthquake, *Bulletin of the Seismological Society of America*, Vol. 71(6), 2011-2038.

Joyner, W. B., and Boore, D. M., (1993). Methods for regression analysis of strong-motion data, *Bulletin of the Seismological Society of America*, Vol. 83(2), 469-487.

Karsan I. D., and Jirsa J.O., (1969). Behavior of Concrete under Compressive Loadings, *Journal of Structural Division, ASCE*, Vol. 95(12), 2543-2563.

Kent D.C., and Park R., (1971). Flexural Members with Confined Concrete, *Journal of Structural Division, ASCE*, Vol. 97(7), 1969-1990.

Khan, F.R., and Sbarounis, J.A., (1964). Interaction of shear walls and frames, *Journal of Structural Division, ASCE*, Vol. 90(3), 285-335.

Krawinkler, H., Medina, R., and Alavi, B., (2003). Seismic drift and ductility demands and their dependence on ground motions, *Engineering Structures*, Vol. 25(5), 637-653.

Leonard, M., (2010). Earthquake Fault Scaling: Self-Consistent Relating of Rupture Length, Width, Average Displacement, and Moment Release, *Bulletin of the Seismological Society of America*, Vol. 100(5A), 1971-1988.

Lilliefors, H., (1967). On the Kolmogorov–Smirnov test for normality with mean and variance unknown, *Journal of the American Statistical Association*, Vol. 62(138), 399-402.

Lin, L., (2008). Development of improved intensity measures for probabilistic seismic demand analysis, Ph.D. Thesis, University of Ottawa Canada. 166 pp.

Lin, L., Naumoski, N.; Saatcioglu, M., and Foo, S., (2011). Improved intensity measures for probabilistic seismic demand analysis. Part 1: development of improved intensity measures, *Canadian Journal of Civil Engineering*, Vol. 38(1), 79-88.

Luco, N., (2002). Probabilistic seismic demand analysis, SMRF connection fractures, and near-source effects, Ph.D. Thesis, Stanford University, Stanford, CA. 260 pp.

Luco, N., and Cornell, C.A., (1998). Effects of random connection fractures on the demand and reliability for a 3-story pre-Northridge SMRF structure, *Proceedings of the 6th U.S. National Conference on Earthquake Engineering*, Seattle, Washington.

Luco, N., Mai, P. M., Cornell, C. A., and Beroza, G. C., (2002). Probabilistic seismic demand analysis at a near-fault site using ground motion simulations based on a stochastic-kinematic earthquake source model, *7th U.S. National Conference on Earthquake Engineering*, July 21-25.

Luco, N., and Cornell, C. A., (2007). Structure-specific scalar intensity measures for near-source and ordinary earthquake ground motions, *Earthquake Spectra*, Vol. 23(2), 357-392.

Luco, N., Ellingwood, B. R., Hamburger, R. O., Hooper, J. D., Kimball, J. K. and Kircher, C. A., (2007). Risk-Targeted Earthquake Ground Motions for the Design of Buildings and Other Structures, *Proceedings of the 76th SEAOC Annual Convention*, Squaw Creek.

MATLAB R2012a, The MathWorks Inc., Natick, MA, 2012.

Mayes, R. L., (1995). Interstory Drift Design and Damage Control Issues, *Structural Design of Tall Buildings*, Vol. 4(1), 15-25.

McGuire, R. K., (1995). Probabilistic Seismic Hazard Analysis and Design Earthquakes: Closing the Loop, *Bulletin of the Seismological Society of America*, Vol. 85(5), 1275-1284.

McGuire R. K., (2004). *Seismic Hazard and Risk Analysis*, EERI, MNO-10, Oakland, CA.

Medina, R. A., and Krawinkler, H., (2005). Evaluation of drift demands for the seismic performance assessment of frames, *Journal of Structural Engineering-ASCE*, Vol. 131(7), 1003-1013.

Metin, A., (2006). Inelastic deformation demands on moment-resisting frame structures, M.Sc. Thesis, Middle East Technical University, Ankara, Turkey.

Miranda, E., (1999). Approximate seismic lateral deformation demands in multistory buildings, *Journal of Structural Engineering-ASCE*, Vol. 125(4), 417-425.

Miranda, E., and Reyes, C. J. (2002). Approximate lateral drift demands in multi-story buildings with nonuniform stiffness, *Journal of Structural Engineering*, ASCE, Vol. 128(7), 840-849.

Miranda, E., and Taghavi, S., (2005). Approximate floor acceleration demands in multistory buildings. I: Formulation, *Journal of Structural Engineering-Asce*, Vol. 131(2), 203-211.

- Miranda, E., and Akkar, S.D., (2006). Generalized interstory drift spectrum, *Journal of Structural Engineering, ASCE*, Vol. 132(6), 840-852.
- Moehle, J. P., (1984). Strong Motion Drift Estimates for R/C Structures, *Journal of Structural Engineering-ASCE*, Vol. 110(9), 1988-2001.
- Moehle, J. P., (1994). Seismic drift and its role in design. *Proceedings of the 5th U.S.-Japan Workshop on the Improvement of Building Structural Design and Construction Practices*, San Diego., 65-78.
- Moehle, J., and Deierlein, G.G. (2004). A framework methodology for performance-based earthquake engineering, *Proceedings of the 13th World Conference on earthquake Engineering*, Vancouver, B.C., Canada, on CD-ROM.
- Muto, K., (1974). Aseismic design analysis of buildings. Tokyo: Maruzen Company, Ltd.
- Neuenhofer, A., and Filippou, F. C., (1997). Evaluation of nonlinear frame finite-element models, *Journal of Structural Engineering-ASCE*, Vol. 123(7), 958-966.
- OpenSees Development Team, (2006). OpenSees: Open System for Earthquake Engineering Simulation Manual, OpenSees version: 2.0.0, Pacific Earthquake Engineering Research Center, University of California, Berkeley, California.
- Priestley, M. J. N., (2000). Performance based seismic design. *12th World Conference on Earthquake Engineering*, Auckland, New Zealand.
- Priestley, M. J. N., Calvi, G. M. and Kowalsky, M. J., (2007). Displacement-based seismic design of structures, Pavia, Italy, IUSS Press: Distributed by Fondazione EUCENTRE.
- Prota, (2008). Probina Orion - Bina Tasarım Sistemi 2008, Teknik Özellikler, Ankara, Turkey.
- Qi, X., and Moehle, J.P., (1991). Displacement design approach for reinforced concrete structures subjected to earthquakes, *Report No. EERC/UCB-91/02*, Earthquake Engineering Research Center, University of California, Berkeley, California.
- Reinoso, E., and Miranda, E. (2005). Estimation of floor acceleration demands in high-rise buildings during earthquakes. *The Structural Design of Tall and Special Buildings*, Vol. 14(2), 107-130.
- Reiter, L., (1990). Earthquake Hazard Analysis: Issues and Insights, New York, Columbia University Press.

Risk Engineering. (2011). EZ-Frisk user manual (version 7.25), Risk Engineering, Inc., Golden, Colorado, United States of America, 365 pp.

Romão, X., Delgado, R., and Costa, A., (2011). Assessment of the statistical distributions of structural demand under earthquake loading, *Journal of Earthquake Engineering*, Vol. 15(5), 724-753.

Schultz, A. E. (1992). Approximating lateral stiffness of stories in elastic frames, *Journal of Structural Engineering, ASCE*, Vol. 118(1), 243-263.

Schwartz, D.P., and Coppersmith K.J., (1984). Fault behavior and characteristic earthquakes: examples from the Wasatch and San Andreas faults, *Journal of Geophysical Research*, Vol. 89(B7), 5681-5698.

Scott B. D., Park R., and Priestley M.J.N., (1982). Stress-Strain Behavior of Concrete Confined by Overlapping Hoops at Low and High Strain Rates, *ACI Structural Journal*, Vol. 79(1), 13-27

SEAOC Blue Book, (1999). Recommended Lateral Force Requirements and Commentary, Seventh Edition, Structural Engineers Association of California, Sacramento, California.

Sezen, H., Elwood K. J., Whittaker A. S., Mosalam K. M., Wallace J. W., and Stanton J. F., (2000). Structural Engineering Reconnaissance of the August 17, 1999 Earthquake: Kocaeli (Izmit), Turkey. PEER Technical Report 2000/09, Pacific Earthquake Engineering Research Center, University of California, Berkeley, 120 pp.

Shome, N., and Cornell, C. A. (1999). Probabilistic seismic demand analysis of nonlinear structures. Rep. No. RMS-35, Department of Civil and Environmental Engineering, Stanford University, Stanford, CA, 320 pp.

Song, J., and Ellingwood, B. R., (1999). Seismic reliability of special moment steel frames with welded connections II, *Journal of Structural Engineering*, Vol. 125(4), 372-384.

Sousa, R., Eroğlu, T., Kazantzidou, D., Kohrangi, M., Sousa, L., Nascimbene, R., and Pinho, R., (2012). Effect of Different Modelling Assumptions on the Seismic Response of RC Structures, *15th World Conference on Earthquake Engineering*, Lisbon Portugal, Paper No: 4333

Sözen, M. A., (1983). Lateral drift of reinforced concrete structures subjected to strong ground motion, *Bulletin of the New Zealand National Society for Earthquake Engineering*, 1988-2001.

Stewart, J.P., Chiou, S.J., Bray, J.D., Graves, R.W., Somerville, P.G., and Abrahamson, N.A., (2001). Ground motion evaluation procedures for performance-based design, *PEER Report 2001/09*, Pacific Earthquake Engineering Research Center, University of California, Berkeley, 229 pp.

Takeda, T., Sozen, M. A., and Nielsen N. N., (1970). Reinforced concrete response to simulated earthquakes, *Journal of Structural Division*, ASCE, Vol. 96(12), 2557-2573.

Thenhaus P. C., and Campbell K. W., (2003). Seismic Hazard Analysis, Chapter 8, *Earthquake Engineering Hand Book*, Wai-Fah Chen and Charles Schawthorn (editors), CRC Press.

Tothong, P., (2007). Probabilistic seismic demand analysis using advanced ground motion intensity measures, attenuation relationships, and near-fault effects, Ph.D. Thesis, Stanford University, Stanford, CA, 210 pp.

Tothong, P., and Luco, N. (2007). Probabilistic seismic demand analysis using advanced ground motion intensity measures, *Earthquake Engng. Struct. Dyn.*, Vol. 36(13), 1837-1860

Turkish Standards Institute, (1997). TS 498, Design loads for buildings, Ankara, Turkey.

Turkish Standards Institute, (2000). TS 500-2000 Requirements for Design and Construction of Reinforced Concrete Structures, Ankara, Turkey.

Turkish Earthquake Code, TEC (2007). Specification for Buildings to be Built in Seismic Zones. Ankara, Turkey, Ministry of Public Works and Settlement, Government of Republic of Turkey.

Umutlu, N., Koketsu, K., and Milkereit, C., (2004). The rupture process during the 1999 Duzce, Turkey, earthquake from joint inversion of teleseismic and strong-motion data, *Tectonophysics*, Vol. 391(1-4), 315-324.

Valley, M., (2011). Applicability of nonlinear MDOF modeling for design, *Structures Congress 2011: Proceedings of the 2011 Structures Congress*, Eds. Ames, D., Droessler T. L., and Hoit, M. I., April 14-16, 2011, Las Vegas, Nevada. Reston, Va: American Society of Civil Engineers.

Vamvatsikos, D., and Cornell, C.A., (2005). Developing efficient scalar and vector intensity measures for IDA capacity estimation by incorporating elastic spectral shape information, *Earthquake Engineering and Structural Dynamics*, Vol. 34 (13), 1573–1600.

Vamvatsikos, D., (2012). Derivation of new SAC/FEMA performance evaluation solutions with second-order hazard approximation, *Earthquake Engineering and Structural Dynamics*, Vol. 42(8), 1171-1188.

Wen, Y. K., (2001). Reliability and performance-based design, *Structural Safety*, Vol. 23(4), 407-428.

Wells, D. L., and Coppersmith, K. J., (1994). New Empirical Relationships among Magnitude, Rupture Length, Rupture Width, Rupture Area, and Surface Displacement, *Bulletin of the Seismological Society of America*, Vol. 84(4), 974-1002.

Westergaard, H. M., (1933). Earthquake-shock transmission in tall buildings, *Engineering News-Record*, Vol. 111(22), 654-656.

APPENDIX A

GROUND-STORY FLOOR PLANS OF THE 3-D BUILDINGS

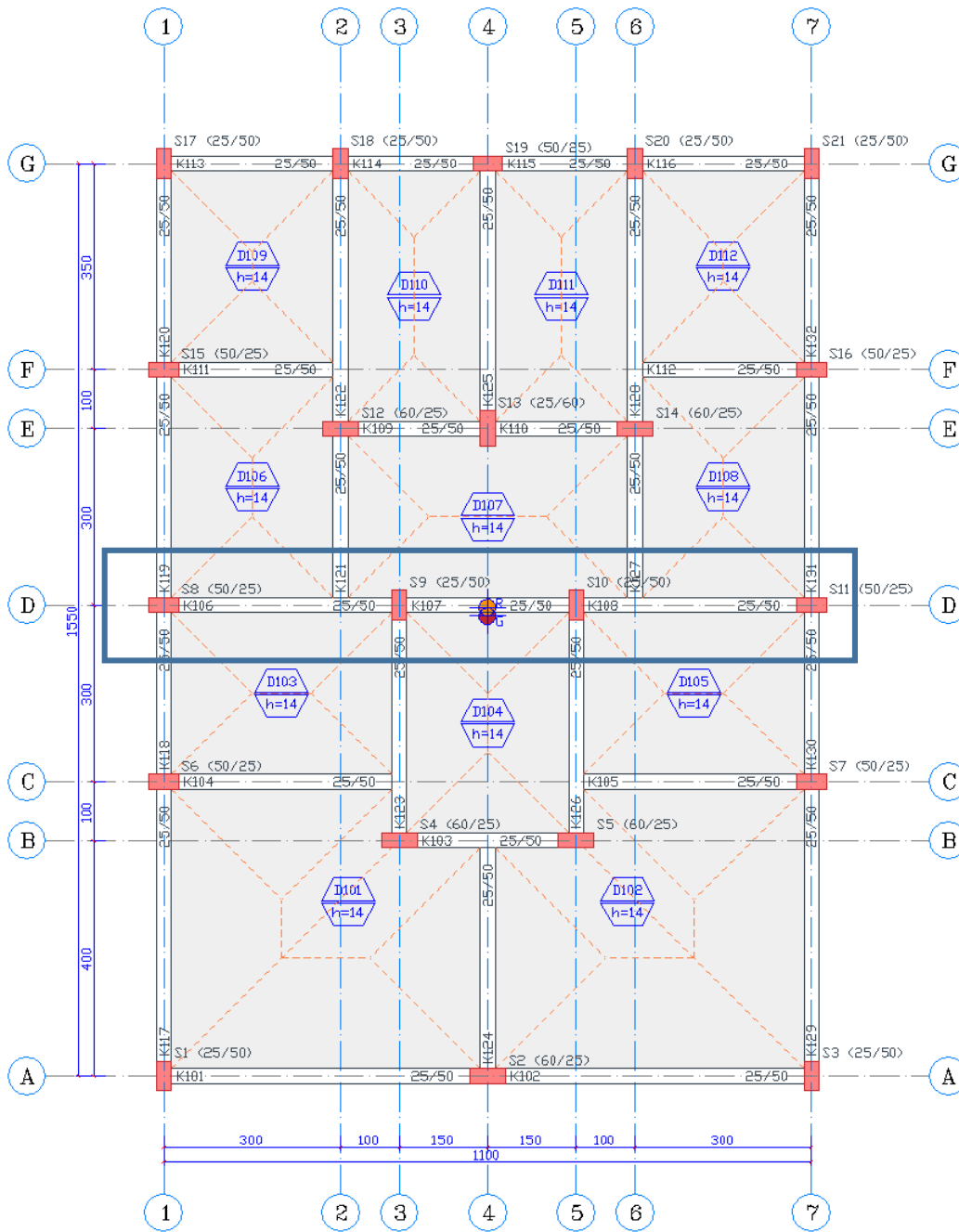


Figure A.1 Ground-story floor plan of the 4-story building that is generated and designed using PROBINA Orion Software (Prota, 2008). The design complies with all relevant Turkish codes including Turkish Earthquake Code (TEC, 2007)

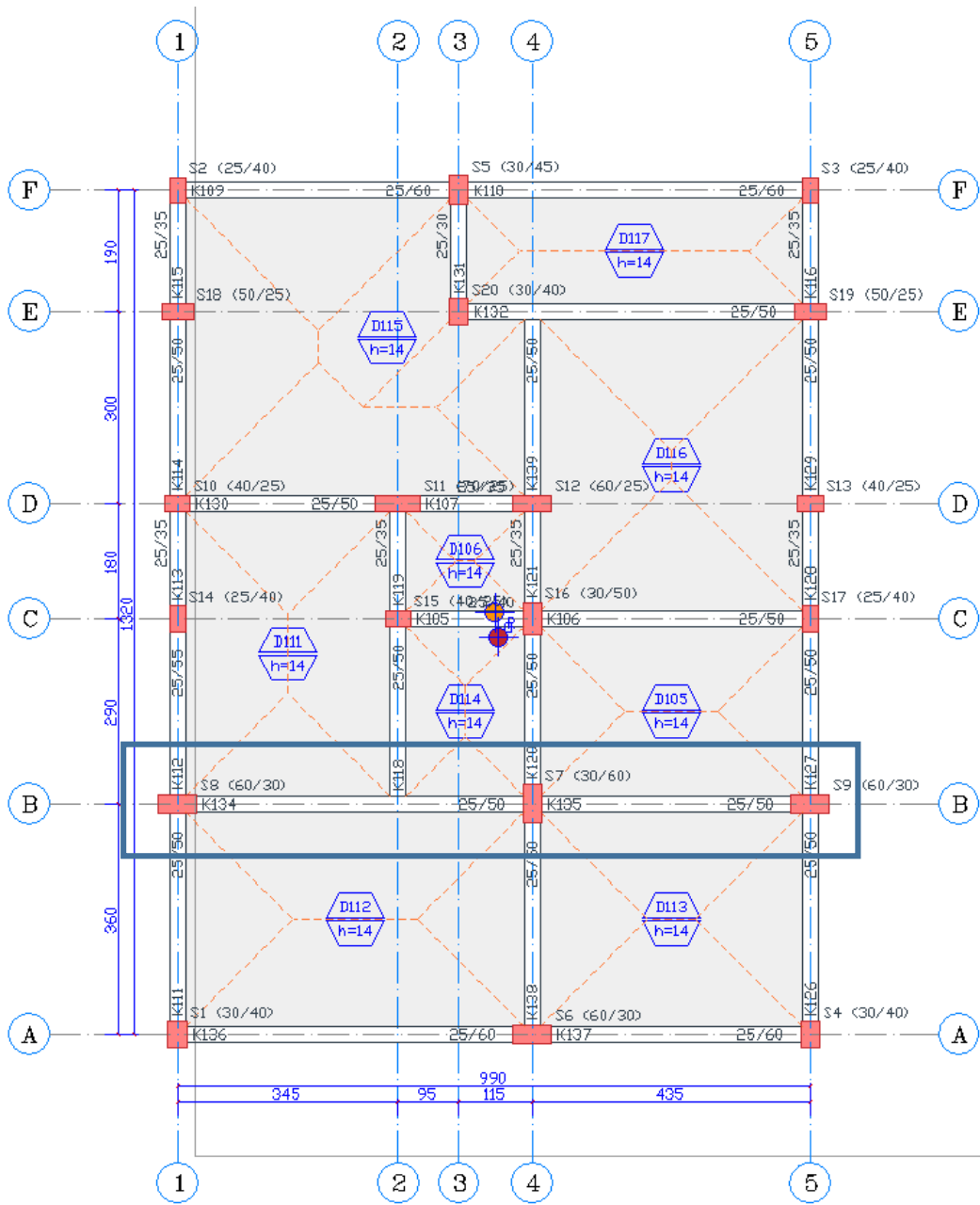


Figure A.2 Ground-story floor plan of the 5-story building that is generated and designed using PROBINA Orion Software (Prota, 2008). The design complies with all relevant Turkish codes including Turkish Earthquake Code (TEC, 2007)

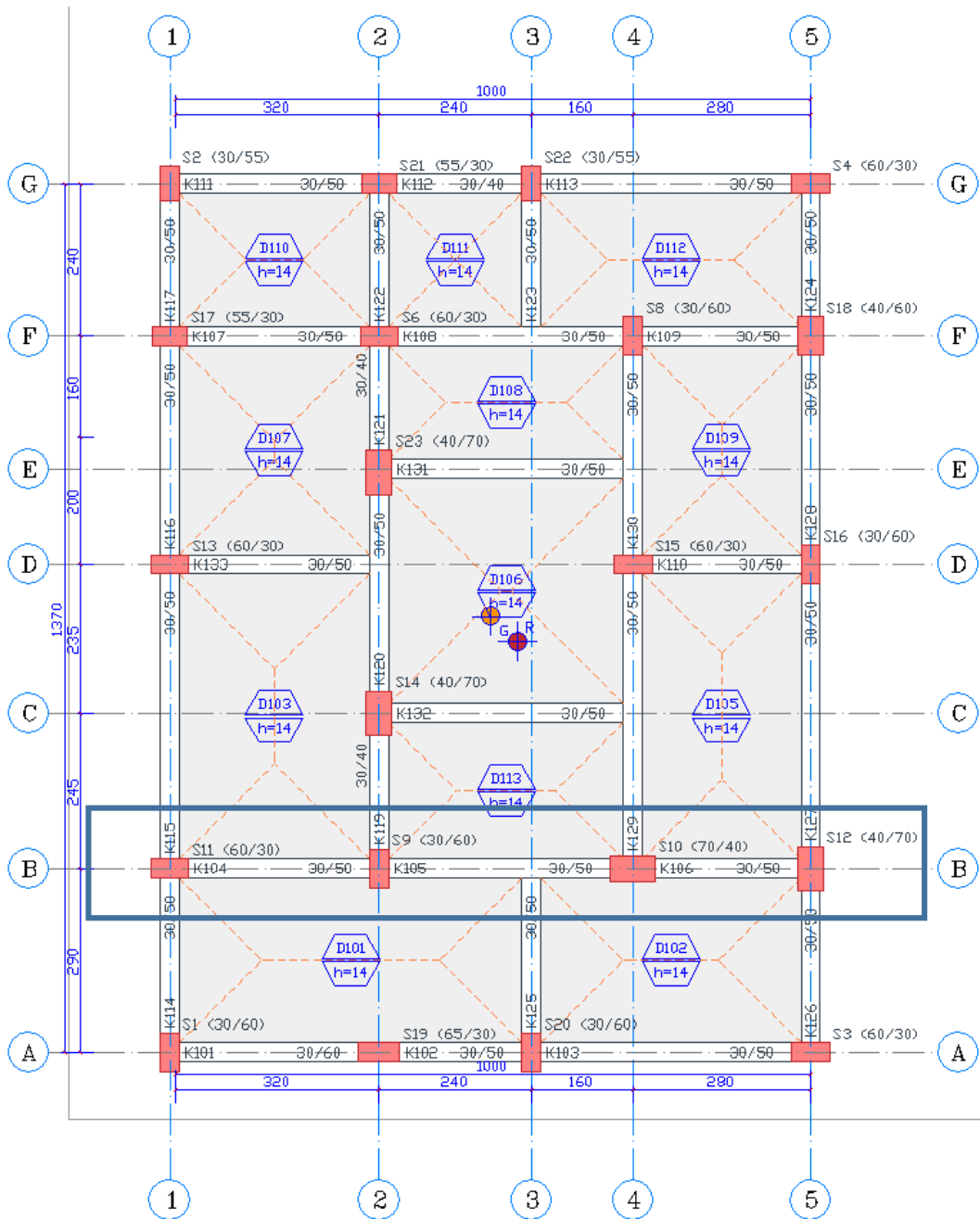


Figure A.3 Ground-story floor plan of the 7-story building that is generated and designed using PROBINA Orion Software (Prota, 2008). The design complies with all relevant Turkish codes including Turkish Earthquake Code (TEC, 2007)

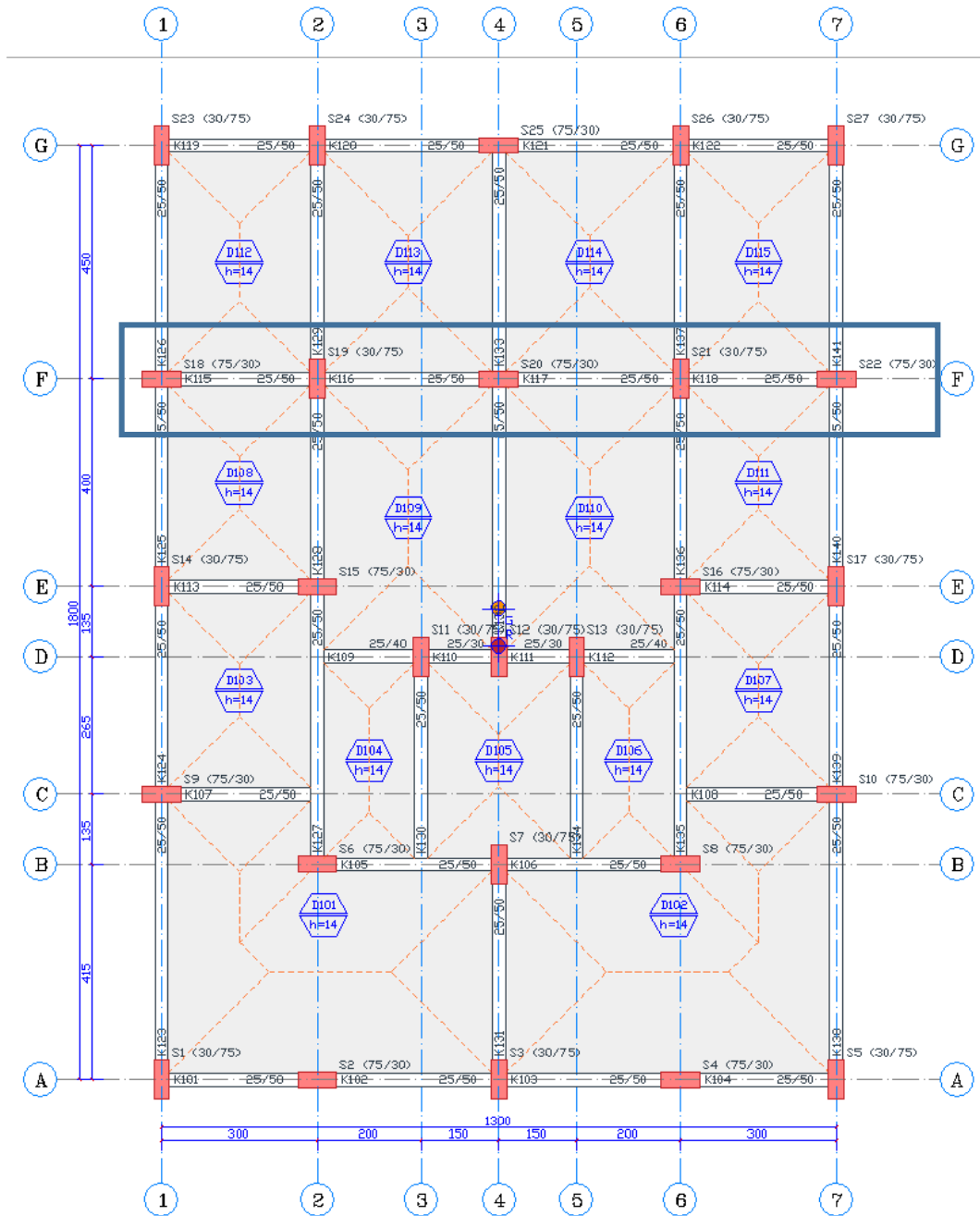


Figure A.4 Ground-story floor plan of the 8-story building that is generated and designed using PROBINA Orion Software (Prota, 2008). The design complies with all relevant Turkish codes including Turkish Earthquake Code (TEC, 2007)

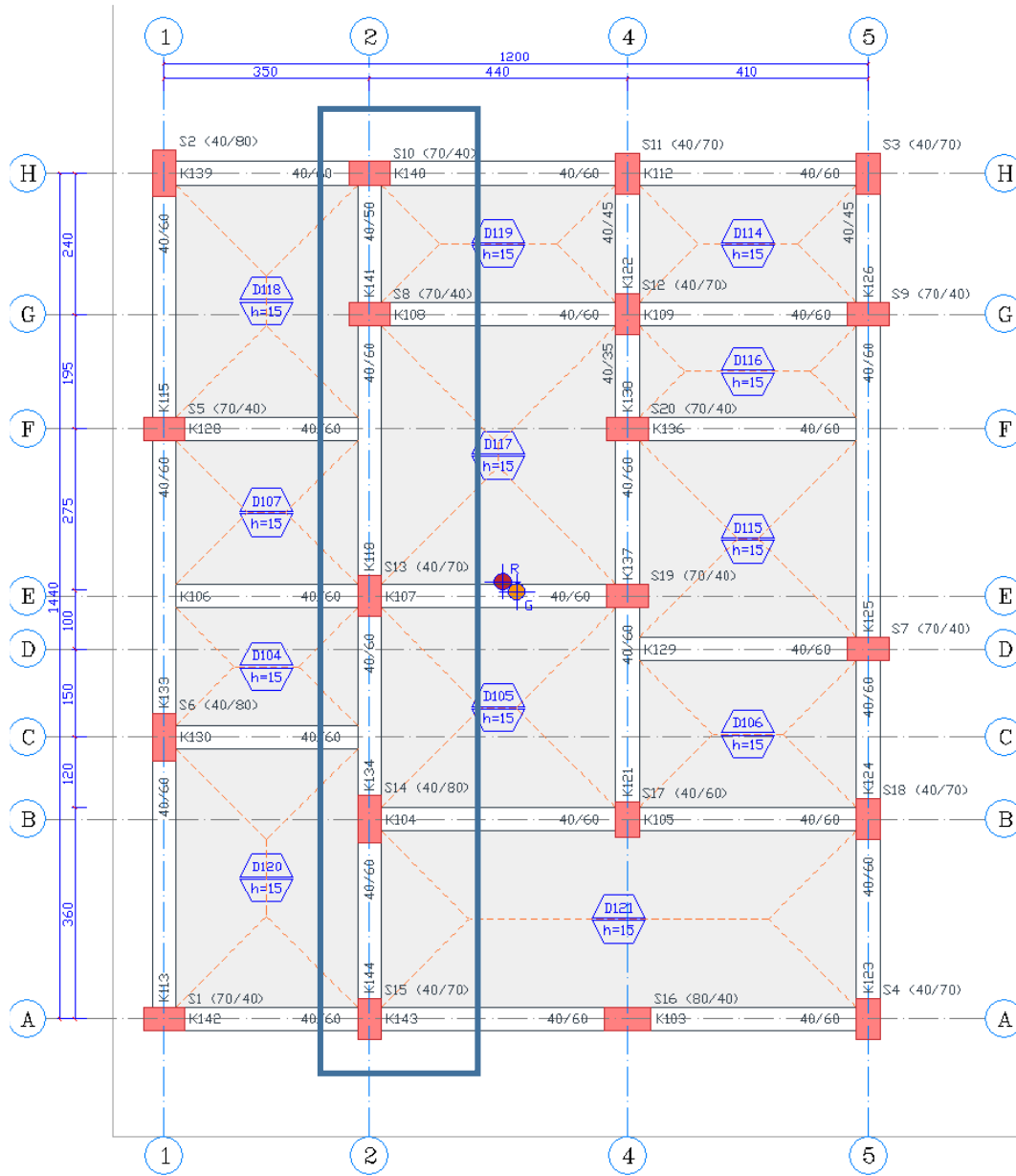


Figure A.5 Ground-story floor plan of the 9-story building that is generated and designed using PROBINA Orion Software (Prota, 2008). The design complies with all relevant Turkish codes including Turkish Earthquake Code (TEC, 2007)

APPENDIX B

GEOMETRY AND MEMBER DIMENSIONS OF THE FRAMES

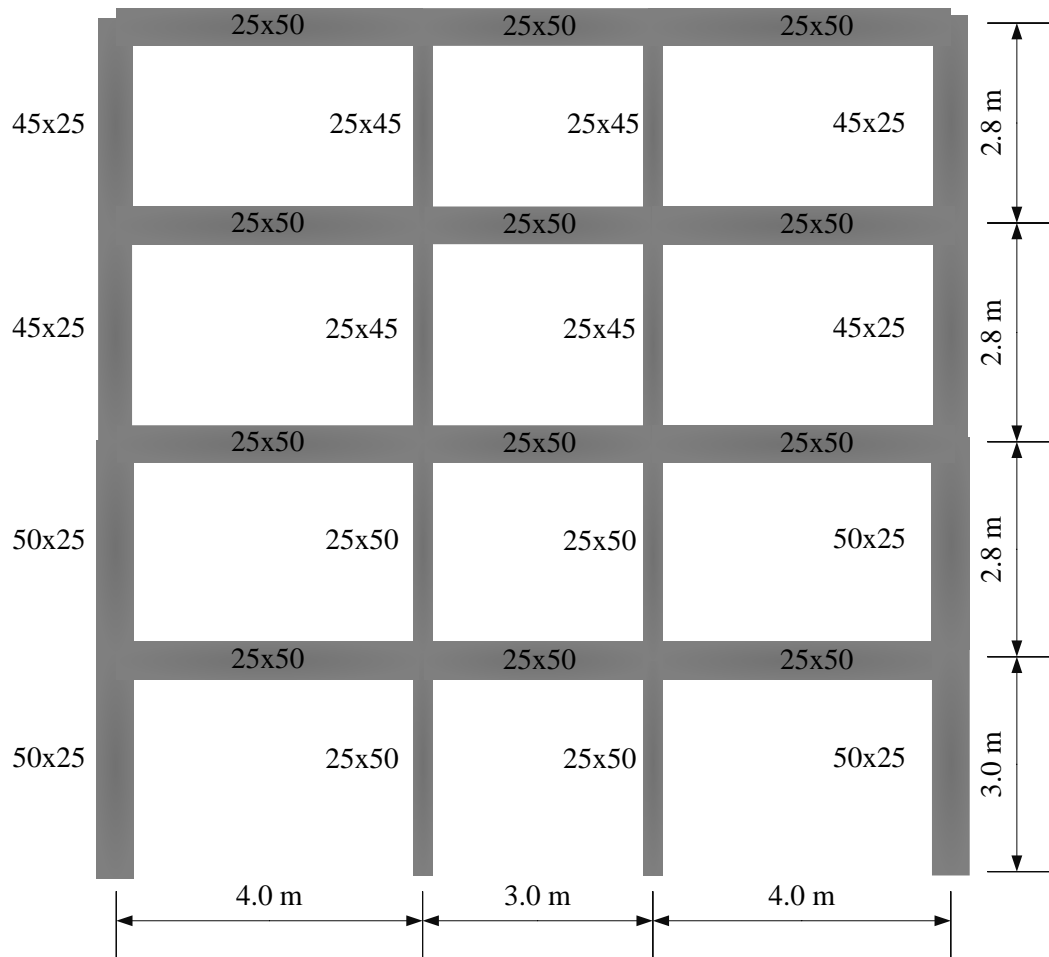


Figure B.1 4S_MRF model and member dimensions

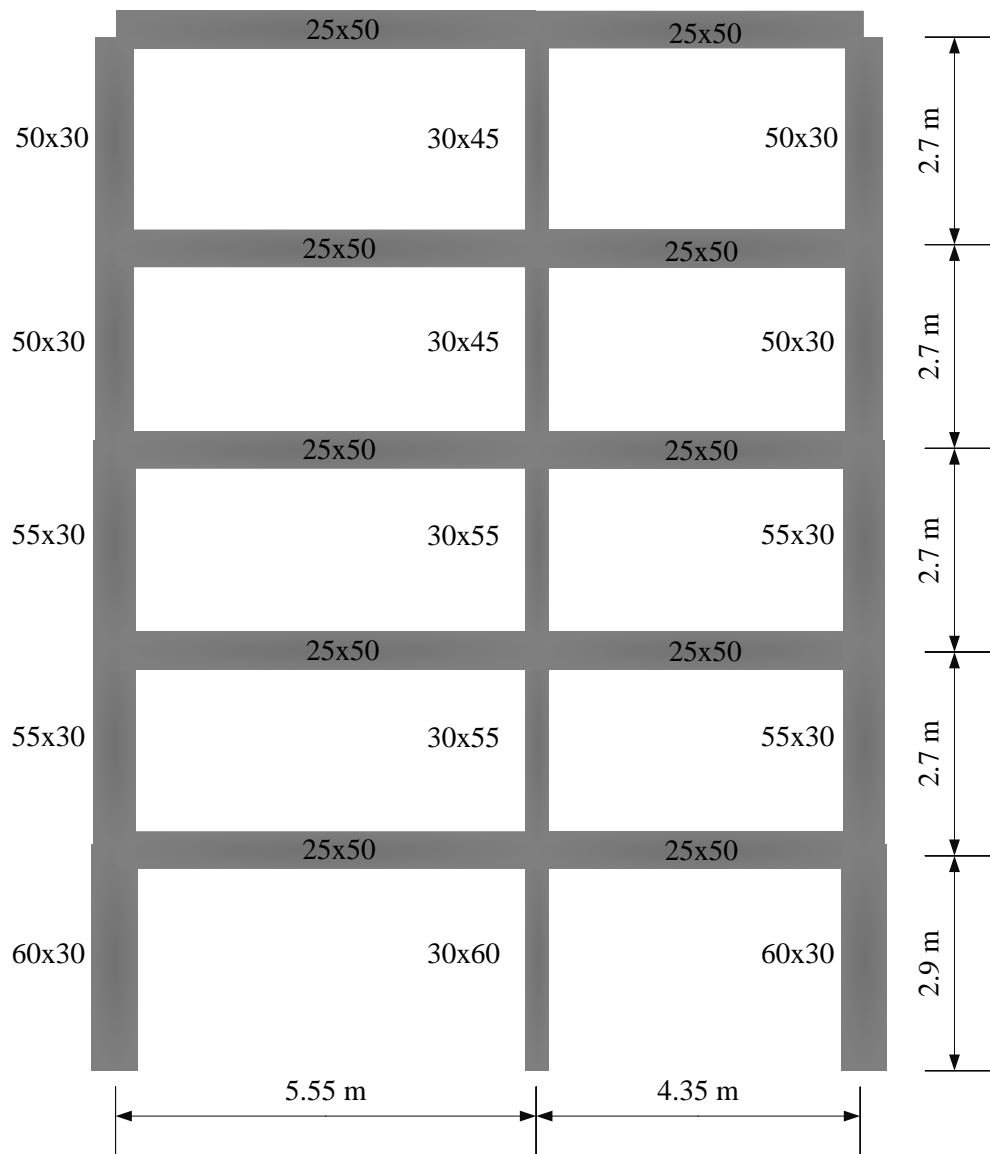


Figure B.2 5S_MRF model and member dimensions

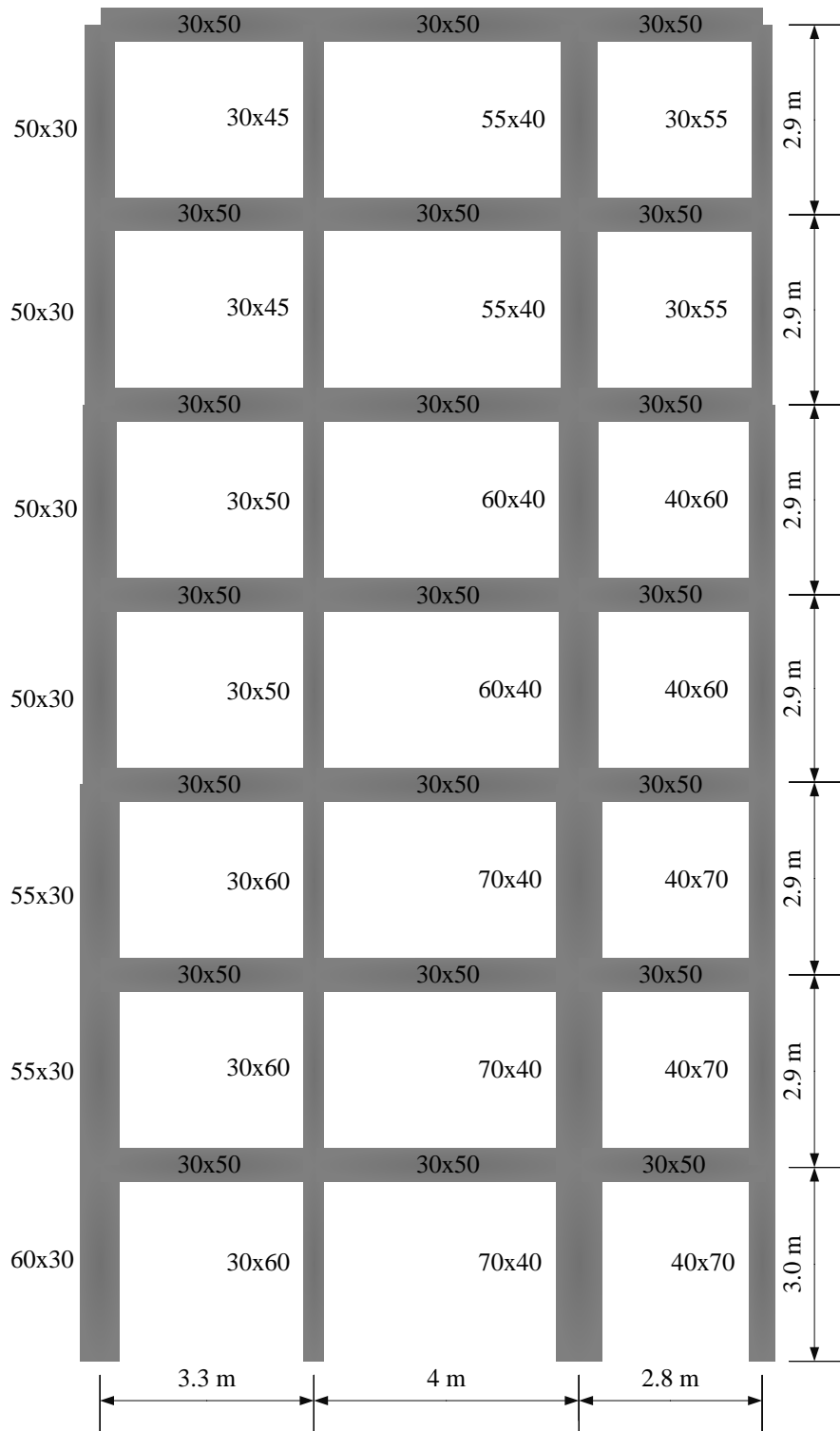


Figure B.3 7S_MRF model and member dimensions

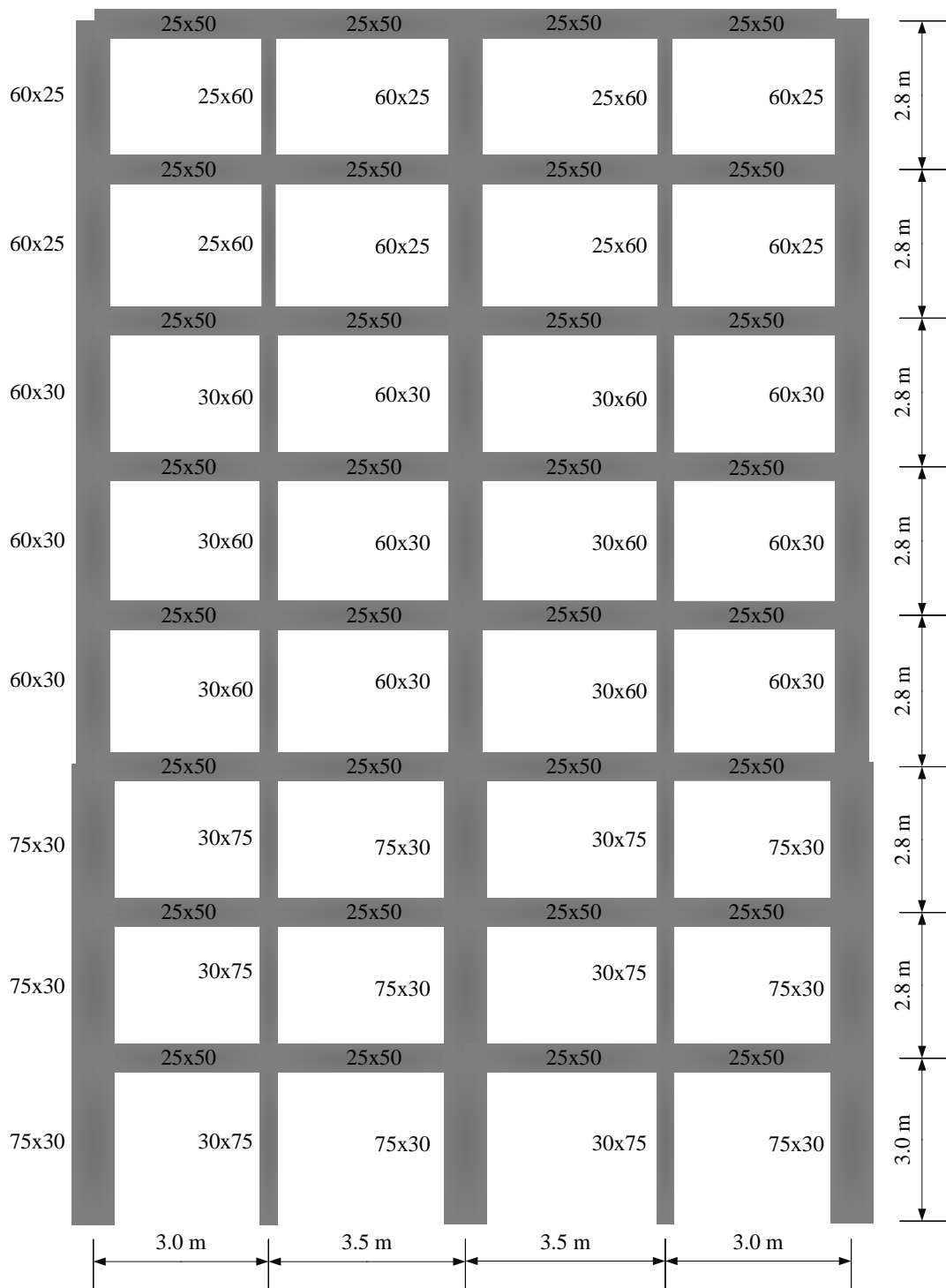


Figure B.4 8S_MRF model and member dimensions

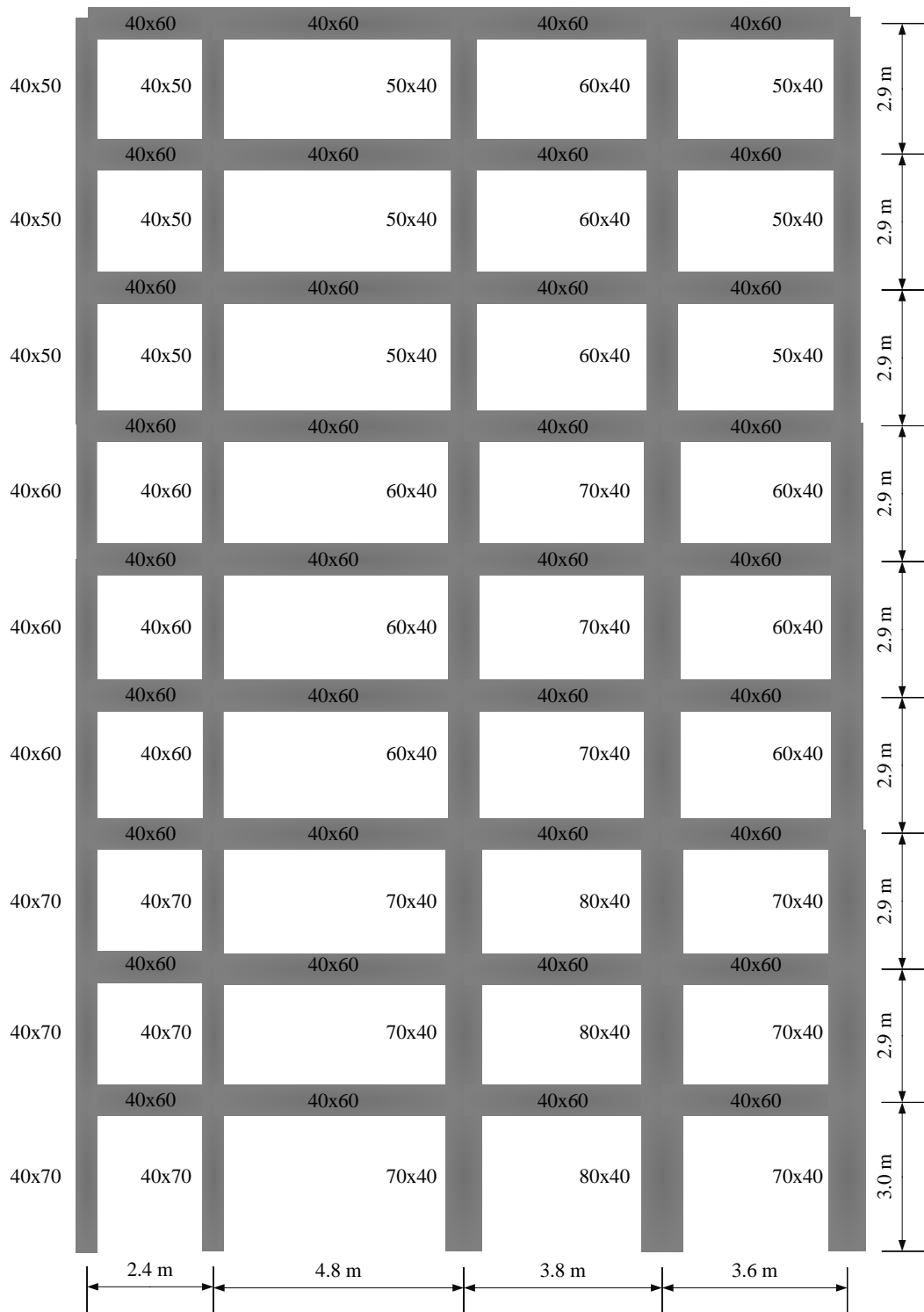


Figure B.5 9S_MRF model and member dimensions

APPENDIX C

GROUND-MOTION RECORDS

Table C.1 Important features of the employed accelerograms

GM Code	EQ Name	Date year/month/day	M _w	R _{jb}	NEHRP Site Class	Hyp. Depth (km)	Fault Style	PGA H ₁ (cm/s ²)	PGA H ₂ (cm/s ²)
TGMB1079	Soma - MANISA	19990724	5.00	37.90	C	10.00	SS	12.97	11.26
TGMB1827	Yigilca - DUZCE	19991113	5.00	0.00	C	5.20	N	45.62	57.29
TGMB1828	Yigilca - DUZCE	19991113	5.00	15.55	D	5.20	N	61.41	32.67
TGMB1829	Yigilca - DUZCE	19991113	5.00	10.72	C	5.20	N	32.37	60.92
TGMB1831	Yigilca - DUZCE	19991113	5.00	10.44	C	5.20	N	113.80	296.26
TGMB3738	GOKOVA GULF	20050111	5.00	25.47	C	14.90	N	17.12	15.69
TGMB3740	GOKOVA GULF	20050111	5.00	82.48	C	14.90	N	2.01	1.83
TGMB1954	Merkez - BOLU	19991116	5.02	60.77	C	5.00	SS	3.40	4.33
TGMB1176	AEGEAN SEA	19990819	5.10	48.00	C	12.00	N	7.02	6.01
TGMB1265	IZMIT GULF	19990831	5.10	70.65	C	4.00	N	7.31	7.31
TGMB1266	IZMIT GULF	19990831	5.10	83.22	C	4.00	N	1.86	1.71
TGMB3901	Poturge - MALATYA	20051126	5.10	56.05	C	19.10	N	7.50	5.50
ECDE1808	Off coast of Levkas island (Greece)	19761201	5.10	21.00	D	21.00	SS	73.22	106.98
ECDE6167	Off coast of Levkas island (Greece)	19761209	5.10	21.00	C	21.00	SS	88.91	101.60
ECDE7343	Azores (Azores Islands, Portugal)	19761219	5.10	13.00	D	13.00	SS	28.83	23.39
TGMB4101	GEMLIK KORFEZI	20061024	5.15	26.97	C	7.90	N	28.38	36.56
TGMB4103	GEMLIK KORFEZI	20061024	5.15	10.73	D	7.90	N	179.77	159.25
TGMB4104	GEMLIK KORFEZI	20061024	5.15	7.28	D	7.90	N	206.19	177.14

Table C.1 Continued

GM Code	EQ Name	Date year/month/day	M _w	R _{jb}	NEHRP Site Class	Hyp. Depth (km)	Fault Style	PGA H ₁ (cm/s ²)	PGA H ₂ (cm/s ²)
TGMB4105	GEMLIK KORFEZI	20061024	5.15	13.73	C	7.90	N	100.42	69.54
TGMB4106	GEMLIK KORFEZI	20061024	5.15	12.66	D	7.90	N	95.34	65.95
TGMB4109	GEMLIK KORFEZI	20061024	5.15	28.50	D	7.90	N	25.66	37.78
TGMB4113	GEMLIK KORFEZI	20061024	5.15	97.47	C	7.90	N	3.22	2.63
TGMB2952	Yigilca – DUZCE	20010826	5.17	22.84	D	8.80	SS	131.64	189.07
TGMB2954	Yigilca – DUZCE	20010826	5.17	99.03	C	8.80	SS	2.14	1.37
TGMB0073	Ilica – ERZURUM	19950129	5.20	19.60	D	28.20	SS	48.52	44.98
TGMB0364	Merkez – CORUM	19970228	5.20	39.81	C	4.90	SS	21.00	21.00
TGMB0544	Dinar – AFYON	19980404	5.20	2.00	D	19.30	N	130.90	134.73
TGMB0545	Dinar – AFYON	19980404	5.20	94.31	D	19.30	N	2.56	2.38
TGMB0547	Dinar – AFYON	19980404	5.20	88.23	D	19.30	N	2.35	2.44
TGMB0553	Karlioiva – BINGOL	19980413	5.20	67.49	C	15.30	SS	8.39	3.45
TGMB0555	Karlioiva – BINGOL	19980413	5.20	36.92	C	15.30	SS	13.50	12.00
TGMB0556	Karlioiva – BINGOL	19980413	5.20	76.04	D	15.30	SS	3.51	2.81
TGMB1088	Soma – MANISA	19990725	5.20	35.07	C	15.20	SS	14.40	12.82
TGMB1460	MARMARA SEA	19990929	5.20	86.04	C	12.20	SS	13.70	11.87
TGMB2153	Mengen – BOLU	20000214	5.27	51.69	D	10.00	SS	29.56	37.56
TGMB2610	Akyazi – SAKARYA	20000823	5.30	14.23	D	10.50	SS	96.69	79.01

Table C.1 Continued

GM Code	EQ Name	Date year/month/day	M _w	R _{jb}	NEHRP Site Class	Hyp. Depth (km)	Fault Style	PGA H ₁ (cm/s ²)	PGA H ₂ (cm/s ²)
TGMB2613	Akyazi – SAKARYA	20000823	5.30	93.55	D	10.50	SS	16.21	21.69
TGMB2614	Akyazi - SAKARYA	20000823	5.30	29.84	C	10.50	SS	27.47	20.84
TGMB3432	Buldan - DENIZLI	20030723	5.30	10.87	D	28.30	N	123.23	90.16
TGMB3438	Buldan - DENIZLI	20030723	5.30	81.30	D	28.30	N	5.28	4.15
TGMB3714	Ula - MUGLA	20041220	5.30	96.05	D	12.50	N	3.53	2.91
TGMB3717	Ula - MUGLA	20041220	5.30	16.24	C	12.50	N	31.04	33.89
TGMB3758	MEDITERRANEAN SEA	20050130	5.30	49.08	D	28.30	SS	10.00	9.50
ECDE6087	Arnaia (Greece)	19761207	5.30	14.00	C	14.00	N	31.52	35.49
TGMB0268	AEGEAN SEA	19960402	5.40	68.56	D	11.00	N	18.50	10.00
TGMB2209	Honaz - DENIZLI	20000421	5.40	22.63	D	19.90	N	17.70	27.56
TGMB2210	Honaz - DENIZLI	20000421	5.40	85.40	D	19.90	N	3.02	2.99
TGMB2902	Erzin - OSMANIYE	20010625	5.40	40.60	C	10.00	N	6.56	6.53
TGMB2905	Erzin - OSMANIYE	20010625	5.40	73.67	C	10.00	N	14.00	11.50
TGMB2917	Pasinler - ERZURUM	20010710	5.40	31.21	C	22.50	SS	21.94	19.53
TGMB3455	Buldan - DENIZLI	20030726	5.40	11.21	D	21.30	N	121.12	107.51
TGMB3459	Buldan - DENIZLI	20030726	5.40	49.94	D	21.30	N	27.16	26.97
TGMB3461	Buldan - DENIZLI	20030726	5.40	79.26	D	21.30	N	6.56	6.07
TGMB3910	Karlioiva - BINGOL	20051210	5.40	64.53	C	18.90	SS	8.79	6.68

Table C.1 Continued

GM Code	EQ Name	Date year/month/day	M _w	R _{jb}	NEHRP Site Class	Hyp. Depth (km)	Fault Style	PGA H ₁ (cm/s ²)	PGA H ₂ (cm/s ²)
TGMB3911	Karlioiva - BINGOL	20051210	5.40	61.87	C	18.90	SS	12.70	9.49
ECDE0192	Montenegro (Albania)	19761115	5.40	13.00	C	13.00	R	73.51	64.48
TGMB2766	Van	20001115	5.50	36.83	C	48.40	SS	11.69	13.31
TGMB3617	Bodrum - MUGLA	20040804	5.50	33.06	C	10.00	N	27.37	17.46
TGMB3846	AEGEAN SEA	20051017	5.50	53.00	D	20.50	SS	16.51	14.98
TGMB3850	AEGEAN SEA	20051017	5.50	73.95	D	20.50	SS	9.00	7.00
ECDE0120	Friuli (aftershock) (Northern Italy)	19761109	5.50	12.00	C	12.00	R	88.35	88.88
ECDE0122	Friuli (aftershock) (Northern Italy)	19761111	5.50	12.00	D	12.00	R	227.39	103.67
TGMB0294	Gumushacikoy - AMASYA	19960814	5.60	44.25	C	2.70	SS	33.00	20.00
TGMB1530	Merkez - KOCAELI	19991111	5.60	29.08	C	7.50	N	31.29	43.26
TGMB1538	Merkez - KOCAELI	19991111	5.60	10.40	C	7.50	N	749.70	946.38
TGMB3645	Sivrice - ELAZIG	20040811	5.60	78.14	C	7.40	SS	3.20	4.24
TGMB3765	Karlioiva - BINGOL	20050312	5.60	62.32	C	7.20	SS	12.24	5.80
TGMB3808	Karlioiva - BINGOL	20050606	5.60	45.38	C	10.50	SS	14.50	15.00
PEER1643	Sierra Madre	19910628	5.61	23.67	C	12.00	R	111.63	89.64
PEER1646	Sierra Madre	19910628	5.61	13.91	C	12.00	R	172.29	274.02
PEER1740	Little Skull Mtn,NV	19920629	5.65	14.12	D	12.00	N	128.75	208.81
PEER1744	Little Skull Mtn,NV	19920629	5.65	63.82	D	12.00	N	15.79	14.82

Table C.1 Continued

GM Code	EQ Name	Date year/month/day	M _w	R _{jb}	NEHRP Site Class	Hyp. Depth (km)	Fault Style	PGA H ₁ (cm/s ²)	PGA H ₂ (cm/s ²)
PEER0235	Mammoth Lakes-02	19800525	5.69	1.44	C	14.00	SS	382.14	432.35
TGMB0289	Merzifon - AMASYA	19960814	5.70	43.47	C	11.90	SS	53.50	27.00
TGMB0342	Merkez - HATAY	19970122	5.70	19.17	C	45.40	N	150.50	136.00
TGMB3163	Seferihisar - IZMIR	20030410	5.70	33.21	D	11.30	SS	37.11	78.58
PEER0148	Coyote Lake	19790806	5.74	6.75	D	9.60	SS	267.29	224.22
PEER0150	Coyote Lake	19790806	5.74	0.42	C	9.60	SS	425.70	310.09
PEER0151	Coyote Lake	19790806	5.74	33.69	D	9.60	SS	38.36	49.26
TGMB0248	Kigi - BINGOL	19951205	5.80	58.93	D	25.50	SS	24.02	28.27
TGMB1370	Merkez - KOCAELI	19990913	5.80	40.34	C	10.40	SS	11.38	11.97
TGMB1374	Merkez - KOCAELI	19990913	5.80	91.32	C	10.40	SS	15.59	14.13
TGMB1379	Merkez - KOCAELI	19990913	5.80	20.48	C	10.40	SS	50.60	42.21
TGMB3749	MEDITERRANEAN SEA	20050123	5.80	75.23	D	12.10	SS	24.00	25.00
TGMB3858	Urla - IZMIR	20051017	5.80	51.25	D	18.60	SS	19.13	22.52
TGMB3864	Urla - IZMIR	20051017	5.80	71.80	D	18.60	SS	9.00	7.00
TGMB3879	AEGEAN SEA	20051020	5.80	54.12	D	15.40	SS	31.92	23.65
PEER0477	Lazio-Abruzzo, Italy	19840507	5.80	12.80	C	14.00	N	91.48	111.30
PEER0480	Lazio-Abruzzo, Italy	19840507	5.80	29.58	D	14.00	N	70.94	69.39
PEER0481	Lazio-Abruzzo, Italy	19840507	5.80	45.47	D	14.00	N	28.98	46.49

Table C.1 Continued

GM Code	EQ Name	Date year/month/day	M_w	R_{jb}	NEHRP Site Class	Hyp. Depth (km)	Fault Style	PGA H₁ (cm/s²)	PGA H₂ (cm/s²)
ECDE0247	Valnerina (Central Italy)	19761119	5.80	4.00	C	4.00	N	41.92	38.40
PEER2259	Chi-Chi, Taiwan-02	19990920	5.90	36.15	C	8.00	R	46.52	31.19
PEER2303	Chi-Chi, Taiwan-02	19990920	5.90	80.57	C	8.00	R	7.86	7.88
PEER2387	Chi-Chi, Taiwan-02	19990920	5.90	4.14	C	8.00	R	229.14	82.46
PEER2392	Chi-Chi, Taiwan-02	19990920	5.90	86.69	D	8.00	R	14.73	13.97
PEER2399	Chi-Chi, Taiwan-02	19990920	5.90	10.13	C	8.00	R	48.13	38.29
PEER2426	Chi-Chi, Taiwan-02	19990920	5.90	22.53	C	8.00	R	29.73	28.29
PEER0135	Santa Barbara	19780813	5.92	23.75	C	12.70	R	70.74	33.27
PEER0136	Santa Barbara	19780813	5.92	0.00	C	12.70	R	99.80	199.24
PEER0609	Whittier Narrows-01	19871001	5.99	62.56	C	14.60	SS	30.04	33.99
PEER0637	Whittier Narrows-01	19871001	5.99	6.00	C	14.60	SS	147.90	163.05
PEER0651	Whittier Narrows-01	19871001	5.99	69.59	C	14.60	SS	34.15	28.13
PEER0653	Whittier Narrows-01	19871001	5.99	65.32	D	14.60	SS	65.97	69.54
PEER0668	Whittier Narrows-01	19871001	5.99	14.37	D	14.60	SS	104.72	243.45
TGMB0035	Menderes - IZMIR	19921106	6.00	38.11	C	17.20	SS	71.80	83.49
TGMB2361	Cerkes - CANKIRI	20000606	6.00	8.19	D	10.00	N	63.16	62.46
TGMB2366	Cerkes - CANKIRI	20000606	6.00	90.90	C	10.00	N	12.12	11.75
TGMB3117	Pulumur - TUNCELI	20030127	6.00	84.26	C	10.00	SS	8.45	6.74

Table C.1 Continued

GM Code	EQ Name	Date year/month/day	M_w	R_{jb}	NEHRP Site Class	Hyp. Depth (km)	Fault Style	PGA H₁ (cm/s²)	PGA H₂ (cm/s²)
PEER0230	Mammoth Lakes-01	19800525	6.06	1.10	D	9.00	SS	408.57	433.20
PEER0512	N. Palm Springs	19860708	6.06	51.91	C	11.00	SS	107.56	93.39
PEER0513	N. Palm Springs	19860708	6.06	42.17	D	11.00	SS	97.33	65.63
PEER0520	N. Palm Springs	19860708	6.06	71.70	D	11.00	SS	40.45	35.84
PEER0527	N. Palm Springs	19860708	6.06	3.67	D	11.00	SS	214.07	201.08
PEER0531	N. Palm Springs	19860708	6.06	67.38	C	11.00	SS	74.04	54.38
PEER0534	N. Palm Springs	19860708	6.06	22.96	C	11.00	SS	245.01	234.35
PEER0535	N. Palm Springs	19860708	6.06	30.71	D	11.00	SS	67.88	61.70
TGMB0001	Merkez - DENIZLI	19760819	6.10	6.43	D	19.80	N	290.36	348.53
TGMB0011	Biga - CANAKKALE	19830705	6.10	47.64	C	6.90	SS	46.51	53.44
TGMB0013	Biga - CANAKKALE	19830705	6.10	37.79	C	6.90	SS	46.77	50.11
PEER0815	Griva, Greece	19901221	6.10	26.75	D	9.45	N	45.55	45.67
ECDE7311	Faial (Azores Islands, Portugal)	19761215	6.10	10.00	C	10.00	SS	18.39	14.48
ECDE7329	Faial (Azores Islands, Portugal)	19761217	6.10	10.00	D	10.00	SS	399.88	368.52
PEER0032	Parkfield	19660628	6.19	63.34	C	10.00	SS	12.00	13.29
PEER0033	Parkfield	19660628	6.19	15.96	C	10.00	SS	350.57	266.62
PEER0459	Morgan Hill	19840424	6.19	9.85	C	8.50	SS	217.96	286.50
PEER0460	Morgan Hill	19840424	6.19	12.06	D	8.50	SS	186.58	110.67

Table C.1 Continued

GM Code	EQ Name	Date year/month/day	M_w	R_{jb}	NEHRP Site Class	Hyp. Depth (km)	Fault Style	PGA H₁ (cm/s²)	PGA H₂ (cm/s²)
PEER0461	Morgan Hill	19840424	6.19	3.45	D	8.50	SS	153.37	305.73
PEER0463	Morgan Hill	19840424	6.19	26.42	D	8.50	SS	86.13	94.10
PEER0469	Morgan Hill	19840424	6.19	70.93	D	8.50	SS	46.92	46.90
PEER0548	Chalfant Valley-02	19860721	6.19	21.55	D	10.00	SS	204.87	174.02
PEER0555	Chalfant Valley-02	19860721	6.19	34.91	D	10.00	SS	41.57	47.14
PEER0557	Chalfant Valley-02	19860721	6.19	50.92	D	10.00	SS	35.93	36.41
PEER0558	Chalfant Valley-02	19860721	6.19	6.44	D	10.00	SS	438.32	392.12
TGMB0587	Yuregir - ADANA	19980627	6.20	57.54	C	46.60	SS	132.12	119.29
PEER0300	Irpinia, Italy-02	19801123	6.20	8.81	C	7.00	N	174.07	161.43
PEER0301	Irpinia, Italy-02	19801123	6.20	43.51	D	7.00	N	40.87	42.43
PEER0302	Irpinia, Italy-02	19801123	6.20	22.68	C	7.00	N	96.93	94.39
PEER2453	Chi-Chi, Taiwan-03	19990920	6.20	88.27	D	8.00	R	38.35	33.39
PEER2484	Chi-Chi, Taiwan-03	19990920	6.20	93.54	D	8.00	R	16.97	24.73
PEER2628	Chi-Chi, Taiwan-03	19990920	6.20	0.00	C	8.00	R	461.72	272.53
PEER2656	Chi-Chi, Taiwan-03	19990920	6.20	31.07	D	8.00	R	74.63	55.78
PEER2757	Chi-Chi, Taiwan-04	19990920	6.20	90.38	D	18.00	SS	32.31	29.41
PEER2895	Chi-Chi, Taiwan-04	19990920	6.20	99.92	D	18.00	SS	10.67	12.13
PEER2921	Chi-Chi, Taiwan-04	19990920	6.20	80.04	C	18.00	SS	13.62	15.24

Table C.1 Continued

GM Code	EQ Name	Date year/month/day	M _w	R _{jb}	NEHRP Site Class	Hyp. Depth (km)	Fault Style	PGA H ₁ (cm/s ²)	PGA H ₂ (cm/s ²)
PEER2962	Chi-Chi, Taiwan-05	19990922	6.20	96.79	D	10.00	R	46.81	42.40
PEER3030	Chi-Chi, Taiwan-05	19990922	6.20	82.66	C	10.00	R	46.54	33.55
PEER0718	Superstition Hills-01	19871124	6.22	17.59	D	10.00	SS	129.48	131.07
PEER0095	Managua, Nicaragua-01	19721223	6.24	3.51	D	5.00	SS	413.26	330.87
TGMB3183	Merkez - BINGOL	20030501	6.30	2.23	C	10.00	SS	276.83	545.53
PEER3277	Chi-Chi, Taiwan-06	19990925	6.30	61.46	D	16.00	R	100.54	95.53
PEER3300	Chi-Chi, Taiwan-06	19990925	6.30	27.57	C	16.00	R	132.19	154.56
PEER3331	Chi-Chi, Taiwan-06	19990925	6.30	47.12	D	16.00	R	28.30	30.51
PEER3392	Chi-Chi, Taiwan-06	19990925	6.30	85.82	C	16.00	R	21.59	36.88
PEER3393	Chi-Chi, Taiwan-06	19990925	6.30	70.00	C	16.00	R	20.13	27.36
PEER3473	Chi-Chi, Taiwan-06	19990925	6.30	5.72	C	16.00	R	249.28	378.83
PEER3475	Chi-Chi, Taiwan-06	19990925	6.30	0.00	C	16.00	R	459.88	527.41
PEER3485	Chi-Chi, Taiwan-06	19990925	6.30	77.11	C	16.00	R	28.06	39.09
PEER3496	Chi-Chi, Taiwan-06	19990925	6.30	35.12	D	16.00	R	59.07	80.87
PEER0265	Victoria, Mexico	19800609	6.33	13.80	C	11.00	SS	609.38	576.14
PEER0266	Victoria, Mexico	19800609	6.33	18.53	D	11.00	SS	146.68	90.10
PEER0268	Victoria, Mexico	19800609	6.33	39.10	D	11.00	SS	99.42	67.18
PEER0323	Coalinga-01	19830502	6.36	55.05	C	4.60	R	39.05	51.59

Table C.1 Continued

GM Code	EQ Name	Date year/month/day	M_w	R_{jb}	NEHRP Site Class	Hyp. Depth (km)	Fault Style	PGA H₁ (cm/s²)	PGA H₂ (cm/s²)
PEER0332	Coalinga-01	19830502	6.36	49.40	D	4.60	R	124.01	99.78
PEER0333	Coalinga-01	19830502	6.36	50.98	D	4.60	R	95.77	98.39
PEER0367	Coalinga-01	19830502	6.36	7.69	D	4.60	R	372.41	279.81
TGMB0117	Dinar - AFYON	19951001	6.40	28.97	D	5.00	N	43.92	41.61
TGMB0119	Dinar - AFYON	19951001	6.40	43.85	C	5.00	N	61.30	65.07
TGMB0120	Dinar - AFYON	19951001	6.40	0.00	D	5.00	N	329.72	281.63
TGMB0121	Dinar - AFYON	19951001	6.40	86.87	D	5.00	N	14.50	16.00
PEER1124	Kozani, Greece-01	19950513	6.40	79.33	D	12.64	N	18.75	20.78
PEER1126	Kozani, Greece-01	19950513	6.40	14.13	C	12.64	N	211.10	136.05
PEER1127	Kozani, Greece-01	19950513	6.40	74.06	D	12.64	N	34.97	29.36
PEER1128	Kozani, Greece-01	19950513	6.40	55.66	D	12.64	N	32.00	25.46
ECDE6329	South Iceland (aftershock) (Iceland)	19761211	6.40	99.00	C	-99.00	SS	107.96	28.33
ECDE6334	South Iceland (aftershock) (Iceland)	19761213	6.40	99.00	C	-99.00	SS	432.10	702.94
TGMB3011	Sultandagi - AFYON	20020203	6.50	51.67	D	22.10	N	94.00	113.50
PEER0122	Friuli, Italy-01	19760506	6.50	33.32	D	5.10	R	60.74	88.75
PEER0125	Friuli, Italy-01	19760506	6.50	14.97	C	5.10	R	344.65	308.83
ECDE1796	Aigion (Greece)	19761129	6.50	10.00	D	10.00	N	124.27	188.56
ECDE4677	South Iceland (Iceland)	19761203	6.50	15.00	C	15.00	SS	270.21	220.45

Table C.1 Continued

GM Code	EQ Name	Date year/month/day	M _w	R _{jb}	NEHRP Site Class	Hyp. Depth (km)	Fault Style	PGA H ₁ (cm/s ²)	PGA H ₂ (cm/s ²)
PEER0163	Imperial Valley-06	19791015	6.53	23.17	D	9.96	SS	125.74	76.95
PEER0164	Imperial Valley-06	19791015	6.53	15.19	C	9.96	SS	165.85	153.85
PEER0165	Imperial Valley-06	19791015	6.53	7.29	D	9.96	SS	265.30	249.26
PEER0729	Superstition Hills-02	19871124	6.54	23.85	D	9.00	SS	177.61	203.26
TGMB0030	Uzumlu - ERZINCAN	19920313	6.60	63.05	C	22.60	SS	85.93	67.21
PEER0313	Corinth, Greece	19810224	6.60	10.27	D	7.15	N	235.50	290.37
ECDE0334	Alkion (Greece)	19761125	6.60	10.00	D	10.00	N	300.39	174.96
PEER0051	San Fernando	19710209	6.61	55.20	D	13.00	R	25.39	40.07
PEER0058	San Fernando	19710209	6.61	92.25	C	13.00	R	26.18	24.19
PEER0069	San Fernando	19710209	6.61	58.99	D	13.00	R	28.29	28.32
PEER0079	San Fernando	19710209	6.61	25.47	C	13.00	R	86.43	108.23
PEER0093	San Fernando	19710209	6.61	39.45	D	13.00	R	97.86	104.57
PEER0036	Borrego Mtn	19680409	6.63	45.12	D	8.00	SS	127.60	55.58
PEER0968	Northridge-01	19940117	6.69	43.20	D	17.50	R	155.27	225.59
PEER0971	Northridge-01	19940117	6.69	36.20	D	17.50	R	151.92	107.03
PEER1005	Northridge-01	19940117	6.69	28.82	C	17.50	R	123.73	180.22
PEER1006	Northridge-01	19940117	6.69	13.80	C	17.50	R	272.59	464.82
PEER1040	Northridge-01	19940117	6.69	71.30	D	17.50	R	78.02	68.44

Table C.1 Continued

GM Code	EQ Name	Date year/month/day	M _w	R _{jb}	NEHRP Site Class	Hyp. Depth (km)	Fault Style	PGA H ₁ (cm/s ²)	PGA H ₂ (cm/s ²)
PEER1042	Northridge-01	19940117	6.69	7.89	C	17.50	R	292.58	265.54
PEER1052	Northridge-01	19940117	6.69	5.26	C	17.50	R	295.35	424.47
PEER1064	Northridge-01	19940117	6.69	98.83	C	17.50	R	57.64	62.39
PEER1078	Northridge-01	19940117	6.69	1.69	C	17.50	R	283.36	227.86
PEER1097	Northridge-01	19940117	6.69	81.54	D	17.50	R	41.27	41.00
ECDE0439	Spitak (Turkey-Georgia-Armenia border region)	19761127	6.70	6.00	D	6.00	R	183.73	180.25
PEER0495	Nahanni, Canada	19851223	6.76	2.48	C	8.00	R	959.25	1074.86
ECDE4893	Off coast of SW Cyprus (Cyprus region)	19761205	6.80	19.00	D	19.00	SS	36.65	28.74
PEER0288	Irpinia, Italy-01	19801123	6.90	22.54	C	9.50	N	213.34	195.32
PEER0289	Irpinia, Italy-01	19801123	6.90	13.34	C	9.50	N	129.87	172.20
PEER0290	Irpinia, Italy-01	19801123	6.90	29.79	D	9.50	N	87.27	142.34
PEER1107	Kobe, Japan	19950116	6.90	22.50	D	17.90	SS	246.67	338.17
PEER1109	Kobe, Japan	19950116	6.90	69.04	C	17.90	SS	68.32	51.38
PEER1112	Kobe, Japan	19950116	6.90	86.94	C	17.90	SS	79.86	58.25
PEER1116	Kobe, Japan	19950116	6.90	19.14	D	17.90	SS	238.61	207.89
ECDE0203	Montenegro (Adriatic Sea)	19761117	6.90	12.00	D	12.00	R	40.81	54.86
ECDE0288	Campano Lucano (Southern Italy)	19761121	6.90	16.00	C	16.00	N	220.92	170.77
ECDE0297	Campano Lucano (Southern Italy)	19761123	6.90	16.00	C	16.00	N	46.03	34.78

Table C.1 Continued

GM Code	EQ Name	Date year/month/day	M _w	R _{jb}	NEHRP Site Class	Hyp. Depth (km)	Fault Style	PGA H ₁ (cm/s ²)	PGA H ₂ (cm/s ²)
PEER0764	Loma Prieta	19891018	6.93	10.27	D	17.48	SS	278.95	236.62
PEER0796	Loma Prieta	19891018	6.93	77.34	C	17.48	SS	97.57	196.14
PEER0801	Loma Prieta	19891018	6.93	14.18	C	17.48	SS	269.35	223.47
PEER0809	Loma Prieta	19891018	6.93	12.15	C	17.48	SS	305.26	378.87
PEER0812	Loma Prieta	19891018	6.93	33.87	C	17.48	SS	78.85	80.60
ECDE0153	Caldiran (Turkey-Iran border region)	19761113	7.00	10.00	C	10.00	SS	101.11	68.65
PEER0825	Cape Mendocino	19920425	7.01	0.00	C	9.60	SS	1468.86	1019.74
PEER0826	Cape Mendocino	19920425	7.01	40.23	D	9.60	R	151.11	174.83
PEER0827	Cape Mendocino	19920425	7.01	15.97	C	9.60	R	113.90	111.86
PEER0828	Cape Mendocino	19920425	7.01	0.00	C	9.60	R	578.43	649.86
PEER0829	Cape Mendocino	19920425	7.01	7.88	D	9.60	R	378.10	538.50
PEER0830	Cape Mendocino	19920425	7.01	26.52	C	9.60	R	224.17	185.18
TGMB1580	Merkez - DUZCE	19991112	7.10	20.53	C	10.40	SS	52.09	24.72
TGMB1583	Merkez - DUZCE	19991112	7.10	0.00	D	10.40	SS	513.78	407.69
TGMB1584	Merkez - DUZCE	19991112	7.10	3.71	D	10.40	SS	254.08	116.74
TGMB1585	Merkez - DUZCE	19991112	7.10	0.00	C	10.40	SS	134.40	149.11
TGMB1591	Merkez - DUZCE	19991112	7.10	6.10	C	10.40	SS	128.51	99.08
TGMB1592	Merkez - DUZCE	19991112	7.10	32.14	D	10.40	SS	58.34	120.99

Table C.1 Continued

GM Code	EQ Name	Date year/month/day	M_w	R_{jb}	NEHRP Site Class	Hyp. Depth (km)	Fault Style	PGA H₁ (cm/s²)	PGA H₂ (cm/s²)
TGMB1594	Merkez - DUZCE	19991112	7.10	0.00	C	10.40	SS	504.23	870.15
TGMB1595	Merkez - DUZCE	19991112	7.10	3.64	C	10.40	SS	121.64	156.96
PEER1767	Hector Mine	19991016	7.13	83.43	C	5.00	SS	19.36	19.49
PEER1773	Hector Mine	19991016	7.13	76.89	D	5.00	SS	35.80	41.35
PEER1776	Hector Mine	19991016	7.13	56.40	D	5.00	SS	65.74	80.29
PEER1782	Hector Mine	19991016	7.13	74.92	D	5.00	SS	51.46	60.40
PEER1783	Hector Mine	19991016	7.13	65.04	D	5.00	SS	123.65	104.06
PEER1787	Hector Mine	19991016	7.13	10.35	C	5.00	SS	260.53	330.37
PEER1791	Hector Mine	19991016	7.13	73.55	D	5.00	SS	93.67	84.86
PEER1792	Hector Mine	19991016	7.13	74.00	D	5.00	SS	81.69	121.39
PEER1794	Hector Mine	19991016	7.13	31.06	C	5.00	SS	143.04	186.05
PEER1795	Hector Mine	19991016	7.13	50.42	C	5.00	SS	76.64	85.91
PEER1812	Hector Mine	19991016	7.13	84.87	C	5.00	SS	59.47	46.65
PEER1824	Hector Mine	19991016	7.13	96.91	C	5.00	SS	32.84	23.74
PEER1831	Hector Mine	19991016	7.13	92.71	C	5.00	SS	58.62	54.36
PEER1833	Hector Mine	19991016	7.13	72.88	D	5.00	SS	20.39	27.38
PEER1836	Hector Mine	19991016	7.13	42.06	C	5.00	SS	64.56	65.78
PEER1838	Hector Mine	19991016	7.13	62.91	D	5.00	SS	52.13	57.58

Table C.1 Continued

GM Code	EQ Name	Date year/month/day	M_w	R_{jb}	NEHRP Site Class	Hyp. Depth (km)	Fault Style	PGA H₁ (cm/s²)	PGA H₂ (cm/s²)
PEER1619	Duzce, Turkey	19991112	7.14	34.30	C	10.00	SS	118.10	55.35
PEER1620	Duzce, Turkey	19991112	7.14	45.16	C	10.00	SS	15.68	22.38
PEER1621	Duzce, Turkey	19991112	7.14	97.51	D	10.00	SS	21.78	15.43
PEER1144	Gulf of Aqaba	19951122	7.20	43.29	D	12.50	SS	94.83	84.69
PEER0832	Landers	19920628	7.28	69.21	D	7.00	SS	112.80	143.31
PEER0848	Landers	19920628	7.28	19.74	D	7.00	SS	277.45	408.97
PEER0855	Landers	19920628	7.28	62.98	D	7.00	SS	111.47	119.95
PEER0860	Landers	19920628	7.28	68.66	D	7.00	SS	79.85	95.22
PEER0864	Landers	19920628	7.28	11.03	C	7.00	SS	268.50	278.63
PEER0879	Landers	19920628	7.28	2.19	C	7.00	SS	713.03	774.16
PEER0880	Landers	19920628	7.28	26.96	D	7.00	SS	124.06	122.95
PEER0884	Landers	19920628	7.28	36.15	D	7.00	SS	74.23	87.27
PEER0886	Landers	19920628	7.28	94.48	C	7.00	SS	45.63	43.42
PEER0887	Landers	19920628	7.28	96.00	C	7.00	SS	41.83	40.39
PEER0888	Landers	19920628	7.28	79.76	D	7.00	SS	76.34	85.32
PEER0897	Landers	19920628	7.28	41.43	C	7.00	SS	78.71	59.18
PEER0138	Tabas, Iran	19780916	7.35	24.07	D	5.75	R	104.58	86.95
PEER0139	Tabas, Iran	19780916	7.35	0.00	C	5.75	R	321.70	398.43

Table C.1 Continued

GM Code	EQ Name	Date year/month/day	M_w	R_{jb}	NEHRP Site Class	Hyp. Depth (km)	Fault Style	PGA H₁ (cm/s²)	PGA H₂ (cm/s²)
PEER0140	Tabas, Iran	19780916	7.35	89.76	D	5.75	R	85.68	105.58
PEER0014	Kern County	19520721	7.36	81.30	C	16.00	R	85.46	124.33
PEER0015	Kern County	19520721	7.36	38.42	C	16.00	R	152.99	174.42
PEER1633	Manjil, Iran	19900620	7.37	12.56	C	19.00	SS	504.79	486.92
PEER1636	Manjil, Iran	19900620	7.37	49.97	D	19.00	SS	180.48	128.25
PEER1637	Manjil, Iran	19900620	7.37	63.96	D	19.00	SS	95.16	84.20
PEER1640	Manjil, Iran	19900620	7.37	93.30	D	19.00	SS	87.06	134.16
PEER1148	Kocaeli, Turkey	19990817	7.51	10.56	C	15.00	SS	214.68	147.05
PEER1176	Kocaeli, Turkey	19990817	7.51	1.38	D	15.00	SS	262.58	342.36
PEER1628	St Elias, Alaska	19790228	7.54	26.46	D	15.70	R	96.98	172.67
PEER1629	St Elias, Alaska	19790228	7.54	80.00	D	15.70	R	81.82	64.08
TGMB1102	Merkez - KOCAELI	19990817	7.60	54.58	C	17.00	SS	45.81	54.32
TGMB1106	Merkez - KOCAELI	19990817	7.60	10.14	C	17.00	SS	141.45	264.82
TGMB1107	Merkez - KOCAELI	19990817	7.60	29.25	D	17.00	SS	117.90	137.69
TGMB1108	Merkez - KOCAELI	19990817	7.60	49.30	C	17.00	SS	42.66	60.67
TGMB1109	Merkez - KOCAELI	19990817	7.60	29.52	D	17.00	SS	123.32	91.89
PEER1196	Chi-Chi, Taiwan	19990920	7.62	42.00	D	6.76	R	56.15	51.73
PEER1237	Chi-Chi, Taiwan	19990920	7.62	58.43	D	6.76	R	77.57	72.36

Table C.1 Continued

GM Code	EQ Name	Date year/month/day	M_w	R_{jb}	NEHRP Site Class	Hyp. Depth (km)	Fault Style	PGA H₁ (cm/s²)	PGA H₂ (cm/s²)
PEER1251	Chi-Chi, Taiwan	19990920	7.62	63.82	C	6.76	R	68.85	58.48
PEER1267	Chi-Chi, Taiwan	19990920	7.62	48.19	D	6.76	R	100.01	78.05
PEER1278	Chi-Chi, Taiwan	19990920	7.62	50.47	C	6.76	R	95.15	77.42
PEER1309	Chi-Chi, Taiwan	19990920	7.62	90.63	D	6.76	R	68.94	57.94
PEER1337	Chi-Chi, Taiwan	19990920	7.62	85.67	D	6.76	R	79.24	61.23
PEER1338	Chi-Chi, Taiwan	19990920	7.62	63.82	C	6.76	R	64.23	63.05
PEER1346	Chi-Chi, Taiwan	19990920	7.62	70.43	C	6.76	R	73.38	79.46
PEER1362	Chi-Chi, Taiwan	19990920	7.62	96.84	D	6.76	R	31.21	29.46
PEER1415	Chi-Chi, Taiwan	19990920	7.62	99.89	D	6.76	R	118.59	87.00
PEER1426	Chi-Chi, Taiwan	19990920	7.62	90.59	C	6.76	R	53.59	64.44
PEER1433	Chi-Chi, Taiwan	19990920	7.62	83.57	D	6.76	R	50.08	52.53
PEER1469	Chi-Chi, Taiwan	19990920	7.62	74.41	C	6.76	R	63.71	72.92
PEER1477	Chi-Chi, Taiwan	19990920	7.62	30.18	C	6.76	R	107.71	120.18
PEER1520	Chi-Chi, Taiwan	19990920	7.62	4.67	C	6.76	R	512.37	498.75
PEER1528	Chi-Chi, Taiwan	19990920	7.62	2.13	D	6.76	R	198.21	245.81
PEER1532	Chi-Chi, Taiwan	19990920	7.62	17.18	C	6.76	R	109.72	126.20
PEER1540	Chi-Chi, Taiwan	19990920	7.62	21.78	D	6.76	R	93.82	114.70
PEER1546	Chi-Chi, Taiwan	19990920	7.62	9.35	C	6.76	R	215.44	255.63

Table C.1 Continued

GM Code	EQ Name	Date year/month/day	M_w	R_{jb}	NEHRP Site Class	Hyp. Depth (km)	Fault Style	PGA H₁ (cm/s²)	PGA H₂ (cm/s²)
PEER1561	Chi-Chi, Taiwan	19990920	7.62	80.39	C	6.76	R	24.40	23.03
PEER1563	Chi-Chi, Taiwan	19990920	7.62	79.62	D	6.76	R	18.45	25.12
PEER1564	Chi-Chi, Taiwan	19990920	7.62	80.38	D	6.76	R	30.33	25.19
PEER1578	Chi-Chi, Taiwan	19990920	7.62	67.42	C	6.76	R	26.66	38.85
PEER1580	Chi-Chi, Taiwan	19990920	7.62	75.89	C	6.76	R	19.03	15.25
PEER1588	Chi-Chi, Taiwan	19990920	7.62	55.47	C	6.76	R	53.72	47.11
PEER1626	Sitka, Alaska	19720730	7.68	34.61	C	29.00	SS	94.38	84.69

APPENDIX D

A COMPUTER SOFTWARE FOR ESTIMATING PROBABILISTIC MIDR DEMANDS

D.1 Introduction

A computer program is developed using MATLAB programming language to facilitate the computational steps in the proposed probability-based seismic design and performance assessment procedures. The program calculates probabilistic MIDR curves in terms of MIDR demands and annual exceedance rates by making use of the MIDR predictive model presented in Chapter 5 by making use of the theory explained in Chapter 6. The software is based on several MATLAB scripts and a user interface that enables the user to easily handle with the inputs and outputs of the program. The main features and capabilities of the developed software are listed below:

- The program works with Cartesian coordinates to input the seismic sources as well as the site where the building is located. The ellipsoidal coordinates in terms of latitude and longitude are converted to the Cartesian coordinates implicitly in the program. The user can specify the site location and the seismic source coordinates using latitude and longitude information. The latitude values should be entered in decimal degrees between -90° and $+90^{\circ}$ and the longitude values should be entered in decimal degrees between -360° and $+360^{\circ}$.
- Multiple single-line and multi-line fault sources can be defined. Background seismic sources has to be defined with a circular geometry.
- The source-to-site distance is calculated in terms of Joyner and Boore distance (R_{jb} , Joyner and Boore, 1981). For single line fault sources, the program is capable of calculating R_{rup} (rupture distance) considering the future needs and improvements. This feature is not implemented for multi-line fault sources yet.
- The program uses linear interpolation to estimate MIDR value for a given mean annual frequency of exceedance rate.
- The mode magnitude, source-to-site distance and epsilon values estimated by the program through deaggregation analysis at the desired return period. Deaggregation results are presented in one-dimensional (i.e., magnitude, source-to-site distance and

epsilon) as well as two-dimensional bin pairs (i.e., magnitude-source-to-site distance).

- The program stores the entire list of the earthquake scenarios that are used in calculation of hazard in ASCII format.
- Based on the functional form of rupture length and earthquake magnitude equation by Wells and Coppersmith (1994), the rupture length of area sources can be decided by the user. If no coefficients are given, the program automatically utilizes related equations of Wells and Coppersmith (1994) regarding the faulting mechanism.

D.2 General Rules and Assumptions of the Software

There are several rules based on simple assumptions while dealing with seismic sources. The following sub-sections address these rules specific to each seismic source type. Simple PSHA analyses are conducted to adjust some of these rules and assumptions through comparisons between the outputs of the developed software and a commercial program; EZ-FRISK (Risk Engineering 2011) using several fault and area sources.

D.2.1 Linear Fault Source

Rupture locations are assumed to be uniformly distributed along the strike of fault sources. Through down-dip of faults, single rupture location is considered that is assumed to be located at the midpoint of the fault width. Ruptures are assumed to generate from rupture centers and propagate along down dip and strike. The area of a fault rupture is calculated using the magnitude-area relationships of Wells and Coppersmith (1994) according to the faulting mechanism. Rupture shape is assumed as square until down-dip fault width is reached. After that, rupture geometry is considered as rectangular. The number of fault ruptures is adjusted according to rupture and fault length. Additionally, in order to avoid excessive number of ruptures, the number of ruptures is controlled with a predefined limit. This limit is adjusted regarding the least computational time provided that accuracy of the results is preserved. The first rupture and the last rupture locations are located by leaving an inset of $L_{\text{rupture}}/2$ at both ends of the fault geometry. Accordingly, rest of the rupture centers are located uniformly within the spanning of the first and last rupture centers. A simple sketch of fault ruptures along the strike is given in Figure D.1.

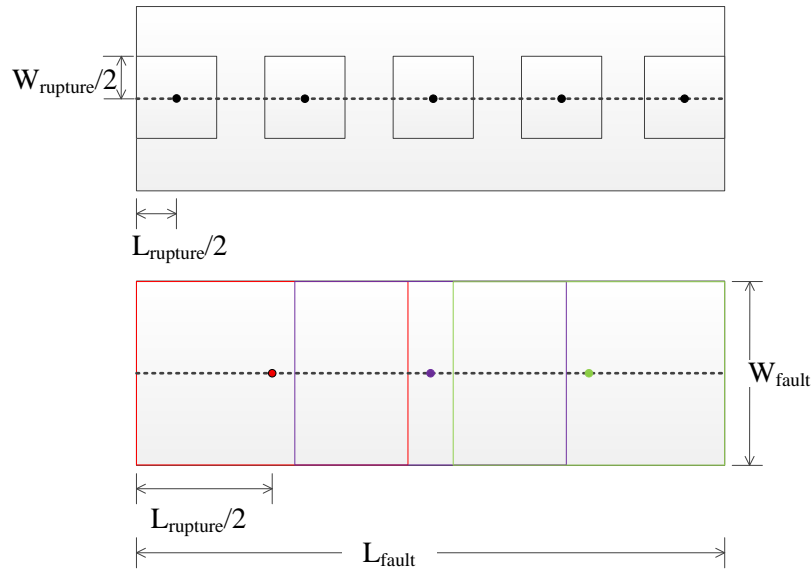


Figure D.1 Simple sketch of possible fault ruptures on a single-line fault. On the upper panel, the centers of the fault ruptures are indicated with black dots. On the lower panel, the centers of fault ruptures and the rupture segments are designated with the same color code

The top panel of Figure D.1 shows the square shaped ruptures and whereas the lower panel shows rectangular ruptures designated with different color codes as overlap on each other. The centers of fault ruptures on the lower panel are also shown with the same color code of the pertinent rupture. Magnitudes above the characteristic magnitude of fault sources theoretically produce rupture lengths and widths that are larger than those of the fault source. Accordingly, for scenario earthquakes with magnitudes greater than the characteristic magnitude of the fault, the entire fault is considered as the rupture. In other words, for such earthquake scenarios the rupture width and length metrics are not allowed to be greater than the fault width and length, respectively.

The multi-line fault sources can be defined without limitation in the number of segments. The above rules for rupture locations on single-line fault sources are also valid for multi-line fault sources. However, for multi-line faults there are some additional complexities while calculating the fault ruptures. For a multi-line fault source with dipping angle different than 90^0 , some discontinuities may exist between the fault segments if the ruptures span on more than one fault segment. Thus, in order to avoid such cases, the rupture surface is assumed to be continuous through the down-dip of the fault. The upper panel of Figure D.2 represents the top-view of a multi-line fault source.

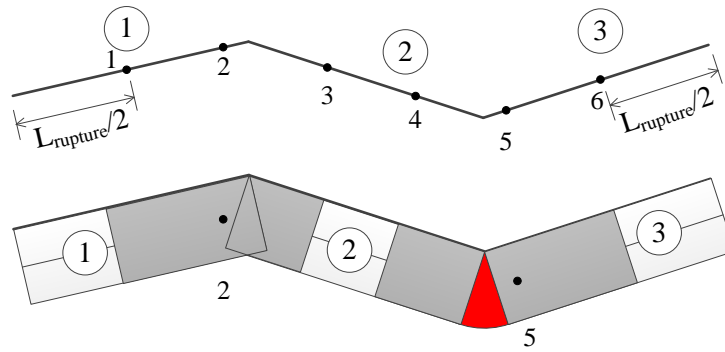


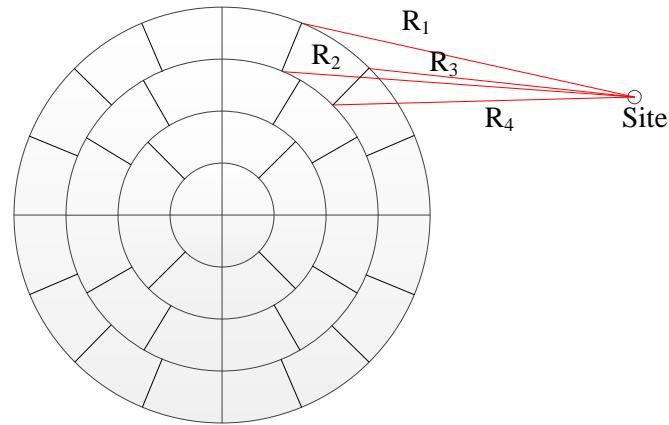
Figure D.2 Schematic illustration of rupture locations (upper panel) and top-view of the selected rupture surfaces of a representative multi-line fault with a slip rate different than 90° (lower panel)

The fictitious multi-line fault source given in Figure D.2 is composed of 3 segments. The numbers in the circles indicate the fault segment number whereas the other numbers without circles show the rupture number. The top panel of Figure D.2 illustrates the rupture locations along the strike of the fictitious multi-line fault source. The lower panel shows the projected surfaces of second and fifth rupture plane on the same multi-line fault source. On the fault source, the fifth rupture starts at the second fault segment and spans through the third fault segment. As indicated in the figure, if the rectangular geometry of rupture plane is kept rectangular through the down-dip, there exists a discontinuity between the two planes of the fifth rupture surface due to the dipping angle. However, this gap (indicated in red) is assumed as a part of the rupture surface and the source-to-site distances are calculated accordingly. This issue is not experienced at the second rupture since the two segments of the rupture surface overlap and no discontinuous surface exists.

For the fault type seismic sources the software enables the user to define three types of magnitude models; truncated normal distribution, characteristic model and composite model.

D.2.2 Background Source

The program subdivides the background source into a number of circles. The width of the circles is determined according to the rupture length and magnitude relationships proposed by Wells and Coppersmith (1994). Accordingly, for each magnitude level the number of circles is adjusted and their widths are computed. The circles are further divided into sub-areas. For each sub-area, the source-to-site distance is estimated as the shortest distance to the site. The sub-division of the background source into the several subareas and the estimation of source-to-site distances are illustrated schematically for a fictitious case.



Background Source

Figure D.3 Schematic illustration of background source geometry, sub-division into the smaller areas

For each subarea in the background source, the source-to-site distances are calculated from the four corners and the shortest one is considered as R_{jb} distance of the scenario.

D.2.3 Graphical User Interface of the Software

The graphical user interface (GUI) provides comfort to the user during the pre-analysis as well as post-analysis stage. Accordingly, users are avoided dealing with complex and time consuming operations (e.g., preparing the input files, plotting the outputs) that are handled with several internal scripts between the GUI and the main body of the program. The user can define multiple fault and background sources and associate these earthquake sources with new or existing projects. The program is able to store the project files and analysis results. A general view of the program for an existing project is given in Figure D.4. The left panel of the main window contains buttons that allow the user to access some basic menus. By making use of this panel, the user can create a new project, open an existing project file or define fault and area sources. Besides, the software has also a useful help menu that is accessible at any stage in order to guide the user.

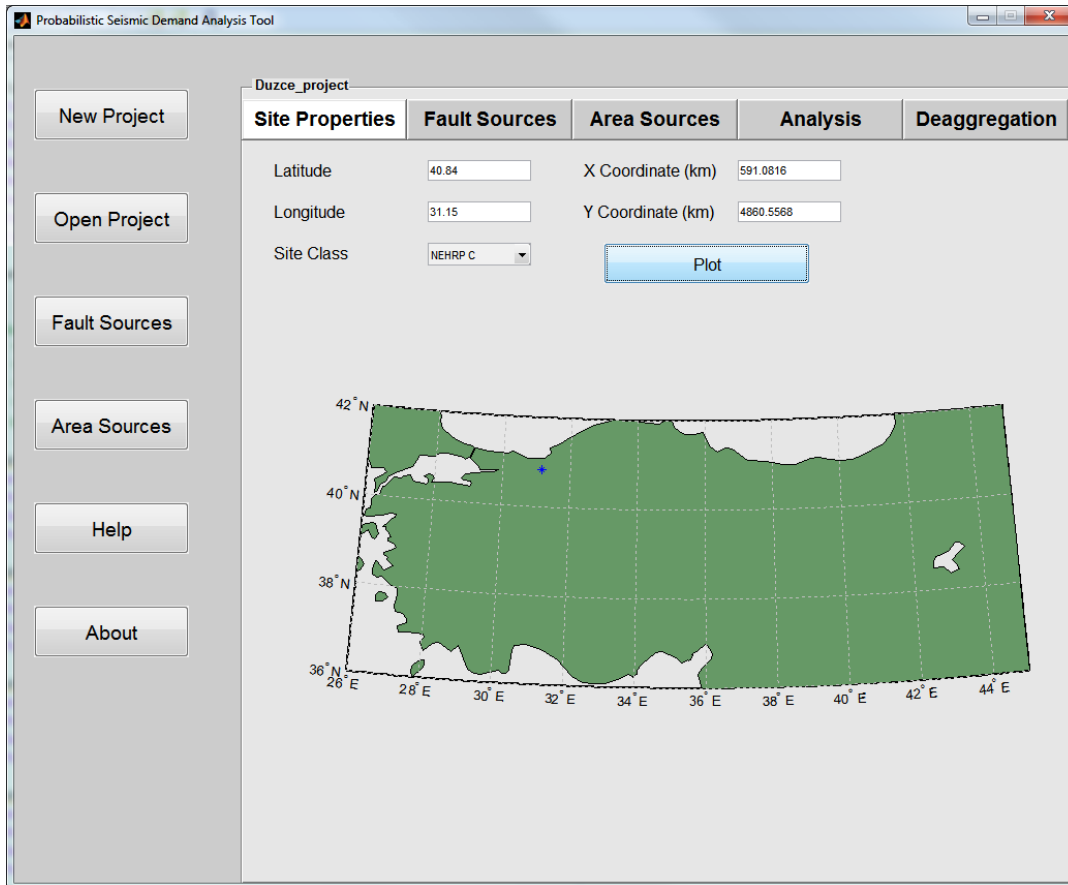


Figure D.4 GUI of the developed software

There is a menu bar on the upper panel of the main window that enables the user to define input parameters such as site properties, fault and area source for the created/opened project or to access the analysis/deaggregation stage.

After defining the project site properties and background and fault sources of concern, the user can proceed with the analysis stage. As the hazard analysis is completed, the program stores hazard and scenario tables in the project folder and plots the structural demand hazard curve in log-log scale. A sample view of the analysis window is given in Figure D.5.

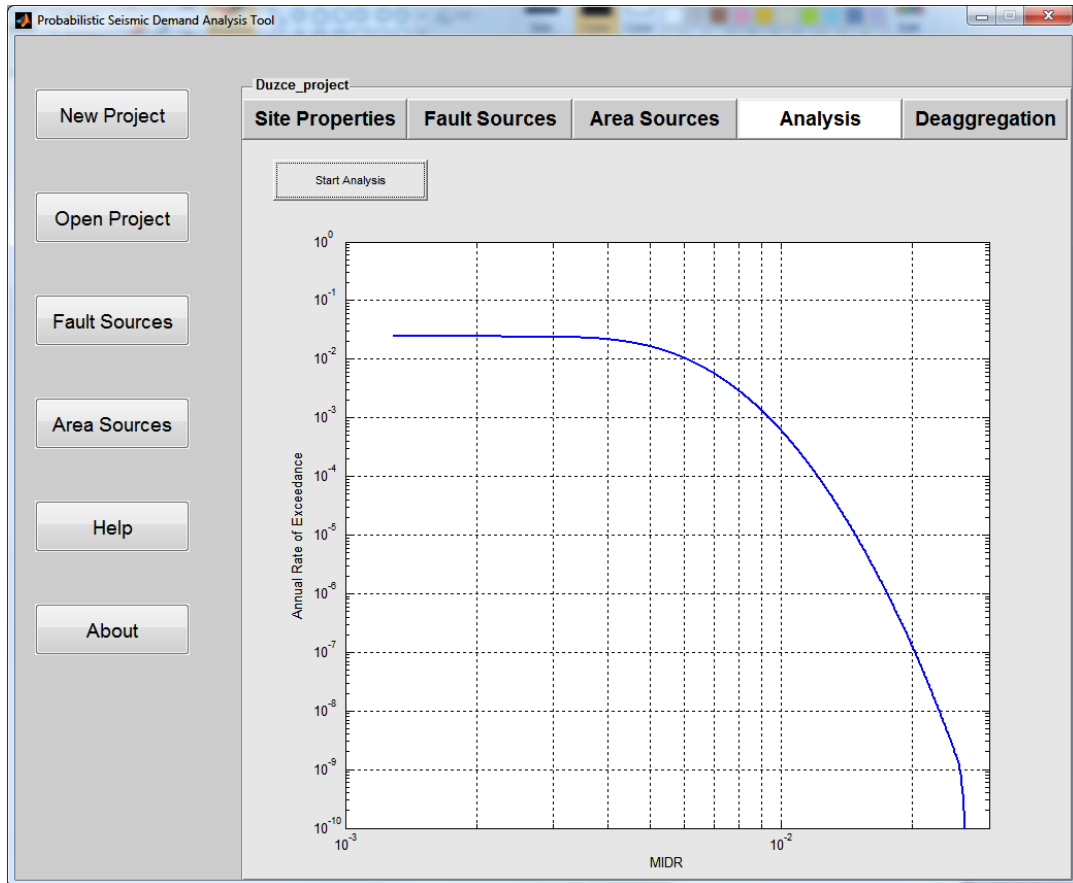


Figure D.5 View of the analysis window of the software

Using the calculated earthquake scenarios of the project, the user can also proceed with the deaggregation analysis that provides mode magnitude, source-to-site distance and epsilon values at a selected return period. The deaggregation analysis window is illustrated in Figure D.6.

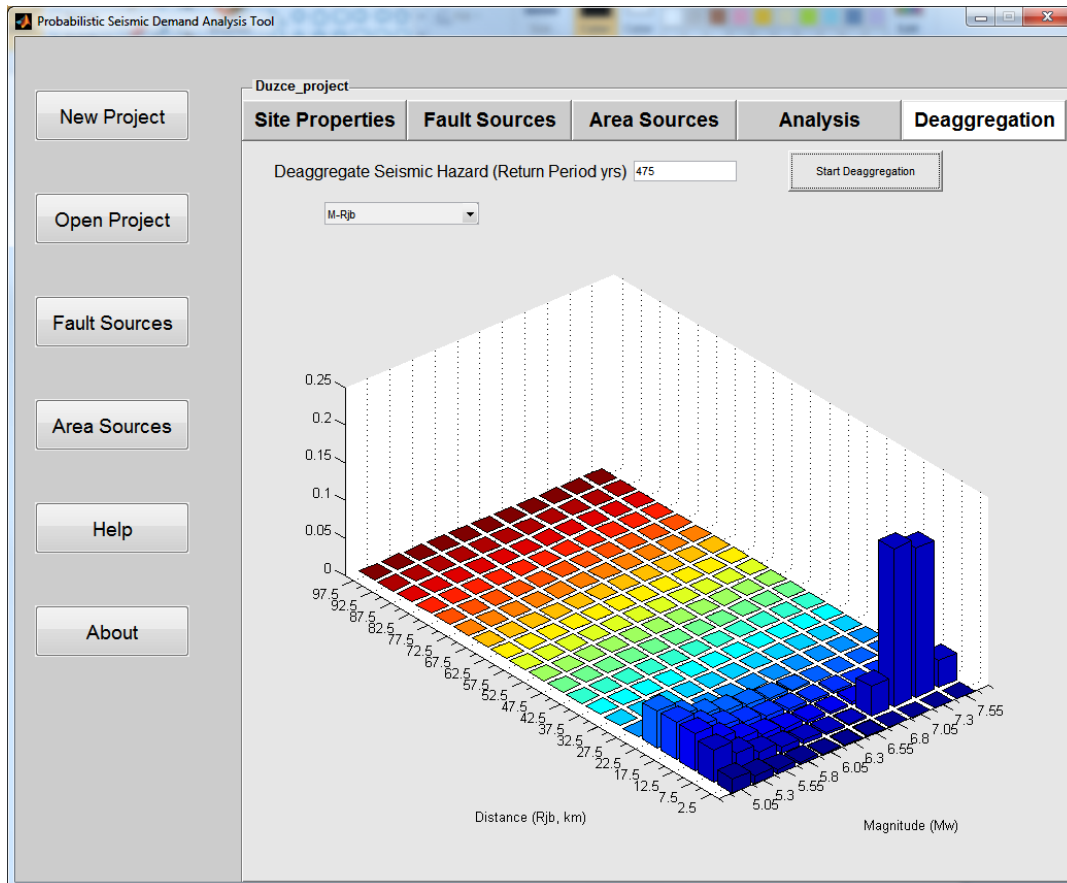


Figure D.6 Sample view of deaggregation analysis window of the program

The developed software is currently capable of providing the necessary inputs to the proposed seismic design and performance assessment methods presented in Chapter 6. The structure of the main body of the program is flexible as it is open to improvements and implementations of new features. In this sense, it is believed that the developed software with future improvements will be helpful for researchers and professionals working on this area.

APPENDIX E

RELATIONSHIP BETWEEN MIDR AND MRDR

This appendix focuses on the relationship between MIDR and MRDR. Confined to the nonlinear RHA results, MIDR versus MRDR scatters are illustrated in Figure E.1. The scatters indicate a fairly good correlation between these two EDPs. However, the observed correlation becomes weaker when MIDR and MRDR attain very small values. This observation can be explained from the dominance of gravitational effects over seismic effects: under small amplitude and distant records the gravity loads dictate the lateral deformation shape. In other words, variations in MIDR are insignificant and negligible until the earthquake action dominates the lateral deformation pattern.

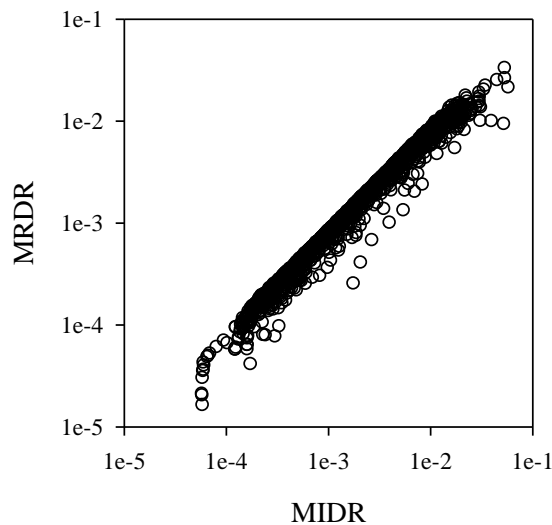


Figure E.1 The relationship between MIDR and MRDR

A linear fit is done on the logarithmic MIDR and MRDR values shown in Figure E.1. This function is given in Eq. (E.1). The seismological features of the ground-motions (i.e.,

magnitude, distance, site conditions and style of faulting) as well as structural properties such as fundamental period and building height are disregarded in this process.

$$\log_{10}(\text{MRDR})=0.995\log_{10}(\text{MIDR})-0.135 \quad (\text{E.1})$$

APPENDIX F

LATERAL STIFFNESS ESTIMATION IN FRAMES AND ITS IMPLEMENTATION TO CONTINUUM MODELS FOR LINEAR AND NONLINEAR STATIC ANALYSIS

F.1 General

Continuum model is a useful tool for approximate analysis of tall structures including moment-resisting frames and shear wall-frame systems. In continuum model, discrete buildings are simplified such that their overall behavior is described through the contributions of flexural and shear stiffnesses at the story levels. Therefore, accurate determination of these lateral stiffness components constitutes one of the major issues in establishing reliable continuum models even if the proposed solution is an approximation to actual structural behavior. This study first examines the previous literature on the calculation of lateral stiffness components (i.e. flexural and shear stiffnesses) through comparisons with exact results obtained from discrete models. A new methodology for adapting the heightwise variation of lateral stiffness to continuum model is presented based on these comparisons. The proposed methodology is then extended for estimating the nonlinear global capacity of moment resisting frames. The verifications that compare the nonlinear behavior of real systems with those estimated from the proposed procedure suggest its effective use for the performance assessment of large building stocks that exhibit similar structural features. This conclusion is further justified by comparing nonlinear response history analyses of single-degree-of-freedom (SDOF) systems that are obtained from the global capacity curves of actual systems and their approximations computed by the proposed procedure.

F.2 Introduction

Reliable estimation of structural response is essential in the seismic performance assessment and design because it provides the major input while describing the global capacity of structures under strong ground motions. With the advent of computer technology and sophisticated structural analysis programs, the analysts are now able to refine their structural

models to compute more accurate structural response. However, at the expense of capturing detailed structural behavior, the increased unknowns in modeling parameters, when combined with the uncertainty in ground motions, make the interpretations of analysis results cumbersome and time consuming. Complex structural modeling and response history analysis can also be overwhelming for performance assessment of large building stocks or the preliminary design of new buildings. The continuum model, in this sense, is an accomplished approximate tool for estimating the overall dynamic behavior of moment resisting frames (MRFs) and shear wall-frame (dual) systems.

Continuum model, as an approximation to complex discrete models, has been used extensively in the literature. Westergaard (1933) used equivalent undamped shear beam concept for modeling tall buildings under earthquake induced shocks through the implementation of shear waves propagating in the continuum media. Later, the continuous shear beam model has been implemented by many researchers (e.g. Iwan, 1997; Gülkan and Akkar, 2002; Akkar et al., 2005; Chopra and Chintanapakdee, 2001) to approximate the earthquake induced deformation demands on frame systems. The idea of using equivalent shear beams was extended to the combination of continuous shear and flexural beams by Khan and Sbarounis (1964). Heidebrecht and Stafford Smith (1973) defined a continuum model (hereinafter HS73) for approximating tall shear wall-frame type structures that is based on the solution of a fourth-order partial differential equation. Miranda (1999) presented the solution of this PDE under a set of lateral static loading cases to approximate the maximum roof and interstory drift demands on first-mode dominant structures. Later, Heidebrecht and Rutenberg (2000) showed a different version of HS73 method to draw the upper and lower bounds of interstory drift demands on frame systems. Miranda and Taghavi (2005) used the HS73 model to acquire the approximate structural behavior up to 3 modes. As a follow up study, Miranda and Akkar (2006) extended the use of HS73 to compute generalized drift spectrum with higher mode effects. Continuum model is also used for estimating the fundamental periods of high-rise buildings (e.g. Dym and Williams, 2007). More recently, Gengshu et al. (2008) studied the second order and buckling effects on buildings through the closed form solutions of continuous systems.

While the theoretical applications of continuum model are abundant as briefly addressed above, its practical implementation is rather limited as the determination of equivalent flexural (EI) and shear (GA) stiffnesses to represent the actual lateral stiffness variation in discrete systems have not been fully addressed in the literature. This flaw has also restricted the efficient use of continuum model beyond elastic limits because the nonlinear behavior of continuum models would be dictated by the changes in EI and GA in the post-yielding stage.

This paper focuses on the realistic determination of lateral stiffness for continuum models. EI and GA defined in discrete systems are adapted to continuum models through an analytical expression that considers the heightwise variation of boundary conditions in discrete systems. The HS73 model is used as the base continuum model since it is capable

of representing the structural response between pure flexure and shear behavior. The proposed analytical expression is evaluated by comparing the deformation patterns of continuum model and actual discrete systems under the first-mode compatible loading pattern. The improvements on the determination of EI and GA are combined with a second procedure that is based on limit state analysis to describe the global capacity of structures responding beyond their elastic limits. Illustrative case studies indicate that the continuum model, when used together with the proposed methodologies, can be a useful tool for linear and nonlinear static analysis.

F.3 Continuum Model Characteristics

The HS73 model is composed of a flexural and shear beam to define the flexural (EI) and shear (GA) stiffness contributions to the overall lateral stiffness. The major model parameters EI and GA are related to each other through the coefficient α (Eq. (F.1)).

$$\alpha = \sqrt{\frac{GA}{EI}} \quad (F.1)$$

As α goes to infinity the model would exhibit pure shear deformation whereas $\alpha=0$ indicates pure flexural deformation. Note that it is essential to identify the structural members of discrete buildings for their flexural and shear beam contributions because the overall behavior of continuum model is governed by the changes in EI and GA. Eq. (F.2) shows the computation of GA for a single column member in HS73. The variables I_c and h denote the column moment of inertia and story height, respectively. The inertia terms I_{b1} and I_{b2} that are divided by the total lengths l_1 and l_2 , respectively, define the relative rigidities of beams adjoining to the column from top (see Figure 3 in the referred paper).

$$GA = \frac{12EI_c}{h^2} \left[\frac{1}{1 + \frac{2(I_c/h)}{(I_{b1}/l_1 + I_{b2}/l_2)}} \right] \quad (F.2)$$

Eq. (F.2) indicates that GA (shear component of total lateral stiffness) is computed as a fraction of flexural stiffness of frames oriented in the lateral loading direction. Accordingly, the flexural part (EI) of total stiffness is computed either by considering the shear-wall members in the loading direction and/or other columns that do not span into a frame in the direction of loading. This assumption works fairly well for dual systems. However, it may fail in MRFs because it will discard the flexural contributions of columns along the loading direction and will lump total lateral stiffness into GA. Essentially, this approximation will reduce the entire MRF to a shear beam that would be an inaccurate way of describing MRF behavior unless all beams are assumed rigid. To the best of authors' knowledge, studies that

use HS73 model do not describe the computation of α in depth while representing discrete building systems as continuum models. In most cases these studies assign generic α values for describing different structural behavior spanning from pure flexure to pure shear¹. This approach is deemed to be rational to represent theoretical behavior of different structures. However, the above highlighted facts about the computation of lateral stiffness require further investigation to improve the performance of HS73 model while simplifying an actual MRF as a continuum model. In that sense, it is worthwhile to discuss some important studies on the lateral stiffness estimation of frames. These could be useful for the enhanced calculations of EI and GA to describe the total lateral stiffness in continuum systems.

F.4 Lateral Stiffness Approximations for MRFs

There are numerous studies on the determination of lateral stiffness in MRFs. The methods proposed in Muto (1974) and Hosseini and Imagee-e-Naiini (1999) (hereinafter M74 and HI99, respectively) are presented in this paper and they are compared with the HS73 approach for its enhancement in describing the lateral deformation behavior of structural systems. Eq. (F.3) shows the total lateral stiffness, k , definition of M74 for a column at an intermediate story.

$$k = \frac{12EI_c}{h^3} \beta; \quad \beta = \frac{\lambda}{2 + \lambda}; \quad \lambda = \frac{I_{b1}/l_1 + I_{b2}/l_2 + I_{b3}/l_3 + I_{b4}/l_4}{2I_c/h} \quad (\text{F.3})$$

The parameters I_c , h , I_{b1} , I_{b2} , l_1 and l_2 have the same meanings as in Eq. (F.2). The moment of inertias (I_{b3} and I_{b4}) and total lengths (l_3 and l_4) are used for the beams spanning to the column from bottom. M74 describes the lateral stiffness of a column at the ground story by modifying its boundary conditions from bottom. This modification takes place in the formulation of β that is given in Eq. (F.4).

$$\beta = \frac{0.5 + \lambda}{2 + \lambda}; \quad \lambda = \frac{I_{b1}/l_1 + I_{b2}/l_2}{I_c/h} \quad (\text{F.4})$$

Note that Eq. (F.2) proposed in HS73 is a simplified version of Eq. (F.3) for unit rotation. The former expression assumes that the dimensions of beams spanning into the column from

¹ In some papers of Miranda and his co-authors α is either readily given for some real buildings (Reinoso and Miranda, 2005) or approximate intervals of α are suggested to represent different structural behavior (Miranda and Reyes, 2002). Miranda (1999) uses an iterative procedure to approximate α for real cases by minimizing the difference between the lateral deformations of actual building and continuum model under triangular loading of different intensities.

top are the same as those spanning into the column from bottom. However, Eqs. (F.2) and (F.3) exhibit a significant conceptual difference: the HS73 approach interprets the resulting stiffness term as the shear contribution whereas M74 considers it as the total lateral stiffness.

The HI99 method defines the lateral stiffness of MRFs through an equivalent simple system that consists of sub-modules of one-bay/one-story frames. Each sub-module represents a story in the original structure and the column inertia (I_c) of a sub-module is calculated by taking half of the total moment of inertia of all columns in the original story. The relative rigidities of upper (k_u) and lower (k_l) beams in a sub-module are calculated by summing all the relative beam rigidities at the top and bottom of the original story, respectively. The total lateral stiffness of a story by HI99 is given in Eq. (F.5).

$$k = \frac{12EI_c}{h^2} \frac{k_c(k_l + k_u) + 6k_l k_u}{k_c^2 + 2k_c(k_l + k_u) + 3k_l k_u} \quad (\text{F.5})$$

The parameter k_c and h denote the relative rigidity and length of the column in the sub-module, respectively. The total lateral stiffness at ground story is computed by assigning relatively large stiffness values to k_l to represent the fixed-base conditions. Eq. (F.5) has a similar functional format as Eqs. (F.2) and (F.3). Since the lateral stiffness computed stands for the total lateral stiffness, it exhibits a more similar theoretical framework to M74.

Discussions presented above indicate that both M74 and HI99 consider the variations in lateral stiffness at the ground story due to fixed-base boundary conditions. However, they ignore the free end conditions at the top story. As a matter of fact, Schultz (1992) pointed that lateral stiffness changes along the building height might be abrupt at boundary stories. The boundary stories defined by Schultz (1992) not only consist of ground and top floors but also the second story because the propagation of fixed-base conditions above the ground story level is prominent at the second story as well. Although Schultz (1992) proposed correction factors for boundary stories of some specific cases, he does not give a general expression that accounts for the stiffness changes at boundary stories.

F.5 Proposed Methodology for Describing Lateral Stiffness in Continuum Models

F.5.1 Computation of Story-dependent α

The importance of heightwise variation of boundary conditions in approximating the lateral stiffness of discrete systems for continuum models is briefly addressed in the previous section. Within this context, a functional form to approximate the heightwise variation of α is computed to enhance the lateral stiffness definition in continuum models.

The story-dependent variation of α is calculated using 8 sets of generic MRFs. Each building set contains 14 models with number of stories varying between 2 and 15. All buildings are 3-bay frames with beam lengths of 5 m and column heights of 3 m. The initial Young's modulus is assumed as 20,000 MPa for the structural members. The objective of having large number of generic buildings is to cover a wide range of MRF behavior while deriving story-dependent α . Table F.1 lists the fundamental period (T_1) intervals of building sets as well as the corresponding joint rotation indices, ρ (Blume, 1968). This parameter measures the relative contributions of shear and flexural behavior by considering the ratio of sum of the beam rigidities to column rigidities at the mid-height story of the building. When Eqs. (F.1) - (F.4) are considered, one can immediately realize that Blume's index accounts for the important variables in the lateral stiffness definitions of continuum and discrete systems. Its calculation is straightforward for building systems and the analyses conducted within the context of this study showed that it correlates fairly well with the story-dependent variation of α that is shown in the following paragraphs. Based on these facts this parameter is used in the analytical expression presented later in this section that can be considered as an improvement for quick adaptation of continuum models to building systems.

Table F.1. Important features of model buildings used in the derivation of story-dependent α variation, comparison of their elastic fundamental periods with those estimated from the continuum model.

Building Set #	ρ	T_1 range discrete models*	T_1 range continuum models*
Set1	0.05	0.18s-2.05s	0.19s-2.14s
Set2	0.10	0.26s-2.10s	0.23s-2.21s
Set3	0.30	0.21s-1.84s	0.22s-1.88s
Set4	0.60	0.32s-2.51s	0.33s-2.65s
Set5	0.75	0.31s-2.40s	0.32s-2.44s
Set6	1.00	0.19s-1.56s	0.19s-1.55s
Set7	1.50	0.15s-1.28s	0.16s-1.26s
Set8	2.00	0.14s-1.23s	0.12s-1.19s

*The lower and upper values correspond to the elastic fundamental periods (T_1) of 2- and 15-story frames in each building set, respectively.

The variation in α along the total height of a discrete building is obtained by calculating the flexural and shear stiffnesses at each story level. The lateral stiffness due to unit displacement at a story is assumed to be the total lateral stiffness of that story. The flexural stiffness at each story is computed by solving a fictitious cantilever column member for a unit displacement. These analyses are conducted by modeling all structural systems in OpenSees (2008) with “*elasticBeamColumn*” element. The sum of column flexural rigidities in the story is assigned to this member for the flexural stiffness calculations. The difference between the total and flexural stiffnesses yields the shear stiffness (GA) for a unit displacement and it must be modified for a unit rotation to be consistent with the corresponding definition in HS73. For the story under consideration, α is then the ratio of shear (GA) and flexural (EI) stiffnesses as presented in Eq. (F.1). [In reinforced concrete

frames, cracked flexural rigidity, EI_{cracked} , can be considered via recommendations of ASCE (2007)]. Computation of story-dependent α as described here is rough because boundary conditions implemented during the calculation of shear and flexural stiffness contributions are inaccurate. Besides, the calculations are based on the models with constant bay lengths and story heights that can be considered as another simplification because these dimensions are basely constant in real buildings. Nevertheless, the results are within the limits of engineering tolerance as will be verified by the case studies discussed in the paper. The heightwise variation of α for 10- and 15-story buildings selected from the generic MRF sets is presented in Figure F.1 in terms of ρ and story number. The figure shows that α is not constant along the building height due to the changes in boundary conditions. Its variation is generally mild along the intermediate stories but it exhibits abrupt changes at lower and top stories. This behavior is consistent with the observations made by Schultz (1992). The gradual variation of α at mid-stories is based on the nominal changes in the boundary conditions at these story levels. Large α at the lower stories suggest that they are dominated by shear behavior and they can be more vulnerable to shear deformation effects. A smaller value of α , as in the case of roof stories, implies considerable flexural effects.

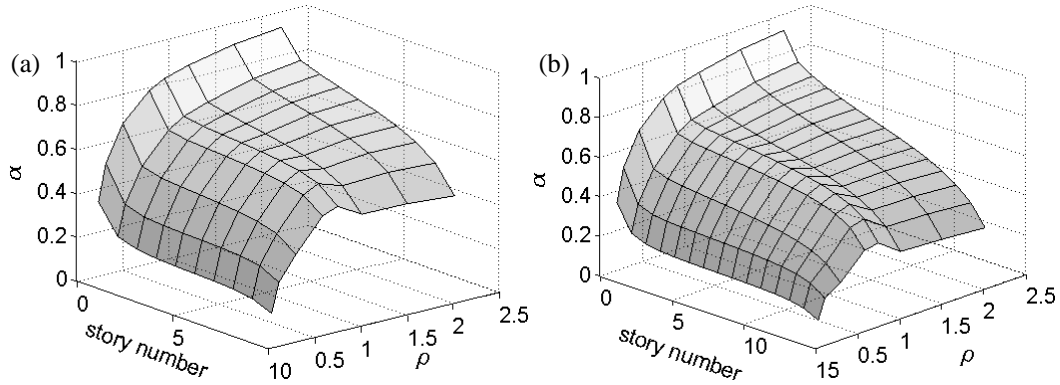


Figure F.1 Heightwise variation of α in (a) 10-story and (b) 15-story frames of building sets 1 to 8

The functional form for approximating the variation of α presented in Figure F.1 is given in Eq. (F.6). The proposed expression is divided into three major components. α for ground story (Eq. (F.6.a)) is computed via the formulation described in HI99 (i.e. Eq. (F.5)) because its performance is similar to the α derived from discrete buildings at ground level. Computation of α for intermediate and roof stories is done by using Eqs. (F.6.b) and (F.6.c), respectively that are obtained from the least square fits to the story-dependent α variation in Figure F.1. The subscript j in these expressions designates the story level (starts from $j=2$) whereas “ n ” denotes the total story number.

$$\alpha_{\text{ground}} = \left[\frac{3}{h^2} \cdot \left[\frac{2(k_c + 6k_u)}{2k_c + 3k_u} - 1 \right] \right]^{0.5} \quad (\text{F.6.a})$$

$$\alpha_{n,j} = (a + bj)\exp(-0.0023\rho + 0.008)$$

$$a = 0.97 - 0.86\exp(-181\rho^{0.69}); \quad b = -\frac{(0.006 + 0.011\rho)}{(1 - 0.38\rho + 0.14\rho^2)} \quad (\text{F.6.b})$$

$$\alpha_{n,\text{roof}} = (cd^n n^e)\exp(-0.0023\rho + 0.008); \quad c = 0.81 * 0.98^{1/\rho} \rho^{0.22}$$

$$d = 0.92 \cdot 0.99^\rho \rho^{-0.03}; \quad e = \frac{-0.028 + 0.311\rho^{1.54}}{0.1 + \rho^{1.54}} \quad (\text{F.6.c})$$

F.5.2 Calibrating the Differences in the Lateral Loading Patterns of Discrete and Continuum Systems

The lateral displacement estimations of continuum model is improved further through a correction factor (CF) that accounts for the differences in the application of lateral loading patterns to discrete and continuum systems. Inherently, the lateral loads are applied at the story levels in discrete systems whereas the lateral loading pattern is distributed over the entire height of the continuum system. Thus, under the same loading amplitude, continuum and discrete systems would not produce the same displacements. Although this difference vanishes with increasing story number, it is pronounced in low-rise buildings. The proposed CF is derived by taking the ratio of tip displacements of a cantilever subjected to continuous and discrete loadings consecutively. Discrete loading is applied at heights corresponding to the story levels to imitate the loading conditions in actual frames. Fundamental-mode loading pattern of each building set is used during the analysis. The variations in tip displacement ratios of discrete to continuous loading for each building set are given in Figure F.2.

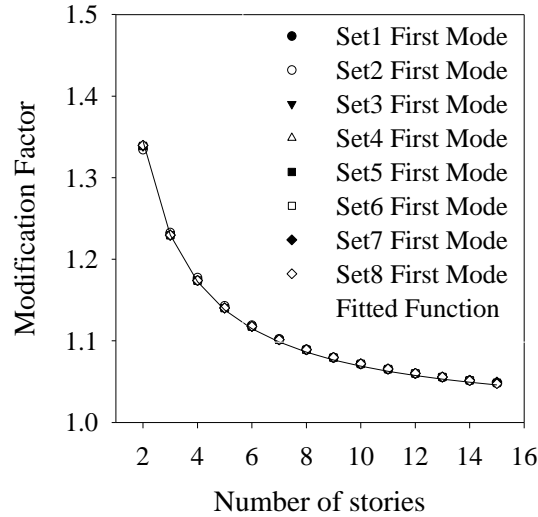


Figure F.2 Variation of CF (solid line) computed from fundamental-mode loading patterns of each building set

Negligible differences in tip displacement ratios between the building sets advocate that CF is independent of MRF behavior (i.e. CF is not a function of α). The validity of this outcome is verified by computing the tip displacement ratios of the cantilever in pure shear and pure flexure. The ratios practically do not change under these marginal cases giving strength to this outcome. Finally, the CF derived from tip displacement ratios applies to the lateral displacements along the entire length of the continuum model that is also validated during these analyses. Eq. (F.7) shows the proposed correction factor as a function of total story number, n , that modifies the lateral displacement estimations of the continuum system under fundamental-mode loading. Apparently, this modifying factor would be influential on the accurate lateral displacement estimations of low-rise structures whereas its effect will be reduced considerably with increasing story number.

$$CF = \frac{u_{\text{discrete load}}}{u_{\text{continuous load}}} = 1.0 + \frac{0.69}{n} \quad (\text{F.7})$$

F.6 Evaluation of Proposed Methodology

The performance of the proposed formulations explained in the previous section is assessed by comparing the fundamental periods and lateral displacements of the model buildings with those estimated from the continuum model. To observe the improvements in lateral displacement estimations better, HS73, M74 and HI99 are also evaluated together with the proposed methodology. A technique similar to the one described in the previous section is followed while implementing M74 and HI99 to the continuum model. The flexural stiffness

contributions at each story level are extracted from the total lateral stiffness expressions by disregarding the contributions of beams framing into upper ends of columns (to replicate free-end conditions). The computed flexural stiffnesses are then subtracted from the total lateral stiffness values (computed either from Eq. (F.3) or (F.5) depending on the methodology) and modified for a unit rotation to obtain the corresponding shear stiffness contributions.

Essentially, the square root of the ratios of shear to flexural stiffnesses yields the corresponding α for each method. Table F.2 compares the resulting α values pointing that HI99 estimations are larger with respect to those computed from M74. Although not shown in Table F.2 for brevity, the α computed by HS73 is infinity (shear beam) for the model buildings for reasons discussed in the previous paragraphs. When the variation of α computed from discrete buildings is compared with those of simplified methodologies, one can immediately note the oversimplification implemented by these methods. They are not sensitive to the variations in α along the building height. This is the consequential effect of disregarding the changes in boundary conditions at the lower stories and at the roof level.

Table F.2 Calculated α values for the methods other than the one proposed in this study

Set	Method	Ground Story	Intermediate Story
		α	α
1	HI99	0.31	0.22
	M74	0.19	0.15
2	HI99	0.51	0.38
	M74	0.32	0.27
3	HI99	0.69	0.56
	M74	0.48	0.41
4	HI99	0.80	0.70
	M74	0.60	0.54
5	HI99	0.83	0.74
	M74	0.65	0.60
6	HI99	0.87	0.79
	M74	0.7	0.66
7	HI99	0.90	0.85
	M74	0.76	0.75
8	HI99	0.93	0.88
	M74	0.81	0.81

This shortcoming may result in significant discrepancies between the lateral deformation patterns of simplified methods and actual systems as it will be shown in the next paragraph. The estimated α values from the proposed methodology (i.e. Eq. (F.6)) and alternative relationships (Table F.2) are implemented to the continuum model to approximate the actual lateral displacement patterns of buildings under fundamental-mode loading. As stated in the previous paragraphs, the discrete buildings are modeled by OpenSees (2008) and are analyzed under the first-mode lateral loading pattern. The calculated lateral displacement profiles by OpenSees are assumed as “*exact*”. The continuum models are solved numerically by applying the transfer matrix method presented in Heidebrecht and Stafford Smith (1973)

through a MATLAB code prepared during the course of this study. The heights of continuum and building models are equal to each other and stories are represented with 90 equal-height slices in the continuum model. The transfer matrix method requires uniform loading at each segment and this is achieved by approximating the continuous lateral loading as a uniform lateral loading along the height of each slice. The correction factor in Eq. (F.7) is also applied to the displacements of continuum model to compensate the effects of continuous vs. discrete loading patterns as discussed in the previous section.

Figures F.3.a to F.3.c present the evaluations of HS73, HI99 and M74 approximations by computing the error between the approximate and “*exact*” roof displacements. The error is given in per-cent and it is defined as the normalized difference between the “*exact*” and approximate roof displacements. The normalization is done with respect to the “*exact*” roof displacements ($\text{error} = 100 \times (\Delta_{\text{top,approx}} - \Delta_{\text{top,exact}}) / \Delta_{\text{top,exact}}$). Positive errors would describe conservative estimations with respect to OpenSees results. Figure F.3.d shows the performance of roof displacement estimations when the story-dependent variation in α (Eq. (F.6)) is used in the continuum model. The error variation in Figure F.3.a shows that the HS73 approach (shear-beam model) would result in significantly safe lateral deformation estimations at low-rise buildings, in particular, when the frame behavior is dominated by flexure (i.e. small ρ). Inherently, the overestimations tend to decrease when the shear behavior starts dominating (i.e. large ρ) and story number increases. Nonetheless, the approximations by HS73 are still large emphasizing the artifacts due to its main assumptions in the lateral stiffness computation of MRFs. Muto approach (Figure F.3.c), though not as much as HS73, also tends to overestimate lateral deformations at low- and mid-rise frames with dominant flexural behavior. On the other hand, HI99 (Figure F.3.b) estimates roof displacements fairly well particularly at low-rise buildings. Given the conceptual similarity between M74 and HI99, the overestimations by M74 for flexure-dominated frames can be attributed to the insufficient performance of its modification factor (β). HI99 performs towards unsafe estimations at high-rise frames regardless of the variations in ρ . This can originate from disregarding the change in boundary conditions at the upper stories that is significant when the story number increases. As it is depicted in Figure F.3.d, the error in lateral displacement estimations decreases significantly, when the variation of boundary conditions along the building height is properly taken into consideration.

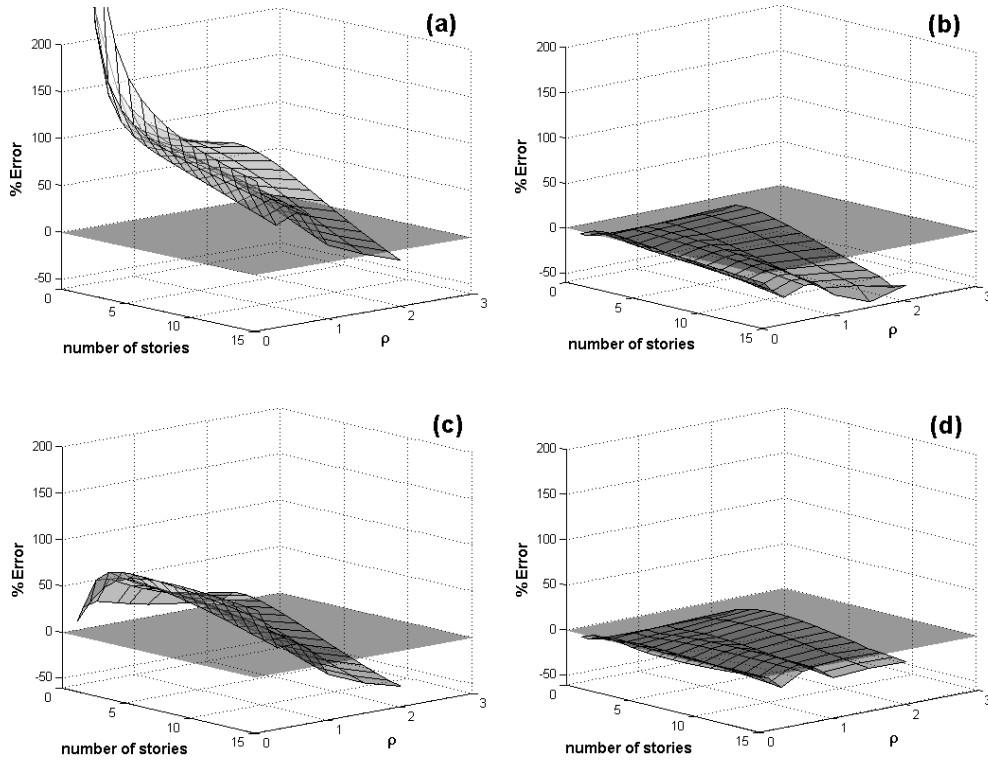


Figure F.3 Error surfaces of roof displacements in percent as a function of story number and ρ for (a) HS73, (b) HI99, (c) Muto and (d) this study under first-mode loading pattern

The prominence of story-dependent α variation is emphasized further in Figure F.4.a by evaluating HS73, HI99, M74 and the proposed methodology through the continuum model that represents the 15-story frame model in Building Set 4 ($\rho=0.6$). A high-rise building model is chosen because it better illustrates the discrepancy between the approximate displacements of analytical methods and the exact displacement profile computed from OpenSees (solid line). The lateral displacement plot of the continuum model that considers story-dependent α variation (Eq. (F.6)) is shown in thick dashed line. The plots in this figure reinforce the observations made from error statistics. The M74 and HS73 methodologies significantly overestimate the actual lateral deformation profile due to their underlying simplifications. The HI99 procedure captures the lateral deformations at lower stories fairly well. It underestimates the displacements at the higher levels as it disregards the changes in boundary conditions at the upper stories. On the other hand, the lateral deformation profile of the continuum model that implements story-dependent α values follows the actual lateral profile closely throughout the entire building height. Figure F.4.b compares the fundamental periods of model buildings (OpenSees) and corresponding continuum systems to evaluate the consistency of dynamic characteristics in the simplified versions of the actual buildings. The fundamental period match between the actual buildings and corresponding simple

continuum models is quite satisfactory. The match between the actual buildings and their simplification is quite satisfactory.

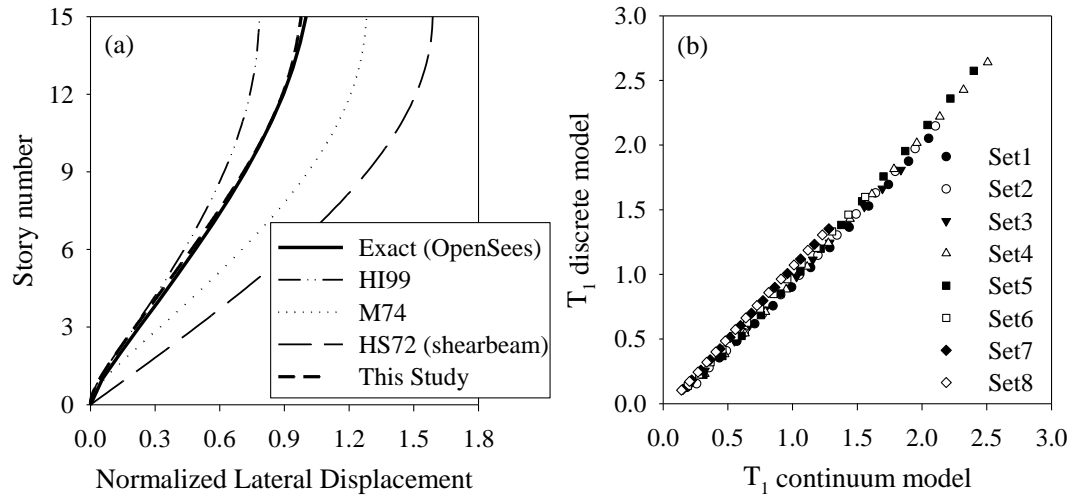


Figure F.4 (a) Exact and approximate elastic lateral displacement profiles of the 15-story frame from Building Set 4, (b) Exact vs. approximate fundamental periods of the entire building models

F.7 Extension of the Proposed Methodology to Nonlinear Frame Behavior

Reasonable implementation of lateral stiffness variation to continuum model via α can lead to its more efficient use for estimating nonlinear structural behavior. Since α establishes a relationship between GA and EI , its coherent estimation associated with the proper variation of EI in the post-elastic stage would be sufficient to achieve this objective. In other words, adjustment of α with the level of nonlinearity would result in a fairly well description of inelastic structural behavior via continuum model. This is discussed in the rest of the text.

Representative moment-curvature (M - ϕ) relationships at the story levels can define the overall variation of EI in the post-elastic range that can be obtained by considering the failure mechanisms (i.e. beam- and column-sway or hybrid) in frame systems. Note that the redistribution (or redundancy) feature in discrete systems cannot be fully achieved in the continuum model. This leads to some simplifying assumptions while defining the global M - ϕ curves. The major assumption at this point is the conservation of work ($\Sigma W_{ext} = \Sigma W_{int}$) to describe the total plastic moments (ΣM_p) for each failure mechanism as well as the continuum system. A similar approach is also used by Borzi et al. (2008) in their simplified nonlinear static methodology. The plastic moment expressions derived from $\Sigma W_{ext} = \Sigma W_{int}$ are used in the scaling of global M - ϕ relationships to remove the systematic differences

between the discrete and continuum systems in the post-elastic stage. This concept is illustrated in Figure F.5. The sketch presents discrete systems failing in beam-sway (Figure F.5.a), column-sway (Figure F.5.b) and the representative continuum model in the post-elastic stage (Figure F.5.c). The plots also display the corresponding internal and external work expressions that are presented under each system. These expressions assume that the lateral forces on the discrete and continuum models are the same that is warranted via Eq. (F.7). Note that the continuum system misrepresents the lateral displacements of column failure that results in a disagreement between the plastic moment expressions of these two systems (i.e. $\Sigma W_{p, col-mech}$ vs. $\Sigma W_{p, continuum}$ presented in Figure F.5). Thus, $\Sigma W_{p, col-mech} / \Sigma W_{p, continuum}$ ratio is used to modify the ordinates of global M- ϕ relationships to correct this discrepancy. The same adjustment is unnecessary for beam-sway mechanism since the continuum model can fairly represent the displacement patterns in this case. In this study, the global M- ϕ adjustment presented for column-sway is assumed to be applicable in hybrid failure because this failure mechanism is also triggered by the plastification of ground-story columns. Thus, its lateral displacement pattern may show similar attributes to column-sway mechanism.

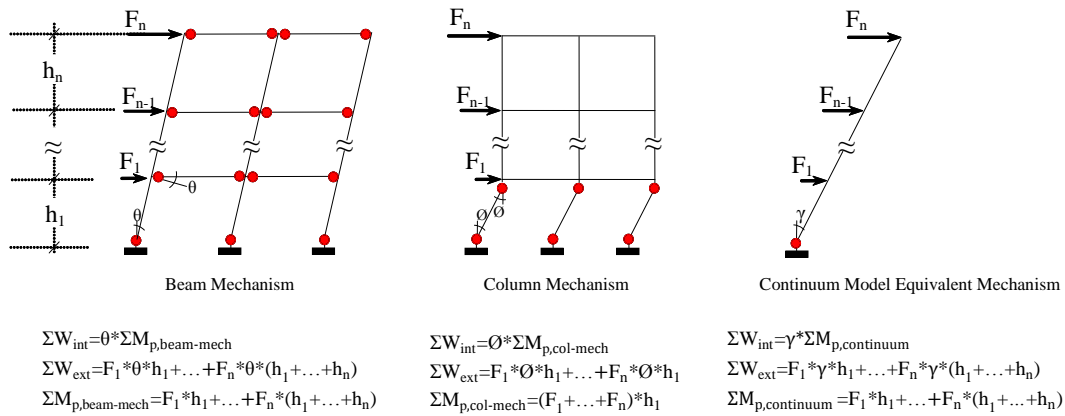


Figure F.5 Failure mechanisms and the conservation of work concept

Figure F.6.a shows the representative M- ϕ plots for column and beam members that are used in deriving the global M- ϕ relationship of the continuum model given on the left panel (Figure F.6.b). In this study, the column and beam moment capacities are computed from OpenSees using the “zerolength section” element. The Kent and Park (1971) model is used in concrete and elastic-perfectly plastic behavior is assumed for steel since the rebars are assumed to be hot-rolled steel. The column M- ϕ relationship must consider the axial loads that can be approximated by simplified methods such as tributary area concept. The axial loads on beams can be assumed as zero for their M- ϕ relationship that result in similar yielding and ultimate moment capacities (Figure F.6.a). The noticeable capacity loss in columns after yielding is the result of excessive axial loading and it mostly leads to negative slope in the post-elastic branch of global M- ϕ diagrams for reinforced-concrete (RC) structures. The decrease in story number (lesser redistribution) increases the value of this

negative slope. (Note: $M-\phi$ relationships shown in Figure F.6.a and accompanying discussions are confined to RC column and beam behavior. On the other hand, these relationships can be extended to any other material behavior). The parameters M_y and M_u in Figure F.6.b refer to global yielding- and ultimate-moment. The intermediate pivot moment, M_{ip} , is introduced to the global $M-\phi$ curve so that it can closely follow the actual nonlinear behavior of the discrete system. The global $M-\phi$ relationship is implemented to the continuum model by considering the lateral stiffness changes at each story level due to story-dependent α behavior as discussed in the previous sections. The cracked-section EI is considered while defining the initial branches in the global $M-\phi$ curves. Depending on the level of gravity loads 50% - 60% of uncracked stiffness is considered for columns whereas this reduction is accepted as 50% in beams (ASCE, 2007). α is varied gradually from its initial value (α_0) upon the commencement of post-elastic range (i.e. between M_y and M_{ip}) in order to simulate hinging patterns in different failure modes that are described in the following paragraphs.

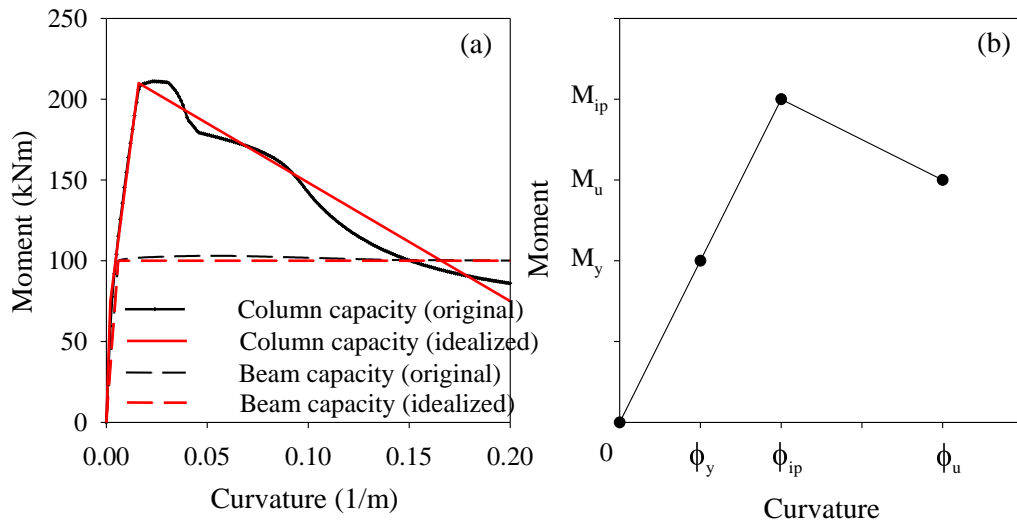


Figure F.6 (a) Representative moment-curvature relations and their idealizations for RC column and beam sections; (b) their implementation to global $M-\phi$ relation of the continuum model

For frames failing in beam-sway, the yielding-moment (M_y) of global $M-\phi$ is the sum of beam yielding moments of the entire system. The ultimate-moment (M_u) for this failure mode is determined from the ultimate moment capacity contributions of all beams in the system as well as the ultimate capacities of ground columns. M_{ip} is calculated as the maximum moment capacities of ground-story columns and the yielding moments of individual beams in the entire system. Since many discrete models failing in beam-sway do not follow a fully idealized beam hinging pattern (see upper stories of 8-story frame in Figure F.8), the variations in α due to nonlinear behavior is kept limited up to mid-height in the continuum model for this failure mode. Below the mid-height level α is assumed as zero when M_{ip} is reached because the resistance against rotation is considered to be negligible

due to the formation of plastic hinging in beams. A linear relationship is established to account for the variation in α that is given in Eq. (F.8). This expression shows the changes in α (denoted by α_j) for moment values M_j that vary between M_y and M_{ip} . α is kept constant (i.e $\alpha=\alpha_0$) for levels above the mid-height for the rest of the continuum model.

$$\alpha_j = \alpha_0 - \frac{\alpha_0}{M_{ip} - M_y} (M_j - M_y) \quad (F.8)$$

In the case of column mechanism, the M_y of $M-\phi$ is the overall maximum moment capacities at the lower-ends of ground-story columns (where the initial plastic hinging is expected to occur). The ultimate-moment capacity, M_u , of $M-\phi$ is computed from the ultimate moment capacities at the lower and upper ends of columns at the ground-level. The intermediate pivot point M_{ip} considers the yielding moments at the upper ends of columns and the maximum moment capacities at the lower ends of the columns in the ground story. The $M-\phi$ relationship for this failure mode is modified further by considering the $\Sigma W_{p, col-mech} / \Sigma W_{p, continuum}$ for the reasons discussed in the previous paragraphs. After performing the described modifications, the global $M-\phi$ is lumped to the representative ground story in the continuum model as the entire nonlinear behavior is supposed to occur at this level. In column-sway failure mechanism, beams are assumed to behave in the elastic range thus α is kept constant until M_{ip} is reached. α is assumed zero after M_{ip} at the first story to accommodate the post-elastic branch of global $M-\phi$. This way the instabilities in the transfer matrix solution are prevented for a possible negative EI.

In this study, the hybrid failure mechanism is assumed to have similar features as in the case of column-sway mode. Therefore, a methodology similar to the above paragraph is followed to derive the global $M-\phi$ relationship in the continuum model. The gradual variation of α after post-yielding is considered similar to the beam-sway mechanism for the entire continuum model using Eq. (F.8) due to the development of plastic hinges in beams. Regardless of the failure mechanism, the post-yielding stiffness in the global $M-\phi$ relationships is controlled by the displacement capacity expressions of Borzi et al. (2008). In other words, the analysis must be terminated at this displacement capacity. Figure F.7 presents a flowchart that summarizes the entire procedure proposed in this study.

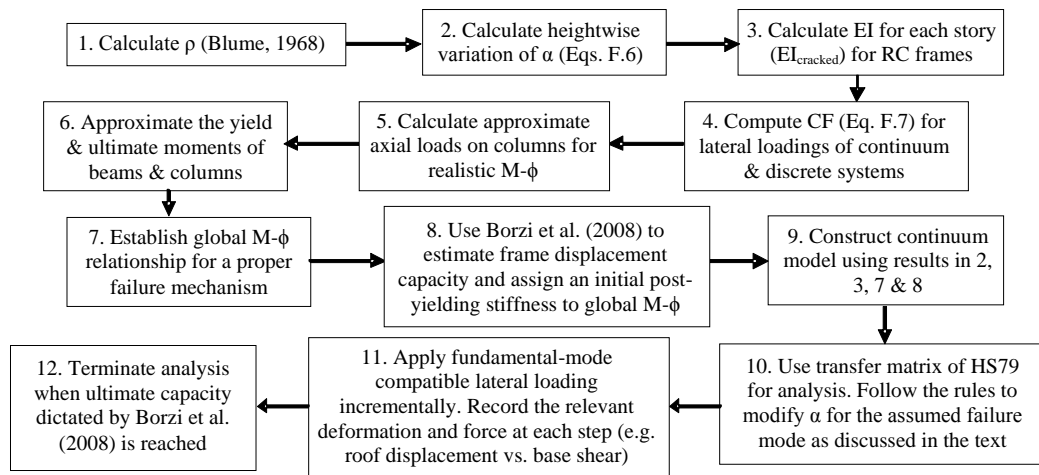


Figure F.7 Flowchart that summarizes the entire steps in the proposed procedure

F.8 Evaluation of Proposed Method for Nonlinear Frame Behavior

The steps presented in the previous section are implemented to approximate the nonlinear global pushover curves (roof displacement vs. base shear) of MRFs under fundamental-mode loading. To test the general applicability of the method, RC frames of 3-, 5- and 8-story buildings are investigated. These buildings feature typical low-to-mid rise building inventory in Turkey. They were modeled and designed in 3-D environment confirming the Turkish seismic code provisions. The 2-D frames presented here are the selected continuous frames from the corresponding 3-D models. The RC column members show loss of strength after yielding due to the facts explained in the previous section. The beam and column dimensions of buildings reduce gradually starting from the 2nd story that is a common design practice in Turkey. The important geometrical properties of 3- and 8-story frames used in the evaluation are presented in Figure F.8.

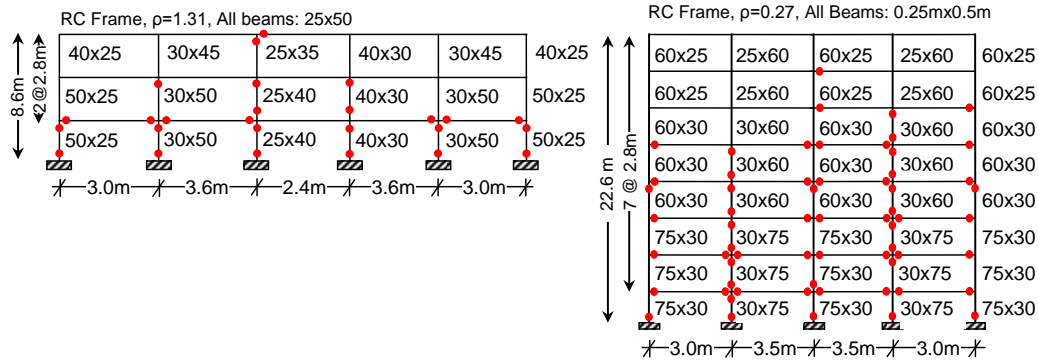


Figure F.8 3- and 8-story RC MRFs from Turkish construction practice that are used in the evaluation of continuum model in the nonlinear range. 3-story frame fails under the hybrid mechanism whereas 8-story frame shows a beam-sway failure pattern

The hinging patterns under first mode lateral loading displayed in Figure F.8 suggest a dominant beam-sway mechanism for 8-story building (a similar behavior is also valid for the 5-story building that is not presented here for spacing concerns). The 3-story building resembles a hybrid mechanism although the ground-floor columns show plastic hinging at both ends due to the differences in story heights between ground story and upper floors. Although the subject frames are designed for strong column–weak beam behavior based on the regulations of Turkish seismic code, the observed hinging pattern in the 3-story frame advocates important differences between 3-D and 2-D structural behavior that should be considered before the application of proposed methodology. Under the discussions presented here the analyst should pay particular attention to the story height, bay width and member length while deciding on a justifiable failure mechanism. In the case of competing mechanisms due to uncertainties in building configuration, the analyst may consider the most inconvenient one among the alternatives to obtain conservative global capacity estimation. Our failure mechanism assumptions can be considered as realistic based on the comparisons presented in the rest of this section.

We first verified our assumption of suppressing the changes in α for floors above the mid-height of the buildings failing in beam-sway mechanism. Figure F.9.a and F.9.b show the results of sensitivity analyses for the 5- and 8-story RC buildings, respectively that primarily deform under beam-sway among the sample frames discussed in the previous paragraph. The sensitivity analyses are based on the approximate pushover (PO) curves computed from the continuum model under fundamental-mode lateral loading. For each building case, a set of PO curves are computed by varying α at different floor levels. (For example, the “Story 1” legend in Figures 9a and 9b designates the PO curves in which α is varied only in the 1st floor level during the entire nonlinear static analysis. Similarly, the “Story 5” legend corresponds to the PO curves when α is varied in the first 5 floors). This way the sensitivity of global PO curves to the variations in α along the building height is obtained. The approximate pushovers are then compared with the “exact” global capacity curves of the

corresponding discrete buildings determined from the OpenSees. (The beam and column members of discrete buildings are modeled by using “*nonlinearBeamColumn*” and “*displacementBeamColumn*” elements in OpenSees, respectively). The comparative plots suggest that variation of α at stories below the mid-height (i.e. “Story 3” in Fig. 9a and “Story 5” in Fig. 9b) yields comparable matches with the global capacity curves obtained from the corresponding discrete models. These observations justify our assumption about limiting the variation of α up to mid-height stories for systems failing under beam-sway mechanism.

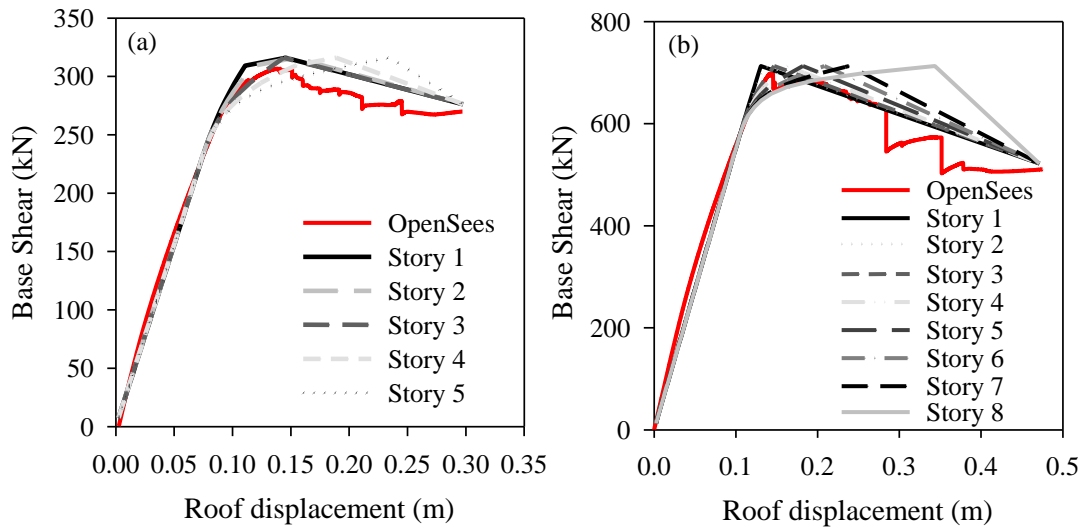


Figure F.9 Sensitivity analyses on the verification of α behavior along the building height for systems failing under beam-sway mechanism

Figure F.10.a compares the overall pushover curves of discrete 3-, 5- and 8-story RC frames with the corresponding approximations obtained from the continuum models. Figure F.10b-F.10.d also shows the lateral displacement profiles of discrete and continuum models during the PO analysis.

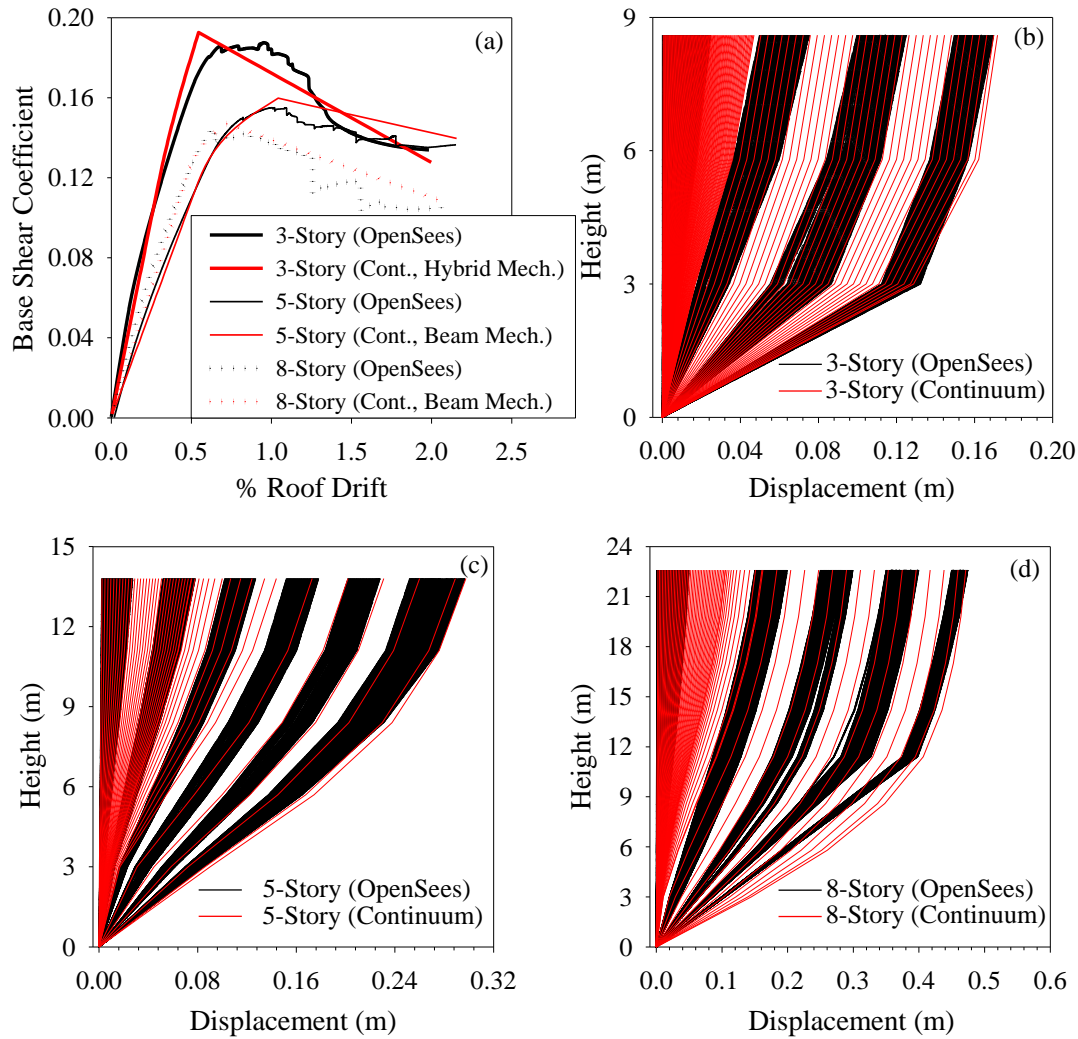


Figure F.10 Comparisons of PO curves and corresponding lateral displacement profiles during the nonlinear static analysis of the sample RC MRFs and the corresponding continuum models. Note that lateral profiles of discrete systems (computed from OpenSees) are given in discrete intervals to compare the genuine and approximate profiles more clearly

When the initial branches of PO curves are of concern (Figure F.10.a) the close behavior of discrete and continuum models advocates the successful estimation of initial α by the proposed method. The pushover curves indicate that the continuum system, therefore the proposed method, is capable of representing the nonlinear behavior when compared to the *exact* solution. The continuum model also captures the lateral displacement profiles of 3- and 5-story frames fairly well (Figs. 10b, 10c). The reliability in the lateral displacement estimations decreases for the 8-story building but they can still be considered within the acceptable limits of accuracy (Fig. 10d). Note that the lateral displacement estimations of the proposed method can be a direct measure to predict the interstory drift capacity of discrete systems. Discrepancy between the continuum system and the actual discrete model

accentuates with the increased nonlinearity that may stem from the overwhelming approximations made in the proposed methodology while mimicking the genuine nonlinear behavior (e.g. simplifications in limit state analysis while describing the global $M-\phi$ relationships or erroneous estimations of actual α variation through Eq. (F.6)). The complicated geometrical variations of actual systems that cannot be fully captured with the continuum model can also contribute to the low performance of the proposed technique with the increased nonlinear deformations. Regardless of these deficiencies, the proposed methodology is still capable of representing the overall nonlinear behavior of actual MRFs and can capture the negative slope in the post-elastic range for systems that are subjected to strength and stiffness loss after yielding. It can also be speculated that the proposed methodology would perform better for systems other than RC buildings because they exhibit less complex hinging patterns that facilitate the estimation of their nonlinear behavior.

The evaluation of the proposed procedure is extended one step further by calculating the nonlinear response history analysis (RHA) of the equivalent single-degree-of-freedom (SDOF) systems that are idealized from the PO curves. Currently, this type of analysis is considered as conventional in simplified nonlinear procedures (ATC, 2004). The “*exact*” (computed from OpenSees) and “*approximate*” (computed from continuum model) PO curves are subjected to trilinear idealization to run the Takeda model (Takeda et al., 1970) in sdof nonlinear RHA. The resulting comparisons between the “*exact*” and “*approximate*” inelastic spectral displacements ($S_{d,ie}$) are presented in Figure F.11 for a total of 300 ground-motion records with moment magnitudes ranging between $5.0 \leq M_w \leq 7.9$ and distances less than 100 km. Ground motions are from active shallow tectonic regions and they are recorded at soft and stiff sites with shear-wave velocities in the upper 30 m soil profile ranging between 180 m/s and 760 m/s. The comparative scatters show the results of 1,800 nonlinear RHA (900 runs from the “*exact*” and 900 runs from the “*approximate*” idealized PO curves) that cover the entire building models considered here.

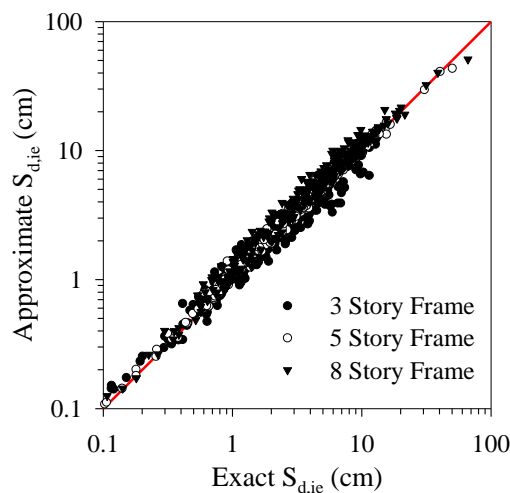


Figure F.11 Exact vs. approximate $S_{d,ie}$ computed from the idealized PO curves of discrete and continuum models

The comparisons in Figure F.11 indicate a good agreement between the $S_{d,ie}$ values determined through the “*exact*” and “*approximate*” PO curves. This observation reinforces the usefulness of the proposed methodology in the rapid assessment of large building stocks of similar geometrical and structural features.

F.9 Concluding Remarks

One of the major outcomes of this study is the description of a rational methodology to adapt the lateral stiffness variation of discrete buildings to continuum models. The proposed methodology accounts for the changes in the boundary conditions along the building height and defines the flexural (EI) and shear (GA) components of total lateral stiffness at the story levels. Moreover, it implements a correction to account for the differences in lateral loading patterns between the discrete and continuum models. This results in a more accurate estimation of lateral deformation profiles of discrete systems through the simplified continuum model. The procedure only requires the girder-to-column stiffness information, ρ , from a representative mid-story of the discrete system to achieve this objective. Such a simplification makes the continuum model more efficient in representing real structural systems and facilitates its implementation in simplified dynamic structural analysis similar to those proposed in Miranda and Akkar (2006) or Miranda and Taghavi (2005). The enhanced description of lateral stiffness variation in the continuum model leads to its practical use for approximating the nonlinear global capacity of building systems. Proper descriptions of global $M-\phi$ relationships at the story levels yield fairly similar pushover curves of building systems via continuum model. The current findings of this study show that the continuum model is capable of estimating the global nonlinear capacity of large building stocks without running detailed nonlinear structural analysis. This can be of use for risk and loss analysis of large building stocks that are composed of building systems exhibiting fairly the same structural features. The improvements brought to the continuum model are confined to the fundamental mode behavior of MRFs. If these improvements are extended for higher mode effects together with the consideration of torsional irregularity that is associated with 3-D behavior, the proposed procedure can become a more viable tool in damage assessment studies.

CURRICULUM VITAE

PERSONAL INFORMATION

Surname, Name: Erođlu Azak, Tuba
Nationality: Turkish (TC)
Date and Place of Birth: 22 February 1979, Ankara
Marital Status: Married
Phone: +90 312 210 74 44
Fax: +90 312 210 22 91
email: etuba@metu.edu.tr

EDUCATION

2003-2013 Ph.D., Civil Engineering, METU
1997-2002 BSc, Civil Engineering, Gazi University
1990-1997 Ankara Anadolu High School

WORK EXPERIENCE

2004-2013 METU Department of Civil Engineering, Research Assistant
2010-2011 EUCENTRE, Pavia, Italy, Researcher

FOREIGN LANGUAGES

Advanced English
Intermediate German

PUBLICATIONS

Türer, A., and Erođlu, T., 2004, "Condition Evaluation and Strengthening Techniques for Kayakapi Ruins in Turkey", FRP Composites in Civil Engineering-CICE 2004, 8-10 December 2004 Adelaide, Australia, pp. 969-975

Erođlu, T., and Türer, A., 2006, "Structural Health Monitoring-A Methodological Approach for Application.", Seventh International Congress on Advances in Civil Engineering, October 11-13, 2006 Yıldız Technical University, Istanbul, Turkey.

Türer, A., and Erođlu, T., 2006, "Structural Analysis of Historic Temple of Augustus at Ankara, Turkey.", V International Conference on Structural Analysis of Historical Constructions, November 6-8, 2006, New Delhi, India.

Eroglu, T. and Akkar, S., 2010, "A simplified continuum model for rapid estimation of nonlinear global capacity in discrete frame systems," 14th European Conference on Earthquake Engineering, Ohrid Skopje, Paper No.869.

Eroğlu, T. and Akkar, S., 2011, Lateral stiffness estimation in frames and its implementation to continuum models for linear and nonlinear static analysis, Bulletin of Earthquake Engineering, Vol 9(4), 1097-1114

Sousa, R., Eroğlu, T., Kazantzidou, D., Kohrangi, M., Sousa, L., Nascimbene, R. And Pinho, R., 2012, Effect of Different Modelling Assumptions on the Seismic Response of RC Structures, 15th World Conference on Earthquake Engineering, Lisbon Portugal, Paper No: 4333

Sousa, R., Eroğlu, T., Kazantzidou, D., Kohrangi, M., Sousa, L., Nascimbene, R. and Pinho, R., 2012, Using Nonlinear Static Procedures for the Seismic Assessment of Irregular RC Buildings, 15th World Conference on Earthquake Engineering, Lisbon Portugal, Paper No: 4343